Master Thesis

Adapting an in-cylinder process model to a 2-stroke Bolnes engine and preparations for ammonia-diesel operation

Frank Schenkel

Delft University of Technology
Marine Technology

Thesis for the degree of MSc in Marine Technology in the specialization of *Marine Engineering*

Adapting an in-cylinder process model to a 2-stroke Bolnes engine and preparations for ammonia-diesel operation

By

Frank Schenkel

Performed at

Chevron Oronite Technology B.V

This thesis MT.23/24.009.M. is classified as confidential in accordance with the general conditions for projects performed by the TUDelft

21 December 2023

Company supervisors

Responsible supervisor:	Ir. M. Verlinde	Chevron Oronite Technology B.V

Thesis exam committee

Chair:	Dr. ir. P. de Vos	Delft University of Technology
Staff Member:	Prof. dr. ir. B. J. Boersma	Delft University of Technology
Scientific Member:	Dr. ir. X.L.J. Seykens	TNO Helmond
Scientific Member:	Dr. ir. L.M.T. Somers	Eindhoven University of Technology
Scientific Member:	Prof. dr. D.J.E.M. Roekaerts	Delft University of Technology
Company Member:	Ir. M. Verlinde	Chevron Oronite Technology B.V

Author Details

Studynumber	4799224

TU Delft

Introduction

Abstract

To achieve the emission goals set out by the International Maritime Organization in 2018. Low or zero-carbon fuels will have to be used. Ammonia is considered to be a possible candidate since it doesn't contain carbon. This thesis will attempt to study two methods that characterize the closed-cylinder process of an internal combustion engine; the Seiliger approach and Wiebe function. Two things are the main focus of this thesis. Namely, the application of these methods and how this process will be different for ammonia-diesel combustion compared to diesel combustion. The application will be done for a two-stroke compression ignition engine. The operating conditions that are considered are four load points 20%, 40%, 60%, and 100% at a constant engine speed.

The application of this method means building an anti-causal and causal simulation model using Matlab Simulink. Both models simulate what happens in one cylinder during the closed-cylinder process, require the engine parameters as input, and produce the same results. The anti-causal model processes the pressure as a function of the crank angle to determine the combustion reaction rate. The causal model simulates the combustion reaction rate using a Wiebe function to determine the pressure. The Wiebe function is determined based on the reaction coordinate produced by the anti-causal model. By using the Wiebe function, the causal model produces smoother results than the anti-causal model. The Seiliger parameters are determined by using a Newton-Rhapson solver with the maximum pressure, maximum temperature, indicated work, and heat input as equivalence criteria.

The results produced by this thesis generally show that the constructed method can produce accurate results. However, this accuracy is correlated to the operating conditions of the engine. As for the changes necessary for ammonia-diesel combustion. These changes have been provided on a conceptual level, with conceptual meaning in terms of equations and assumptions. These changes have not been implemented into a computer model that has been verified and validated. The fundamental difference for the constructed method according to this thesis is the fact that the combustion parameters; start and end of combustion for the two fuels have to be incorporated in the combustion model used for the anti-causal and causal model. This change has to be made, along with assumptions that the injected fuel evaporates and combusts almost simultaneously. This assumption is considered to be highly questionable for ammonia.

Acknowledgements

This report has been written as the conclusion to my Master's program in Marine Technology at the University of Technology in Delft. I want to use this opportunity to thank all of the people who have assisted me during not only my Master's thesis but also during my time at the TU Delft as a whole.

First of all, I would like to thank my daily supervisor at the TU Delft Peter de Vos for his guidance during my Master's thesis. He was the one who introduced me to the concept of using ammonia as a fuel for an internal combustion engine and made it possible for me to make this the topic of my thesis. Second of all, I want to thank my supervisors at Chevron Oronite. I want to thank my daily supervisor Marcel Verlinde for his assistance in obtaining the right data for my Thesis. Additionally, I want to thank Peter van Houten for his feedback on my thesis.

Lastly, I want to thank all of my friends and family for their unwavering support during my entire time as a student. These last five years were challenging at times but with their support, I have enjoyed them and most of all, learned a lot.

Frank Schenkel
Delft, December 2023

Nomenclature

Symbol	Definition	Unit
a	*iso-volumetric pressure ratio Seiliger process*	$[-]$
a	*combustion efficiency parameter Wiebe*	$[-]$
A	*area*	$[m^2]$
A_B	*bore area*	$[m^2]$
b	*isobaric volume ratio in Seiliger process*	$[-]$
b	*weighting factor Wiebe*	$[-]$
c	*isothermal volume ratio in Seiliger process*	$[-]$
c_d	*orifice flow coefficient*	$[-]$
c_m	*mean piston speed*	$[m/s]$
c_p	*specific heat at constant pressure*	$[kJ/kg \cdot K]$
c_v	*specific heat at constant volume*	$[kJ/kg \cdot K]$
C_2	*empirical coefficient Woschni*	$[J/m^2K]$
C_3	*empirical coefficient Woschni*	$[-]$
C_4	*empirical coefficient Woschni*	$[-]$
D_B	*bore diameter*	$[m]$
E	*energy*	$[J]$
e_f	*energy of the fuel*	$[J/kg]$
f	*fraction of ammonia reacting compared to total reaction rate*	$[-]$
g	*gravitational constant*	$[m/s^2]$
h	*enthalpy*	$[J/kg]$
J	*polar moment of intertia*	$[m^4]$
L_{CR}	*Length of the connecting rod between the crank and cylinder*	$[m]$
L_s	*Stroke length*	$[m]$
m	*mass*	$[kg]$
m	*shape parameter Wiebe*	$[-]$
$\dot{m}$	*mass flow*	$[kg/s]$
M	*torque*	$[kNm]$
n_c	*polytropic exponent compression stroke Seiliger process*	$[-]$
n_e	*engine speed*	$[rpm]$
n_{exp}	*polytropic exponent expansion stroke Seiliger process*	$[-]$
n_{cyl}	*number of cylinders*	$[-]$
p	*pressure*	$[Pa]$
P	*power*	$[kW]$
Q	*heat*	$[kJ]$
$\dot{Q}$	*heat flow*	$[kW]$
r_c	*compression ratio Seiliger process*	$[-]$
r_{exp}	*expansion ratio Seiliger process*	$[-]$
R	*gas constant*	$[J/kg \cdot K]$
$S_A(0)$	*initial size zone A Sui MVEM*	$[-]$
t	*time*	$[s]$
T	*temperature*	$[K]$
u	*internal energy*	$[J/kg]$
v	*speed*	$[m/s]$
V	*volume*	$[m^3]$
W	*work*	$[kJ]$
$\dot{W}$	*work flow*	$[kW]$
w_t	*tangential swirl velocity*	$[m/s]$

Symbol	Definition	Unit
x	*compression stroke effectiveness*	$[-]$
x	*quality of the air mixture*	$[-]$
x_j	*mass fraction*	$[-]$
x_r	*fuel rack position*	$[-]$
X	*non-dimensional reaction coordinate Wiebe*	$[-]$
z	*height*	$[m]$
Z	*non-dimensional combustion reaction rate Wiebe*	$[-]$
α	*heat transfer coefficient*	$[J/m^2K]$
α	*crank angle*	$[-]$
γ	*ratio of specific heats*	$[-]$
ϵ	*geometric compression ratio*	$[-]$
ϵ_{INL}	*effectiveness air inlet*	$[-]$
η	*efficiency*	$[-]$
θ	*normalized temperature*	$[-]$
λ	*air excess ratio*	$[-]$
λ_{CR}	*crank/rod ratio*	$[-]$
ξ	*combustion reaction rate*	$[kg/s]$
π	*pressure ratio*	$[-]$
ρ	*density*	$[kg/m^3]$
σ	*stoichiometric air to fuel ratio*	$[-]$
τ	*temperature ratio*	$[-]$
τ	*non-dimensional time coefficient Wiebe*	$[-]$
ϕ	*crank angle*	$[°]$
χ	*ratio of specific heats at constant pressure*	$[-]$

Abbreviations

AFC	Alkaline Fuel Cell
AFR	Air to fuel ratio
AHRR	Apparent Heat Release Rate
ASR	Ammonia Substitution Ratio
BSFC	Brake Specific Fuel Consumption
BTE	Brake Thermal Efficiency
CAS	Crank Angle Solved
CFD	Computational Fluid Dynamics
CHT	Conjugate Heat Transfer
CI	Compression Ignition
CRR	Combustion Reaction Rate
DI	Direct Injection
EC	Exhaust valve closes
EGR	Exhaust Gas Recirculation
E&FMs	Emptying & Filling models
EO	Exhaust valve opens
EOC	End Of Combustion
FIP	Fuel Injection Pressure
GAHRR	Gross Apparent Heat Release Rate
GHG	Greenhouse Gasses
GWP	Global Warming Potential
HCCI	Hydro Carbon
HCCI	Homogeneous Compression Charge Ignition
HPDF	High-Pressure injection Dual Fuel
ICE	Internal Combustion Engine
IC	Inlet valve closes
IDI	Indirect Injection
IMO	International Maritime Organization
IO	Inlet valve opens
ISFOC	Indicated Specific Fuel Oil Consumption
ITE	Indicated Thermal Efficiency
KPI	Key Performance Indicators
LES	Large Eddy Simulation
LHV	Lower Heating Value
LPDF	Low-Pressure injection Dual Fuel
LSHFO	Low Sulpher Heavy Fuel Oil
MDO	Marine Diesel Oil
MDM	Multi-dimensional Model
MVEM	Mean Value Engine Model
MVFPP	Mean Value First Principle Parametric
NAHRR	Net Apparent Heat Release Rate
PEMFC	Proton Exchange Membrane Fuel Cell
PM	Particulate Matter
RCCI	Reactivity Controlled Compression Ignition
RCO	Reaction Coordinate
SCR	Selective Catalytic Reduction
SI	Spark Ignition
SOFC	Solid Oxide Fuel Cell
SOI	Start Of Injection
SOC	Start Of Combustion
SSE	Sum of Squared Errors
TDC	Top Dead Centre
URANS	Unsteady Reynolds Averaged Navier-Stokes
WAMs	Wave Action Models

Subscripts

a	Air
B	Brake
BDC	Bottom Dead Centre
comb	Combustion
bld	Mass of air in the cylinder when blowdown starts
bld-out	Mass of air blown out of the cylinder during blowdown
c	Charged conditions
c	Compression stroke
comb	Combustion
CR	Crank/rod
cv	Control volume
cyl-in	Air coming into the cylinder
cyl-out	Air coming out of the cylinder
e	Effective
e	Exhaust gas receiver
e	Engine
eq	Equivalent
exh	Exhaust gasses leaving the cylinder during blowdown
exp	Expansion stroke
f	Fuel
f	Friction
hl	Heat loss
i	Indicated
in+	Inflow including kinetic energy
inl	Inlet
kin	Kinetic
m	Mean
m	Mechanical
me	Mean effective
mi	Mean indicated
o	Outlet
out+	Outflow including kinetic energy
p	Piston
res	Residual still left from the previous cycle
ret	Retained air in the cylinder after scavenging
s	Stroke
s	Scavenging air receiver
sc	Scavenging
sc(0)	Start of scavenging
sc-out	Out due to scavenging
sc-tr	Trapped after scavenging
sg	Stoichiometric gass
t	Tangential
TC	Turbocharger
td	Thermodynamics
TDC	Top Bottom Centre
vol	Volumetric
0	Engine condition no fuel injected
1	Trapped condition
2	Stage 2 of the Seiliger process
3	Stage 3 of the Seiliger process
4	Stage 4 of the Seiliger process
5	Stage 5 of the Seiliger process
6	Stage 6 of the Seiliger process

Contents

List of Figures

List of Tables

1

Background information

In recent decades, the increased usage of fossil fuels for transportation, heating, and the generation of electricity has led to an increase in Greenhouse Gases (GHG). This alongside deforestation and a decrease in biodiversity reduces the ability of the earth to remove the most dominant greenhouse gas CO_2. This in turn has caused the increase in global temperature, with 90% of this warming happening between 1971 and 2010 (Nadeau et al., 2022). According to Lindsey and Blunden (2023), the ten warmest years recorded over the last 143 years have occurred since 2010. This rising temperature has increased the frequency of forest fires, flooding, heat waves, droughts, hurricanes, and dust storms.

According to the International Maritime Organization (IMO), global shipping accounted for 2.89% of global emissions in 2018 (Faber et al., 2021). That is why in that same year, the IMO set out as its goal to reduce annual GHG by at least half in 2050 compared to 2008. To do this, they say, low and zero-carbon fuels such as ammonia, hydrogen, methanol, and/or fuel cells are needed (International Maritime Organization, 2019). This is the reason why ammonia has been studied as a possible alternative fuel to decarbonize the Maritime Industry.

1.1. Ammonia as fuel in the Maritime Industry

There are some interesting examples throughout history of ammonia being used as fuel. In 1822 Sir Goldsworthy Gurney developed a locomotive that used ammonia gas and during World War II there was a massive shortage of diesel which meant engineers invented a way to use ammonia alongside coal for the public buses in Belgium (Di Blasio et al., 2022). Ammonia is now listed by the IMO as a possible zero-carbon alternative fuel that can be used to achieve the decarbonization of the Maritime Industry (International Maritime Organization, 2019). But what requirements does a potential new fuel have to meet for it to be a suitable candidate for the Maritime Industry?

Ships exist in a wide variety of sizes and types, and require, therefore, different approaches to achieve the set-out goals by the IMO. On the 22 of September, a fully electric ferry was commissioned in Norway (Prevljak, 2022). This ferry is fully powered by electricity supplied by batteries and can run on the same timetable as the diesel-powered ferry. The ferry can do this by constantly recharging when it has reached its destination (Tech HK, 2023). However, other ships do not have the luxury of being able to stop and recharge. Instead, they will be at sea for weeks which means batteries will not be a feasible option. This means they require more dense sources of energy such as zero or low-carbon fuels. Some characteristics of different fuels are listed in table 1.1. The table includes conventional fuel sources such as Low Sulphur Heavy Fuel Oil (LSHFO) and Marine Diesel Oil (MDO) but also alternative fuel sources such as hydrogen, ammonia, and methanol.

Table 1.1: Maritime fuel characteristics (Di Blasio et al., 2022)

Characteristics	MDO	LSHFO	Ammonia	Hydrogen	LNG	Methanol
Chemical formula	C_{10}-C_{15}	C_8-C_{25}	NH_3	H_2	CH_4	CH_3OH
Auto-ignition temperature (° C)	210	230	651	571-585	450-540	464
Lower heating value (MJ/kg)	43.5	≈ 43.5	18.5	120.1	38.1	19.9
Flame speed (cm/s)	87	≈ 87	14	270	38	50
Energy density (MJ/m^3)	36,403	≈ 36,403	11,333	2101/8539	22.020	15,600
Storage temperature (° C)	25	25	25	25/-253	-162	25
Storage pressure (bar)	1	1	10	248/1	1	1

The main reason for using either ammonia or hydrogen would be that they do not contain carbon or sulphur which means no CO_2 or SO_X emissions. Ammonia has one clear advantage over hydrogen: it is already one of the largest chemical industries in the world (Ayvalı et al., 2021). This means that the necessary infrastructure for production, transportation, and storage already exists. Important to note is that the production method of ammonia also influences whether the fuel is environmentally friendly or not. ”Brown” and ”blue” ammonia are produced from fossil fuels, with the difference being that blue ammonia production involves carbon capture which reduces the carbon intensity of the production process. However, ”green” ammonia is produced entirely through electrolysis by using renewable energy sources. Although green ammonia is currently more expensive to produce than brown ammonia these costs are expected to reach the same level by 2050 (Mallouppas et al., 2022). Another advantage ammonia has over hydrogen is its storage characteristics. Hydrogen has to be stored at either incredibly high pressure or low temperature, while the storage characteristics of ammonia are more favourable. Finally, despite hydrogen having a higher Lower Heating Value (LHV), it has a lower energy density than ammonia because of its storage characteristics.

The auto-ignition temperature of ammonia is an advantage but also a disadvantage. It makes ammonia safer to store but it means it will be more difficult to use in an Internal Combustion Engine (ICE). Ammonia also has some other disadvantages (Mallouppas et al., 2022):

- Ammonia has a very slow flame propagation speed compared to the other fuels.
- Ammonia is a highly corrosive and toxic substance meaning additional storage challenges.
- Ammonia has high NO_X emissions which means that exhaust after-treatment is required in the form of Selective Catalytic Reduction (SCR). The majority of NO_x emissions (≈90%) are NO with 5-10% being NO_2. Concerns surrounding NO_x emissions are the depletion of the ozone layer, NO_2 being an irritant gas that could cause a high accumulation of fluid in the lung tissue, and both NO and NO_2 being able to react with water and oxygen to form acid rain (Stapersma, 2010e).
- One other emission produced by ammonia also has cause for concern: N_2O. N_2O has a Global Warming Potential (GWP) of 280 times that of CO_2 (United Nations Climate Change, n.d.) over 20 years. This means that if N_2O is produced too much it could offset the benefits of reducing CO_2 emissions.
- Unburned ammonia emissions are also a reason for concern since ammonia gas is an irritating and corrosive gas (Department of Health, 2005).
- There is a current lack of regulations for the usage of ammonia in the Maritime Industry.

Ammonia has been studied as a possible fuel in the Maritime Industry for several different power plant concepts. Namely as fuel for an ICE, as fuel for a fuel cell (Kim et al., 2020), and as fuel for a gas turbine

(Chiong et al., 2021). There are many types of fuel cells possible in this power plant concept including a Solid Oxide Fuel Cell (SOFC), a Proton Exchange Membrane Fuel Cell (PEMFC), and an Alkaline Fuel Cell (AFC). The ammonia can either be directly used in a fuel cell as is the case for the SOFC or by cracking the ammonia into hydrogen and nitrogen. The latter uses ammonia instead of hydrogen because of its more favourable storage characteristics. As was mentioned, it is difficult to achieve combustion with ammonia in an ICE. There are two possibilities to solve this: by injecting another fuel next to ammonia or by using spark plugs (Ayvalı et al., 2021). Imhoff et al. (2021) found that using an ICE is more efficient than using a gas turbine. de Vries (2019) found that while using an SOFC is more efficient than using an ICE, an ICE is less expensive and more robust with an acceptable load response and power density. This is why using an ICE powered by ammonia is the preferred option. This explains why some major companies in the Maritime Industry are developing ammonia-fuelled ICEs. MAN Energy Solutions intends to have a commercially available two-stroke ammonia engine as early as 2024 (Lindstrand, n.d.) and has reported its first successful tests using ammonia in an ICE in July of 2023 (MAN Energy Solutions, 2023). Wärtsilä will coordinate a consortium of shipping stakeholders to develop demonstrators of four and two-stroke marine engines running on ammonia (Wärtsilä Corporation, 2022). WinGD and Hyundai Heavy Industries will cooperate to develop a two-stroke ICE capable of running on ammonia (Atchison, 2022).

1.2. AmmoniaDrive research project

In 2023, the AmmoniaDrive research project started. This project consists of a consortium of six Dutch universities, three Dutch applied research institutes, and 16 companies. The project is centred around a power plant concept that uses ammonia as its fuel and is shown in figure 1.1. The concept is a hybrid solution using both an ICE as well as a fuel cell. The ICE requires a so-called pilot fuel to achieve combustion with ammonia. This fuel is hydrogen, which is produced by the SOFC. The ammonia is thus both used in the SOFC as well as in the ICE. The fuel cell also generates electricity by creating hydrogen. This electricity can be used for propulsion, or/and for auxiliary power. As was also mentioned in the previous section a major disadvantage of using ammonia is that it has high NO_X emissions. To solve this problem SCR is used.

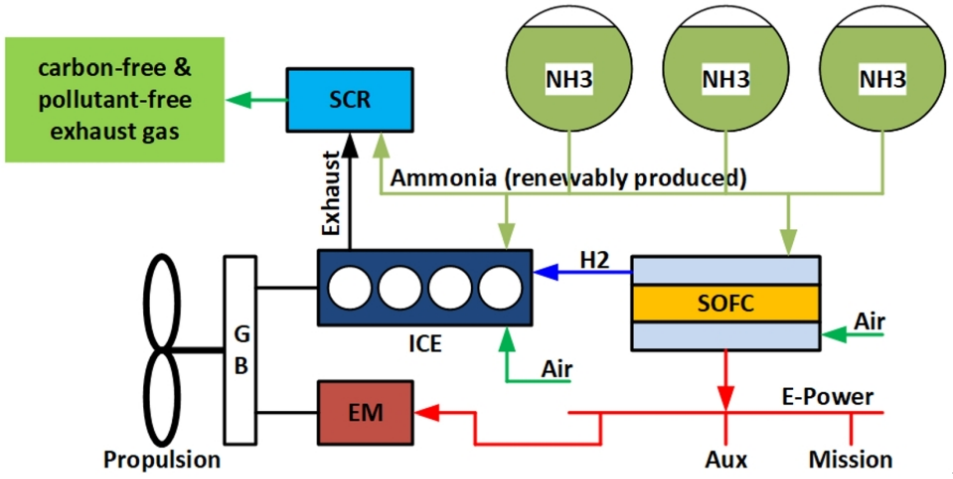

Figure 1.1: AmmoniaDrive power plant concept (de Vos et al., 2022)

This power plant setup is the main inspiration for this thesis to study ammonia as a fuel for an ICE. This chapter has discussed the relevant background information for this Master's thesis. The next chapter will focus on its research scope.

2

Research scope

This chapter will discuss the scope of this Master's thesis and the main research question it will try to answer. This thesis consists of two phases: a literature study and a main research part. The literature study is designed to accomplish two things. Namely to provide the necessary background information for the next phase and to identify the gap in the available literature this thesis will attempt to fill. The main research part consists of producing the necessary information to answer the main research question of this thesis. The main research question is supported by several sub-questions for further clarification. The main research question will be explained in section 2.1. The topics that were selected for the literature study will be discussed in section 2.2 along with the sub-research questions. The conclusions from the literature will be explained in chapter 6, along with the overall structure of the main research part of this thesis.

2.1. Main research question

One of the main objectives of the AmmoniaDrive research project is to investigate how the power plant concept performs on Key Performance Indicators (KPIs) like emissions, efficiency, cost-effectiveness, etc. A ship has to operate in various operating conditions so the power plant concept has to be capable of doing this as well. A model of the engine can be constructed to investigate the behaviour of an Internal Combustion Engine (ICE). There are several possible types of engine models, usually distinguished by their level of complexity. Generally speaking, more complex models provide more accurate insight into the engine's behaviour, but this comes at the price of a higher computational load. What type of model should be used depends on the application. If the application requires the model to simulate the engine cycle faster than in real-time, then some more complex models are not capable of doing this due to their high computational load. This thesis will focus on two possible methods for the modelling of the closed-cylinder process: the Seiliger approach and the Wiebe function. Ding (2011) already constructed a process of determining the necessary parameters for both methods, so his work will form the basis for the main research part of this thesis. This thesis hopes to expand on this process by answering the following research question:

How can the necessary parameters be found for both the Seiliger approach and Wiebe function to characterize the closed-cylinder process in an internal combustion engine and how will this process be different on a conceptual level when it attempts to characterize ammonia-diesel instead of diesel combustion?

Important to note is that the power plant of the AmmoniaDrive research project described in chapter 1 will be powered by a mixture of ammonia and hydrogen. However, the first step in researching the feasibility will be to analyse a mixture of ammonia and diesel. The process proposed by Ding (2011) requires measurements from an actual ICE. These measurements have been obtained from the company Chevron Oronite. The ICE in question is a two-stroke Bolnes engine. Unfortunately, the ICE has not been operating on a combination of ammonia-diesel fuel. This is why the research question specifically states that the proposed changes from this thesis will be provided on a conceptual level. Conceptual consists of assumptions, algorithms, relationships, and data that describe the reality of interest from

which a mathematical model and validation experimental can be constructed (Thacker et al., 2004). In essence, the process proposed by Ding (2011) will be analysed for each step to see where necessary changes should be made to analyse ammonia-diesel operation.

2.2. Topics and structure of the literature study

As was stated in the previous section, additional sub-research questions have been constructed to support the main research question. There are distinct questions for the literature study and the main research part. The questions for the main research part will be listed in chapter 6. The questions for the literature study are listed below:

- Why is ammonia considered a potential alternative fuel for the Maritime Industry?
- What is the definition of a mean value engine model? How does it compare to the other types of engine models and what is/are suitable application(s) for this kind of engine model?
- How is the closed-cylinder process of an internal combustion engine generally modelled in a mean value engine model?
- What are the main similarities and differences between the diesel combustion process and the ammonia combustion process?

These questions will be answered in chapter 6. Based on the main research question and associated sub-questions a set of topics were defined for the literature study. They can generally be divided into four categories: context, mean value engine modelling, diesel combustion process, and ammonia combustion process. The topics are listed below along with their related sub-topics.

Context:

- Ammonia as fuel in the Maritime Industry
- AmmoniaDrive power plant design

These topics were already discussed in chapter 1. They provide background information as to why this thesis will focus on ammonia as a fuel for the Maritime Industry and the power plant set-up of the AmmoniaDrive Research project.

Mean value engine modelling:

- Definition of an MVEM
- In-cylinder process in an MVEM
- In-cylinder process in the reference model
- Accuracy of an MVEM

The aforementioned Seiliger approach is commonly used in a Mean Value Engine Model (MVEM). The following set of topics concerns this type of engine model and is discussed in chapter 3. It starts by listing different complexity levels in terms of engine modelling. For this thesis, an already-developed engine model by Sui Congbiao (2021) was obtained as a reference model. The next two topics first discuss what techniques are commonly used in an MVEM to model the closed-cylinder process and what technique is used in the reference model. Finally, the chapter will discuss the accuracy of an MVEM.

Diesel combustion process:

- Ignition methods
- Injection strategies

- Heat release rate
- Heat losses

The expectation is that the largest difference between using ammonia as the primary fuel source will be in the combustion process which is why this topic will be investigated in more detail. These topics will go into more detail about the combustion process of diesel. The aforementioned Wiebe function is used for modelling the heat release rate and is also discussed in this chapter. These topics will be discussed in chapter 4

Ammonia combustion process:

- Ignition methods
- Injection strategies
- Mixtures
- Performance analysis
- Heat release rate
- Heat losses

The next set of topics concerns ammonia combustion. They are very similar to the topics selected for diesel combustion. That is intentionally done to say something about the difference between using diesel or ammonia as the primary source of fuel. Two topics were added to this category; mixtures and performance analysis. ”Mixtures” will discuss what ratio is used between ammonia and the ”pilot fuel”. Diesel is the main focus but since the literature can be limited, other secondary fuels are considered as well. At the same time ”performance analysis” will analyse whether conventional methods that are used for the performance analysis of diesel combustion can still be applied for ammonia. What is meant by performance analysis should be further specified since this term covers a wide range of parameters. This topic will first discuss what can be expected from ammonia in terms of engine efficiency. Secondly, it will discuss whether methods used in an MVEM can be used to calculate have already been used for ammonia. These topics will be discussed in chapter 5.

After the listed topics have been discussed, chapter 6 will discuss the main takeaways from the literature study. This chapter will also use these takeaways to discuss the overall project approach for the next phase of the thesis; the main research part. The contents of this thesis were also used to write a concept scientific article which is shown in appendix A. Some topics were originally included in the literature study. However, these topics were proven not to be relevant to the main research part of the thesis and have, therefore, been excluded. These topics are listed below:

- Non-cylinder components in an MVEM
- Non-cylinder components in the reference model
- Open-cylinder process in an MVEM
- Open-cylinder process in the reference model
- Emissions diesel combustion process
- Emissions ammonia combustion process

Interested readers can still read about the modelling of the non-cylinder components along with the open-cylinder process for both the reference model as well as generally for an MVEM in appendix B. The studied literature for both diesel as well as ammonia emissions is discussed in appendix C.

II

Literature Study

3

Mean value engine modelling

This chapter will discuss a few aspects of a Mean Value Engine Model (MVEM) that are relevant to this thesis. Section 3.1 will explain the definition of an MVEM and compare its advantages and disadvantages compared to other types of engine models along with possible applications. Section 3.2 will address how the closed-cylinder process is modelled in the studied literature for this thesis. Finally, section 3.3 will discuss what results are generally produced by an MVEM and their accuracy. Readers further interested in mean value engine modelling can find additional information in appendix B. The definition of the symbols, abbreviations, and subscripts used in this section can be found in the nomenclature of this report.

3.1. What is a mean value engine model?

When it comes to modelling an ICE, there are different types of models available. These can mainly be sorted based on their level of complexity. Their complexity ranges from simple linear transfer functions to complex 3D models using Computational Fluid Dynamics (CFD). What model is used depends on the application, with aspects such as accuracy and computational costs determining what type(s) of models are suitable (Alberer et al., 2012). The following groups of engine models were identified by both Alberer et al. (2012) as well as Rakopoulos and Giakoumis (2006):

- Mean Value Engine Models: these models generally neglect the in-cycle variation of physical quantities such as flow, pressure etc. Instead, they predict the average value of these variables. They can either be data-driven, which means they're derived empirically from obtained data of an ICE or they can use first principle thermodynamics such as mass and energy balances. The reference model for this thesis is an MVEM based on first principle thermodynamics. This is referred to by Sui Congbiao (2021) as a Mean Value First Principle Parametric (MVFPP) engine model.
- Emptying-and-filling models (E&FMs): these are often referred to as Crank Angle Solved (CAS) models. They use first-principle thermodynamics like MVEMs but additionally describe the in-cycle variations of the gas within the cylinder as well. They are a function of the crank angle rather than time which is why they are called CAS models. The Wiebe function and how it is used can be filed in this category. The application of this function will be discussed in more detail in chapters 4 and 9.
- Wave action models (WAMs). These models expand on the 0D representation of the in-cylinder process of CAS models by the inclusion of momentum conservation and thus representing wave effects. This creates a 1D representation of the inlet and exhaust manifolds as well.
- Multi-dimensional models (MDM): these models will use CFD and a detailed 3D system description. CFD is based on the Navier-Stokes equations.

The groups that were identified are listed based on their fidelity level. Multi-dimensional models are generally speaking the most accurate, but they require a lot of computational power and time. The characteristics for each group of engine models have been summarized in table 3.1.

Table 3.1: Different groups of engine models (Rakopoulos & Giakoumis, 2006)

	MVEM (empirical)	**MVEM (non-empirical**	**E&FMs**	**WAMs**	**Multi-dimensional**
Complexity	Very low	Low	Adequate	Adequate	High
Spatial resolution	0D	0D	0D	1D	3D
Physical description	Very low	Low	Low	Medium	Complex
Computational time required	Negligible	Negligible	Limited	Increased	Very large

Based on their computational efficiency, MVEMs are used for control applications when the cycle has to be repeated multiple times (Lee & Jung, 2016). For the same reason, they're also used to analyse transient engine behaviour, which they're able to simulate accurately (Theotokatos, 2010). They are also suitable to be used as a building block if the entire propulsion plant of a ship needs to be analysed (Sui et al., 2017). Important to note that if it is possible to calibrate an MVEM with existing experimental data, they can be more accurate than more complex models listed in table 3.1 (Alberer et al., 2012). However, if the same model is subsequently used for another engine they tend to struggle, in particular, if it is an empirically based MVEM. If the MVEM is thermodynamically based it will do a better job (Lee & Jung, 2016). Other limitations are listed below (Alberer et al., 2012):

- Because MVEMs neglect in-cycle variations of the pressure at the inlet and exhaust valves this can result in deviations of up to 20% in trapped air mass. This can be solved by using so-called volumetric efficiency maps.
- MVEMs do not include a detailed physical description of the air intake system, this can result in variations on a cylinder-to-cylinder basis for the trapped air.
- Exhaust Gas Recirculation (EGR) cannot be easily mapped in an MVEM.
- Because an MVEM does not include a detailed description of the combustion process it cannot accurately predict the formation of pollutants since they strongly depend on the in-cycle variation of the gas and fuel mixture in the cylinder.

As for the trapped conditions, the reference model developed by Sui Congbiao (2021) constructed a multi-zone gas exchange model to better approximate the scavenging process of a two-stroke ICE. Information about this model can be found in appendix B.

3.2. Modelling of closed cylinder process

As was mentioned in section 3.1, MVEMs generally neglect in-cycle variations of parameters such as pressure and temperature. However, this is not entirely true, as will be discussed in this section. In the literature that has been studied, the closed-cylinder process is modelled with varying degrees of complexity. The performance of the engine is for a large part determined by the brake power that is produced by the engine P_B. There are several possible approaches for calculating P_B. Theotokatos (2010) and Shen et al. (2020) both calculate the mean indicated pressure p_{mi}. p_{mi} is a function of the fuel rack position x_r and the combustion efficiency η_{comb} which is a function of the air-to-fuel ratio afr and the friction mean effective pressure p_f. x_r is adjusted by a PI-controller. This controller uses the error between the set engine speed $n_{e,set}$ and the actual engine speed n_e and adjusts x_r until the error is eventually reduced to zero. p_f is considered to be a linear function of the n_e and p_{mi}. The mean effective pressure p_{me} is calculated by subtracting p_f from p_{mi}. R. Li et al. (2013) calculate the effective torque M_e by subtracting the friction torque M_f from the indicated torque M_i. M_i is based on the indicated efficiency η_i, the fuel injected into the cylinder $\dot{m}_f$ and the Lower Heating Value (LHV) of the fuel. η_i is based on n_e and afr. M_f is based on n_e and the mean piston speed c_m. Guan et al. (2015) use a similar approach, but M_i is instead based on the maximum pressure in the cylinder and c_m. So although these approaches all use slightly different parameters, they are generally the same. The power is based on taking into account the engine efficiency and calculating the heat input

from the fuel that is injected into the cylinder while using an empirical relation for the mechanical losses.

Another method to calculate P_B is to use an air-standard analysis. This method approximates the pressure, volume, and temperature at different stages of the closed-cylinder process. These values can be used to calculate the power and heat input of the engine cycle. Several engine cycles can be used for this and for a detailed description as to how this can be done, please consult Moran's principles of engineering thermodynamics (Moran et al., 2017). Llamas and Eriksson (2019) use an ideal Otto cycle to calculate the indicated power P_i. They model the mechanical efficiency as a function of the engine speed to calculate P_B. The p-V and temperature-entropy (T-s) diagram of an Otto cycle are shown in figure 3.1.

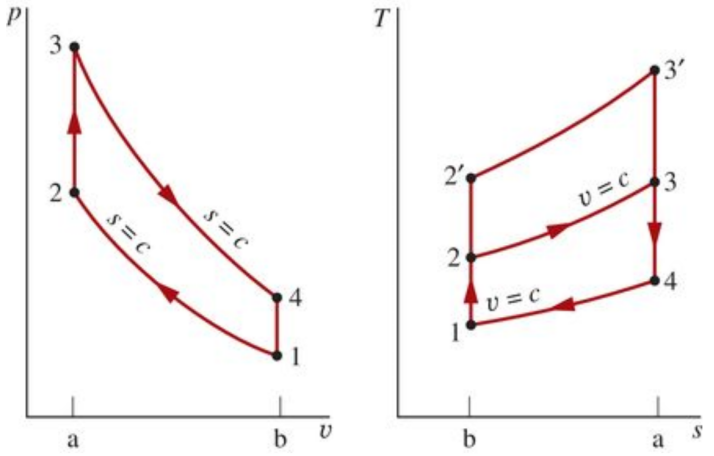

Figure 3.1: p-V and T-s diagram of an Otto cycle (Moran et al., 2017)

S. Zhu et al. (2020) use a similar approach but use a combination of the standard diesel and Miller cycle. The p-V diagram is shown in figure 3.2 for both cycles. The mechanical losses are computed based on the maximum pressure p_{max} and c_m. Using an air-standard analysis, therefore, doesn't completely ignore the pressure and temperature variations of the in-cylinder process. However, only considering these variations at distinct points during the cycle instead of the entire cycle can save a lot of computational time.

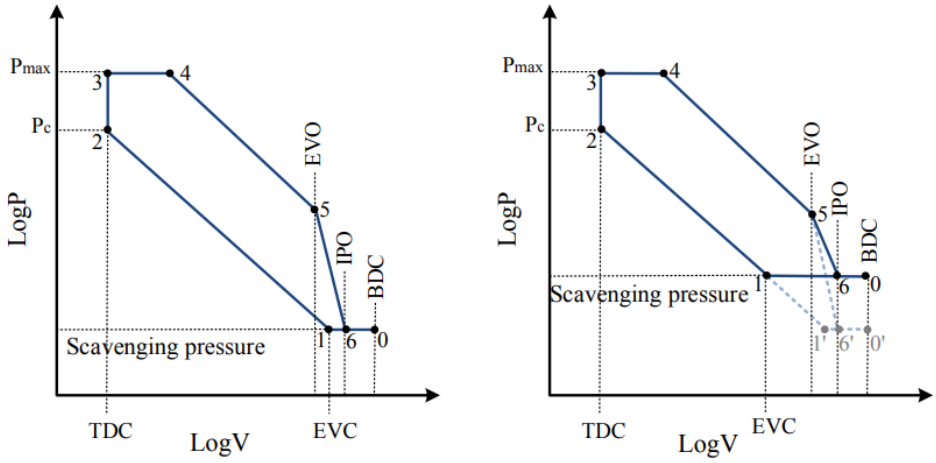

Figure 3.2: p-V and T-s diagram of a standard diesel cycle (left) and miller cycle (right) (S. Zhu et al., 2020)

Some of the studied literature choose to expand the MVEM to incorporate elements of a CAS model. The danger of doing this is that the computational load could become too high. The authors, therefore, try to deal with this problem. Shen et al. (2020) expand an MVEM to include the variation of the

in-cylinder pressure as a function of the crank angle. The pressure variation is based on an analytical model, because this means there is no need to solve any differential equations it doesn't increase the computational load of the model that much. Tang et al. (2017) also incorporate some elements of a CAS model. The in-cylinder pressure along with M_i is calculated by the CAS model, while the mass flow and temperature are calculated using an MVEM. The authors simplify the calculation method for the in-cylinder pressure during the gas exchange process since the pressure is mostly constant during this phase. Doing this saves around 33% of the computational load.

The obtained reference model for this thesis developed by Sui Congbiao (2021) uses an air-standard analysis to model the closed-cylinder process. The model uses the Seiliger approach. This process consists of using the so-called Seiliger parameters to relate the pressure, temperature, and volume at different stages of the closed-cylinder process along with determining the heat input and indicated work. Because finding these Seiliger parameters is explained in chapter 8 the Seiliger process is discussed in detail here as well.

3.3. Results and accuracy

Having discussed the general techniques used for the closed-cylinder process in an MVEM. The question is what kind of results does an MVEM produce and how accurate are those results? An example of the results that are produced by an MVEM is shown in table 3.2.

Parameter	**Engine load MCR %**			
	100	75	50	25
	Error %			
Brake power	-1.02	-1.01	-0.99	-0.92
Brake specific fuel consumption	0.16	0.55	-0.08	0.18
Maximum cylinder pressure	0.71	0.07	-1.46	-0.59
Turbocharger speed	0.03	-0.41	-1.47	-4.52
Scavenging air receiver pressure	1.39	0.40	-0.89	-0.54
Exhaust gas receiver pressure	-0.20	-2.23	-4.11	-3.13
Scavenging air receiver temperature	-0.72	-0.39	-0.45	-0.24
Exhaust gas receiver temperature	2.52	-1.18	-0.99	-3.25

Table 3.2: Results produced by an MVEM (Guan et al., 2015)

The results shown in table 3.2 were reported by Guan et al. (2015). Generally, the accuracy lies within a margin of 5%. This seems to be common among the studied literature, with Llamas and Eriksson (2019) reporting an accuracy of 3.35% and Alegret et al. (2015) around 6.28%. Important to note is that Llamas and Eriksson (2019) concluded that the model could produce accurate results for both static as well as dynamic operations. As was eluded to in section 3.1, EGR cannot be easily mapped in an MVEM. This was also concluded by Llamas and Eriksson (2019) who stated that the accuracy decreased when EGR was introduced in their model.

Both Shen et al. (2020) as well as Tang et al. (2017) constructed a CAS model for the in-cylinder pressure. The results are plotted against the measured data as is shown in figure 3.3 and 3.4 respectively. Looking at both figures it can be concluded that the calculated in-cylinder pressure matches the experimental results really well.

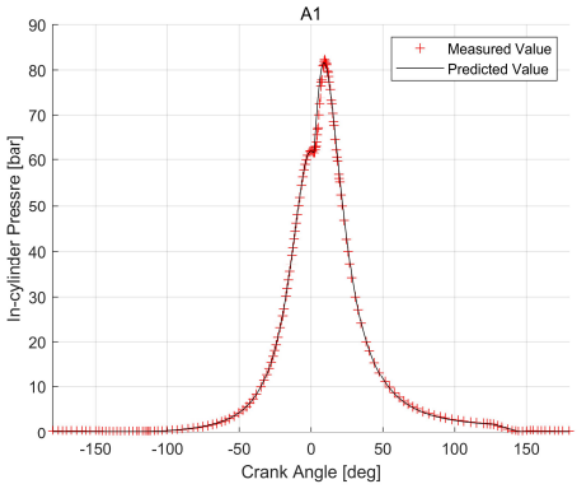

Figure 3.3: In-cylinder pressure as a function of the crank angle ϕ (Shen et al., 2020)

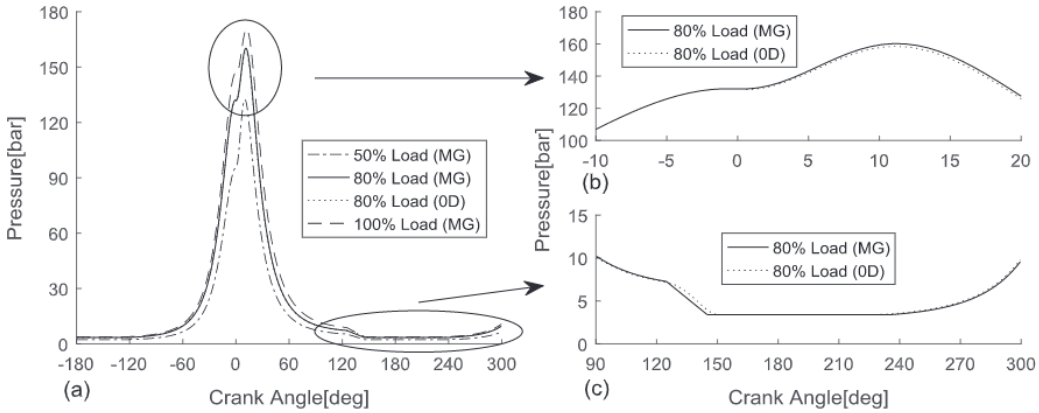

Figure 3.4: In-cylinder pressure as a function of the crank angle ϕ (Tang et al., 2017)

The chapter has discussed the definition of an MVEM, along with its limitations and how it compares to other available engine models. The main focus has been on the techniques used to model the closed-cylinder process. The next chapter will look in more detail at the combustion process.

4

Diesel combustion process

This chapter will take a closer look at the combustion process in an Internal Combustion Engine (ICE). This chapter will start by providing some information about the ignition methods and injection strategies. This will be done in sections 4.1 and 4.2 respectively. After that, section 4.3 will explain how the heat release rate can be modelled. Similar to general engine modelling discussed in chapter 3 this can be done with varying degrees of complexity. This section will also introduce the Wiebe function which was mentioned in chapter 2. Finally, the heat losses that occur in an ICE and how they are modelled are discussed in section 4.4.

This chapter will discuss ignition methods such as spark ignition and compression ignition. However, because the engine used to obtain experimental data is a two-stroke compression ignition engine, the main focus will be on this type of ICE. How the heat is released during combustion in the cylinder is of primary importance for the pollutants that will be formed. This is why the emissions were originally included in the literature study, along with possible equations to calculate them. However, these topics did not prove to be relevant for the main research part of this Master's thesis and have, therefore, been excluded. Interested readers can still read about the studied literature in appendix C. The definition of the symbols, abbreviations, and subscripts used in this section can be found in the nomenclature of this report.

4.1. Ignition methods

Two main methods can be distinguished when talking about achieving ignition in an ICE. These two methods are Spark Ignition (SI), which is commonly used in petrol-powered engines, and Compression Ignition (CI), which is commonly used in diesel engines (Zheng, 2020). CI achieves ignition by compressing the air and fuel when the piston is moving upwards. Eventually, a combination of the pressure and temperature exceeds a certain threshold causing the ignition to take place (Stapersma, 2010d). SI achieves ignition by producing a spark within the cylinder (Stone, 1999). To determine the threshold for a CI engine, an explosion diagram as shown in figure 4.1 can be used.

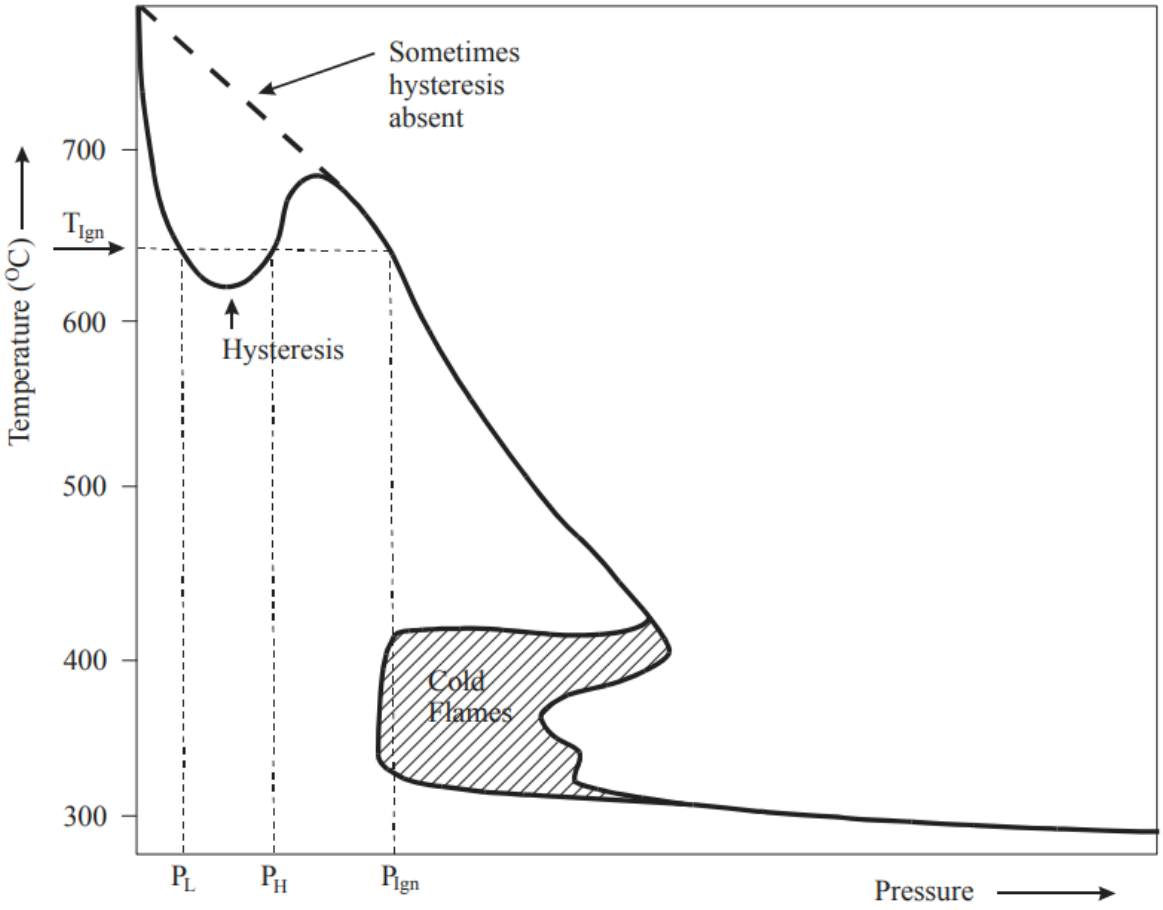

Figure 4.1: Explosion diagram example (Stapersma, 2010d)

There are also more advanced methods of ignition methods available such as Homogeneous Compression Charge Ignition (HCCI). This method mixes gaseous fuel with air before it enters the combustion chamber of the engine (Zheng, 2020). HCCI can reduce the amount of Nitrogen-Oxide emissions NO_X and Particulate Matter PM, whilst simultaneously achieving high thermal efficiency with an ability to work with a wide variety of fuels (Zhao et al., 2003). However, there are still major challenges associated with HCCI such as high Hydro-Carbon (HC) and Carbon-mono-Oxide (CO) emissions, cold-start problems, combustion phase control, and extension of the operation range (Yao et al., 2009).

Another ignition concept is Reactivity Controlled Compression Ignition (RCCI). This method uses two types of fuel with both having different auto-ignition characteristics to control both the phasing as well as the duration of the combustion process (Zheng, 2020). Similar to HCCI, RCCI reduces the NO_X emissions as well but both the HC and CO emissions are higher compared to a conventional diesel ICE because of the lower peak temperatures that are achieved by using RCCI (Paykani et al., 2016). Paykani et al. (2016) also concluded that RCCI has a higher indicated efficiency compared to HCCI because of its lower heat losses. A higher in-cylinder temperature leads to more NO_x emissions but reduces the HC and PM emissions and vice-versa. This trade-off is often referred to as the ”Diesel Dilemma” (Stapersma, 2010e).

4.2. Injection strategies

For SI engines, the common practice is to inject the fuel into the air intake manifold instead of the cylinder because otherwise, the injectors would have to withstand the high temperatures and build-up of combustion deposits in the cylinder. For a CI engine fuel is injected either through Direct Injection (DI) or In-Direct Injection (IDI) (Stone, 1999). Injection pressures for CI engines have risen significantly

throughout history. First, because of turbocharging, more fuel is required in combination with the additional air by the turbocharger. Current injection pressures can exceed 2000 [bar] to suffice a shorter injection time and a late start of injection (Stapersma, 2010d). Stapersma (2010d) also stated that the start of late injection is implemented to reduce NO_x emissions while shortening the overall injection time is used to reduce the formation of HC and soot formation.

Several injection techniques have been researched to determine whether they can improve the performance of an ICE and in particular the emissions. Kontoulis et al. (2008) concluded that pilot injections of the fuel before the majority of the fuel is injected could improve the overall performance of the engine without contributing to the NO_x emissions. E. Zhang et al. (2019) also looked at pilot injection and additionally at post-injection. The authors concluded that pilot injection could improve the trade-off between NO_x emissions and soot. The authors also concluded that post-injection could lead to a reduction of 82% in soot with an increase of 18.1% for NO_x emissions. Seol et al. (2021) concluded that a double-injection method, the injection of the fuel in two phases instead of one, can lead to a reduction of NO emissions of 24.16% and soot by 68%. However, the double-injection method increases carbon dioxide CO_2 emissions by 7.58% and increases the Indicated Specific Fuel Oil Consumption (ISFOC) by 23.55%. Ji et al. (2019) concluded that water added to the cylinder could also lead to a reduction in NO_x emissions.

Jayashankara and Ganesan (2010) looked at the effects of injection timing through Computational Fluid Dynamics (CFD) analysis. They concluded that early injection would result in an increase in the in-cylinder pressure, temperature, heat release, and NO_x emissions. A late injection will result in a decrease in the above-mentioned parameters. Agarwal et al. (2013) looked at both injection timing as well as Fuel Injection Pressure (FIP). The authors concluded that the engine performed best at low FIPs meaning a lower Brake Specific Fuel Consumption (BSFC) and a higher Brake Thermal Efficiency (BTE). Both can further be improved by advancing the Start Of Injection (SOI).

4.3. Heat release rate

As was already eluded to in sections 4.1 and 4.2 the in-cylinder variations that occur in an ICE have a large effect on the emissions and performance of the ICE. Specifically, the heat release rate during combustion will have a large effect. The combustion process of an ICE can be divided into four different phases according to Stapersma (2010d):

- Ignition delay: as the fuel is injected into the cylinder there is an apparent period for which the ignition threshold has not been reached yet. This means there is a delay between the fuel injection and the start of heat being released in the cylinder.
- Premixed combustion: when the threshold is eventually reached the large quantity of fuel that was already present in the cylinder ignites as well causing the peak in the heat release.
- Diffusive combustion: the fuel that is injected into the cylinder ignites almost immediately, causing the heat release rate to be in step with the fuel injection rate.
- Late combustion phase: the latter part of the diffusive combustion phase slowly decays at the end of the expansion stroke which is why it is often referred to as the late combustion phase.

These four combustion phases along with the fuel injection rate, in-cylinder pressure, in-cylinder temperature, and heat release rate are shown in figure 4.2.

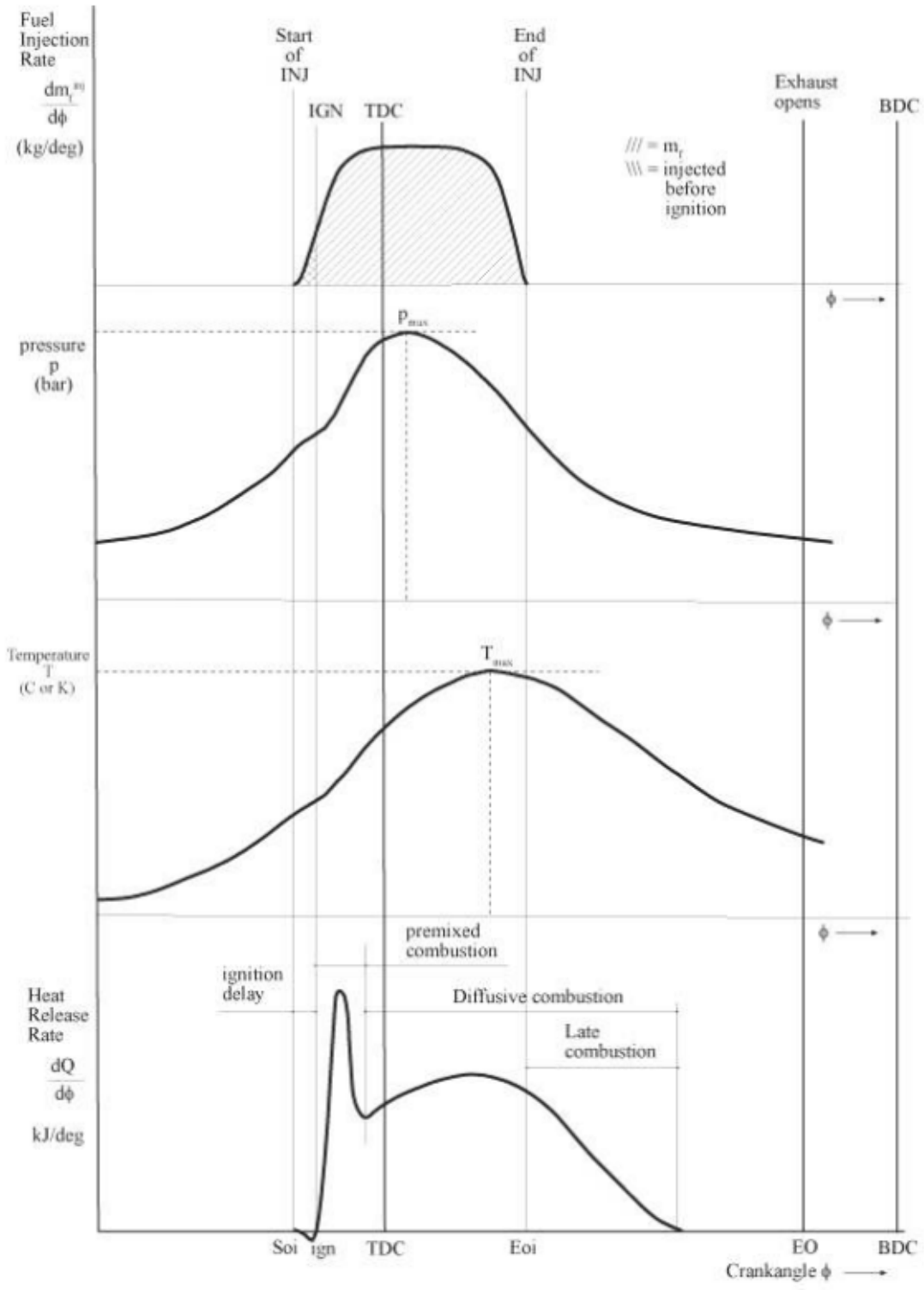

Figure 4.2: Fuel injection rate, pressure, temperature, heat release rate during different combustion phases (Stapersma, 2010d)

Modelling the heat release rate during combustion is extensively researched in the literature that has been studied. However, it is not possible to measure the heat release directly within the cylinder. Instead, the in-cylinder pressure is used alongside first-principle thermodynamics (Stapersma, 2010d), (Ding, 2011). Typically, there are three different categories of combustion models according to Ding (2011): a thermodynamic or zero-dimensional model, a phenomenological or quasi-dimensional model,

or a CFD/multidimensional model. These models are listed based on their respective increasing levels of complexity. The remaining part of this section will introduce some different types of heat release models found in the literature. These models will be discussed according to the aforementioned categories.

A zero-dimensional model for the heat release rate was developed by Ma et al. (2015). This model uses the Krieger and Borman approach. This approach computes the in-cylinder pressure as a function of the fuel-burning rate. The model uses the first law of thermodynamics along with the ideal gas law. The model assumes a thermodynamic equilibrium during the in-cylinder combustion process. The model ignores temperature gradients, pressure waves, nonequilibrium conditions, fuel vaporization, and mixing. The final equation for the heat release rate is a function of the specific heat ratio, in-cylinder pressure, cylinder volume, and crank angle. Ding (2011) constructed a zero-dimensional model as well. The derivative of the in-cylinder temperature w.r.t. time is based on the combustion heat, heat losses, fuel energy, in-cylinder pressure, and derivative of the volume w.r.t. time. The combustion heat is calculated by using the Combustion Reaction Rate (CRR). CRR (ξ) is estimated with a Wiebe function. The fuel energy accounts for two things: the difference caused by the phase change of the fuel from liquid to gas, and the difference between the fuel injection pressure and in-cylinder pressure. Finally, the model takes into account the heat losses to the cylinder wall, cylinder cover, and piston crown. The heat losses are based on the temperature in the cylinder, the temperature of the considered component, the area of the considered component and the heat transfer coefficient. The temperatures of the considered components are estimated and kept constant, the heat transfer coefficient is based on the semi-empirical methods developed by Woschni (this will be further discussed in section 4.4). Because some of the mentioned parameters depend on each other, the model requires a structure as is shown in figure 4.3 so it can be solved numerically. This method will form the basis for the main research part of this thesis and is therefore discussed in more detail in chapter 7.

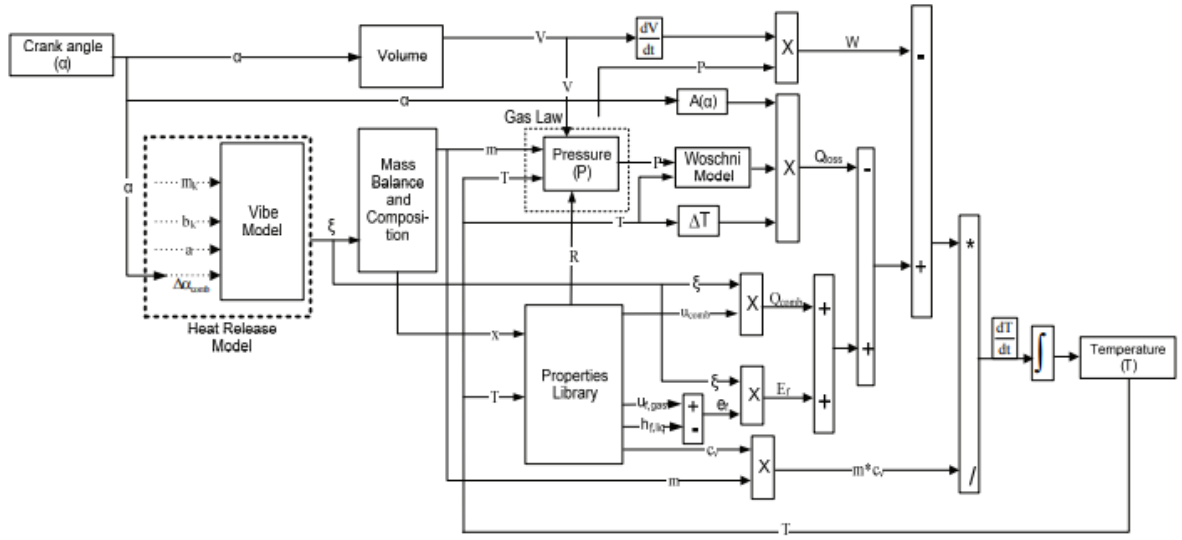

Figure 4.3: In-cylinder process model (Ding, 2011)

Raptotasios et al. (2015) developed a phenomenological multi-zone combustion model to evaluate the engine's performance and NO_x emissions. The model divides the fuel spray into discrete zones with 5 and 8 zones for the radial and circumferential directions respectively. The model assumes a constant pressure for the entire combustion chamber, but each zone does have a distinct temperature and composition. To predict the conditions in each individual zone, the first law of thermodynamics along with mass and energy conservation is used. The model produces accurate results for the in-cylinder pressure when these are compared to experimental data as is shown in figure 4.4.

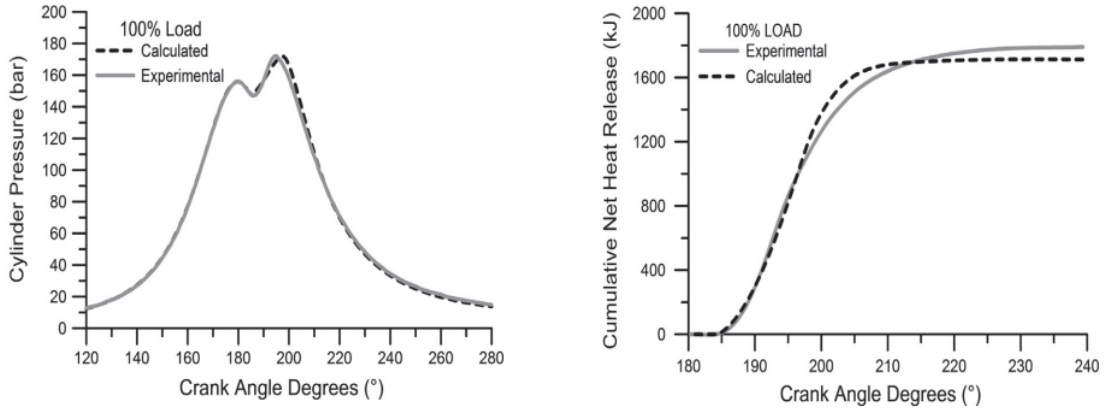

Figure 4.4: Results for heat release and pressure compared to experimental data (Raptotasios et al., 2015)

A similar multi-zone combustion model is used by both Muše et al. (2020) and Jurić et al. (2022). The fuel spray is once again divided into individual zones in the radial and circumferential directions. It is assumed that there is no mixing or passing between the zones. The zones are generated for each time step of the fuel injection process. Each individual zone has its own progression of temperature, pressure, and composition. The combustion is assumed to begin for each zone once the ignition delay time has elapsed. The heat release is calculated for each zone individually by using reaction kinetics. The model shows a good ability to predict the in-cylinder pressure (accurate within 1%) and can predict the engine power and specific fuel consumption with an accuracy of around 5%.

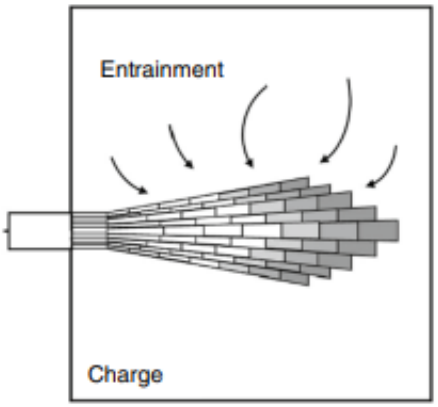

Figure 4.5: Multi-zone fuel spray model (Muše et al., 2020)

Sun et al. (2017) compared two different CFD combustion models along with two different alternative fuels. All of the CFD models can predict the in-cylinder pressure accurately with a maximum deviation of 4.1%. Important to note is that the authors conclude that the combustion models have almost the same integrated heat release. However, the contours of the temperatures and emissions are different. This is the reason, according to the authors, that the models compute different results for the engine performance. Important as well is that from these results, it can be concluded that the shape of the heat release rate influences the emissions since the integrated heat release is the same but the contour and emissions are different. Nemati et al. (2022) compare two different CFD turbulence methods: Unsteady Reynolds Averaged Navier-Stokes (URANS) and Large Eddy Simulation (LES). The models can predict both the compression and peak pressure in the cylinder with an accuracy of 2% and 4% respectively compared to experimental data.

4.4. Heat losses

Modelling the in-cylinder heat losses accurately is important for determining engine performance (Stapersma, 2010e). However, modelling the heat transfer that occurs between the gas to the cylinder walls has proven to be complicated (Dahlström, 2016). According to Stapersma (2010e), the most heat is lost during the combustion because of the large heat loss flux, specifically in the crank angle segment just after the cylinder has reached Top Dead Centre (TDC). Stapersma (2010e) also stated that although the heat loss flux is lower during the expansion and compression stroke, there will still be heat losses to the cylinder walls because of the larger area that is exposed. Despite the larger exposed area, however, the heat transfer during the gas exchange process is small compared to the total heat transfer (Stone, 1999). Sigurdsson et al. (2014) studied the convective heat transfer during the scavenging of a low-speed two-stroke ICE. They concluded that the convective contribution to the in-cylinder heat losses is around 3.2% of the fuel energy flow.

Similar to modelling the heat release rate discussed in section 4.3, modelling the heat losses in the cylinder is done with varying degrees of complexity. Several empirical attempts have been made, but CFD has also been applied. According to Moran et al. (2017), there are three mechanisms of heat transfer:

- Conduction: Takes place between solid, liquid and gaseous substances. It is defined as the transfer of energy from energetic particles to adjacent particles that contain less energy.
- Convection: Energy transfer between a solid surface and an adjacent gas or liquid which has a different temperature. The heat which is transported is mainly the result of macroscopic fluid flow (Stapersma, 2010e).
- Radiation: Energy transfer as a result of changes within the electronic configurations of the atoms. Radiation requires no medium for the energy to be transferred, unlike convection and conduction.

For determining the heat losses, Stapersma (2010b) categorized the heat losses into three main areas: cylinder head, piston crown and the cylinder wall as is shown in figure 4.6.

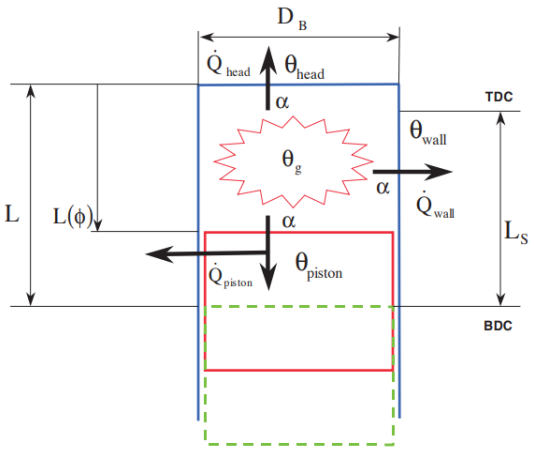

Figure 4.6: Cylinder heat losses (Stapersma, 2010b)

The heat losses can be categorized according to equation B.7

$$\dot{Q}_{loss} = \alpha \cdot A \cdot (T_g - T_w) \tag{4.1}$$

With α, A, T_g, T_w being the heat transfer coefficient, area, gas temperature, and temperature of the wall respectively. Now the equation on its own is not very complicated. However, α, T_g, T_w all vary both in space as well as in time. For the cylinder wall, even A is a function of time. Stapersma (2010e) concluded that there are reasonable assumptions that can be made for the temperature and area. This is solved by taking some sort of average, mean, or mean effective value to calculate the mean heat flow.

The difficulty lies, however, in estimating α from empirical data. Several attempts have been made over the last century to estimate α, some examples are Eichelberg (1922) and Eichelberg (1939), Elser (1954), Sitkei (1962), Annand (1963), and Woschni (1967). However, these methods are sometimes more than 50 years old. So are these methods capable of predicting the heat losses in an ICE?

Finol and Robinson (2006) concluded that the different methods to estimate the heat losses produce large variations. In addition to this, significant improvements are absent by using more complicated equations and the authors state that it makes little sense to include a single value for the gas temperature and pressure despite its enormous spatial and temporal variation. Because of this, it makes using the methods for estimating heat losses highly questionable. Žák et al. (2016) came to the same conclusion. The authors state the frequently used models cannot deliver the desired level of accuracy and are therefore not suitable for predicting the in-cylinder heat transfer. However, the authors do state that it's possible to adjust the formulas to make them suitable for a unique application. De Cuyper et al. (2017) came to a different conclusion. The authors evaluated the Woschni and Annand models and state that even with calibration, both models are still unable to predict both the peak heat flux as well as the total amount of heat loss. They did this by comparing the results for both models to date from fill gauge heat flux sensors. Important to note is that De Cuyper et al. (2017) studied SI engines for their research. Further research into calibration was done by Y. Zhang et al. (2022). The authors attempted to adjust the Woschni method for operation at different altitudes. To do this, a temperature index m was introduced. m was used as a key correction variable. The relation between m, the altitude, and the engine speed was fitted by using the least-squares method. The resulting average heat transfer coefficient increased by 45.69% after calibration so the authors concluded that the traditional Woschni model was unsuitable for operation at different altitudes. However, the modified method was able to predict the results with an accuracy of around 5%. This means that the modified method can operate under various operating conditions. Xin and Zheng (2009) developed a model for the estimation of the miscellaneous heat losses of an ICE. The model uses theoretical, numerical, experimental, and empirical approaches. From their theoretical approach, the authors concluded that the miscellaneous heat losses are a function of the gas temperature, surrounding temperature of ambient air, engine speed, and engine load. The authors use a constructed equation based on this relation and then fit the equation with experimental data. The authors conclude based on their results. The expression is validated by comparing it to a GT-POWER simulation, which is an industry-standard engine performance simulation (GAMMA Technologies, 2023). The authors conclude, based on their results, that an empirical expression can be used to estimate the miscellaneous heat losses.

If a more detailed description of the in-cylinder heat transfer mechanisms is required then other methods have to be used. Broatch et al. (2019) stated that using 0D-1D models does not provide a detailed description of, for example, the temperature distribution on the different surfaces in the cylinder. CFD can be applied but has one major drawback, namely the heat loss through the engine walls cannot be modelled accurately. To do this, some form of a Finite Element Method (FEM) has to be used but this makes the overall approach computationally inefficient. A better approach is to use the Conjugate Heat Transfer (CHT) method. This approach can simultaneously solve the solid and fluid regions through a unique computational iterative process. However, CHT requires the solid parts of the ICE to have a very fine mesh which increases the computational time. Rakopoulos et al. (2010) analysed four popular CFD methods for determining heat transfer in a variety of engine types and configurations. The paper also constructs its own CFD method. From the results, it can be concluded that even some popular CFD methods fail to capture the heat transfer mechanisms accurately. Important to note is that in contrast to some of the 0D-1D methods mentioned previously in this section, no tuning/calibration efforts were made for any of the CFD methods. Y. Li and Kong (2011) developed a CHT for the prediction of heat conduction in the solid domain and spray combustion in the fluid domain of the cylinder. The constructed method can be used for a multi-dimensional engine simulation. The model can predict both the spatial as well as temporal variation of the temperature on the combustion chamber surface.

This chapter has discussed the ignition methods, injection strategies, modelling of the heat release rate, and modelling of the heat losses for diesel combustion in an ICE. The next chapter will focus on roughly the same topics but then on ammonia combustion.

5

Ammonia combustion process

This chapter will discuss the combustion of ammonia in an Internal Combustion Engine (ICE). As was mentioned in chapter 1 of this report, ammonia alone is considered to be unsuitable as a fuel for an ICE, which is why another fuel is often injected along with ammonia to achieve combustion. Different possible fuels can be injected alongside ammonia as section 5.1 will discuss. However, for this chapter, only the combustion of diesel or hydrogen with ammonia will be discussed. The reason for this has already been explained in chapters 1 and 2 of this report. Namely, the AmmoniaDrive Power plant concept will use hydrogen, but the goal of this thesis is to study the combustion of ammonia with diesel. This chapter is written with a similar set of topics compared to chapter 4. The reason for this is that one of the primary questions the literature study will try to answer is what the differences are between diesel and ammonia-diesel combustion. Section 5.1 will therefore discuss the found ignition methods for an ammonia-fueled ICE. Section 5.2 will address the injection strategies that are used. Section 5.3 will discuss the ratio of ammonia and the used ”pilot fuel” and how it affects the combustion process. The performance analysis of the ammonia combustion process will be discussed in section 5.4. Finally, the heat release rate and heat losses will be addressed in section 5.5 and 5.6, respectively. Similar to chapter 4, emissions were originally studied for ammonia combustion as well but are not included in this chapter. Interested readers can still read about emissions in appendix C. The definition of the symbols, abbreviations, and subscripts used in this section can be found in the nomenclature of this report.

5.1. Ignition methods

As was discussed in chapter 1 of this report, it is difficult to achieve combustion with ammonia due to its high auto-ignition temperature, slow flame speed, and narrow flammability (T. Li et al., 2022). Therefore, to use ammonia in an engine two methods can be used to achieve combustion. Either the fuel is ignited through Spark Ignition (SI) or Compression Ignition (CI) in combination with another high-reactivity fuel (Liu, Wu, et al., 2022). The usage of only ammonia as a fuel for a CI engine has been researched in the past. However, only engine designs with high compression ratios of 35:1 to 100:1 could achieve combustion (Dimitriou & Javaid, 2020). In comparison, the compression ratio for diesel engines lies typically between 12:1 to 20:1 (Stapersma, 2010b). Large two-stroke engines still serve as the primary source of propulsion for ocean shipping today (J. Zhu et al., 2023). However, the enormous ignition energy that is required for large-bore marine engines limits the usage of SI engines which is why most ammonia applications use CI engines. (Liu, Wu, et al., 2022).

So to achieve the combustion of ammonia in a CI engine a secondary highly reactive fuel is needed. This fuel is often referred to as pilot fuel. Many different fuels can be used as pilot fuel. Including natural gas, methanol, diesel, and gasoline, which are fuels that still contain carbon (Y. Wang et al., 2023). This method will therefore reduce Greenhouse Gas (GHG) emissions but not eliminate them. An example of a carbon-free pilot fuel is hydrogen (Koekkoek, 2021). Hydrogen can also be used for SI engines as a combustion promoter (Lhuillier et al., 2020). Ammonia can also be mixed with a

highly reactive substance such as H_2O_2 or NH_4NO_2 (Y. Wang et al., 2023). When diesel is used as pilot fuel, researchers have determined that combustion can be achieved with compression ratios as low as 15.2:1, with the minimum compression ratio for the stable operation being highly dependent on the cetane number of the pilot fuel (Dimitriou & Javaid, 2020). Y. Wang et al. (2023) studied the feasibility of using a hydrogen jet flame to achieve combustion. This is the practice of using SI to ignite hydrogen in the pre-combustion chamber to form a hydrogen jet flame. This jet flame is used to achieve the ignition of ammonia in the cylinder. This practice only requires 1.68% hydrogen to meet full-load power output. The practice also results in such a low overall in-cylinder combustion temperature that the NO_x emissions can meet the emission standard of tier II and in some cases even the standard of tier III. According to Koekkoek (2021) it is also possible to use ammonia in a Homogeneous Compression Charge Ignition (HCCI) type ICE. HCCI was discussed in more detail in chapter 4.

5.2. Injection strategies

The injection strategies consist of aspects that are very similar to the ones discussed in chapter 4. The injection timing and pressure are once again important for the performance of the ICE. However, one aspect that is very different from a diesel-powered ICE is the interaction between ammonia and the used pilot fuel. As was already mentioned before, the literature is very limited for the combustion of ammonia and hydrogen in a two-stroke ICE. The literature that is available for the combustion of ammonia-diesel is more extensive which is what this section will, therefore, start with.

Ammonia can either be directly or port injected as a liquid but can also be injected as gas. Direct injection has its advantages such as a higher energy density, higher injection pressure, and the possibility of controlled charge stratification (Y. Zhang et al., 2023). In terms of injection timing, Dimitriou and Javaid (2020) concluded that satisfactory combustion can only be achieved if the ammonia is injected no later than 40 [° CA] before the Top Dead Centre (TDC). They also stated that the late injection of ammonia can result in misfiring, and a secondary peak in heat release due to the combustion of residual fuel near the cylinder liner. One of the primary emission concerns of an ammonia-fuelled ICE is N_2O. The authors claim that multiple diesel injections are an effective measure for the reduction of both N_2O and unburned ammonia emissions. Liu, Tan, et al. (2022) concluded that using a four-stage pulse fuel injection of an ammonia-hydrogen mixture can achieve a constant combustion pressure of 30 [MPa], resulting in a reduction of NO_x emissions while only having a power loss of 1.6%. J. Zhu et al. (2023) also concluded that multiple diesel injections are an effective measure to reduce both N_2O and unburned ammonia emissions, with a dual injection diesel injection strategy reducing the unburned ammonia emissions by 83.5% compared to a single diesel injection strategy. The authors also state that advancing the injection timing can reduce N_2O and the overall Greenhouse Gas (GHG) emissions while maintaining a thermal efficiency similar to a diesel-fuelled ICE.

T. Li et al. (2022) compare the combustion and emission characteristics of the Low-Pressure injection Dual Fuel (LPDF) and High-Pressure injection Dual Fuel (HPDF) for a diesel pilot-ignition ammonia combustion engine. These characteristics are studied numerically. For the LPDF mode, a lower concentration of ammonia should be used than for the HPDF mode (80% compared to 97%). The HPDF mode has a similar indicated thermal efficiency, cooling, and exhaust losses compared to a diesel-fuelled ICE. The HPDF mode also can significantly reduce GHG emissions with only a slight increase in unburned ammonia emissions. The HPDF mode also has the potential for a reduction in NO_x emissions. The LPDF mode has the potential to achieve a higher indicated thermal efficiency than a diesel-fuelled ICE. However, the trade-off is that this does increase N_2O emissions which offsets the benefit of reducing CO_2 emissions. Based on this, the authors conclude that the LPDF mode requires an optimisation of the combustion chamber geometry along with exhaust gas after-treatment.

Scharl and Sattelmayer (2022) examined the heat release rate under various spatial and temporal spray interaction configurations. The authors conclude that the highest ammonia heat release rate is achieved for a strong spatial interaction, which means converging sprays. The same can be said for advanced diesel pilot injections. With the stated configurations, the ammonia spray interacts intensely with the already ignited diesel pilot fuel. The authors also conclude that short pilot injection durations with a high mass flux reduce the ignition delay. This conclusion also follows from the research con-

ducted by Ichikawa et al. (2022). The authors propose a fuel injection concept that uses a three-layer model. This concept consists of a middle layer of liquid ammonia sandwiched by two layers of pilot fuel $C_{16}H_{34}$. In comparison to a two-layer model, the combustion process of the three-layer model is quicker. For the three-layer model, this also means a peak in heat release rate at the end of combustion. Because of the three-layer model, the N_2O emissions were drastically reduced. The NO and NO_2 emissions were significantly lower for the three-layer model compared to the combustion of pure $C_{16}H_{34}$. The authors conclude that based on the results a smaller fraction of fuel NO was produced compared to thermal NO. The conversion ratios of CO were lower for the three-layer model compared to the combustion of pure $C_{16}H_{34}$, and the fraction of unburned ammonia in the burned gasses was also sufficiently low.

B. Wang, Yang, Wang, Hu, Duan, et al. (2023) studied the combustion of hydrogen and ammonia by studying different combinations of compression ratios and fuel injection timing. The authors use four groups of compression ratios from 13.5 to 16.5 while using eight groups of injection timing from 12 [° CA] before TDC to 24 [° CA] before TDC. The authors state that the mixing of hydrogen can improve both the ignition as well as the combustion performance of ammonia. The addition of hydrogen can increase the NO_x emissions. However, delaying the injection timing results in a lower peak temperature, which will reduce the NO_x emissions. However, delaying the injection time too much will result in insufficient power generation. A delay in injection timing results in a more uniform combustion shape with an acceleration in the flame propagation speed. Based on the results from the performed simulations, it can be concluded that if the compression ratio is kept constant, delaying the injection timing of ammonia/hydrogen as mixed fuel will shorten the ignition delay. This means less power and economic performance of the engine and an increase in HC, CH_2O, CO, soot, and N_2O emissions. The NO_x emissions will be reduced. If the injection timing is kept constant, increasing the compression ratio will advance the ignition time, reduce the ignition delay, and the power and economy of the engine will be greatly improved. HC, CH_2O, CO, and soot increase but only slightly. The emissions of N_2O and NO_x increase. Finally, if the injection timing is again delayed then the performance and economy of the engine gradually decline but the NO_x emissions improve significantly. A reasonable selection of compression ratio and injection timing can achieve NO_x emissions that meet Tier III requirements while ensuring the engine's power performance.

5.3. Mixtures

In contrast to a diesel-fuelled ICE, an ammonia-fuelled ICE has to be assisted by some pilot fuel in a CI engine. But what is the correct composition of the fuel that is injected into the cylinder? Reiter and Kong (2008) studied the feasibility of ammonia combustion in a CI engine. The authors claim that different diesel-ammonia ratios can be used to achieve the same engine torque. The ammonia energy ratio can be as high as 95% and still achieve successful engine operation. The ammonia energy ratio should be between 40-80% to achieve a reasonable fuel consumption. Dimitriou and Javaid (2020) made a similar claim that for ammonia-diesel operation a combustion efficiency of 95% can be achieved with ammonia fuel energy rates between 40-80%. According to Reiter and Kong (2008), NO_x emissions are reduced compared to a diesel-fuelled ICE if the ammonia energy ratio does not exceed 60%. In successive research performed by both authors (Reiter & Kong, 2011), they conclude that if only 5% of diesel energy is used, the overall fuel efficiency will be poor, along with the raw ammonia emissions being high. The authors state that the preferred range for diesel fuel energy in terms of overall fuel efficiency was between 40-60%. Unsurprisingly, increasing the ammonia energy ratio will result in a longer ignition delay. If the diesel fuel energy ratio exceeds 60%, the ammonia-air mixture may become too lean for it to achieve effective combustion. This will also reduce the overall combustion temperature and thus reduce the combustion efficiency. This means the fuel consumption of ammonia will be high. However, if the diesel energy ratio is reduced below 40%, the fuel consumption of diesel will be high. In terms of emissions, if the diesel energy ratio does not exceed 60%, the NO emissions of the dual fuel engine will be lower compared to the diesel-fuelled engine. This is caused by the lower combustion temperature in the cylinder. However, if the diesel energy ratio falls below 40%, then the NO emissions increase significantly because of the fuel-bound nitrogen in ammonia. J. Zhu et al. (2023) take a similar approach, analysing the Ammonia Substitution Ratio (ASR). This is defined as the energy ratio of ammonia compared to diesel. The authors conclude that increasing the ASR will reduce the CO_2

emissions, but increasing the ASR above 40% will significantly increase the NO_x emissions. Important to note is that when ASR exceeds 80% misfiring can take place. In terms of the air-to-fuel ratio for the dual fuel operation with diesel and ammonia. Z. Zhang, Long, et al. (2023) studied the ammonia diesel dual fuel direct injection mode of a two-stroke low-speed engine. The air-to-fuel ratios that were used for the three cases were 3.1, 3.4, and 3.8.

If the pilot fuel is hydrogen, the air-to-fuel ratio will be different again. The air-to-fuel ratios if either ammonia or hydrogen is used alone for combustion are 6.14 and 34.3 respectively (B. Wang, Yang, Wang, Hu, Duan, et al., 2023). According to Zheng (2020), the chemical kinetics are complex for the combustion process, but if some assumptions are made then equation 5.1 can be used for a quick indication of the air-to-fuel ratio for ammonia-hydrogen combustion.

$$AFR = \frac{\frac{3 - c_{H_2}}{4} \cdot (O_2 + 3.76N_2)}{(1 - x_{H_2})NH_3 + x_{H_2}H_2} \tag{5.1}$$

Among the literature that has been studied (Zheng, 2020), (van Duijn, 2021), (Y. Wang et al., 2021), (B. Wang, Yang, Wang, Hu, Duan, et al., 2023), there seems to be a common consensus that the ammonia/hydrogen ratio should be 70/30%. This ratio should be used to obtain decent efficiencies at low compression ratios and intake pressure according to Zheng (2020). The percentage of hydrogen can be reduced if the compression ratio is increased. However, this increases the probability of engine ringing, which is the phenomenon where a rapid fuel burn creates an excessive in-cylinder pressure which can result in shock waves that possibly damage the engine (van Duijn, 2021). Y. Wang et al. (2021) studied different ammonia/hydrogen ratios for different equivalent ratios (ratio of the fuel-to-oxidizer ratio compared to the stochiometric fuel-to-oxidizer ratio). The authors conclude that for an ammonia/hydrogen ratio of 70/30%, the engine always operated on the right side of the fire line, which is the ignition boundary of the fuel.

5.4. Performance analysis

The literature for the performance analysis of ammonia-diesel and/or ammonia-hydrogen-fuelled engines is very limited. In terms of what to expect from an ammonia-fuelled engine, Z. Zhang, Long, et al. (2023) investigated the performance of a large two-stroke engine. The authors concluded that the Indicated Thermal Efficiency (ITE) was very similar for dual-fuel operation (ammonia plus diesel) compared to diesel-only operation. The highest ITE measured was 38.8%. Kane et al. (2019) looked into the ammonia-diesel usage for a four-stroke CI engine. Important to note is that this concept decomposes ammonia into an intake-fumigated ammonia-hydrogen mixture to allow for higher fuel replacements. The authors conclude that when the ammonia fraction of the fuel is increased, this will reduce the combustion efficiency η_{comb} as is shown in figure 5.1. As a result, this will also decrease the overall indicated thermal efficiency (ITE) of the engine. According to the authors, this was mainly due to valve overlap as well as cold areas present in the combustion chamber.

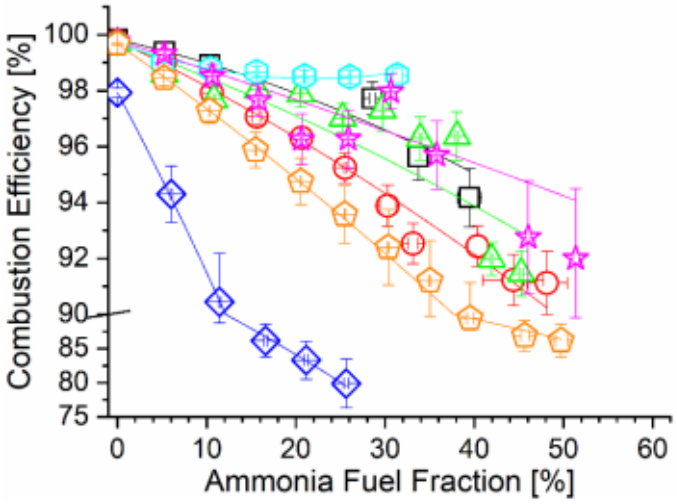

Figure 5.1: Combustion efficiency as a function of ammonia fuel fraction (AFF) (Kane et al., 2019)

Yousefi, Guo, Dev, Liko, et al. (2022) investigated the performance of an ammonia-diesel-fuelled heavy-duty engine. The authors state that at the optimal point in terms of GHG emissions, the engine operated with an ITE of 37.85% compared to 38.53% in diesel-only mode. At this optimal point, a reduction of 12% in GHG emissions along with an increase of 10% in CO and 20% in NO_x were recorded. The unburned ammonia emissions were registered at 4445 [ppm]. The authors state that these results mean that appropriate in-cylinder strategies along with exhaust-after treatment will certainly be required for ammonia-diesel-fuelled engines. Yousefi, Guo, Dev, Lafrance, et al. (2022) expanded on their previous work by investigating the performance of a split diesel injection strategy. The recorded ITE increased to 39.72% by applying this injection strategy. The GHG emissions were reduced by 23.7%. However, this strategy did come at a cost of 10% higher NO_x emissions. The GHG emissions could be reduced even further to 30.6% but this would come at a cost of a 2.2% decrease for the ITE and an increase of 52.4% for the NO_x emissions. Important to note is that for both cases, the amount of unburned ammonia decreased dramatically to levels below 900 [ppm].

As for how to model the performance of an ammonia-fuelled engine, there seems to be no decisive method yet. Several previous Master Theses were written that propose applying methods similar to the ones described in chapter 3. van Duijn (2021) uses the basis of the Mean Value Engine Model (MVEM) that is very similar to the reference model for this thesis developed by Sui Congbiao (2021). The author investigated how to use MVEM for the combustion of ammonia and diesel. The author proposes a couple of changes to the model, such as changes to the thermodynamic properties of both the air intake as well as exhaust gas composition. The author does not change the used six-point Seiliger cycle, because the in-cylinder temperature and pressure do not differ significantly between ammonia-diesel and diesel-only operation. The author does state, however, that this assumption might be questionable because of the lower flame propagation speed and Lower Heating Value (LHV) value for ammonia compared to diesel. The author introduces a so-called ”ammonia share ratio” which is the energy ratio contributed by ammonia. This ratio is used along with an empirical relation to determine the ignition delay and to determine the heat released during combustion. Zheng (2020) constructs a combustion model for ammonia-hydrogen combustion. The author uses a single-Wiebe function for the combustion model. Koekkoek (2021) uses a simplified approach compared to Zheng (2020) by using a five-point Seiliger cycle and calculating the heat produced during combustion as a function of LHV and an estimation of the combustion efficiency. All three of the mentioned Master Theses (van Duijn, 2021), (Zheng, 2020), and (Koekkoek, 2021) have to deal with the lack of experimental data for ammonia combustion. Both van Duijn (2021) and Koekkoek (2021) validate the engine model with existing data of a four-stroke diesel engine. Zheng (2020) applies engine scaling laws to an automotive-sized engine. The author does state that this method is not preferable but was necessary because of the lack of experimental data. Because of their respective methods used, all three authors acknowledge the uncertainty in their respective methods because of the lack of experimental data for validation. To say

something about the suitability of an MVEM and its commonly used methods, literature concerning dual-fuel operation was consulted. Gholami et al. (2022) studied the implementation of hydrogen for a dual-fuel engine used in a very large crude carrier. The engine uses a combination of diesel and hydrogen as fuel. The authors use an already-developed MVEM to study the performance of the engine and conclude that the MVEM produces sufficiently accurate results. Mavrelos and Theotokatos (2018) used the GT-Power software to model a dual-fuel two-stroke engine. The authors construct a 0D/1D model using the software and manage to produce accurate results for the in-cylinder pressure, brake power, and NO_x emissions with a maximum error of 3.6%. Sapra et al. (2020) investigated the ability of both the Seiliger approach as well as a double Wiebe function to capture the behaviour of an SI marine natural gas engine for different blends of H_2-CH_4, engine leaning, and engine loads. The authors conclude that the Seiliger approach can capture the combustion process with high accuracy. The double Wiebe function can capture the in-cylinder pressures and temperatures reasonably well but produces high errors when estimating the power output and heat produced during combustion with a maximum error of 5.2%. The Seiliger approach produced better results with a maximum error of 2%.

5.5. Heat release rate

According to Karim (2003), the heat release rate of a dual-fuel engine can be divided into three overlapping zones. Zone I consists of the combustion of the pilot fuel, Zone II consists of the combustion of the gaseous fuel within the near vicinity of the pilot fuel, and Zone III consists of the preignition reaction activity and the turbulent flame propagation. The schematic representation for both a light load as well as a heavy load are shown in figure 5.2a and 5.2b respectively.

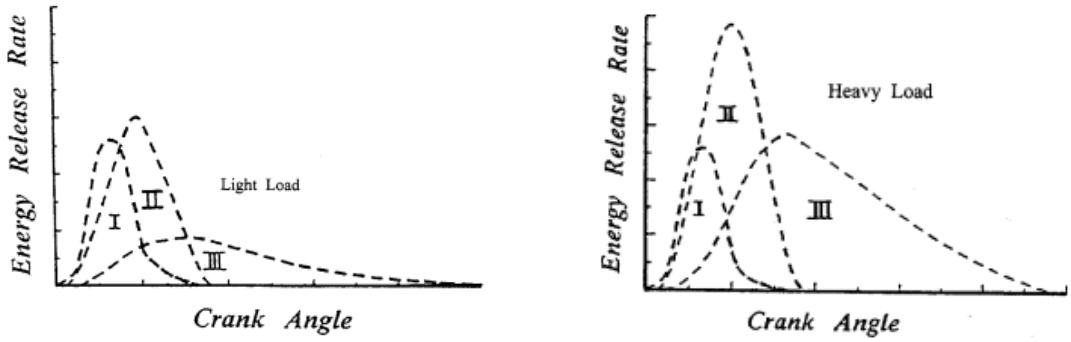

(a) Schematic representation of the heat release rate for a dual-fuel engine (Light Load) (Karim, 2003)

(b) Schematic representation of the heat release rate for a dual-fuel engine (Heavy Load) (Karim, 2003)

Figure 5.2: Heat release rate schematic representation

J. Zhu et al. (2023), T. Li et al. (2022), and Reiter and Kong (2011) all investigated the heat release rate of ammonia-diesel combustion. J. Zhu et al. (2023) looked at the Apparent Heat Release Rate (AHRR) for a two-stroke marine dual-fuel engine. The results are plotted for different Ammonia Substitution ratios (ASR) in figure 5.3a. As was already eluded to in section 5.3, increasing the ASR leads to an advance in the ignition delay. This will increase the initial heat release rate. This is also the case when comparing the heat release rate for a 3% energy contribution from diesel compared to 10% investigated by T. Li et al. (2022). Although important to note is that the initial heat release rate peak is higher for pure diesel combustion which seems odd. When taking a look at the results produced by Reiter and Kong (2011) this is confirmed as well. The results are shown in figure 5.4 and show similar behaviour: increasing the energy contribution of ammonia will increase the ignition delay and, therefore, the initial heat release rate peak.

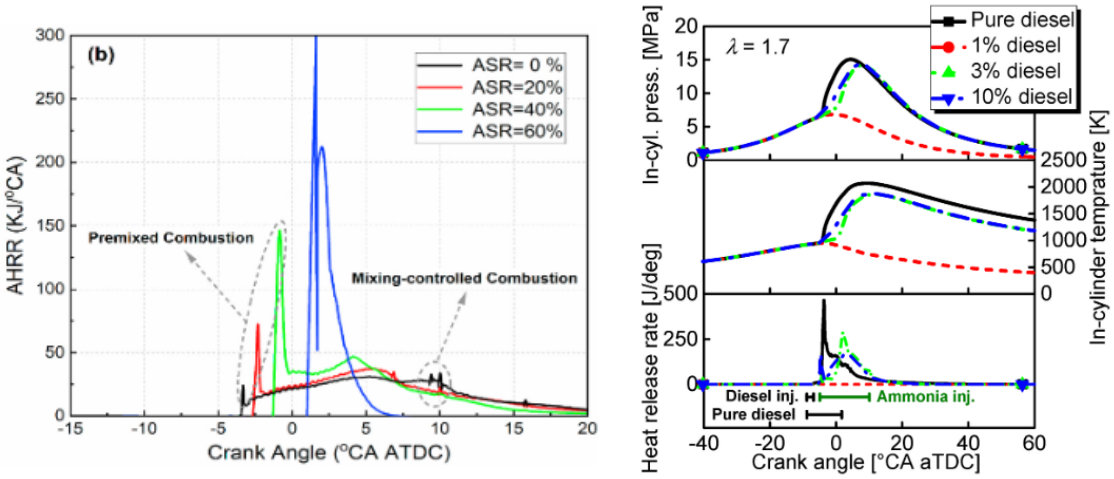

(a) Heat release rate for different Ammonia Substitution Ratios (ASR) (J. Zhu et al., 2023)

(b) Heat release rate for different diesel energy fractions (T. Li et al., 2022)

Figure 5.3: Heat release rates for ammonia diesel combustion as a function of the crank angle (CA)

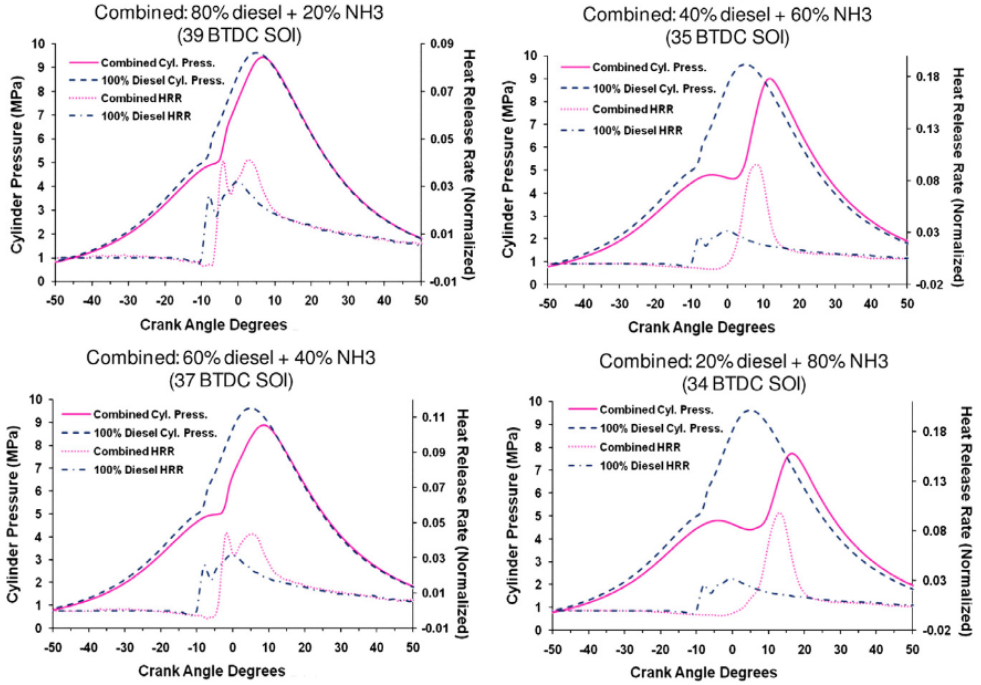

Figure 5.4: Heat release rates for ammonia diesel combustion as a function of the crank angle (CA) (Reiter & Kong, 2011)

B. Wang, Yang, Wang, Hu, and Wang (2023) study the effect of hydrogen addition to the combustion of ammonia. Important to note is that diesel is still used for ignition. Figure 5.5 shows the heat release rate for pure diesel combustion. Figure 5.6 shows the heat release rate for ammonia hydrogen combustion with different hydrogen blending ratios. The hydrogen blending ratio is based on the ratio of the hydrogen heating value and the total heat value of the ammonia hydrogen mixture. The first peak does not change all that much so this is probably caused by the diesel fuel used for ignition. Comparing figures 5.5 and 5.6 it seems that the maximum heat release rate and combustion duration are similar between ammonia-hydrogen and pure diesel. Increasing the hydrogen blending ratio will shorten the combustion duration and increase the maximum heat release rate.

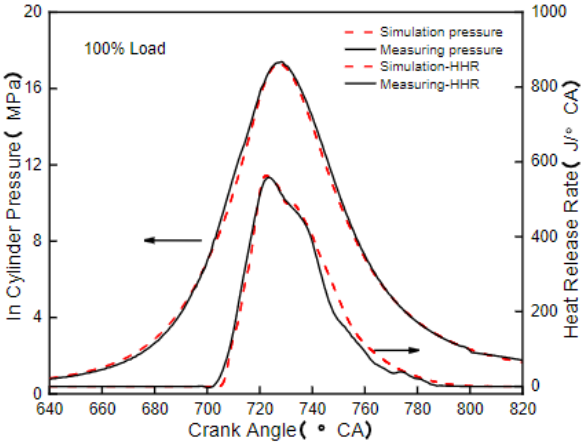

Figure 5.5: Heat release rates for diesel combustion as a function of the crank angle (CA) (B. Wang, Yang, Wang, Hu, & Wang, 2023)

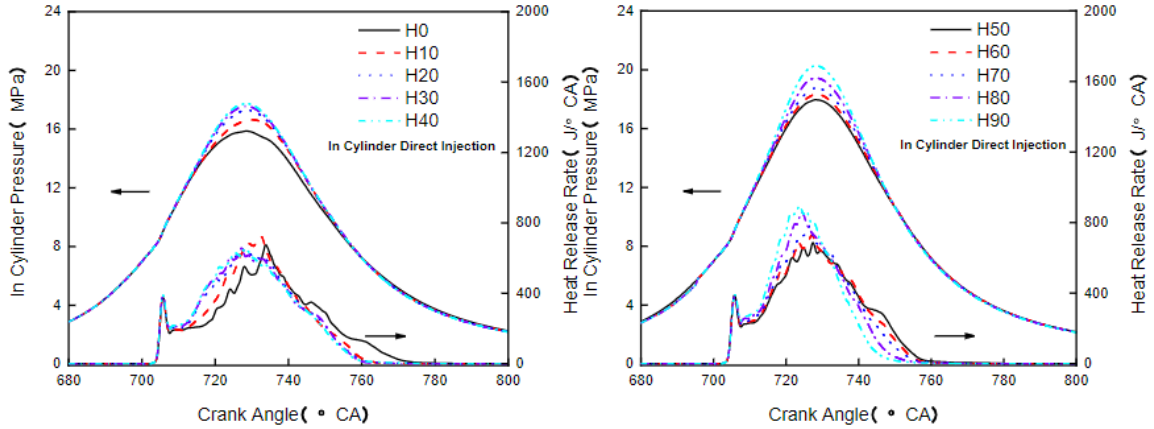

Figure 5.6: Heat release rates for ammonia hydrogen combustion as a function of the crank angle (CA) (B. Wang, Yang, Wang, Hu, & Wang, 2023)

5.6. Heat losses

In terms of available literature, there isn't any literature about studying the heat losses for ammonia-diesel or ammonia-hydrogen combustion. Chapter 4 already discussed some proposed methods for determining the heat losses within the cylinder. The same heat transfer mechanisms will still apply for ammonia-diesel or ammonia-hydrogen combustion. However, as was also discussed in chapter 4, some of the empirical methods for estimating heat losses generally assume a constant temperature on their respective surface. Now it was already stated that this will not be true in reality, but when two fuels are used which have different combustion characteristics such as auto-ignition temperature and flame propagation speed this assumption will make even less sense.

6

Conclusions & Findings from the literature study

This chapter will discuss the main conclusions and findings that were derived from the conducted literature study. Chapter 2 has listed the four research questions that will be answered by the findings from the literature study, along with the topics selected for the literature study, and the overall research question that will be answered by this thesis:

How can the necessary parameters be found for both the Seiliger approach and Wiebe function to characterize the closed-cylinder process in an internal combustion engine and how will this process be different on a conceptual level when it attempts to characterize ammonia-diesel instead of diesel combustion?

Chapters 1, 3, 4, and 5 have discussed the selected topics for the literature study in detail. As was also explained in chapter 2, the literature study serves two main purposes: to provide background information, and to analyse the gap in the available literature that this thesis will attempt to fill.

The sub-research questions will be answered in section 6.1. The overall gap in the available literature for this thesis has turned out to be quite extensive, so this thesis will not be able to fill it completely. The gap this thesis will try to fill will be discussed in section 6.2. Finally, the overall project approach of the main research part of this thesis will be explained in section 6.3. This section will also construct new relevant research questions that the main research part of this thesis will try to answer.

6.1. Conclusions from literature study

The constructed sub-research questions for the literature study discussed in chapter 2 are listed below along with their answer:

- **Why is ammonia considered a potential alternative fuel for the Maritime Industry?**
  To meet the goals set out by the International Maritime Organization (IMO) for the reduction of Greenhouse Gases (GHG), zero-carbon alternative fuels are required (International Maritime Organization, 2019). Ammonia does not contain carbon which means it would produce almost no CO_2 emissions. It also produces no SO_x emissions since it doesn't contain sulphur either. One major advantage for ammonia compared to other potential alternative fuels like hydrogen is that ammonia is already one of the largest chemical industries in the world (Ayvalı et al., 2021). Ammonia also has to potential to be produced sustainably. "Green" production of ammonia is expected to reach the same level in terms of costs by 2050 compared to conventional "brown" ammonia (Mallouppas et al., 2022). Ammonia has good storage capacities certainly when compared to hydrogen. Concerns around ammonia consist of its bad combustion characteristics. Namely its slow flame propagation speed (Mallouppas et al., 2022) high auto-ignition temperature (Di Blasio et al., 2022), and long quenching distance (Dimitriou & Javaid, 2020). Other concerns are its high corrosiveness, toxicity, NO_x emissions, and lack of regulations (Mallouppas et al., 2022).

- **What is the definition of a mean value engine model? How does it compare to the other types of engine models and what is/are suitable application(s) for this kind of engine model?**
  A Mean Value Engine Model (MVEM) is considered a compromise between accuracy and computational efficiency when compared to the various available engine models. That being said, an MVEM can achieve a higher level of accuracy than some more complex models when calibrated using an actual Internal Combustion Engine (ICE) (Alberer et al., 2012). An MVEM generally neglects the in-cycle variations of physical quantities such as flow, pressure, temperature, etc. and can be based on both first-principle thermodynamics or experimental data (Alberer et al., 2012). An MVEM uses the mean value for the aforementioned physical quantities. An MVEM can struggle with calculating the trapped air mass because it neglects the physical description of the air intake system (Alberer et al., 2012). An MVEM can be used well for control applications because this requires the model to simulate the engine cycle faster than in real-time (Lee & Jung, 2016). For the same reason, it is also suitable for analysing transient engine behaviour (Theotokatos, 2010). Because of its low computational load compared to other engine models, it can also be used as a building block for a larger model describing the entire power plant of the ship (Sui et al., 2017).

- **How is the closed-cylinder process of an internal combustion engine generally modelled in a mean value engine model?**
  The closed-cylinder process is modelled with varying degrees of complexity. Some MVEMs neglect the in-cylinder variations of physical quantities such as pressure and temperature entirely (Theotokatos, 2010) (Shen et al., 2020) (R. Li et al., 2013) (Guan et al., 2015). These models use efficiency maps for the indicated or the combustion efficiency and then calculate the brake power of the engine based on this and the fuel that is injected into the cylinder. Most of these approaches also include an empirical function to calculate the mechanical losses of the engine. Using an air-standard analysis, other models only consider the pressure and temperature at specific stages of the closed-cylinder process (Llamas & Eriksson, 2019) (S. Zhu et al., 2020). Some models go even further by incorporating elements from Crank Angle Solved (CAS) engine models (Shen et al., 2020) (Tang et al., 2017). This approach does compute the in-cylinder variations of for example the pressure. Doing this increases the computational load, so to compensate for this, the MVEMs try to simplify the model without compromising accuracy. This can be done by using analytical instead of differential equations (Shen et al., 2020) or by using a simplified function where in-cylinder variations are almost negligible. (Tang et al., 2017).

- **What are the main similarities and differences between the diesel combustion process and the ammonia combustion process?**
  Ammonia can either be directly or port injected as a liquid but can also be injected as gas. Direct injection has its advantages such as a higher energy density, higher injection pressure, and the possibility of controlled charge stratification (Y. Zhang et al., 2023). Ammonia can be used in a Compression Ignition (CI) engine similar to diesel. The main difference is that if only ammonia is used high compression ratios of 35:1 to 100:1 are required to achieve combustion (Dimitriou & Javaid, 2020). To solve this problem, ammonia is injected alongside a so-called ”pilot fuel”. There are several possible pilot fuels, but the ones that were primarily studied for this thesis were diesel and hydrogen. Regarding factors that influence the combustion characteristics. The injection timing and the number of injections have been studied for both diesel and ammonia-diesel combustion. For diesel combustion, an advance in the injection timing will result in a higher pressure, temperature, and heat release rate, and subsequently in more NO_x emissions (Jayashankara & Ganesan, 2010) and a better engine performance (Agarwal et al., 2013). In terms of injection timing, ammonia shows similar behaviour. For ammonia and its high auto-ignition temperature, a late injection can result in misfiring (Dimitriou & Javaid, 2020). Multiple-injection strategies have also been researched for both diesel and ammonia-diesel combustion. Before most of the diesel is injected, pilot injections of diesel can improve the engine performance while not increasing the NO_x emissions (Kontoulis et al., 2008). A double-injection method can reduce a diesel engine's NO and soot emissions. However, this results in a higher fuel consumption and subsequently higher CO_2 emissions (Seol et al., 2021). Similar behaviour for ammonia-diesel and ammonia-hydrogen combustion can be concluded. Multiple injections of diesel as pilot fuel can reduce

both the N_2O and unburned ammonia emissions (Dimitriou & Javaid, 2020). A four-stage pulse fuel injection for an ammonia/hydrogen mixture can also reduce NO_x emissions while maintaining roughly the same performance (Liu, Tan, et al., 2022).

One major difference between the diesel and ammonia-diesel combustion processes is that the fuel injection strategy must also consider the interaction between the injected fuel sprays. Interaction between the two fuels should be encouraged according to Scharl and Sattelmayer (2022). The authors found that converging fuel sprays improve combustion. The same can also be said based on the study conducted by Ichikawa et al. (2022), which found that a three-layer model of ammonia being sandwiched by pilot fuel showed better combustion characteristics than a two-layer model. The air-to-fuel ratio will also change when ammonia-diesel or ammonia-hydrogen is used instead of diesel (Z. Zhang, Long, et al., 2023) (B. Wang, Yang, Wang, Hu, Duan, et al., 2023). For ammonia-diesel combustion, changes will also have to be made to the thermodynamic characteristics of the air intake gasses and exhaust gasses (van Duijn, 2021). The same is likely true for ammonia-hydrogen combustion as well.

The literature available on the performance analysis of either ammonia-diesel or ammonia-hydrogen combustion is very limited. van Duijn (2021) proposes a model for ammonia-diesel combustion while Zheng (2020) and Koekkoek (2021) propose one for ammonia-hydrogen combustion. All three incorporate performance analysis methods that are also used to analyse diesel combustion. However, these models have not been validated due to the lack of experimental data. To say something, this report looked into dual-fuel operations. Gholami et al. (2022) stated that an already developed MVEM produced sufficiently accurate results for a dual-fuel engine. Mavrelos and Theotokatos (2018) concluded the same thing for their constructed 0D/1D model. Sapra et al. (2020) investigated the ability of the Seiliger approach and double Wiebe function for $H_2 - CH_4$ combustion, both are also used for diesel combustion and concluded that the Seiliger approach can capture the combustion process with sufficient accuracy while the double-Wiebe function does so reasonably well. However, it should again be noted that the research was conducted using an SI engine. This means there is a good chance the method can also be used for this thesis but there will still be some uncertainty.

The heat release rate for ammonia-diesel combustion has a similar shape compared to the heat release rate for diesel combustion. However, the heat release rate is highly dependent on the ammonia-diesel ratio. Increasing the amount of ammonia will increase the peak of the heat release rate while delaying the combustion (Reiter & Kong, 2011). Increasing the amount of ammonia will also shorten the eventual combustion duration (J. Zhu et al., 2023). There isn't any literature available on the heat release rate of ammonia-hydrogen combustion. One study found that the heat release rate is similar to diesel combustion but for this study diesel was still used to achieve combustion for the ammonia-hydrogen mixture (B. Wang, Yang, Wang, Hu, & Wang, 2023). Heat losses have always been difficult to predict with even some multi-dimensional Computational Fluid Dynamics (CFD) models failing to produce accurate results (Rakopoulos et al., 2010). Some empirical methods have been incorporated into MVEMs to consider heat losses. These methods assume a temperature that is evenly distributed within the cylinder. If two fuels with different combustion characteristics are used, this assumption will make even less sense than it already did.

6.2. Gap analysis

As was mentioned throughout this report, the literature for ammonia-diesel and ammonia-hydrogen is very limited, in particular for either CI engines or two-stroke engines. To illustrate this, the number of search results from Google Scholar has been plotted in figure 6.1. Please note that this is not a very sophisticated way to determine the available literature.

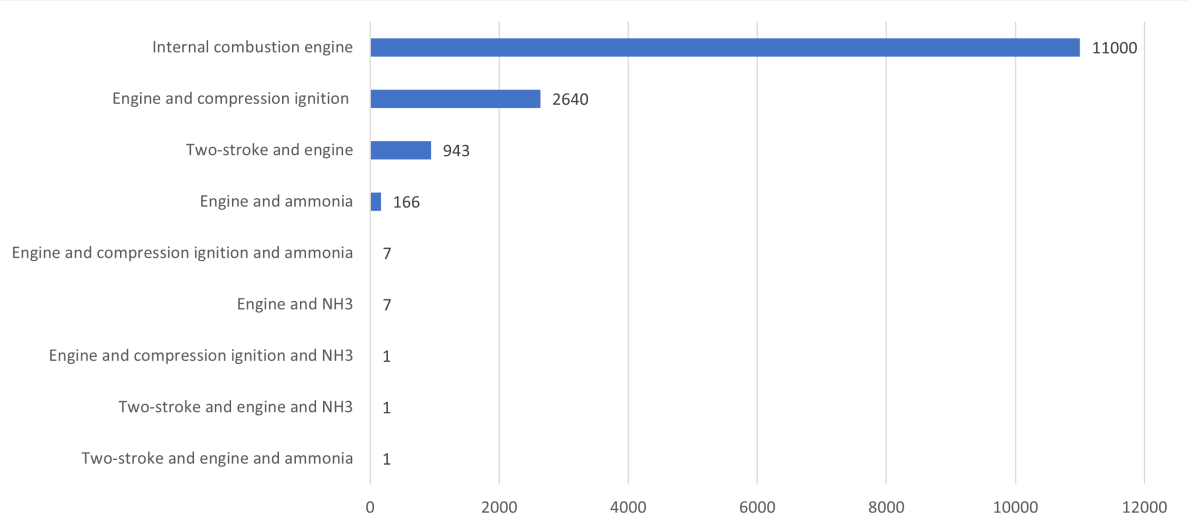

Figure 6.1: Search results Google Scholar (03/05/2023)

What can be determined from figure 6.1, is that there is an enormous gap in the available literature surrounding ammonia combustion for a two-stroke engine. It will, therefore, be impossible for this thesis to fill this entire gap. This means that a decision has to be made about what this thesis will attempt to research.

Of the examined literature for chapter 5, the studied literature can roughly be divided into three different categories: feasibility/general overview (Dimitriou & Javaid, 2020) (Scharl & Sattelmayer, 2022), injection/ignition (T. Li et al., 2022) (Y. Wang et al., 2023) (Ichikawa et al., 2022) (B. Wang, Yang, Wang, Hu, Duan, et al., 2023) (Y. Zhang et al., 2023), and emissions/combustion characteristics (Liu, Tan, et al., 2022) (Liu, Wu, et al., 2022) (Xin & Zheng, 2009) (Lhuillier et al., 2020) (J. Zhu et al., 2023) (Y. Zhang et al., 2022) (Mounaïm-Rousselle et al., 2022) (Kane et al., 2019). So looking at the topics selected for the literature review for ammonia combustion: ignition methods, injection strategies, mixtures, emissions, performance analysis, heat release rate, and heat losses. It seems that for performance analysis and heat losses, the gap in available literature is most evident. For the performance analysis, this needs to be further specified since there is some available information about the combustion performance and overall performance of ammonia combustion. However, investigations as to whether existing methods used for engine modelling, such as the Seiliger cycle, can still be applied for ammonia combustion are generally lacking.

To see what gap this thesis will attempt to fill, the literature closest to this thesis should be looked at. Ding (2011) constructing a method to obtain the necessary parameters for the Seiliger approach and Wiebe function. Koekkoek (2021) studied the AmmoniaDrive power plant but looked at the entire power plant instead of just the ICE. van Duijn (2021) studied how to adapt an earlier version of the MVEM developed by Sui Congbiao (2021) for ammonia-diesel combustion. Zheng (2020) applied the Wiebe function to analyse the combustion of ammonia-hydrogen for a Homogeneous Compression Charge Ignition (HCCI). This thesis expands on the constructed method of Ding (2011) by looking conceptually at ammonia-diesel combustion. It will look at more than just using the Seiliger approach but also finding the Seiliger parameters compared to van Duijn (2021). Finally, it will discuss conceptually how to apply the Wiebe function to ammonia-diesel instead of ammonia-hydrogen combustion compared to Zheng (2020).

6.3. Overall project approach

Chapter 2 already stated that the overall project approach for the main research part of this thesis is based on the method proposed by Ding (2011). Ding (2011) used the method to analyse the combustion in a four-stroke engine for three different operating points: 100%n_e-100%P_B, 100%n_e-25%P_B, and 80%n_e-50%P_B. This thesis will focus on a two-stroke engine at four different load points with the same engine speed: 100%n_e-100%P_B, 100%n_e-60%P_B, 100%n_e-40%P_B, and 100%n_e-20%P_B. The proposed method consists of designing and testing three things: an anti-causal simulation model, a causal simulation model, and a Newton-Rhapson solver. All three models require the engine parameters as input. The anti-causal model uses the pressure curve which is measured as a function of the crank angle as input and is discussed in chapter 7. It produces different results, of which the most important are the equivalence criteria and the Reaction Coordinate (RCO). The former is the input for the Newton-Rhapson solver while the causal simulation model uses the latter. These will be discussed in chapters 8 and 9 respectively. The whole process is summarized by the schematic representation shown in figure 6.2. Each model produces its own set of results as is shown in table 6.1.

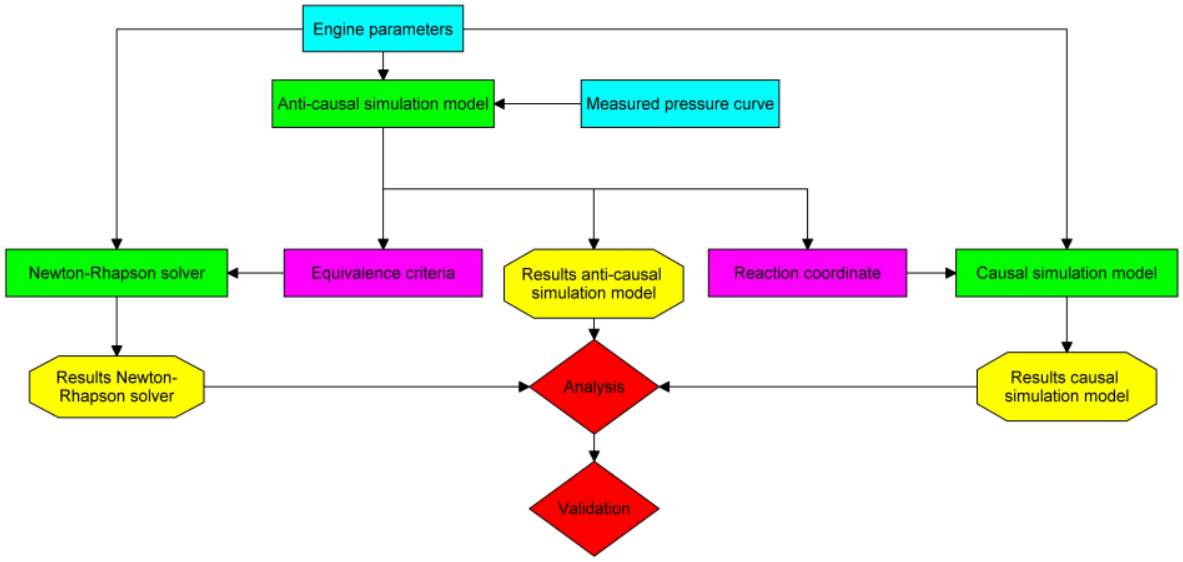

Figure 6.2: Overall structure of the main research part

Newton-Rhapson Solver	Anti-Causal Model	Causal Model
p_{max}	p_{max}	p_{max}
T_{max}	T_{max}	T_{max}
W_{in}	W_{in}	W_{in}
Q_{in}	Q_{in}	Q_{in}
$p(\phi)$	$p(\phi)$	$p(\phi)$
$T(\phi)$	$T(\phi)$	$T(\phi)$
a	$CRR(\phi)$	$CRR(\phi)$
b	$RCO(\phi)$	$RCO(\phi)$
c	$NAHRR(\phi)$	$NAHRR(\phi)$
r_c	$GAHRR(\phi)$	$GAHRR(\phi)$
n_c	$Q_{loss}(\phi)$	$Q_{loss}(\phi)$
r_{exp}	$W_i(\phi)$	$W_i(\phi)$
n_{exp}		

Table 6.1: Results produced by the different constructed models

Looking at the results listed in table 6.1 there's a lot of overlap between the three models. As for the first four parameters: p_{max}, T_{max}, W_{in}, and Q_{in} these are the so-called equivalence criteria. These will be

used by the Newton-Rhapson solver to calculate the Seiliger parameters a, b, c, r_c, n_c, r_{exp}, and n_{exp}. All three models produce the next two results which are the pressure and temperature as a function of the crank angle. Both the anti-causal as well as the causal model produce the Combustion Reaction Rate (CRR), Reaction Coordinate (RCO), Net Apparent Heat Release Rate (NAHRR), Gross Apparent Heat Release Rate (GAHRR), heat losses, and indicated work as a function of the crank angle. The difference is that because of the structure of the causal model, its results will present a much smoother curve than the anti-causal model.

Now this thesis will not only use three different models to simulate the in-cylinder process but will also transfer results between them. These models will have to make certain simplifications and assumptions so they come with a degree of uncertainty. As the British statistician George Box wrote "All models are wrong but some are useful" (Clear, n.d.). Therefore, the entire pressure data analysis process should verified and validated. But what is exactly meant by this? Verification is the process of determining that the model depicts its conceptual description and solution to the model (Thacker et al., 2004). Verification means asking the question: Am I building the model right? Validation consists of determining whether the model is an accurate representation of the real process it's trying to simulate (Thacker et al., 2004). This means asking the question: Am I building the right model? To understand the development of a model schematic representation constructed by Thacker et al. (2004) is shown in figure 6.3.

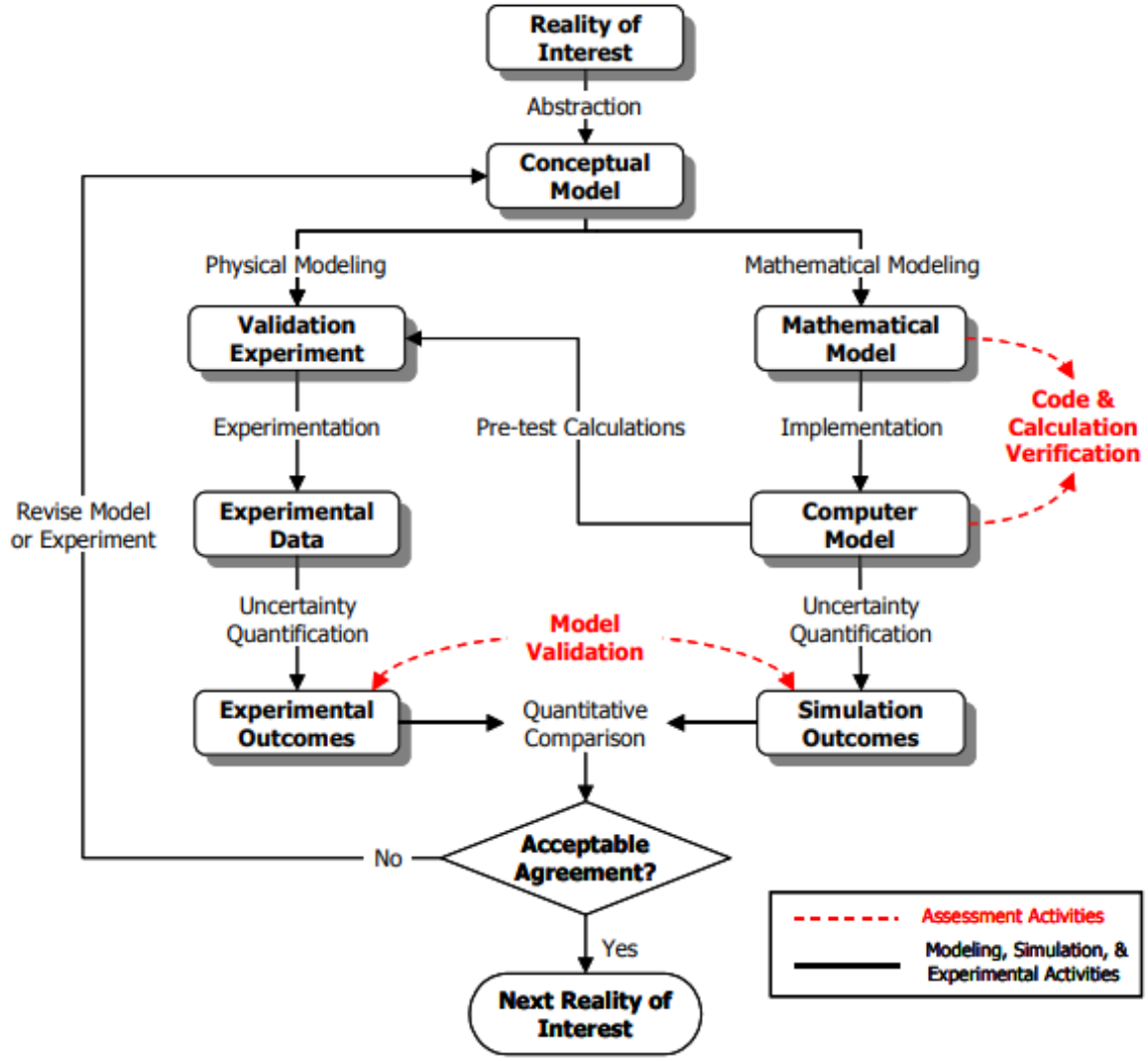

Figure 6.3: Model development including verification & validation (Thacker et al., 2004)

Figure 6.3 also gives a good overview of the different levels that exist in terms of modelling. For diesel combustion, a conceptual model has been designed and implemented into a computer model in the form of the anti-causal model, causal model, and the Seiliger approach. These models will be validated using experimental data, namely the measured pressure within the cylinder. These models will also be verified by looking at their behaviour. Namely, are the models producing results that are to be expected when modelling the combustion process of an ICE? For further verification, an already smoothed pressure curve produced by a causal model has been obtained. This pressure curve can be processed by the anti-causal model and subsequently by the causal model to see if the same pressure curve is reproduced. The Seiliger approach is also used to approximate this pressure curve to see if it can be an accurate representation. If this is not the case then there must be a fundamental fault within the process. Figure 6.3 also clarifies what is meant by only designing the model for ammonia-diesel combustion at a conceptual level. It means that necessary changes will only be described in theory, based on conclusions from literature and/or observations from produced results. No definitive mathematical model will designed, implemented or verified/validated.

The overall research question of this thesis was first stated in chapter 2 and has been discussed again at the beginning of this chapter. Chapter 2 also constructed four sub-research questions that were answered in this chapter. For the main research part of the thesis, two new sub-research questions have been constructed:

- How representative is the Seiliger process at characterizing the diesel combustion process at different load points?
- How representative is the Wiebe function at characterizing the diesel combustion process at different load points?

These sub-questions, along with the main research question will be answered in chapter 11. This chapter has discussed the conclusions and findings from the literature study, outlined the gap in literature this thesis will attempt to fill, and explained the overall project approach for the main research part of this thesis. The next chapter will start will explaining the anti-causal simulation model.

III

Main research part

7

Anti-causal simulation model

The chapter will describe how the so-called anti-causal simulation model has been built. It has been constructed using Matlab Simulink. The model is used to process the measured pressure curve as a function of the crank angle $p(\phi)$. As was already mentioned back in chapter 4, $p(\phi)$ has to be used as input since it is impossible to measure the heat release rate in the model directly. The model is made up of several ”building blocks” all of which will be discussed in this chapter. The overall design of the model is shown in figure 7.1. The design of the model is based on the methodology described by both Ding (2011) and Stapersma (2010d).

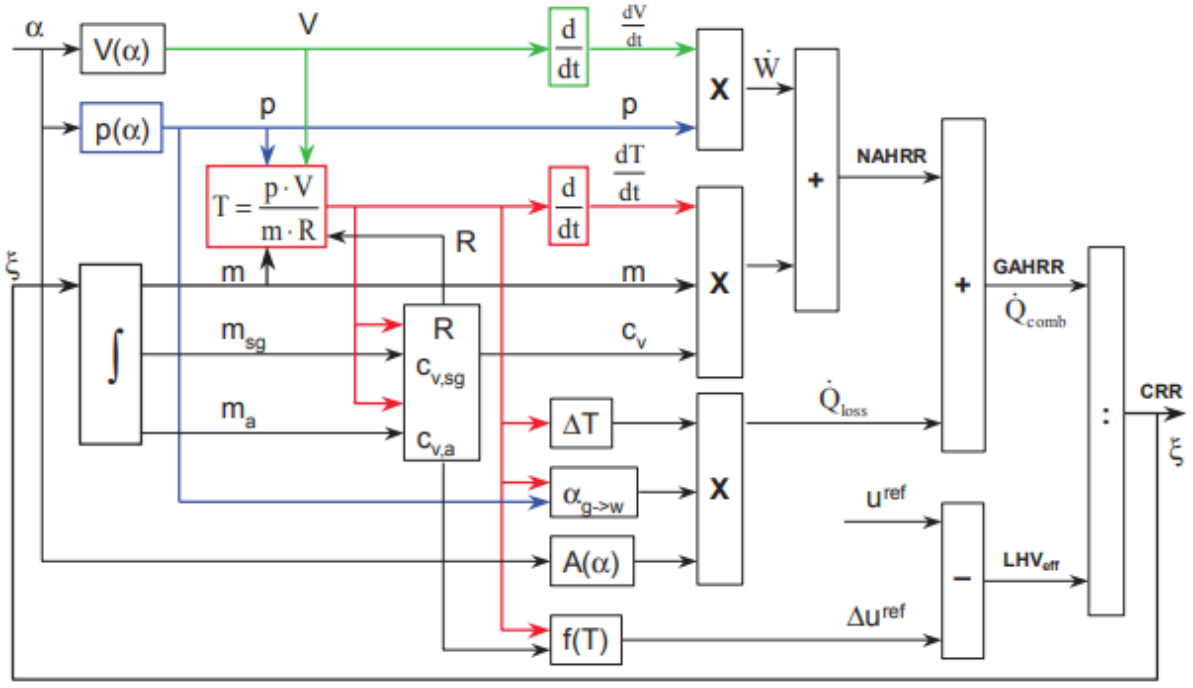

Figure 7.1: Schematic representation of the heat release model (Stapersma, 2010d)

The ultimate goal of the anti-causal model is to find the Combustion Reaction Rate (CRR), which can be integrated to obtain the Reaction Coordinate (RCO). RCO is approximated by a Wiebe function in the causal simulation model as is described in chapter 9. The model can also be used to calculate the equivalence criteria that are used to find the Seiliger parameters, which will be explained in chapter 8. Section 7.1 will start by discussing how CRR is calculated and subsequently used for the model. Section 7.2 will discuss what parameters are a function of the crank angle ϕ. Section 7.3 will elaborate

on the thermodynamic properties that are required for the model. Section 7.4 will discuss how the trapped conditions are determined. Section 7.5 will discuss how the heat losses are modelled. Finally, the results produced by the anti-causal model will be discussed in section 7.7. The definition of the symbols, abbreviations, and subscripts used in this chapter can be found in the nomenclature of this report.

7.1. Combustion reaction rate

Ultimately, CRR is calculated according to equation 7.1. The pressure multiplied by the derivative w.r.t. time is equal to the work performed ($\dot{W}$). Adding the second term in the numerator gives the Net Apparent Heat Release Rate (NAHRR). If the heat losses $\dot{Q}_{loss}$ are also included, this adds up to the Gross Apparent Heat Release Rate (GAHRR) (Stapersma, 2010d). Please note that within the model, transitions between ϕ, α, and t frequently take place according to equations 7.2 and 7.3 (Stapersma, 2010d). The model for this thesis is constructed as a function of t, but any unit of the three aforementioned is sufficient as long as it's used consistently.

$$CRR = \frac{p \cdot \frac{dV}{dt} + m \cdot c_v \cdot \frac{dT}{dt} + \dot{Q}_{loss}}{u_{comb} + e_f} \tag{7.1}$$

$$d\alpha = \frac{2\pi}{360} \cdot d\phi \tag{7.2}$$

$$dt = \frac{1}{2\pi \cdot n_e} \cdot d\alpha \tag{7.3}$$

CRR is integrated for each time step of the simulation to obtain RCO. RCO is equal to the mass of the fuel that has burnt if a combustion efficiency of 100% is assumed. This means a single-zone model is used that assumes the fuel evaporates and burns almost immediately after being injected. The model also assumes that the mass within the cylinder is made up of three constituents: fuel m_f, air m_a, and stoichiometric gas m_{sg}. The relation between these three constituents can be expressed using CRR, the stoichiometric air-to-fuel ratio σ, the trapped mass m_1, and the quality of the trapped mixture x_1. This is shown in the equations listed below (Stapersma, 2010d).

$$m_a = m_1 - \sigma \cdot \int_{t_0}^{t_1} CRR \tag{7.4}$$

$$m_{sg} = (1 + \sigma) \cdot \int_{t_0}^{t_1} CRR \tag{7.5}$$

$$m_f = \int_{t_0}^{t_1} CRR \tag{7.6}$$

$$x = \frac{m_1 \cdot x_1 - \sigma \cdot \int_{t_0}^{t_1} CRR}{m_1 + \int_{t_0}^{t_1} CRR} \tag{7.7}$$

The CRR is determined by the model and then integrated for each time step to obtain the RCO. The initial value of the RCO is set to zero since it assumes there's no fuel present in the cylinder at the start of the closed-cylinder process.

7.2. Parameters that depend on the crank angle

Four parameters are a function of the crank angle: pressure, volume, the derivative of the volume, and the area of the cylinder wall. The pressure is measured as a function of the crank angle within the cylinder. The volume, area, and derivative of the volume are shown in equation 7.8, 7.9, and 7.10, respectively (Stapersma, 2010d).

$$V(\alpha) = A_B \cdot L_s \cdot \left[\frac{1}{\epsilon - 1} + \frac{1}{2} \cdot \left\{(1 - cos(\alpha)) + \frac{1}{\lambda_{CR}} \cdot \left(1 - \sqrt{1 - \lambda_{CR}^2 \cdot sin^2(\alpha)}\right)\right\}\right] \tag{7.8}$$

$$A_{wall}(\alpha) = \pi \cdot D_B \cdot L_s \cdot \left[\frac{1}{\epsilon - 1} + \frac{1}{2} \cdot \left\{(1 - cos(\alpha)) + \frac{1}{\lambda_{CR}} \cdot \left(1 - \sqrt{1 - \lambda_{CR}^2 \cdot sin^2(\alpha)}\right)\right\}\right] \tag{7.9}$$

$$\frac{dV(\alpha)}{dt} = \pi \cdot n_e \cdot V_s \cdot \left[0.5 \cdot \left\{sin(\alpha) + \lambda_{CR} \cdot \left(\frac{sin(\alpha) \cdot cos(\alpha)}{\sqrt{1 - \lambda_{CR}^2 \cdot sin^2(\alpha)}}\right)\right\}\right] \tag{7.10}$$

$$\lambda_{CR} = \frac{0.5 \cdot L_s}{L_{CR}} \tag{7.11}$$

L_s is the stroke length of the engine, D_B is the bore diameter, ϵ is the geometric compression ratio, V_s is the stroke volume, and n_e is the engine speed. λ_{CR} is shown in equation 7.11 (Stapersma, 2010d) with L_{CR} being the length of the connecting rod between the crank and piston. All of these parameters are defined by the geometry of the Internal Combustion Engine (ICE) so these can be implemented directly.

As was already mentioned in chapter 6, the pressure is measured at four different loads: 75 [kW], 150 [kW], 225 [kW], and 375 [kW]. The pressure curve for 375 [kW] is shown in figure 7.2b as an example. The combined pressure curves for all four load points are shown in figure 7.2a. Important to note is that the pressure is measured in all three cylinders of the Bolnes engine. For the analysis by the anti-causal model, the average value of these three measurements is used. Also important to note is that the measured pressure is synchronized with the crank angle by estimating that the maximum value occurs at 10 [° CA] after Top Dead Centre (TDC).

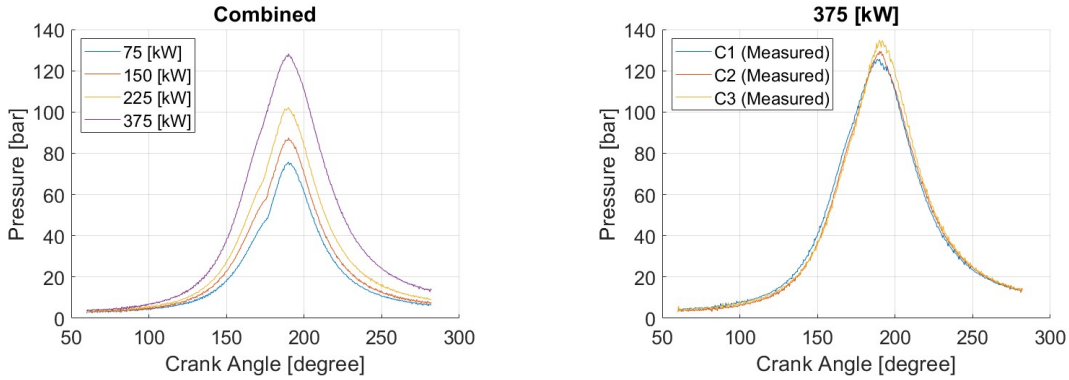

(a) Combined pressure curves

(b) Pressure measured in cylinders 1,2, and 3 for 375 [kW]

Figure 7.2: Pressure as a function of crank angle

Looking at figure 7.2b, it seems that the largest difference between the measured values is roughly 10% which is consistent for every operating point. It also seems that the pressure curve registered in one cylinder occasionally lags behind the other curves. Both are important to take into account when analysing the final results in both chapters 8 and 9.

As will be discussed in section 7.5, the heat losses require the pressure as a function of the crank angle when no fuel is injected p_0. This value has not been measured directly but has been constructed by taking the measured pressure up to and including TDC and then mirroring this curve to obtain the pressure for the entire combustion cycle.

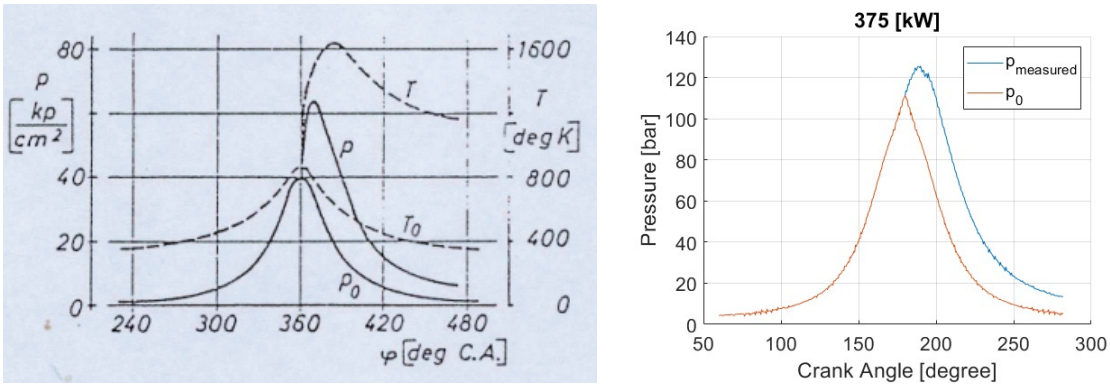

(a) Example p_0 curve (Stapersma, 2010e)

(b) p_0 combined with p as a function of crank angle

Figure 7.3: Pressure as a function of the crank angle for no fuel injected

Looking at figure 7.3 it seems that there is good agreement between the function p_0 from Stapersma (2010e) and the constructed p_0. However, just for comparison, the causal model, which will be discussed in chapter 9, has been constructed. This version does not simulate the injection and subsequent evaporation and burning of fuel. This means it calculates the pressure for no fuel injection. However, looking at its results, it produces a pressure higher than the measured pressure which seems impossible. Therefore, the constructed version based on the measured pressure was used instead.

7.3. Thermodynamic properties

The thermodynamic properties that are used in equation 7.1 are the heat of combustion u_{comb} and the energy of the fuel e_f (Ding, 2011). u_{comb} is the internal energy when the cylinder is modelled as a closed system. e_f takes into account the heat that is required to heat up and evaporate the fuel since it enters at a lower temperature compared to the reference temperature along with the kinetic energy caused by the difference between fuel injection pressure and the in-cylinder pressure. Since the cylinder is not an actual closed system Additionally, the gas constant R and specific heat c_v are also used (Ding, 2011). Equation 7.1 is the result of how the combustion process is modelled. Namely, this is done as a single-zone combustion model. This combustion model, along with the aforementioned thermodynamic properties are discussed in detail in chapter 10. This is done since the combustion model requires significant changes if it is applied to ammonia-diesel combustion.

7.4. Trapped conditions

Section 7.1 already showed that the model requires the trapped conditions of the gas mixture within the cylinder. x_1 and m_1 are used in equation 7.7 to determine the gas composition x. These parameters are determined by the trapped pressure p_1, volume V_1, and temperature T_1. These trapped conditions not only need to be determined for the anti-causal simulation model, but they will also have to be used to find the Seiliger parameters in chapter 8, and for the causal model in chapter 9. p_1 can be obtained from the measured pressure as a function of the crank angle if the valve timing for the engine is known. This valve timing can also be used to calculate the trapped volume V_1 as well. Both values are computed for the crank angle when the Exhaust valve Closes (EC). Please note that this is only true for a two-stroke engine (Stapersma, 2010c). The trapped temperature is not measured but instead calculated through a method proposed by Ding (2011) (equation 7.12). The trapped mass m_1 is calculated using the ideal gas law (equation 7.13).

$$T_1 = T_c + \epsilon_{INL} \cdot (T_{inl} - T_c) \tag{7.12}$$

$$m_1 = \frac{p_1 \cdot V_1}{T_1 \cdot R} \tag{7.13}$$

With regards to equation 7.12, $T_{inl} = 513K$ and $\epsilon_{INL} = 1/6$ (Ding, 2011). For the quality of the trapped mixture, the value obtained from Ding (2011) was not used, but instead, the value used by Sui Congbiao

(2021). This was done because Ding (2011) analysed a four-stroke engine, while Sui Congbiao (2021) looked at a two-stroke engine.

7.5. Heat losses

Chapter 4 already discussed how heat losses were generally modelled in the literature that has been studied for this thesis. Chapter 4 has discussed that modelling the heat losses accurately is very challenging, with even complex models using Computational Fluid Dynamics struggling. To get an accurate representation, Conjugate Heat Transfer has to be applied. However, this is not a feasible option for the heat release model. Ding (2011) proposed using an empirical method, Chapter 4 already stated that these methods cannot provide an accurate representation of the heat losses. However, given the circumstances, it seems to be the best option for this model.

Chapter 4 discussed the fact that it is generally assumed that the heat losses follow three main paths. Namely through the cylinder wall, cylinder head, and the piston crown. The heat losses are calculated using equation 7.14. The area is constant and assumed to be equal to the bore area for the piston crown and cylinder head, while section 7.2 already showed the used equation for the area of the cylinder wall.

$$\dot{Q}_{loss} = \alpha \cdot A \cdot (T - T_{wall}) \tag{7.14}$$

Chapter 4 stated that several methods can be used to calculate the heat transfer coefficient α. For this thesis the same method as used by Ding (2011) is used namely the equation proposed by Woschni (1967) (equation 7.15).

$$\alpha = C_2 \cdot \frac{1}{D_B^{0.214}} \cdot \frac{p^{0.786}}{T^{0.525}} \cdot \left(C_3 \cdot c_m + C_4 \cdot \frac{p - p_0}{p_1} \cdot \frac{V_s}{V_1} \cdot T_1 \right)^{0.786} \tag{7.15}$$

Looking at the parameters in equation 7.15. p and T are both determined by the model. V_s and D_B depend on the dimensions of the engine and can therefore be implemented directly. The trapped conditions that are required, T_1, V_1, and p_1 were discussed in section 7.4. c_m is the mean piston speed and is calculated using equation 7.16 (Stapersma, 2010b).

$$c_m = 2 \cdot L_s \cdot n_e \tag{7.16}$$

Since the engine speed is constant for the measured values this value will remain constant as well. p_0 is the pressure within the cylinder when no fuel is injected and has been discussed in section 7.2. Finally C_2, C_3, and C_4 are coefficients proposed by Woschni (1967). Woschni proposes a value of 130 for C_2. Ding (2011) uses a different value for C_2 at different operating points. C_4 is equal to 0.00324 [m/s · K] for a direct injection engine (Stapersma, 2010e). C_3 is different during the gas exchange process and during compression and expansion, as is shown in equations 7.17 and 7.18 (Stapersma, 2010e).

$$C_3 = 6.18 + 0.417 \cdot \frac{w_t}{c_m} \quad \text{during gas exchange} \tag{7.17}$$

$$C_3 = 2.28 + 0.308 \cdot \frac{w_t}{c_m} \quad \text{during compression and expansion} \tag{7.18}$$

w_t is the tangential swirl velocity of the gas mixture in the cylinder and is very difficult to measure. According to Ding (2011) the ratio between w_t and c_m varies between 5-50, and uses a value of 10. Important to note that is that since Ding (2011) looked at a four-stroke engine, w_t is most likely higher for a two-stroke engine since the air inlet ports used in a two-stroke engine will enhance the swirl velocity. This velocity can be maintained and even increased during compression (Stapersma, 2010e).

Finally, the wall temperatures of the three mentioned components need to be estimated. Ding (2011) uses constant values for all three components. Something which will not be true in reality. As chapter 4 already eluded to, the temperature within the engine will, most likely, experience a temporal as well as spatial variation of the temperature within the cylinder. Moreover, the wall temperatures will also, in all likelihood, be different at different operating points because lower temperatures will be present at lower loads for the cylinder.

This section has described the modelling of the heat losses in the causal model. As is evident, this part of the model is not without its limitations, since it has made some questionable assumptions. For this reason, the heat losses will be the first thing that will be adjusted if the model seems to be producing unreliable or inaccurate results. This can still be done, however, based on a theoretical approach instead of just by trial and error. Such as by adjusting the wall temperature for different operating points and by increasing the swirl velocity when comparing the results from a four-stroke to a two-stroke engine.

7.6. Vertical shift for reaction coordinate

The anti-causal model has been used to process the data for the four load points. However, the resulting RCO curve shows a specific issue for 75 [kW], 150 [kW], and 225 [kW]. Namely, the RCO curve decreases during the compression stroke before it starts to increase indicating the Start Of Combustion (SOC). This issue does not occur at 375 [kW]. The RCO for each of the four load points is shown in figure 7.4.

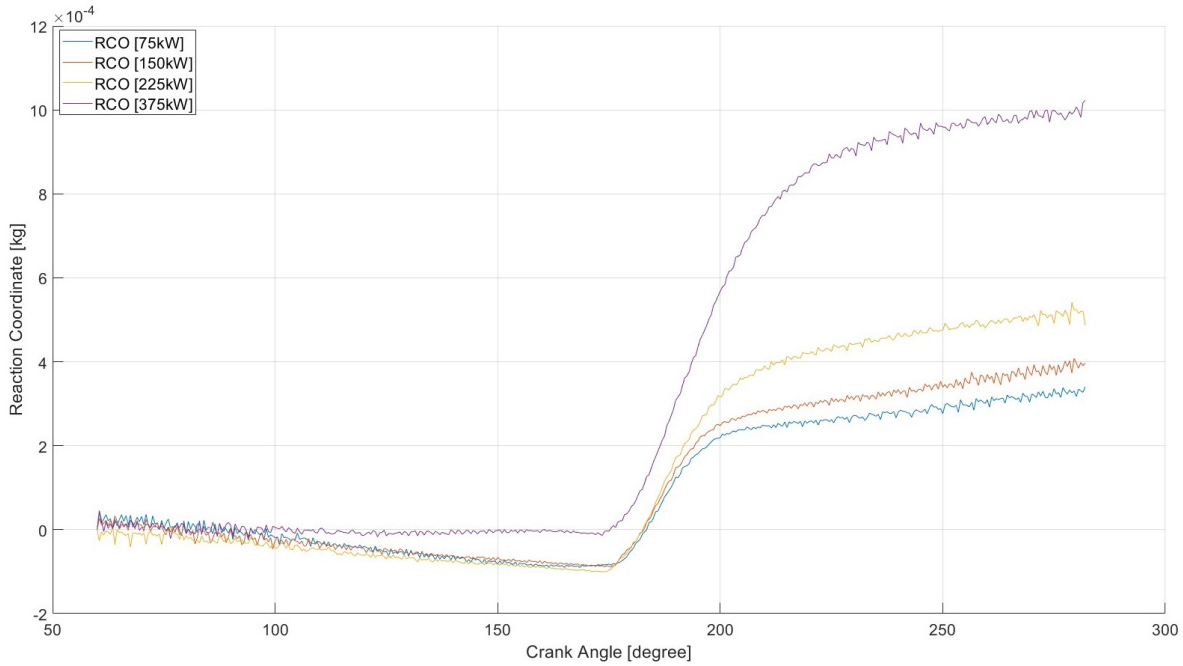

Figure 7.4: Reaction coordinate without vertical shift at different loads

This becomes a problem when the causal model, which will be discussed in chapter 9, is used to construct a pressure curve based on the Wiebe function. The Wiebe function will simulate the CRR for the causal model and is by design equal to zero before SOC. So for 100% power, this is not a problem since the RCO is roughly equal to zero. However, the negative value for RCO for the other load points does cause a problem. Namely that the pressure calculated by the causal model will be too high during the compression stroke. The RCO is calculated by integrating CRR (section 7.1) so to investigate this issue, the three main factors that contribute to the CRR have been plotted for the four load points in the figures below.

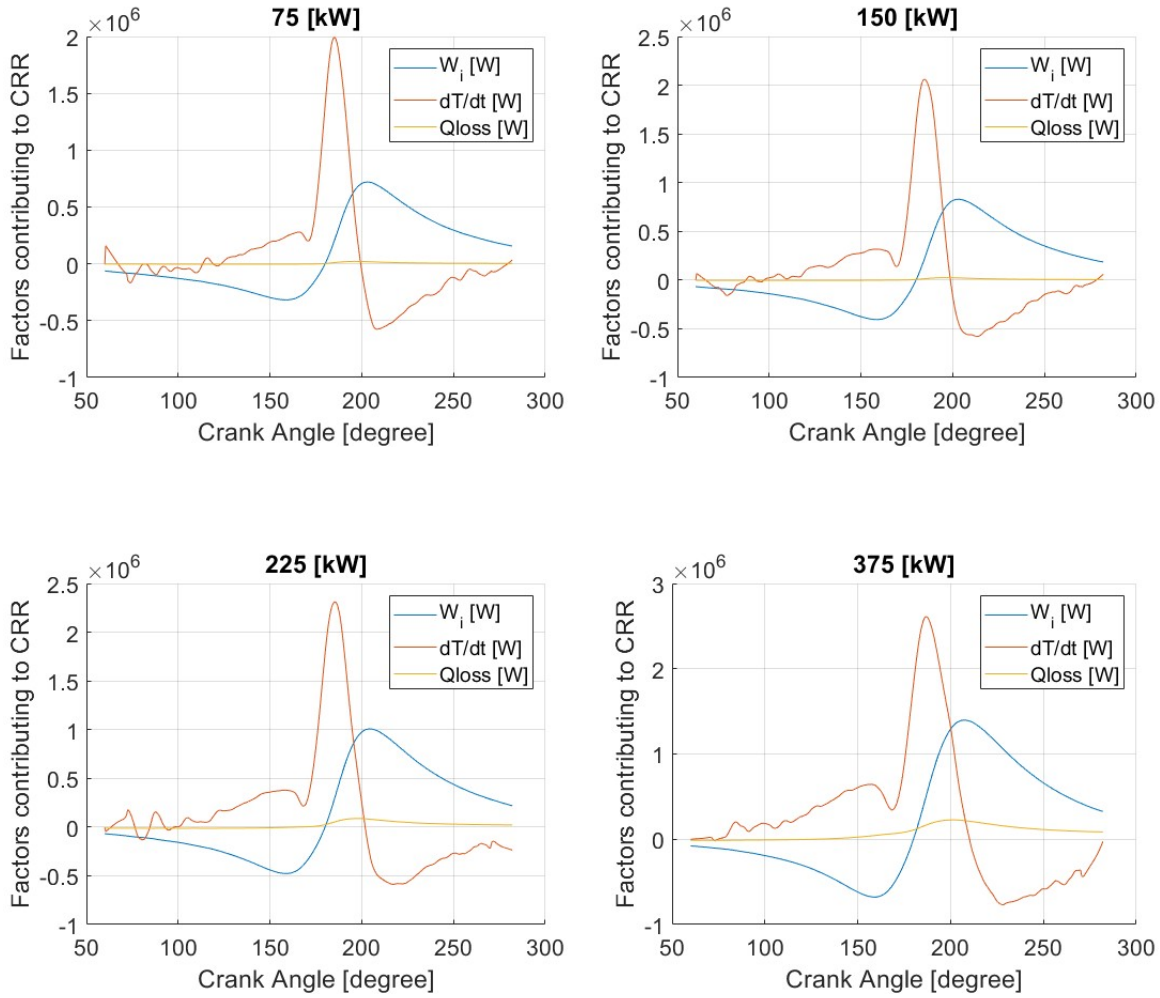

Figure 7.6: CRR factors as a function of crank angle

The three contributing factors are the indicated work, heat losses, and the term referred to as dT/dt (equation 7.19). Please note that this factor fluctuates significantly and that the results plotted in figure 7.6 are computed by ”smoothing” the pressure curves. The pressure curves are still a good representation after they’re smoothed as is shown in figure 7.7.

$$m \cdot c_v \cdot \frac{dT}{dt} \tag{7.19}$$

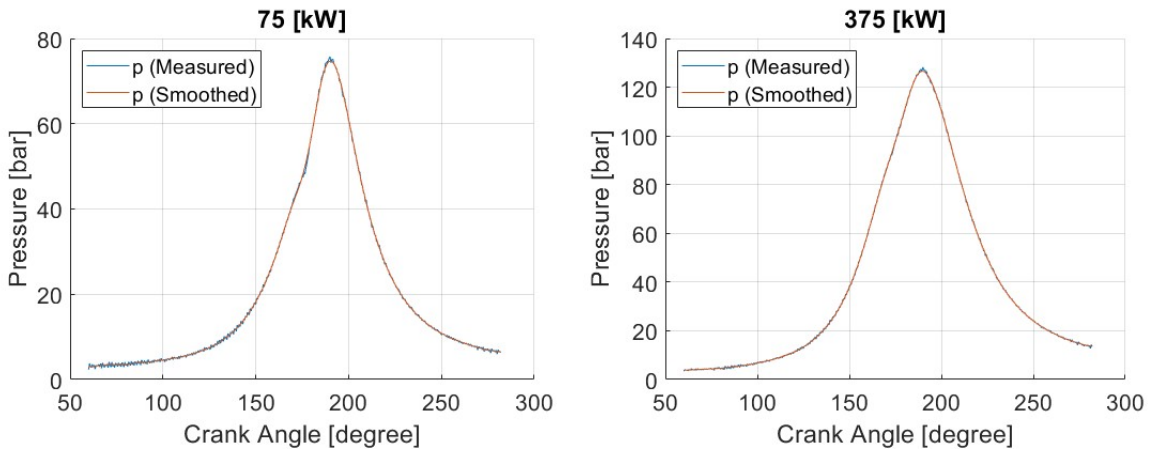

Figure 7.7: Smoothed pressure curves

What can be seen in figure 7.6 is that for full power, the dT/dt factor can compensate for W_i to make sure the RCO is roughly zero before SOC. However, at lower loads, it is not able to do this. An attempt was made to compensate for this effect by adjusting the heat losses. However, from figure 7.6 it's also evident that the heat losses are a lot smaller compared to the other two factors. This meant that the heat losses could not solve the RCO problem. As for W_i, the resulting curve is expected as will be further discussed in the next section. However, the results for the dT/dt factor are very strange. The derivative at lower loads not only fluctuates but is negative. This makes little sense since it would indicate a decreasing temperature during the first phase of the closed-cylinder process. This would be strange since the wall temperatures are higher than the trapped temperature and the upwards-moving piston is compressing the air.

Ding (2011) ran into a similar issue. However, the RCO function was increasing rather than decreasing. Ding (2011) attributes the negative value at the start of the combustion to the heat losses. To solve the issue, the author applies a vertical shift to make sure the RCO has a value around zero before SOC. This shift is shown in figure 7.8.

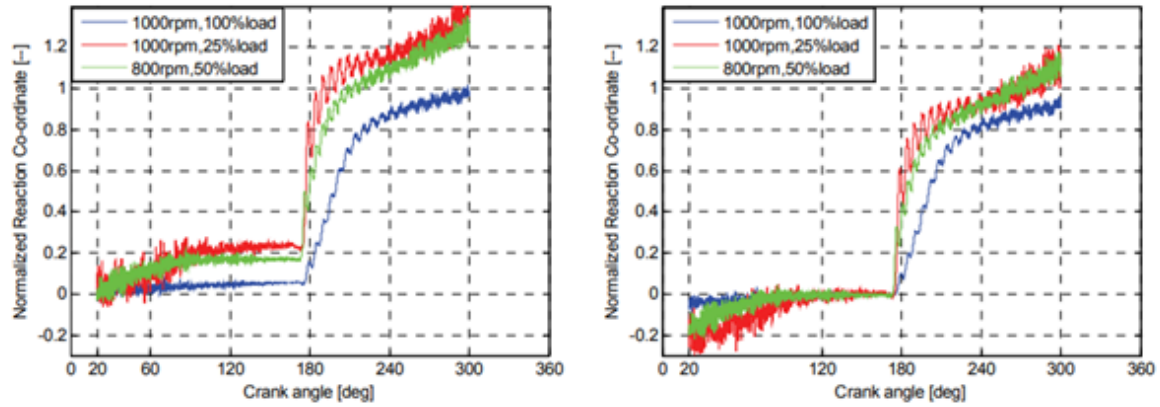

Figure 7.8: RCO shift (Ding, 2011)

Also important to note looking at figure 7.8 it seems that this issue is more dominant at lower loads since the red curve fluctuates significantly compared to the blue curve. What may seem strange is that the RCO is increasing in figure 7.8 while this thesis found it was decreasing. The heat losses and indicated work calculated by Ding (2011) seem to be in the same order of magnitude as this thesis so it must be the dT/dt factor that is the deciding factor in all this.

Another reason for the results might be the trapped conditions as discussed in section 7.4. The trapped pressure and mass calculated for this thesis are shown in figure 7.9. For comparison, the trapped pressure and mass from the reference model developed by Sui Congbiao (2021) are also shown in figure 7.9.

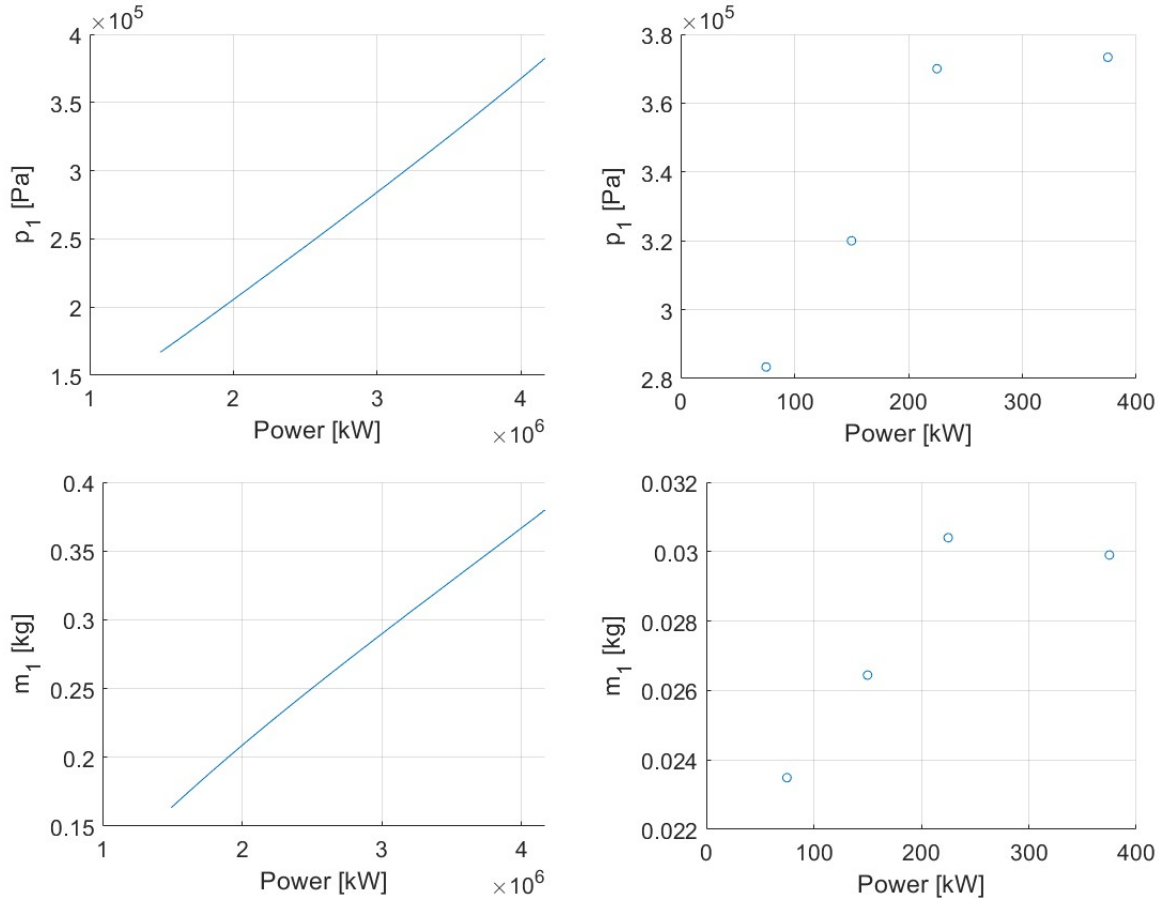

Figure 7.9: Trapped pressure and mass for the Bolnes engine and the reference model

Comparing the trapped conditions from the Bolnes engine and the reference model. It seems strange that the trapped mass is lower for 375 [kW] compared to 225 [kW] since the trapped mass should increase proportionally to the engine power. This effect is caused by the trapped pressure not increasing proportionally to the engine power. At first, it seems that the trapped conditions for 375 [kW] are the outlier here since it is expected that the trapped pressure would increase more than it does. However, it seems more logical, when looking at the overall results, that the other three points are incorrectly registered since no RCO shift is required for 375 [kW]. What can be noted, is that this is perhaps an indication that the pressure sensor struggles when registering the pressure at the beginning of the closed-cylinder process. If the trapped pressure for 75 [kW], 150 [kW], and 225 [kW] were to have a lower value, this would mean that the pressure would increase more during the compression stroke if it is assumed the sensor only struggles to measure at low-pressure values. This increase would lead to a steeper increase in the temperature as well since they're related via the ideal gas law. This steeper increase subsequently means that the derivative of the temperature w.r.t. time, which is one of the factors influencing CRR, could increase as well. This inaccuracy could lead to the RCO problem in this section. However, this should be further investigated to confirm whether this is the definitive reason.

To address the RCO problem, this thesis applies a vertical shift similar to Ding (2011) however, this shift has been applied for the dT/dt factor only. This shift has been scaled to make sure the RCO value is roughly zero for the interval between EC and SOC. It is therefore only applied before SOC, afterwards, this shift is not applied. This has been done because when the entire RCO was moved upwards, the

resulting value for the RCO should be roughly equal to the fuel injected. However, the RCO value with a shift was much higher than the value that was measured. The RCO with and without the vertical shift is shown in figure 7.10.

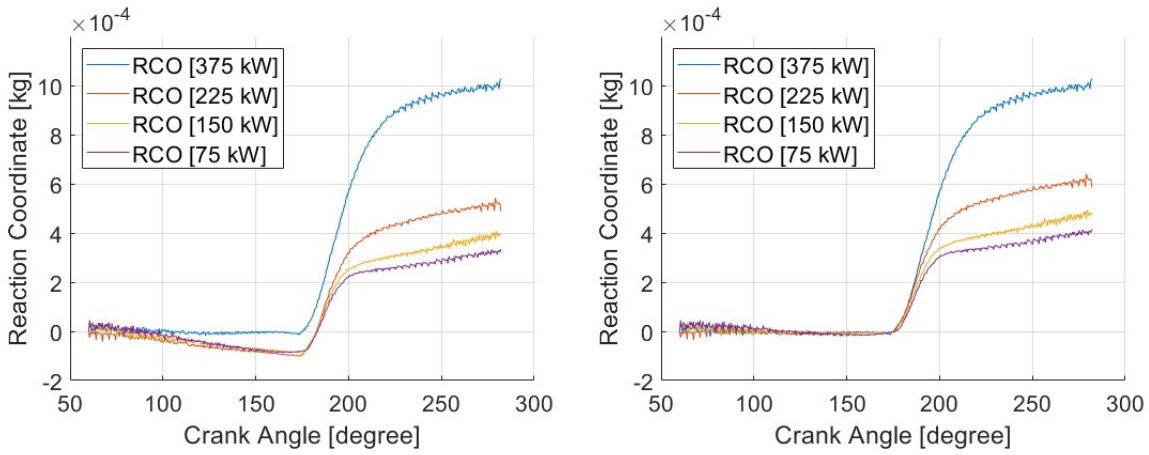

Figure 7.10: RCO with and without the vertical shift

The heat losses have been scaled to make sure the RCO levels out as much as possible around the measured amount of fuel at each load point. Please note that this shift has to be applied to the Causal model as well, which will be explained in chapter 9. To see whether this shift can contribute to a better fit for the causal model can be discussed in chapter 9. The resulting RCO curves will be discussed more in the next section.

7.7. Results

The results produced by the anti-causal model are shown below. The pressure curves have already been shown in section 7.2 so they will be left out. The final results consist of the temperature T, the reaction coordinate RCO, the Net Apparent Heat Release Rate $NAHRR$, the heat losses Q_{loss}, and the indicated work W_i. Please note that the results have been determined with the previously mentioned vertical shift. As for the values that are produced for the equivalence criteria by the model, these will be shown in chapters 8 and 9 so they can be compared to the values produced by the Seiliger approach and causal simulation model.

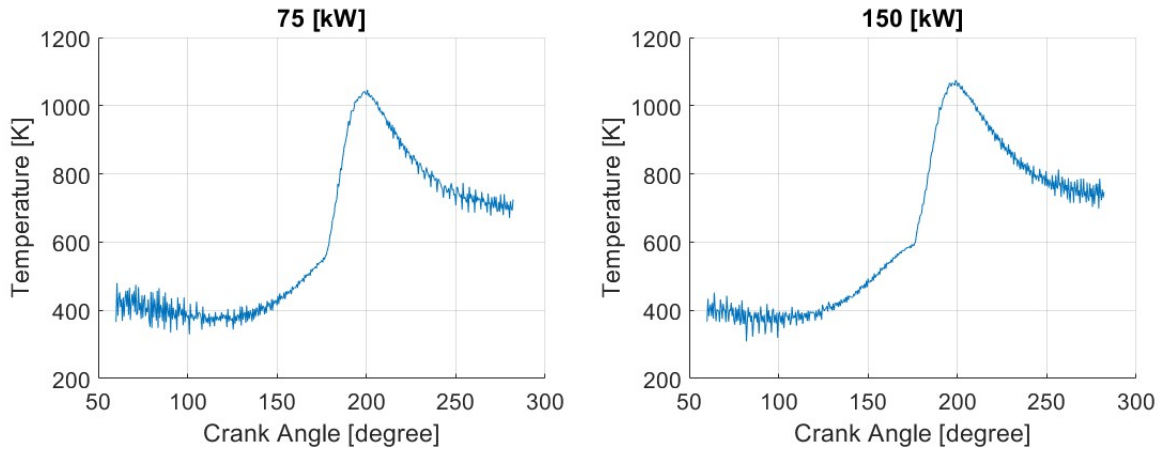

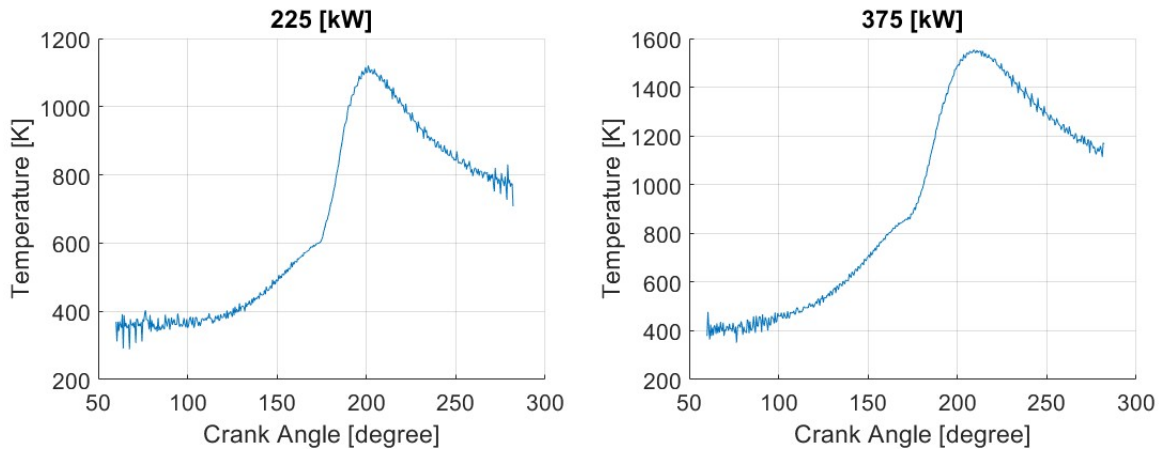

Figure 7.12: Temperature as a function of the crank angle using the anti-causal model

The temperature is shown in figure 7.12. The temperature increases during the compression stroke because of the increasing pressure and decreasing volume within the cylinder. This increase becomes less prevalent at lower loads. Mainly because the pressure isn't increasing as steeply as it does at higher loads. For 75 [kW] and 150 [kW], the temperature is even decreasing at the beginning. This can be attributed to the decreasing RCO value, with even the vertical shift not compensating for this. This result seems odd, especially since the temperature of the mixture in the cylinder is lower than the estimated wall temperatures: 580 [K], 500 [K], and 600 [K] for the cylinder head, cylinder wall, and piston crown respectively (Ding, 2011). It can mainly be attributed to the decreasing RCO and the factors contributing described or the inaccuracy in measuring the trapped pressure described in section 7.6.

Analysing figure 7.12 it seems that the maximum temperature is increasing as the power increases, but its value also occurs later within the cycle. Most likely this can be attributed to a later end of combustion since more fuel is injected at higher loads. The earlier peak temperature also causes the temperature curve to "flatten out" more at lower loads, since the wall temperatures are lower than the in-cylinder temperatures there is more time available for the in-cylinder temperature to decrease. Lastly, the temperature shows more fluctuations at the beginning and end of the closed-cylinder process. This result is caused by the larger fluctuations in pressure measurements shown in figure 7.2.

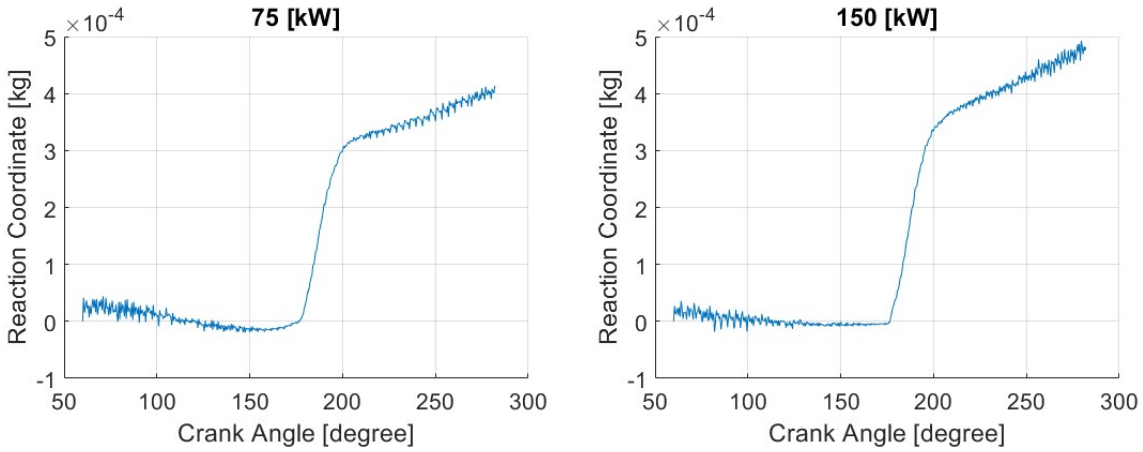

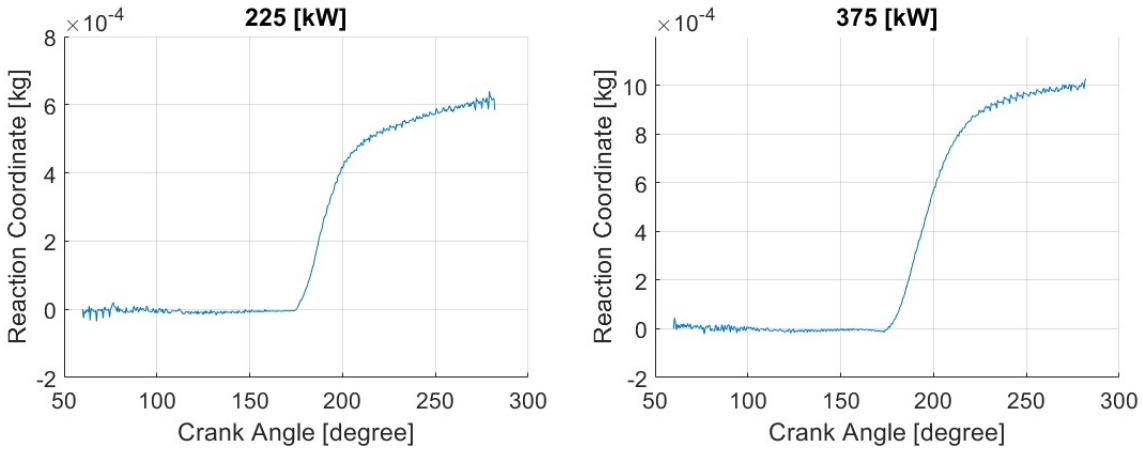

Figure 7.14: Reaction coordinate as a function of the crank angle using the anti-causal model

The RCO has been shown separately for each load point in figure 7.14. For 375 [kW] and 225 [kW], it seems the vertical shift can keep the RCO value roughly around zero before SOC. However, for 75 [kW] and 150 [kW], it struggles to keep the value around zero. It's more the case that the average value over the interval equals zero. This is especially the case for 75 [kW]. The larger fluctuations at the beginning and end of the closed-cylinder process that are present for the temperature curve, also show up in the RCO. Something else which seems to occur at lower loads is that the RCO does not seem the flatten out to indicate the end of combustion. Instead, the curve seems to obtain a certain slope and continues to increase at the same rate. This is similar to the results produced by Ding (2011) presented in section 7.6.

To apply the vertical shift as was discussed in section 7.6 SOC has to be identified. The End Of Combustion (EOC) needs to be determined as well because it is used in the causal model described in chapter 9. It is difficult to see in figure 7.14, but SOC can be identified quite clearly from the determined RCO curve as is shown by figure 7.15. The SOC is delayed as the power drops since it takes a little longer for the pressure and temperature to reach the threshold as discussed in chapter 4 to achieve combustion.

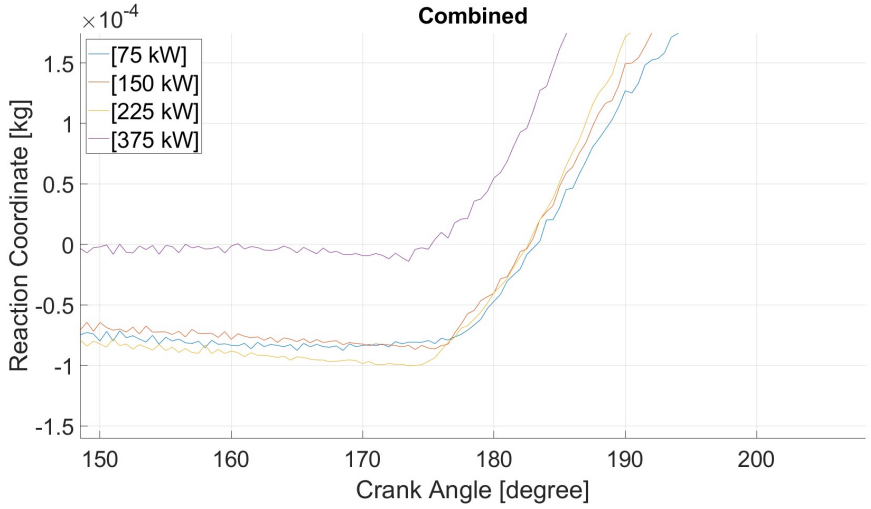

Figure 7.15: RCO for determining SOC

As for the end of combustion, the heat losses have scaled to make sure the RCO "flattens out" as much as possible around the amount of fuel injected in the cylinder. This means that EOC is taken as the crank angle where the RCO intersects with the amount of fuel injected within the cylinder. This is not a great way to determine EOC since it automatically assumes a combustion efficiency of 100%. This

approach was chosen since it's generally difficult to determine EOC (Ding, 2011).

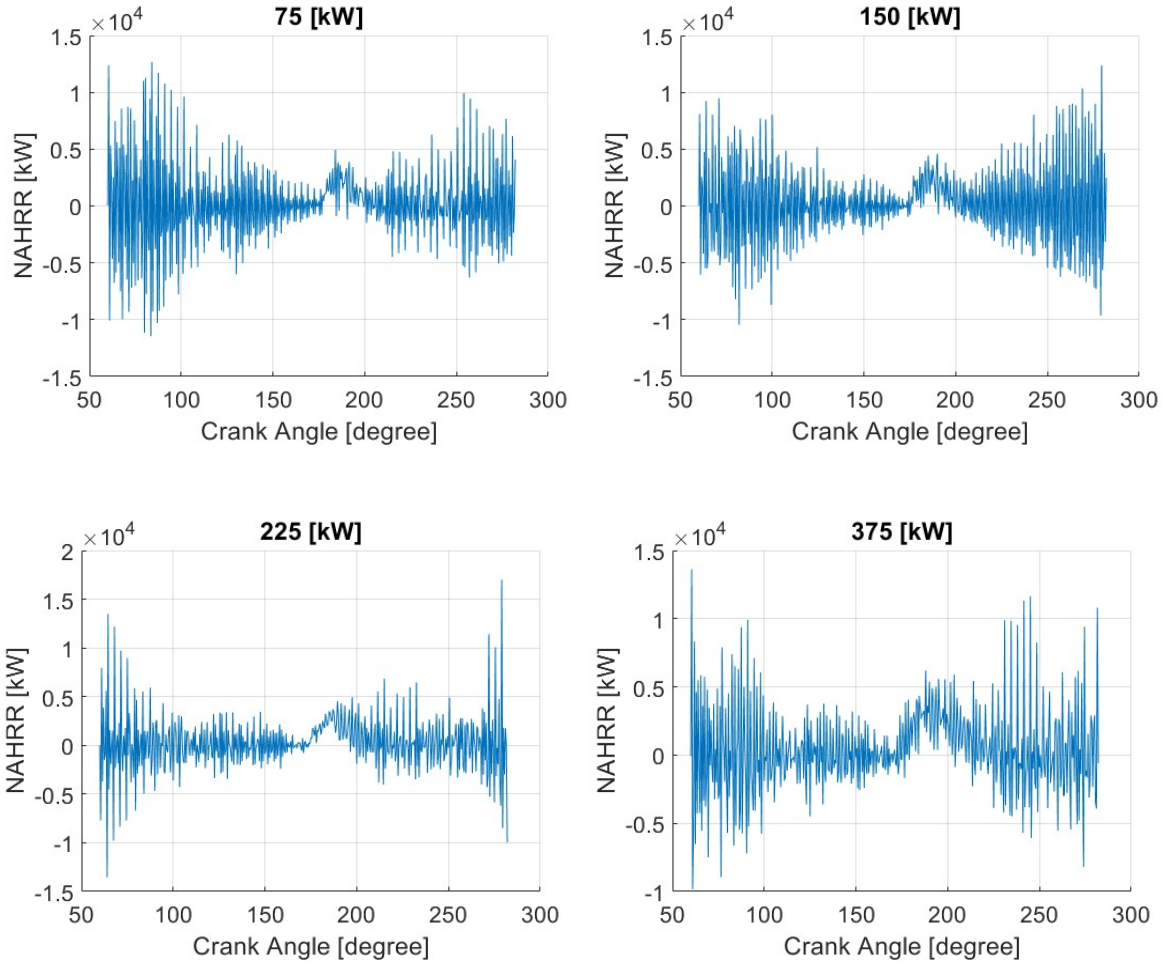

Figure 7.17: Net Apparent Heat Release Rate as a function of the crank angle using the anti-causal model

The Net Apparent Heat Release Rate (NAHRR) is shown in figure 7.17. The Combustion Reaction Rate (CRR) has not been plotted but is very similar to NAHRR. The fluctuations in temperature that were discussed earlier in this section have a large effect on the NAHRR. In the beginning, their values reach very high and low values compared to the average value. This effect is caused by the factor shown in equation 7.19. Since the temperature fluctuates significantly, the derivative does as well causing the large peaks in figure 7.17. This makes it difficult to identify SOC as well as the End of Combustion (EOC). When looking closely at figure 7.17, a small increase can be identified in the area where the RCO starts to increase as well. This shape is something which will be simulated in the causal model by the Wiebe function and will be discussed in chapter 9.

As has already been mentioned when discussing the different contributing factors to CRR, the heat losses are significantly smaller than the NAHRR. This means that the Gross Apparent Heat Release Rate (GAHRR) is very similar to NAHRR since the only difference is that GAHRR also includes the heat losses. This means that the GAHRR is not shown in this section for the different operating points.

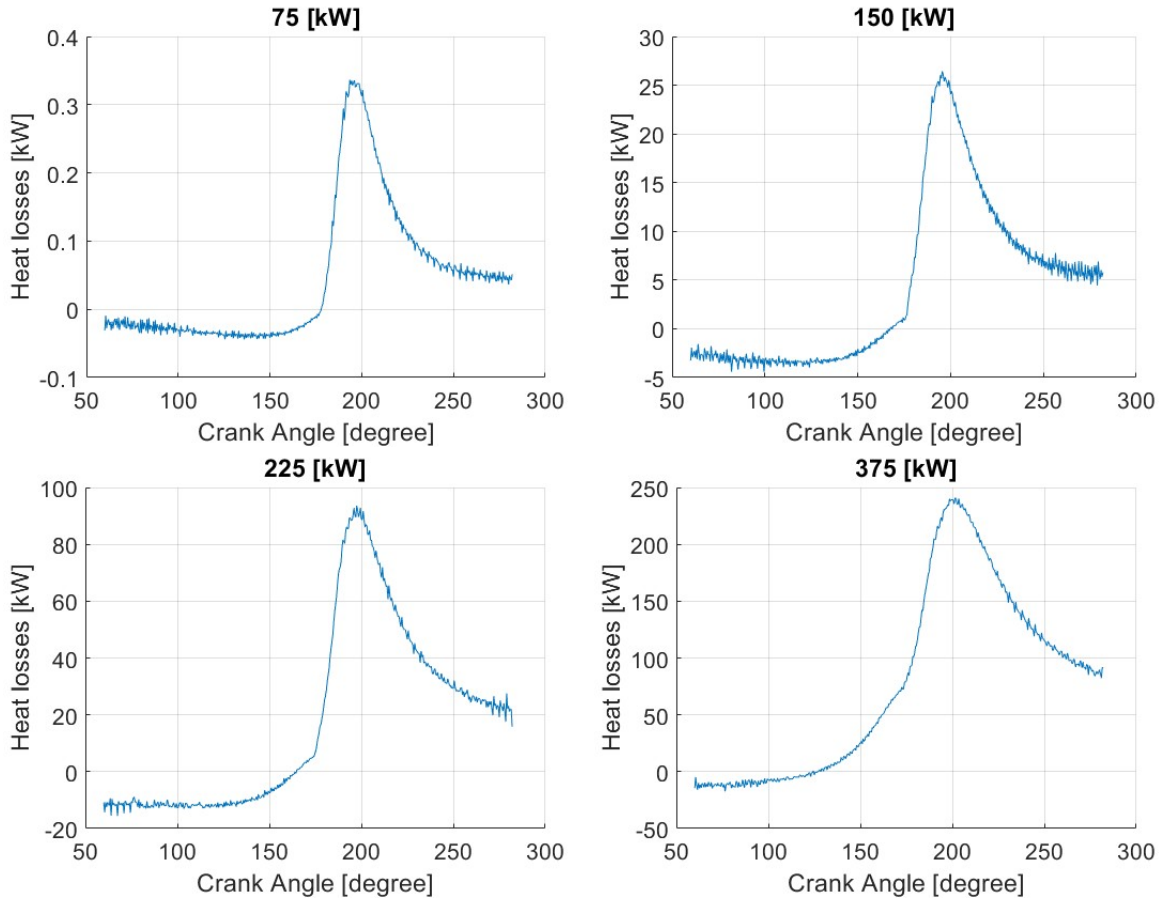

Figure 7.18: Heat losses as a function of the crank angle using the anti-causal model

The heat losses are shown in figure 7.18. The heat losses generally follow the same trend as the temperature since they depend largely on the difference between the wall temperature and in-cylinder temperature. This is why the heat losses are negative at first, the wall temperature is kept constant while the in-cylinder temperature starts at a lower value. The temperature increases during the compression stroke, with it rising quicker at higher loads, causing the heat losses to flip to positive earlier at higher loads. Since the heat losses have been scaled to shape the RCO as was discussed in section 7.6. This means that the heat losses are a lot smaller for 75 [kW] than for 375 [kW].

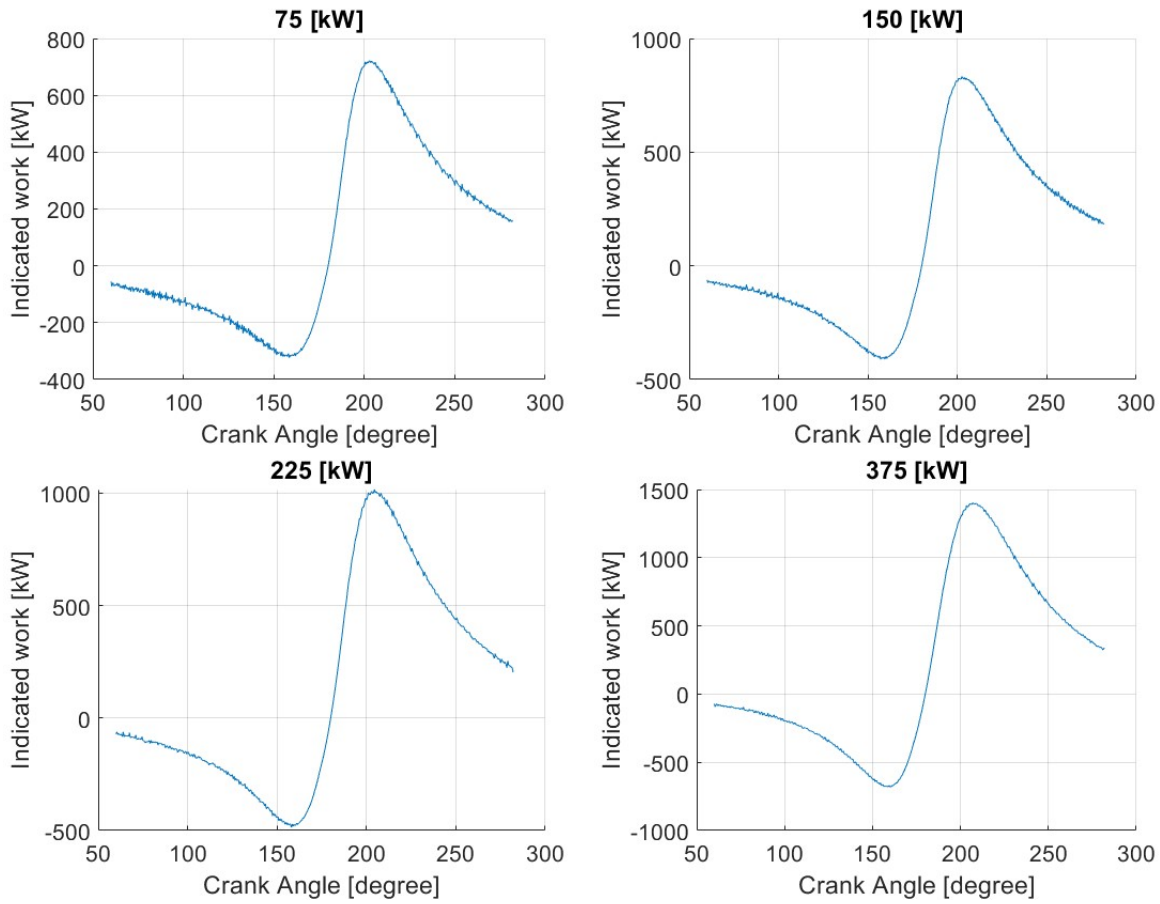

Figure 7.19: Indicated work as a function of the crank angle using the anti-causal model

The indicated work is shown in figure 7.19. These results seem logical. The indicated work is negative at first because the compression stroke requires work instead of delivering it. At some point, the work starts to increase significantly indicating the sudden pressure increase due to combustion. After that, the work starts to decrease again since the pressure decreases again. These results are not all that interesting but at least they do verify that the work that is calculated in the model gives a realistic representation.

This chapter has discussed how the anti-causal simulation model has been built in a Matlab Simulink environment, along with discussing the results produced by the anti-causal model. The next chapter will discuss the usage of the Newton-Rhapson solver to find the Seiliger parameters.

8

Finding the Seiliger parameters

Chapter 3 discussed the application of a so-called air-standard analysis, and that the reference model for this thesis uses the Seiliger process to model the closed cylinder process. This chapter will explain how the so-called Seiliger parameters: r_c, n_c, r_{exp}, n_{exp}, a, b, and c that constitute the Seiliger process can be found. This method has been constructed by Ding (2011) during his doctoral dissertation. The method uses the results from the anti-causal model described in chapter 7 to do this. Section 8.1 will explain the theory behind the Seiliger process. Section 8.2 will describe the Newton-Rhapson solver, an iterative process to find the root of the function. Of the above-mentioned Seiliger parameters r_c and n_c can actually be calculated directly, while r_{exp}, n_{exp}, a, b, and c should be estimated using the Newton-Rhapson solver. This will be explained in sections 8.3 and 8.4 respectively. The definition of the symbols, abbreviations, and subscripts used in this section can be found in the nomenclature of this report.

8.1. Seiliger process

The Seiliger process divides the closed-cylinder process into 6 stages. A description of the stages is provided below (Ding, 2011), while the pressure-volume (p-V) diagram is shown in figure 8.1.

- 1-2: polytropic compression, indicating the net heat loss
- 2-3: iso-volumetric combustion
- 3-4: isobaric combustion and expansion
- 4-5: isothermal combustion and expansion
- 5-6: polytropic expansion indicating the net heat input caused by the combustion process

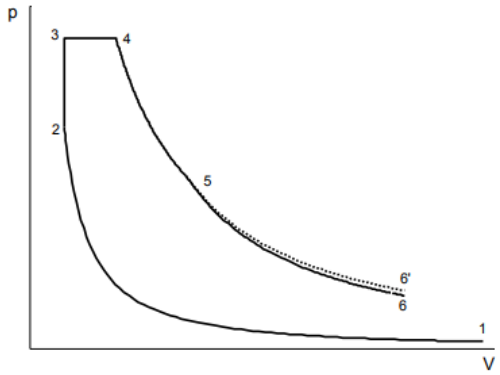

Figure 8.1: Basic and advanced Seiliger process (Ding, 2011)

The difference between the basic and advanced cycles is that the advanced cycle does take into account the heat losses to the wall.

The Seiliger process can be characterised by the Seiliger parameters which are characterised by the volume, pressure, and temperature ratios between the different stages of the Seiliger process, as shown in table 8.1. These parameters can be used alongside the trapped temperature T_1, specific heat c_v, and specific heat ratio γ to compute the specific heat and work for each stage of the Seiliger process as is shown in table 8.2.

Table 8.1: Seiliger parameters (Sui Congbiao, 2021)

Stage	Volume ratio	Pressure ratio	Temperature ratio
1-2	$\frac{V_1}{V_2} = r_c$	$\frac{p_2}{p_1} = r_c^{n_c}$	$\frac{T_2}{T_1} = r_c^{n_c-1}$
2-3	$\frac{V_3}{V_2} = 1$	$\frac{p_3}{p_2} = a$	$\frac{T_3}{T_2} = a$
3-4	$\frac{V_4}{V_3} = b$	$\frac{p_4}{p_3} = 1$	$\frac{T_4}{T_3} = b$
4-5	$\frac{V_5}{V_4} = c$	$\frac{p_4}{p_5} = c$	$\frac{T_5}{T_4} = 1$
5-6	$\frac{V_6}{V_5} = r_{exp}$	$\frac{p_5}{p_6} = r_{exp}^{n_{exp}}$	$\frac{T_6}{T_5} = r_{exp}^{1-n_{exp}}$

Table 8.2: specific work and heat for each state of the Seiliger process (Stapersma, 2010b)

Stage	specific work *w* [J/kg]	specific heat *q* [J/kg]
1-2	$-c_{v,12} \cdot T_1 \cdot \frac{\gamma_{12}-1}{n_c-1} \cdot (r_c^{n_c-1}-1)$	$c_{v,12} \cdot T_1 \cdot \left(1 - \frac{\gamma_{12}-1}{n_c-1}\right) \cdot (r_c^{n_c-1}-1)$
2-3	0	$c_{v,23} \cdot T_1 \cdot r_c^{n_c-1} \cdot (a-1)$
3-4	$c_{v,34} \cdot T_1 \cdot (\gamma_{34}-1) \cdot r_c^{n_c-1} \cdot a \cdot (b-1)$	$c_{v,34} \cdot T_1 \cdot \gamma_{34} \cdot r_c^{n_c-1} \cdot a \cdot (b-1)$
4-5	$c_{v,45} \cdot T_1 \cdot (\gamma_{45}-1) \cdot r_c^{n_c-1} \cdot a \cdot b \cdot ln(c)$	$c_{v,45} \cdot T_1 \cdot (\gamma_{45}-1) \cdot \cdot r_c^{n_c-1} \cdot a \cdot b \cdot ln(c)$
5-6	$c_{v,56} \cdot T_1 \cdot \frac{\gamma_{56}-1}{n_{exp}-1} \cdot r_c^{n_c-1} \cdot a \cdot b \cdot \left(1 - \frac{1}{r_{exp}^{n_{exp}-1}}\right)$	$-c_{v,56} \cdot T_1 \cdot \left(1 - \frac{\gamma_{56}-1}{n_{exp}-1}\right) \cdot r_c^{n_c-1} \cdot a \cdot b \cdot \left(1 - \frac{1}{r_{exp}^{n_{exp}-1}}\right)$

8.2. Newton-Rhapson method

The Newton-Rhapson method is an iterative process that estimates the value of a variable based on a function and its derivative. This process is shown in equation 8.1.

$$x_{n+1} = x_n - \frac{f(x_n)}{f'(x_n)} \tag{8.1}$$

The equation updates the value of the variable each time, and this process can be repeated indefinitely. However, if the value of the variable converges to a value with the desired accuracy, then it makes sense to stop the process. It helps to have a good initial estimation of the variable. For the Seiliger parameters, however, equation 8.1 has to be adapted to solve a system of equations. For a system with n variables, equation 8.2 can be used, with $\mathbf{f}$ and $\mathbf{A}$ being defined in equation 8.3.

$$\mathbf{x}[n+1] = \mathbf{x}[n] - \mathbf{A}^{-1}\mathbf{f}[n] \tag{8.2}$$

$$\mathbf{f} = \begin{bmatrix} f_1(x_1, \cdots, x_n) \\ \vdots \\ f_n(x_1, \cdots, x_n) \end{bmatrix}, \mathbf{A} = \begin{bmatrix} \frac{\partial f_1}{\partial x_1} & \cdots & \frac{\partial f_1}{\partial x_n} \\ \vdots & \ddots & \vdots \\ \frac{\partial f_n}{\partial x_1} & \cdots & \frac{\partial f_n}{\partial x_n} \end{bmatrix} \tag{8.3}$$

The exact vectors that are used will be shown in section 8.4.

8.3. Finding r_c and n_c

Stage 1 of the Seiliger process is equal to the trapped conditions previously discussed in chapter 7. Chapter 7 also discussed how the volume can be calculated while the pressure is measured as a function of the crank angle. Stage 2 marks the beginning of combustion, as was discussed in section 8.1. This means that the volume V_2 and pressure p_2 for stage 2 can be measured for the crank angle value that marks the Start Of Combustion (SOC). r_c and n_c can, therefore, be calculated using equations 8.4 and 8.5 respectively.

$$r_c = \frac{V_1}{V_2} = \frac{V(EC)}{V(SOC)} \tag{8.4}$$

$$n_c = log\left(\frac{p_2}{p_1} - r_c\right) \tag{8.5}$$

The final values for both are shown in section 8.5.

8.4. Finding r_{exp}, n_{exp}, a, b, and c

Since there are still five Seiliger parameters that need to be found, at least five equations are required. r_{exp} can be expressed as a function of b, c, and the volume ratio between stages 2 and 6 r_{26}:

$$r_{exp} = \frac{V_6}{V_5} = \frac{V_6}{b \cdot c \cdot V_2} = \frac{1}{r_{26} \cdot b \cdot c} \tag{8.6}$$

The volume at stage 6 is equal to the volume in the cylinder when the exhaust valve opens:

$$V_6 = V_{EO} \tag{8.7}$$

This means that a system with four equations has to be constructed to solve the remaining parameters. The four equations that are used to calculate the so-called ”equivalence criteria” by Ding (2011) are shown in equations 8.8 up to and including 8.11.

$$p_3 = p_1 \cdot r_c^{n_c} \cdot a \tag{8.8}$$

$$T_4 = T_1 \cdot r_c^{n_c} \cdot a \cdot b \tag{8.9}$$

$$q_{in} = q_{23} + q_{34} + q_{45} + q_{56} \tag{8.10}$$

$$w_{in} = w_{12} + w_{34} + w_{45} + w_{56} \tag{8.11}$$

Ding (2011) used different sets of equivalence criteria to find the Seiliger parameters. This thesis selected the set that was rated highest instead of using multiple sets. The specific work and heat for each stage of the Seiliger process are shown in table 8.2. As for c_v and γ, they are a function of the in-cylinder temperature and gas composition. However, they are kept constant for each distinct stage of the Seiliger process. Each stage of the Seiliger process does have a distinct value for both c_v and γ. The four functions that will be used for the vector $\mathbf{f}$ will be the difference between the values calculated by equations 8.8 up to and including 8.11 and the values calculated by the anti-causal model described in chapter 7. The subsequent functions are shown below:

$$f_1(a, b, c, n_{exp}) = p_3 - p_{max} \tag{8.12}$$

$$f_2(a, b, c, n_{exp}) = T_4 - T_{max} \tag{8.13}$$

$$f_3(a, b, c, n_{exp}) = q_{in,seil} - q_{in.meas} \tag{8.14}$$

$$f_4(a, b, c, n_{exp}) = w_{i,seil} - w_{i.meas} \tag{8.15}$$

Please note that the heat release model determines the total instead of specific work and heat input. Therefore, these values need to be divided by the trapped m_1. In reality, the mass within the cylinder changes as fuel is injected, but this difference in mass is quite small and is thus neglected. The next step is to determine the tolerances for each of the four equivalence criteria, which are listed below:

$$|p_3 - p_{max}| \leq 1[bar], \quad |T_4 - T_{max}| \leq 1[K] \tag{8.16}$$

$$|q_{in,Seil} - q_{in,meas}| \leq 1[J/kg], \quad |w_{i,Seil} - w_{i,meas}| \leq 1[J/kg] \tag{8.17}$$

The Newton-Rhapson solver that is constructed has a finite amount of iterations to make sure it eventually stops if no solution can be found. If, however, the produced results are within the specified tolerances, the process is also stopped. Ding (2011) proposed a range for each Seiliger parameter used along with the Newton-Rhapson solver. This range has also been implemented as a limit during the Newton-Rhapson solver. What this means is that if the value of one of these parameters exceeds this limit, it will automatically remain fixed at either minimum or maximum value. The value can still be changed during the next iteration, but not stay within this limit. This thesis found that the limit for the Seiliger parameter c is especially important since the solver would otherwise produce large values for c. This meant that the Seiliger fit, which will be described in more detail in section 8.5, would keep the temperature at its maximum value for an interval which seemed too long. These limits can differ at different loads and can be adjusted to obtain a better Seiliger fit. The used limits are shown in table 8.3.

Table 8.3: Limits for Seiliger fit

Seiliger parameter	Range 75 [kW]	Range 150 [kW]	Range 225 [kW]	Range 375 [kW]
a	1-2	1-2	1-2	1-2
b	1-2	1-2	1-2	1-2
c	1-1.35	1-1.35	1-2	1-3
n_{exp}	1.2-1.31	1.2-1.31	1.2-1.31	1.2-1.31

8.5. Results

With the described process in this chapter, the Seiliger parameters have been found for the operating conditions discussed in chapter 6. These parameters were used to compute the pressure and temperature as a function of the crank angle. The Seiliger parameters that were used are shown in table 8.4, while the results that were produced are shown in table 8.5.

Table 8.4: Seiliger parameters for different operating points

Seiliger parameter	75 [kW]	150 [kW]	225 [kW]	375 [kW]
r_c	10.96	10.96	10.96	10.96
n_c	1.16	1.19	1.20	1.35
a	1.65	1.60	1.56	1.37
b	1.17	1.15	1.19	1.28
c	1.25	1.35	2	2.61
r_{exp}	4.84	4.99	2.55	2.79
n_{exp}	1.24	1.23	1.31	1.31

Table 8.5: Results produced by Seiliger parameters vs results anti-causal model

Seiliger parameter		75 [kW]	150 [kW]	225 [kW]	375 [kW]
p_{max}	(anti-causal)	75.63 [bar]	88.87 [bar]	102.9 [bar]	130.03 [bar]
p_{max}	(Seiliger)	75.63 [bar]	88.87 [bar]	102.9 [bar]	130.03 [bar]
T_{max}	(anti-causal)	1046.6 [K]	1074.9 [K]	1121 [K]	1533.9 [K]
T_{max}	(Seiliger)	1046.6 [K]	1074.9 [K]	1121 [K]	1533.9 [K]
W_i	(anti-causal)	6.51 [kJ]	7.43 [kJ]	9.78 [kJ]	14.94 [kJ]
W_i	(Seiliger)	6.51 [kJ]	7.43 [kJ]	9.78 [kJ]	14.94 [kJ]
Q_{in}	(anti-causal)	16.61 [kJ]	18.91 [kJ]	21.99 [kJ]	34.25 [kJ]
Q_{in}	(Seiliger)	16.61 [kJ]	18.91 [kJ]	21.99 [kJ]	34.25 [kJ]

Comparing the results produced by the anti-causal model and the Seiliger approach it seems the method proposed by Ding (2011) can produce very accurate results. The values are almost identical between the two models. This makes sense since the Newton-Rhapson solver is trying to produce results as close as possible for these four parameters. Please note that the results are not identical but that they have been rounded off for this report.

To plot both the pressure and temperature as a function of the crank angle according to the Seiliger process two things have to be done. First, the crank angle associated with each stage has to be found. Second, the equations describing the pressure and temperature curves during each stage have to be constructed. The crank angle can be found using the relations between the volumes at different stages in table 8.1. Since each volume is associated with a crank angle, the found Seiliger parameters can be used to compute the volume at each stage, and the subsequent crank angle. Please note that since the piston in the engine is moving both towards Top Dead Centre (TDC) and away from it one has to take into account the fact that for stages 4, 5, and 6 the crank angle will be reached after TDC instead of before.

The equation for each stage can be constructed based on the relations listed in table 8.1 as well. For stage 1-2, the trapped pressure p_1, trapped volume V_1, and n_c are used along with the volume as a function of the crank angle to calculate the temperature and pressure in equations 8.18 and 8.19 respectively.

$$p_{1-2}(\phi) = p_1 \cdot \left(\frac{V_1}{V(\phi)}\right)^{n_c} \tag{8.18}$$

$$T_{1-2}(\phi) = T_1 \cdot \left(\frac{V_1}{V(\phi)}\right)^{n_c-1} \tag{8.19}$$

For stage 2-3, both the pressure and temperature make a sudden jump to a higher value. This means that the crank angles for points 2 and 3 are identical in the Seiliger cycle, which makes sense since their volumes are the same according to table 8.1.

$$p_{2-3}(\phi) = p_3 = p_4 = p_{max} \tag{8.20}$$

$$T_{2-3}(\phi) = T_3 \tag{8.21}$$

For stage 3-4, the pressure remains constant at the maximum pressure that occurs within the cylinder. The temperature, however, does still increase for this stage according to equation 8.23.

$$p_{3-4}(\phi) = p_3 = p_4 = p_{max} \tag{8.22}$$

$$T_{3-4}(\phi) = \frac{T_3 \cdot V(\phi)}{V_3} \tag{8.23}$$

For stage 4-5, the pressure will start to decrease since the volume at this point is increasing in equation 8.24. The temperature has now reached its maximum value and will remain at this value during the entire stage.

$$p_{4-5}(\phi) = \frac{p_4 \cdot V_4}{V(\phi)} \tag{8.24}$$

$$T_{4-5}(\phi) = T_4 = T_5 = T_{max} \tag{8.25}$$

For the final stage, both the pressure and the temperature are decreasing again according to equation 8.26 and 8.27 respectively.

$$p_{5-6}(\phi) = p_5 \cdot \left(\frac{V(\phi)}{V_5}\right)^{n_{exp}} \tag{8.26}$$

$$T_{5-6}(\phi) = T_5 \cdot \left(\frac{V(\phi)}{V_5}\right)^{n_{exp}-1} \tag{8.27}$$

With the equations and results listed above, the pressure and temperature curves have been computed for 75 [kW], 150 [kW], 225 [kW], and 375 [kW] in figures 8.3 and 8.4 respectively.

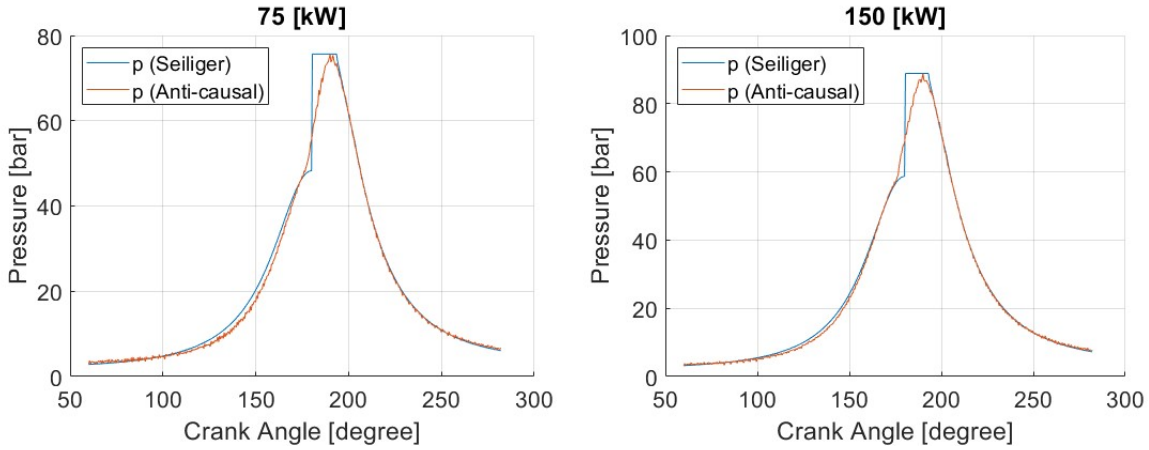

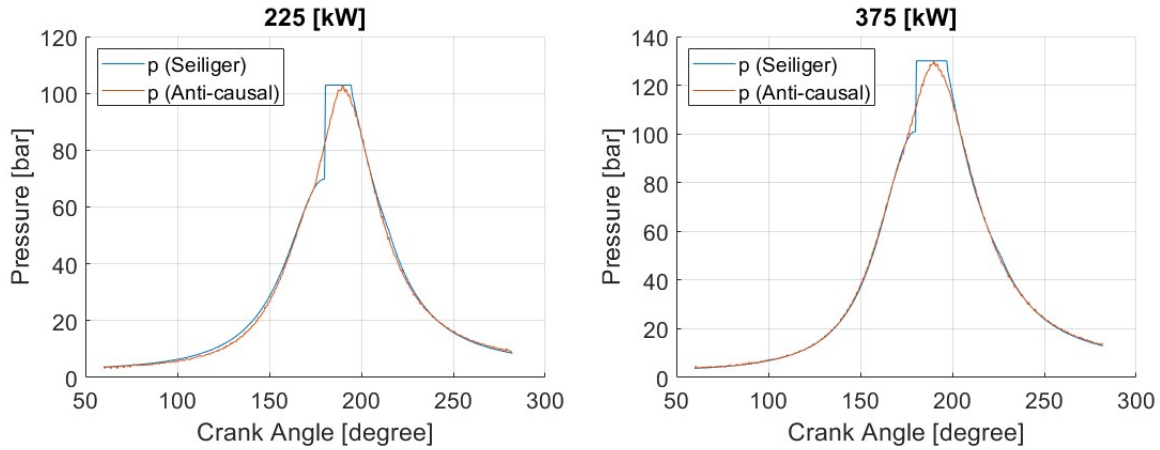

Figure 8.3: Pressure as a function of the crank angle

Analysing the computed pressure curves one thing seems to be evident. The results become less representative at lower loads. Looking at the results for full power, the pressure curve follows the compression (stage 1-2) and expansion (stages 4-5 and 5-6) well. For the combustion phase, the Seiliger process is not able to follow the measured pressure well because of the way that it's set up, however, it does compute a value very close to the maximum pressure that was measured. So despite its shape, the Seiliger function approximates the combustion phase quite well. The same can be said for the expansion phase.

However, for lower loads, it seems like the pressure curve becomes less accurate as the power decreases. The pressure curves show more and more deviation for the compression phase, something which almost didn't exist and full power. An attempt has been made to compensate for this fact by scaling the heat losses differently, however, this means that the Reaction Coordinate (RCO) will not be scaled as was described in chapter 7. Moreover, even when the heat losses were scaled significantly, this did not make much of a difference.

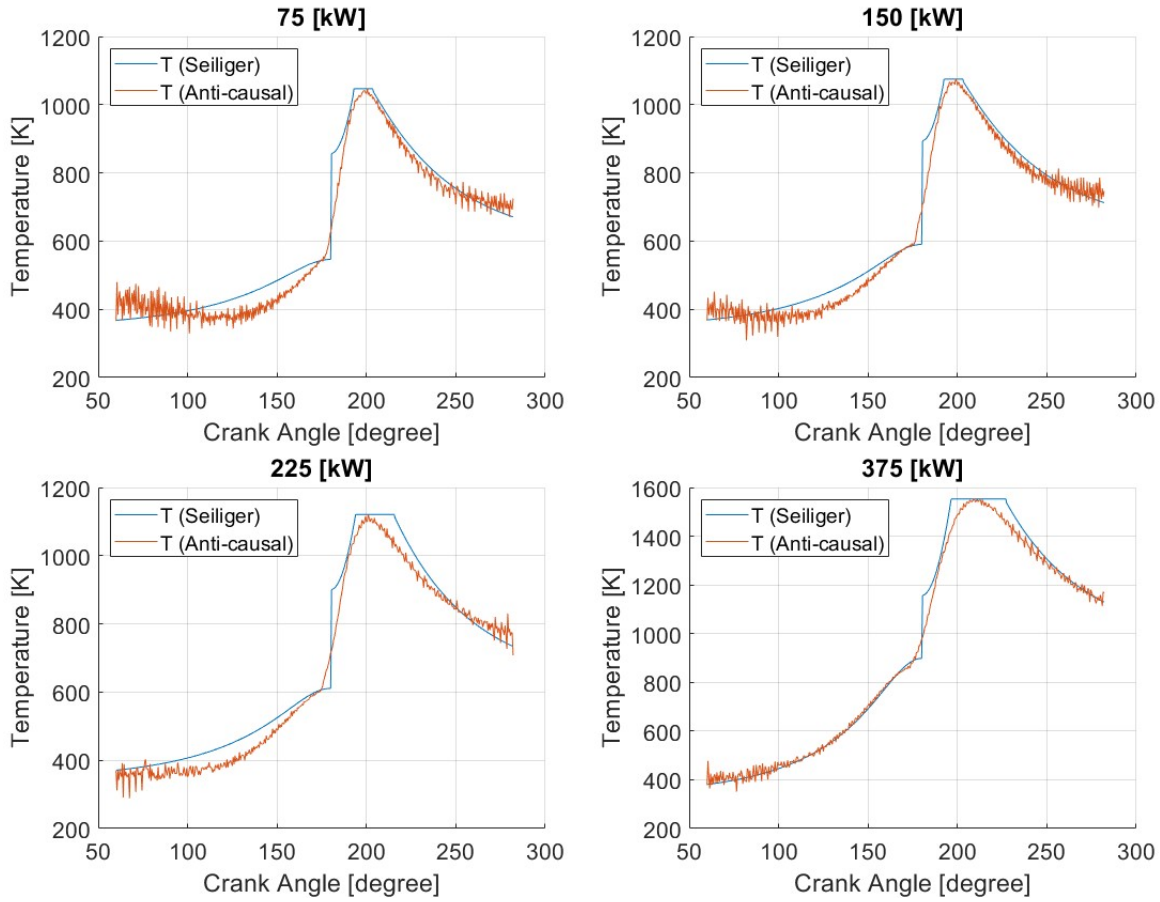

Figure 8.4: Temperature as a function of the crank angle using the Seiliger fit

As for the temperature, the expansion stage is again approximated well, but the compression stroke is already more difficult. The maximum value again is approximated well and the function fits the combustion phase adequately. However, deviations for the compression phase that exist for the pressure curve, are even more significant for the temperature. Again this deviation seems to get worse as the power decreases. The Seiliger process manages to achieve the maximum temperature well for every load. For the compression phase, the Seiliger process will predict that the temperature will be increasing, however, this is not the case for the temperature curve produced by the anti-causal model. This phenomenon can also not be mitigated by adjusting the heat losses for the anti-causal model, for the same reason as described in chapter 7. As for the expansion phase, the Seiliger process is a decent representation compared to the anti-causal model.

This chapter has discussed the theory behind the Seiliger process, along with using a Newton-Rhapson to find the Seiliger parameters. Additionally, this chapter has discussed the accuracy of the results produced by the Seiliger approach. The next chapter will discuss the causal simulation model.

9

Causal simulation model

This chapter describes the causal simulation model that has been constructed for this thesis. This model is very similar to the anti-causal simulation model described in chapter 7. In essence, the causal model can be created by rearranging the different ”building blocks” with two important differences. Instead of calculating the Combustion Reaction Rate (CRR), as is done in the anti-causal model, CRR is simulated by using a Wiebe function. This is done by using the determined Reaction Coordinate (RCO) from the anti-causal model to obtain the parameters for the Wiebe function. The second difference of the causal model is that the pressure is calculated by using the ideal gas law instead of using the measured pressure curve. By using the Wiebe function, the causal model will produce the same results as the anti-causal model but the results are much smoother. This method of smoothing is considered preferable compared to mathematical means of smoothing because it's based on first-principle thermodynamics. As for the parameters that are a function of the crank angle, the thermodynamic properties, the trapped conditions and the heat losses. These are modelled the same as for the anti-causal and have already been discussed in chapter 7. A schematic representation of the causal model is shown in figure 9.1.

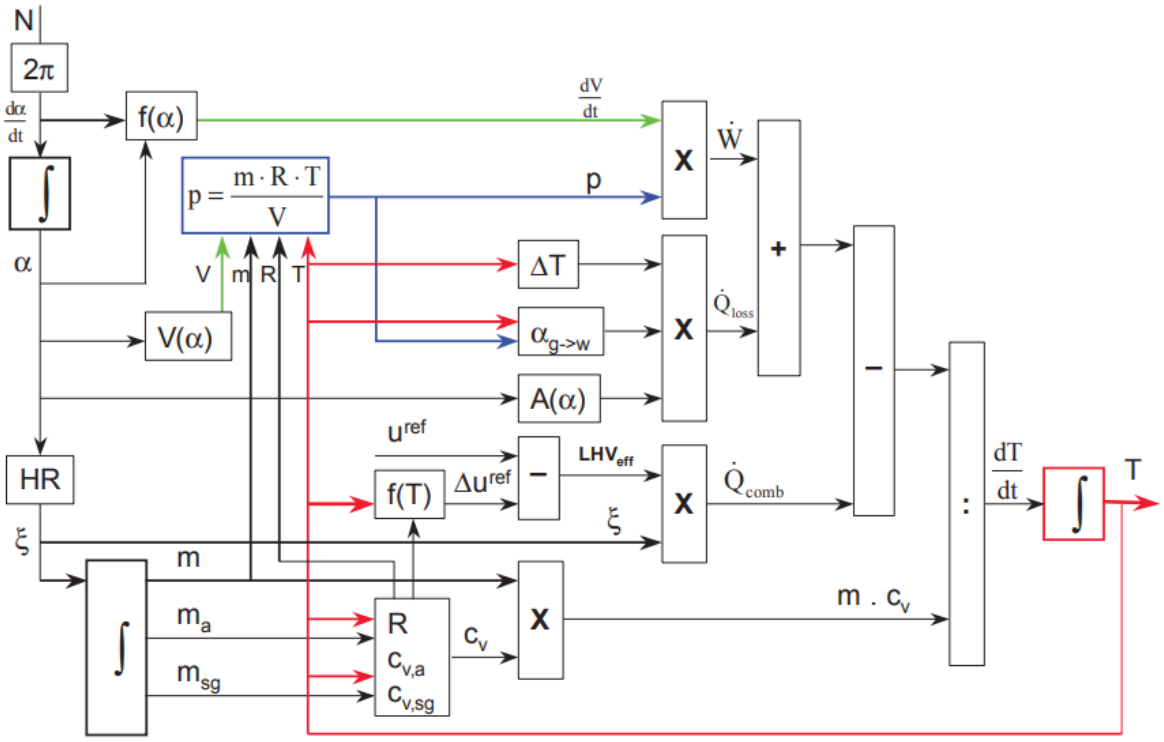

Figure 9.1: Causal model (Stapersma, 2010d)

The Wiebe function that has been used is described in section 9.1. The entire process of using the anti-causal, Newton Rhapson solver, and causal model in succession has been verified by taking an already processed pressure curve to see if the model can obtain the same result. This has been discussed in section 9.2. Finally, the results produced by the causal model are shown in section 9.3. The results will also be compared to the results shown in chapters 7 and 8. The definition of the symbols, abbreviations, and subscripts used in this section can be found in the nomenclature of this report.

9.1. Wiebe function

Since CRR is simulated by the Wiebe function, another parameter will ultimately be calculated by the model. For the causal model, this is the derivative of the temperature w.r.t. time (equation 9.1) and the equation is obtained by rewriting equation 7.1 presented in chapter 7.

$$\frac{dT}{dt} = \frac{(u_{comb} + e_f) \cdot \xi - \dot{Q}_{loss} - p \cdot \frac{dV}{dt}}{m \cdot c_v} \tag{9.1}$$

RCO can be expressed according to equation 9.2 (Stapersma, 2010d). $m_{f,0}^{comb}$ is equal to the fuel that is injected during the closed cylinder cycle. X is the parameter that is modelled by using a Wiebe function. The typical combustion shape of a diesel engine was discussed in chapter 4. The base Wiebe function is not suitable for the modelling of the combustion process since it gives too little freedom in shaping the combustion process (Stapersma, 2010d). Therefore, multiple Wiebe functions should be used as is shown in equation 9.3 (Stapersma, 2010d).

$$RCO = X \cdot m_{f,0}^{comb} \tag{9.2}$$

$$X = \sum_{k=1}^{N} b_k \cdot \left(1 - e^{-a \cdot \tau^{m_k+1}}\right) \tag{9.3}$$

$$a = -ln(1 - \eta_{comb}) \tag{9.4}$$

$$\tau = \frac{t - t_{SOC}}{\Delta t_{comb}} \tag{9.5}$$

$$\Delta t_{comb} = t_{EOC} - t_{SOC} \tag{9.6}$$

a can be obtained from the combustion efficiency as is shown in equation 9.4 (Stapersma, 2010d). τ is the non-dimensional time coefficient (equation 9.5 (Stapersma, 2010d)). τ depends on the Start Of Combustion (SOC) (t_{SOC}) and the End Of Combustion (EOC) (t_{EOC}). How both SOC and EOC have been determined was discussed in chapter 7. Ding (2011) looked at using multiple Wiebe functions so this thesis did the same. However, while using a double Wiebe function is necessary, using a third or fourth-order function does not improve the fit. Therefore, this thesis has only used the double Wiebe fit shown in equation 9.7 (Stapersma, 2010d). This function is used to fit the normalized RCO obtained from the anti-causal model as is shown in equation 9.2 (Stapersma, 2010d).

$$X = b_1 \cdot \left(1 - e^{-a \cdot \tau^{m_1+1}}\right) + b_2 \cdot \left(1 - e^{-a \cdot \tau^{m_2+1}}\right) \tag{9.7}$$

b_1 and b_2 are the so-called weighting factors while m_1 and m_2 are the so-called shape factors. To obtain a value for the Wiebe parameters, the curve-fitter tool from Matlab has been used which uses the least squares theory. Since the Wiebe function is fitted to the normalized RCO, the sum of b_1 and b_2 must equal 1. The causal model does not use equation 9.7 directly but uses its derivative to simulate CRR. The equations for CRR are shown in equations 9.8 and 9.9 (Stapersma, 2010d).

$$CRR = Z \cdot \frac{m_{f,0}}{\Delta t_{comb}} \tag{9.8}$$

$$Z = b_1 \cdot a \cdot (m_1 + 1) \cdot \tau^{m_1} \cdot e^{-a \cdot \tau^{m_1+1}} + b_2 \cdot a \cdot (m_2 + 1) \cdot \tau^{m_2} \cdot e^{-a \cdot \tau^{m_2+1}} \tag{9.9}$$

Finally, the vertical shift that has been applied to solve the RCO issue described in chapter 7 has to be applied here as well. For the causal model, this means that it is a downward shift. This has to be applied because the pressure that is calculated by the causal model will otherwise be too high during the compression stroke.

9.2. Verification of the pressure data analysis process

As was already stated in chapter 6, before processing the pressure curve from the Bolnes engine. The entire process consisting of the anti-causal model, Newton-Rhapson solver, and causal model should be verified to see if it behaves as expected. For verification, the pressure curve produced by the Wiebe fit from Ding (2011) is used. This is a smoothed pressure curve by using a 2nd order Wiebe function. The expectation is that by processing this pressure curve, the anti-causal model produces an RCO that is similar to the one produced by Ding (2011). If a good fit is obtained for the RCO, the causal model should then produce a pressure and temperature curve that is very similar to the one produced by the anti-causal model. This should be the case since the causal model is effectively trying to replicate a result that has already been produced by the causal model designed by Ding (2011). The results produced by Ding (2011) are shown in figure 9.2 while the results produced for this thesis are shown in figure 9.3 for comparison.

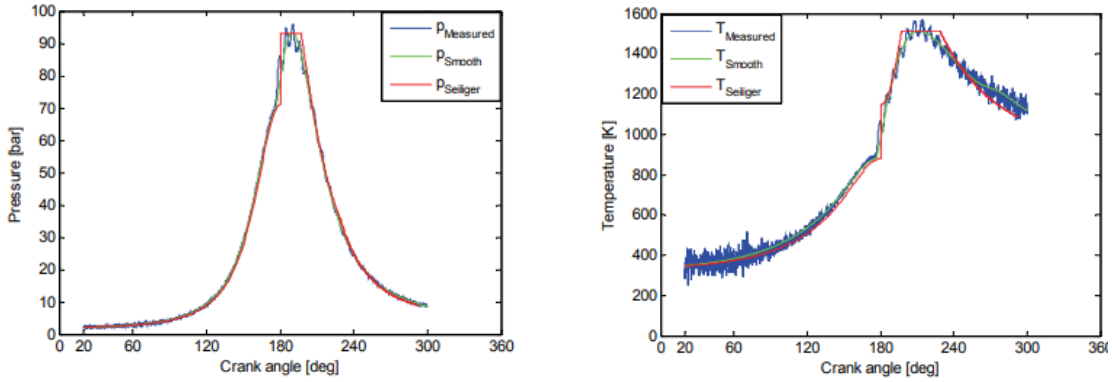

Figure 9.2: Pressure and temperature curves from Ding (2011)

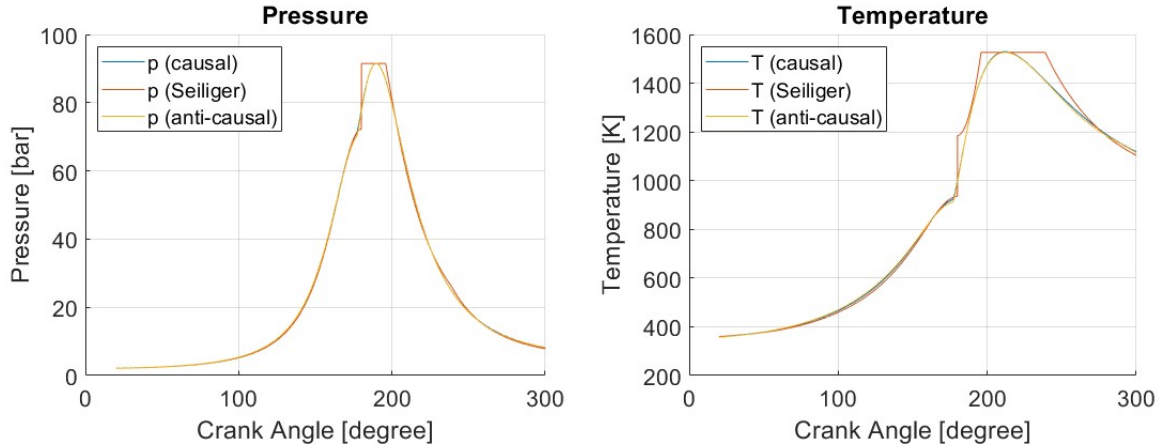

Figure 9.3: Resulting pressure and temperature curve from processing the example data

Comparing the results shown in figures 9.2 and 9.3 it seems there is good agreement between the two. Both the Wiebe fit as well as the Seiliger fit are similar for this thesis compared to the results produced by Ding (2011). Looking at the data produced by this thesis, there is good agreement between the temperature and pressure from the anti-causal, Seiliger approach, and causal model. Further results produced by processing the example data are shown in figure 9.4.

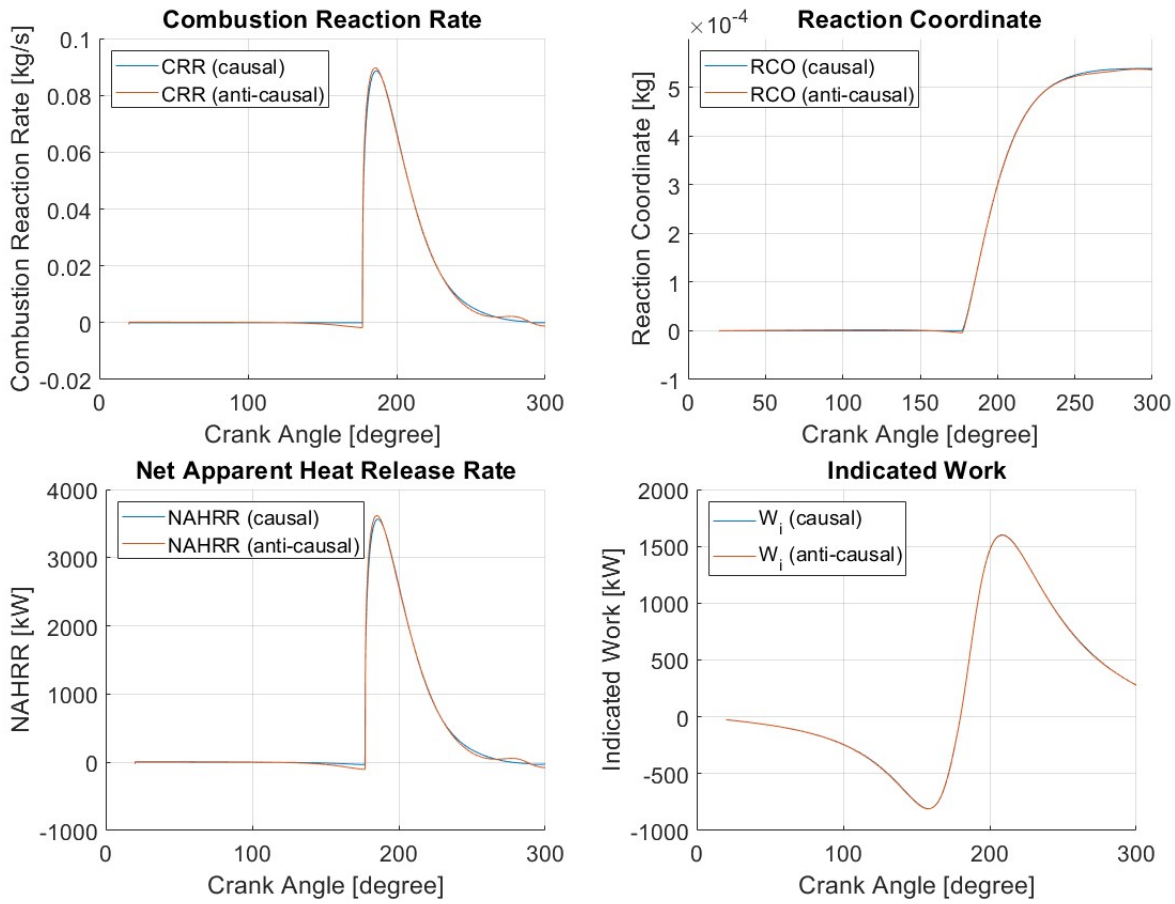

Figure 9.4: Results from processing the example data

Comparing the CRR and RCO from the anti-causal and causal model shown in figure 9.4, there is a good agreement between the two. The resulting Net Apparent Heat Release Rate (NAHRR) curves are also similar for both as is the indicated work. From these results, it can be concluded that there are no fundamental errors in the implementation of any of the conceptual models into a computer model. Based on the shown results, the entire pressure data analysis process as it's called in this thesis behaves as expected.

9.3. Results

This section will present the entire set of results produced by the anti-causal model, Newton-Rhapson solver, and causal model. These results will be shown for all of the operating points mentioned in chapter 6. While this section will show the results for the entire pressure data analysis process, the main focus will be on the results produced by the causal model. This is done because the results produced by the anti-causal model and Newton-Rhapson solver have already been discussed in chapters 7 and 8 respectively. Despite its main focus, this section will also compare the produced results to each other since this is the overall goal of the pressure data analysis process. All of the parameters that were used in the causal simulation model are shown in table 9.1. The results that have been produced by the three models are shown in table 9.2. R^2 and the Sum of Squared Errors (SSE) indicate the accuracy of the Vibe fit.

Table 9.1: Used parameters in the causal model for different operating points

Used parameter	**75 [kW]**	**150 [kW]**	**225 [kW]**	**375 [kW]**
SOC	177	176	174	174
EOC	225	246	267	270
a	6.908	6.908	6.502	6.528
m_1	0.6475	0.3214	0.3596	0.6134
m_2	0.6477	15.4763	15.267	0.6212
b_1	0.0455	0.9728	0.9384	0.26
b_2	0.9545	0.0272	0.0616	0.74
m_{f0}	$3.4069 \cdot 10^{-4}$	$4.1156 \cdot 10^{-4}$	$6.0861 \cdot 10^{-4}$	$9.8592 \cdot 10^{-4}$
C_2	1	15	45	65
$Shift$	$0.85 \cdot 10^5$	$0.9 \cdot 10^5$	$1.05 \cdot 10^5$	$0 \cdot 10^5$
R^2	0.9974	0.9937	0.995	0.9984
SSE	0.0245	0.0012	0.0775	0.0295

Table 9.2: Results produced by anti-causal, Seiliger, and causal model

Results		**75 [kW]**	**150 [kW]**	**225 [kW]**	**375 [kW]**
p_{max}	(anti-causal)	75.63 [bar]	88.87 [bar]	102.9 [bar]	130.03 [bar]
p_{max}	(Seiliger)	75.63 [bar]	88.87 [bar]	102.9 [bar]	130.03 [bar]
p_{max}	(causal)	75.28 [bar]	89.21 [bar]	103.38 [bar]	129.86 [bar]
T_{max}	(anti-causal)	1046.6 [K]	1074.9 [K]	1121 [K]	1532.9 [K]
T_{max}	(Seiliger)	1046.6 [K]	1074.9 [K]	1121 [K]	1532.9 [K]
T_{max}	(causal)	1061.5 [K]	1064.2 [K]	1093.8 [K]	1553.9 [K]
W_{in}	(anti-causal)	6.51 [kJ]	7.43 [kJ]	9.78 [kJ]	14.94 [kJ]
W_{in}	(Seiliger)	6.51 [kJ]	7.43 [kJ]	9.78 [kJ]	14.94 [kJ]
W_{in}	(causal)	6.18 [kJ]	7.18 [kJ]	9.54 [kJ]	14.73 [kJ]
Q_{in}	(anti-causal)	16.61 [kJ]	18.91 [kJ]	21.99 [kJ]	34.25 [kJ]
Q_{in}	(Seiliger)	16.61 [kJ]	18.91 [kJ]	21.99 [kJ]	34.25 [kJ]
Q_{in}	(causal)	10.32 [kJ]	12.64 [kJ]	18.79 [kJ]	32.38 [kJ]

The results from the anti-causal model and Seiliger approach have already been compared in chapter 8. The results produced by the causal model generally are close to the results produced by the other two. However, for the heat input Q_{in} they are not even close. Interestingly, chapter 5 stated that Sapra et al. (2020) found the same to be true. This phenomenon seems to get worse as the power decreases. Partially this is caused by how the Wiebe function approximates the RCO from the anti-causal model which will be discussed later in this section. Despite this, there is good agreement for the other three results. The values produced by the causal model are not as close as those produced by the Seiliger approach. However, this is to be expected because the Newton-Rhapson solver is specifically trying to find Seiliger parameters to produce accurate results for the equivalence criteria. As will be discussed later in this section, the casual model is a more accurate representation compared to the

Seiliger approach for the pressure and temperature if the entire closed-cylinder process is considered instead of just the equivalence criteria.

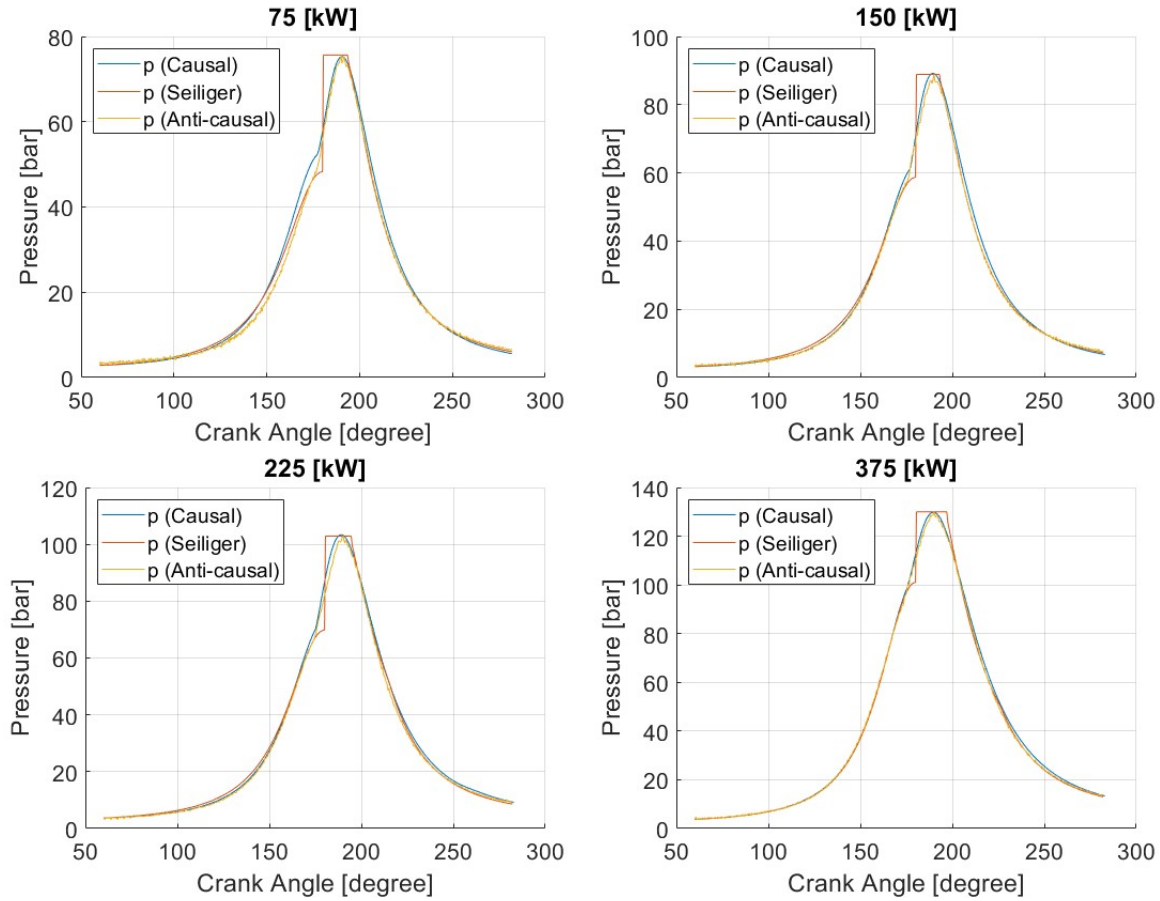

Figure 9.5: Pressure as a function of the crank angle

The resulting pressure curves for all operating points are shown in figure 9.5. The Wiebe function obtains a good fit for the measured pressure within the cylinder, especially at higher loads. For 375 [kW] the Wiebe function is almost identical compared to the measured pressure with a slight difference for the latter stage of the expansion stroke. However, similar to what was discussed in chapter 8 for the Seiliger approach. The Wiebe function produces a higher pressure for the compression stroke than was measured. This problem, again similar to what was discussed in chapter 8, seems to get worse as the power decreases. This problem seems to be caused by the issues surrounding the RCO produced by the anti-causal model. These issues were discussed in chapter 7

Except for the compression stroke, the Wiebe function can produce a pressure that is similar to the measured value. The maximum pressure, the pressure during the combustion process, and the pressure during the expansion stroke all seem to be similar to their measured values. Attempts were made to address the issue surrounding the compression stroke. Either by increasing the heat losses, or increasing the vertical shift discussed in section 9.1. However, both methods did not produce better results. Important to note again is that the measured value between the three cylinders also showed deviations that were up to 10%. Also important to note is that because of the way that the pressure measurements have been aligned with the crank angle, the corresponding crank angle can deviate somewhat. This means that the measured curves have been shifted occasionally by 1 degree of crank angle to obtain a better fit. Chapter 7 mentioned that without the vertical shift applied the calculated pressure by the causal model would become too high. Since this is still the case one might think that the vertical shift applied unnecessarily. However, please note that the difference was far more significant without this shift.

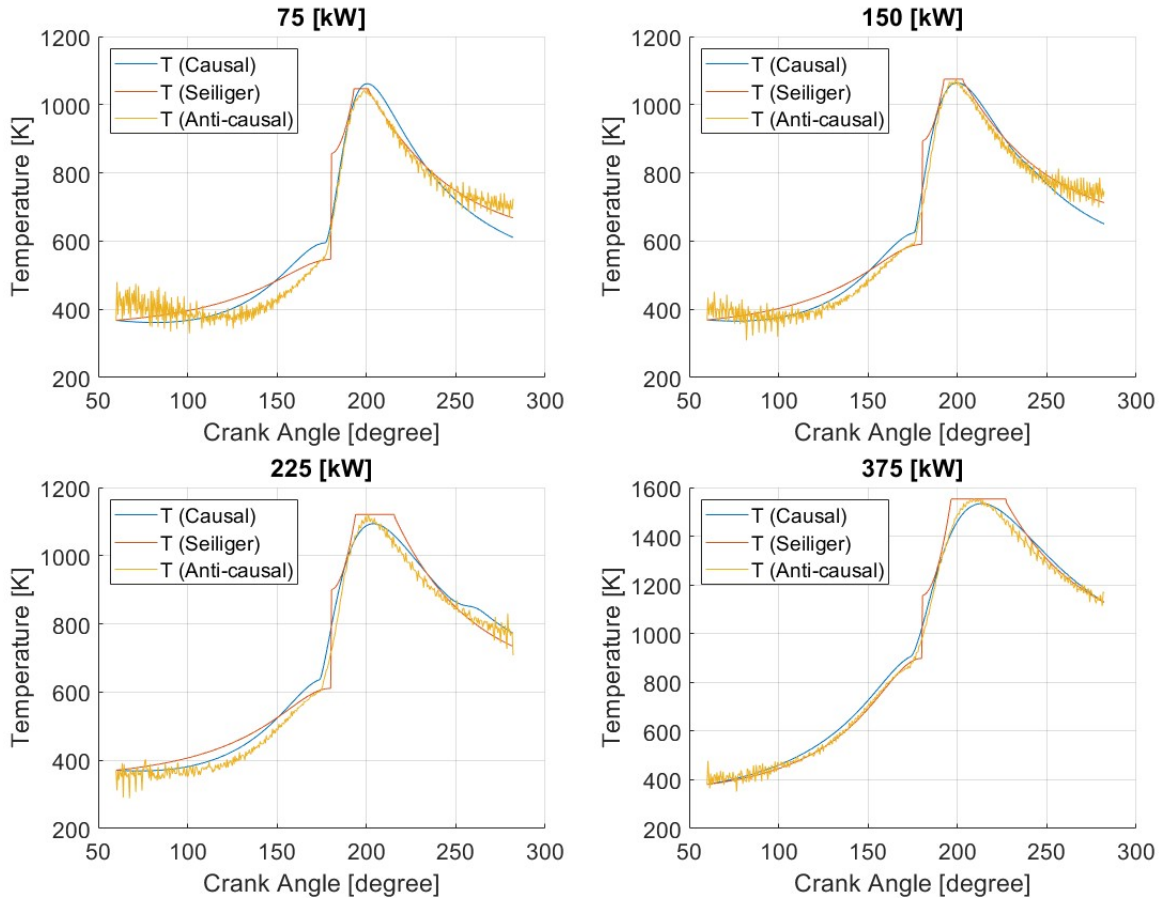

Figure 9.6: Temperature as a function of the crank angle

The temperature is shown as a function of the crank angle in figure 9.6. The same phenomena can be observed here as for the pressure curve. Namely that the Wiebe function and the Seiliger fit show deviation during the compression stroke and that this difference increases as the power decreases. In terms of maximum temperature, both do a decent job of representing the measured value. Important to note for 75 [kW] and 150 [kW] is that since the RCO produced by the anti-causal model is still increasing after the end of combustion, the temperature that is produced by the anti-causal model is higher during this phase than the one produced by the causal model.

Overall the temperature is not something which based on these results, can be adequately represented by the Wiebe function at lower loads. The same can be said for the Seiliger cycle when it comes to compression stroke. The expansion stroke is captured better by the Seiliger cycle. It should be noted that in fitting, the pressure curve is given priority over the temperature curve since the pressure is a direct measurement and the temperature is not. A better fit can in all likelihood be obtained for the temperature but this would sacrifice the fit for the pressure curve.

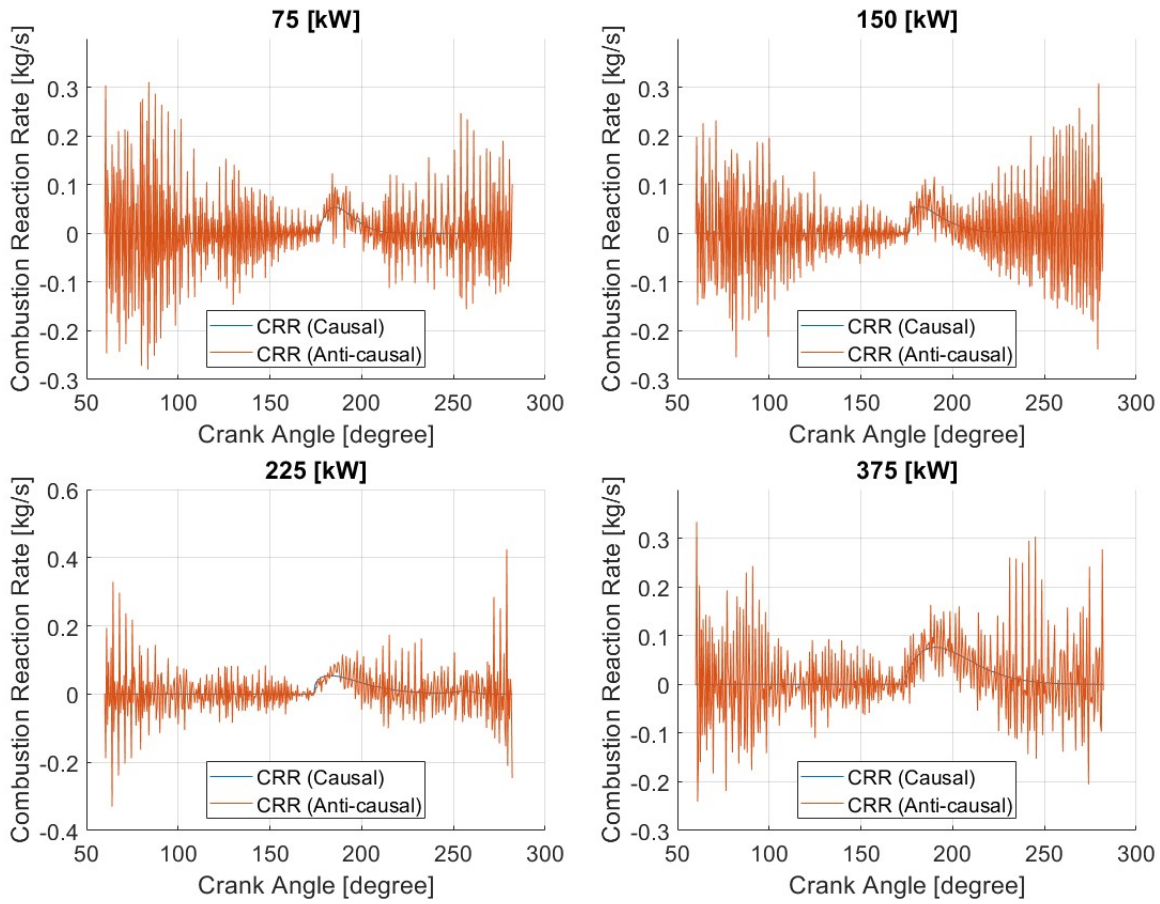

Figure 9.7: Combustion reaction rate as a function of the crank angle

As for the CRR, it is very difficult to say whether or not the Wiebe function is a good approximation. As was already stated in chapter 7, looking closely at figure 9.7, a certain interval can be distinguished where the mean value of the measured CRR seems to lie above zero. For this interval, the Wiebe function looks to be a good approximation of this mean value. As for the NAHRR, its results are very similar to the CRR and are shown in figure 9.9.

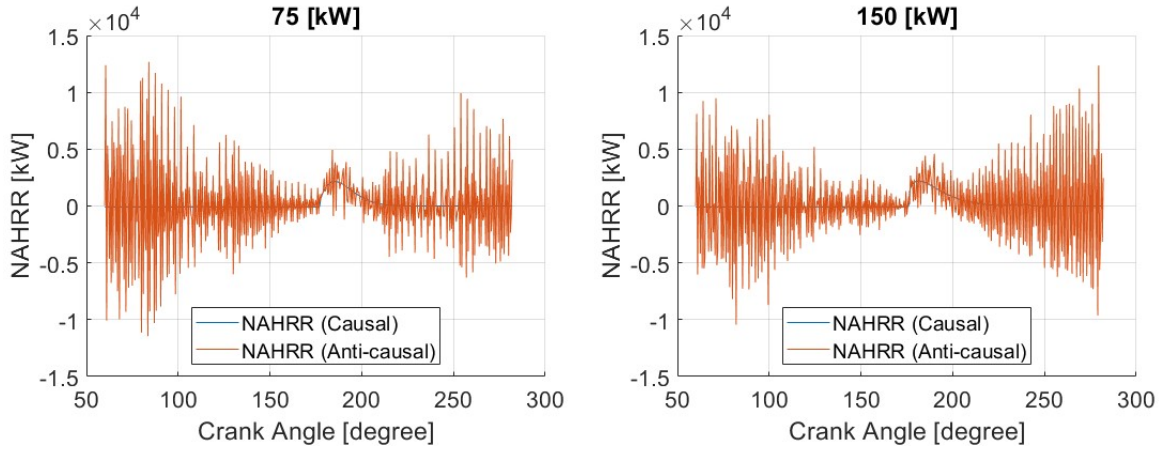

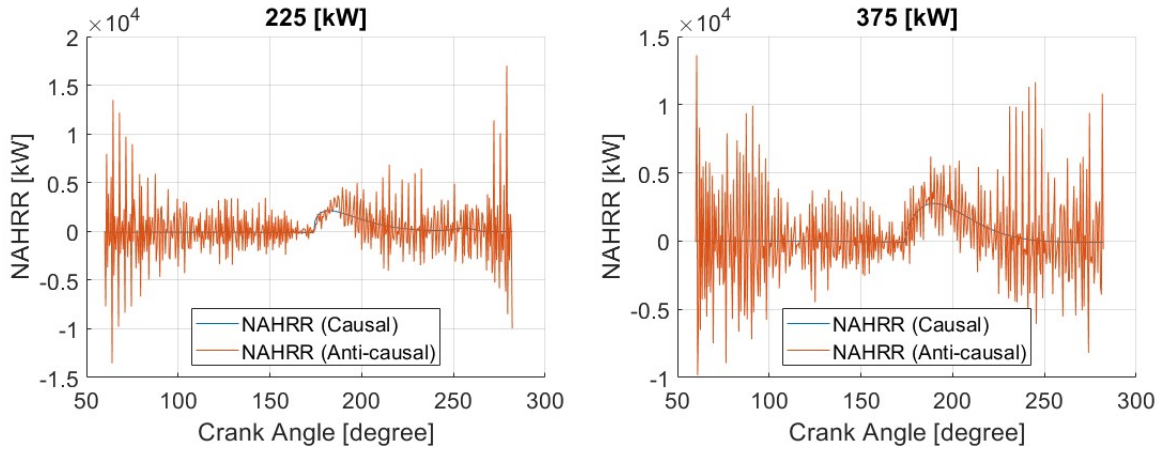

Figure 9.9: Net Apparent Heat Release Rate as a function of the crank angle

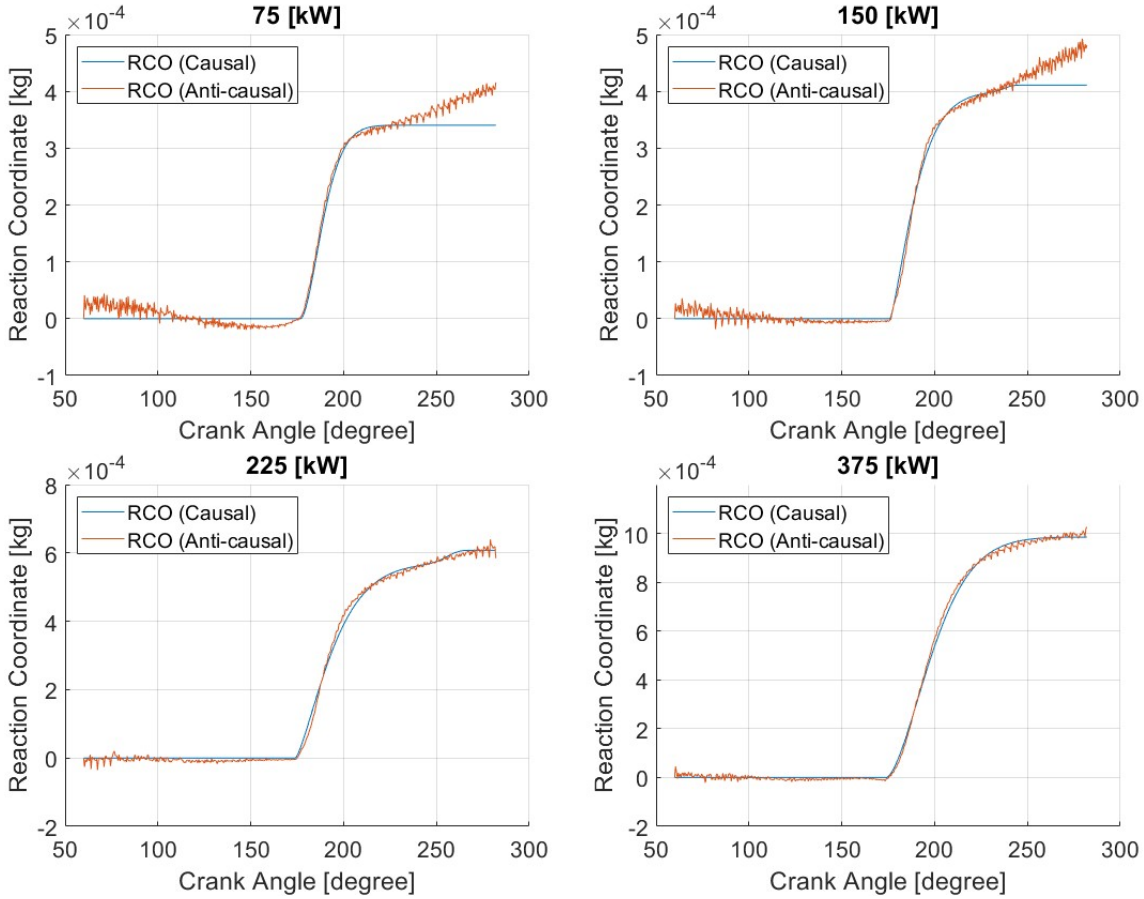

Figure 9.10: Reaction coordinate as a function of the crank angle

As for the RCO, the results shown in figure 9.10 explain why the resulting fits at lower loads are less accurate. For 225 [kW] and 375 [kW], the Wiebe function is an accurate representation of the RCO curve which is produced by the anti-causal model. The Wiebe function is by design equal to zero before the start of combustion which is also true for those two load points. The function is also able to reasonably fit the sharp increase in the RCO after the start of combustion (premixed combustion) but also the latter stage (diffusive combustion). Because the Wiebe function is a good approximation of the RCO, the earlier discussed results such as the pressure and temperature are also similar.

However, for 75 [kW] and 150 [kW], the Wiebe function is not able to capture its behaviour accurately. The RCO determined by the anti-causal model is decreasing before SOC. This is an issue since the Wiebe function is equal to zero for this phase, and even a vertical shift is not able to compensate for this phenomenon. For the premixed combustion phase, the Wiebe function can capture the behaviour, as can be seen in figure 9.10. However, it again struggles to capture the latter stage since the Wiebe function assumes that the RCO eventually levels off at a final value to indicate the EOC.

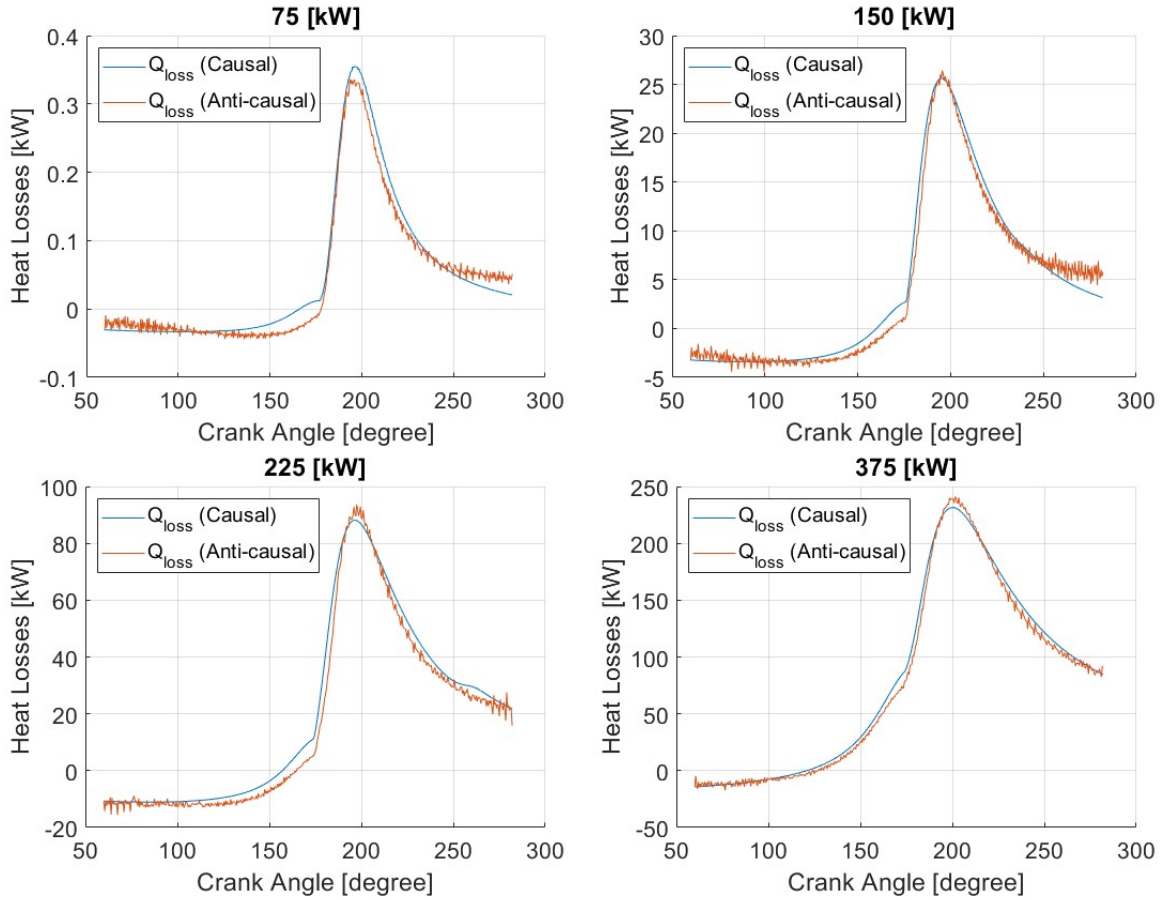

Figure 9.11: Heat losses as a function of the crank angle

The heat losses are shown in figure 9.11. The heat losses were modelled according to the empirical method described in chapter 7. To model the heat losses the same parameters were used for both the anti-causal as well as the causal model. So the differences between the two can only be explained by the difference in pressure and temperature. The fact that the heat losses are higher during the compression stroke is caused by the higher temperature and pressure produced by the Wiebe function. The lower maximum value is caused by the reverse effect. The expansion stroke is again similar between the two simulation models for 225 [kW] and 375 [kW]. However, for 75 [kW] and 150 [kW] the heat losses from the causal model are lower. This is caused by the lower temperature, which in turn is caused by the RCO still increasing in the anti-causal model, but not in the causal model.

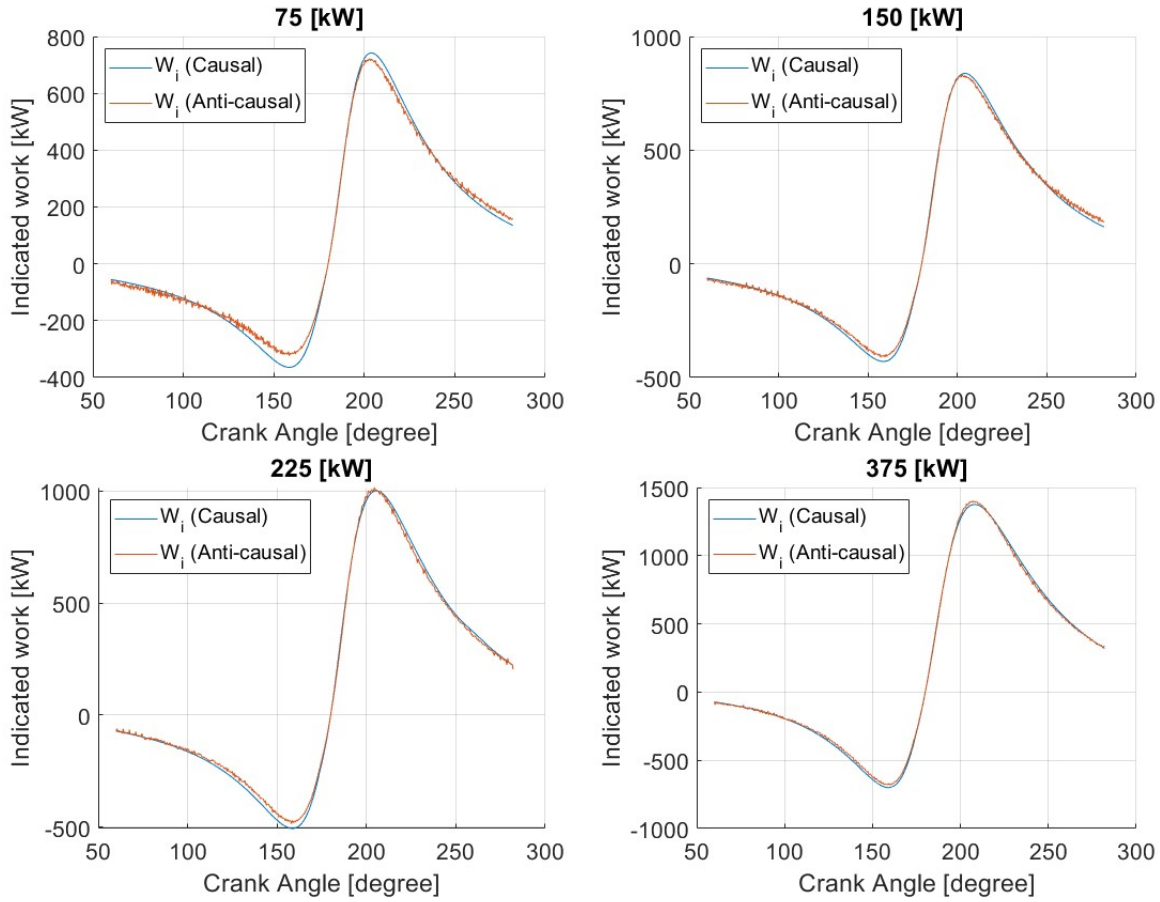

Figure 9.12: Indicated work as a function of the crank angle

Finally, the indicated work for the four load points is shown in figure 9.12. The indicated work is determined by the pressure multiplied by the derivative of the volume w.r.t. time. The latter is equal for all four of the load points so the difference can only be caused by the pressure. This is why the work determined by the anti-causal and causal model is almost identical at 375 [kW]. Namely, because the pressure curves are also almost identical. The reason causes the anti-causal to predict a larger value during the compression and expansion stroke, with this effect becoming more visible as the power decreases.

This chapter has discussed the design of the causal simulation model, along with the verification of the entire pressure data analysis process. Finally, this chapter has discussed the results produced by the causal model. The next chapter will discuss the conceptual changes necessary to the pressure data analysis process if it is used for ammonia-diesel instead of diesel combustion.

10

Conceptual changes necessary for ammonia combustion

This chapter will discuss the conceptual changes that should be applied to the pressure data analysis process when used to analyse ammonia-diesel combustion instead of diesel combustion. This process consists of using an anti-causal simulation model, the Newton-Rhapson solver, and a causal simulation model described in chapters 7, 8, and 9 respectively. Chapters 2 and 6 have explained that conceptual changes are changes that only concern assumptions and equations used to model combustion, but that these changes will not be implemented into a mathematical model which is verified and validated due to time constraints and the lack of experimental data.

These changes will, therefore, be based on the studied literature from chapters 4 and 5. Additionally, during the time this thesis was written, the 30th CIMAC congress was held in Busan. Ammonia was a prominently featured topic at this congress so the papers presented there serve as additional literature for this chapter. Based on the findings from the literature study, the assessment has been made that no changes are required for the Newton-Rhapson solver. However, the anti-causal and causal models do require changes. Specifically, changes to the single-zone combustion model are required. To understand the proposed changes, the single-zone combustion model used in both the anti-causal as well as causal simulation model will be explained in section 10.1. Section 10.2 will discuss the injection strategies and the shape of the heat release rate of ammonia-diesel operation and how it will be different from diesel operation. Section 10.3 will discuss the proposed changes to the single-zone combustion model. The definition of the symbols, abbreviations, and subscripts used in this section can be found in the nomenclature of this report.

10.1. Single-zone combustion model

The anti-causal and causal models both have a cylinder process variable as an objective. For the anti-causal model, this is the Combustion Reaction Rate (CRR) ξ shown in equation 10.1. For the causal model, this is the derivative of the temperature w.r.t. time shown in equation 10.2.

$$CRR = \frac{p \cdot \frac{dV}{dt} + m \cdot c_v \cdot \frac{dT}{dt} + \dot{Q}_{loss}}{u_{comb} + e_f} \tag{10.1}$$

$$\frac{dT}{dt} = \frac{(u_{comb} + e_f) \cdot \xi - \dot{Q}_{loss} - p \cdot \frac{dV}{dt}}{m \cdot c_v} \tag{10.2}$$

These equations are the result of how the closed-cylinder process is modelled. This process is modelled as a single-zone combustion model. Essentially this means modelling the cylinder as a control volume. The control volume consists of air, stoichiometric gas, and the fuel that is injected as is shown in figure

10.1. For the control volume, the energy balance and mass balance are shown in equations 10.3 and 10.4 respectively.

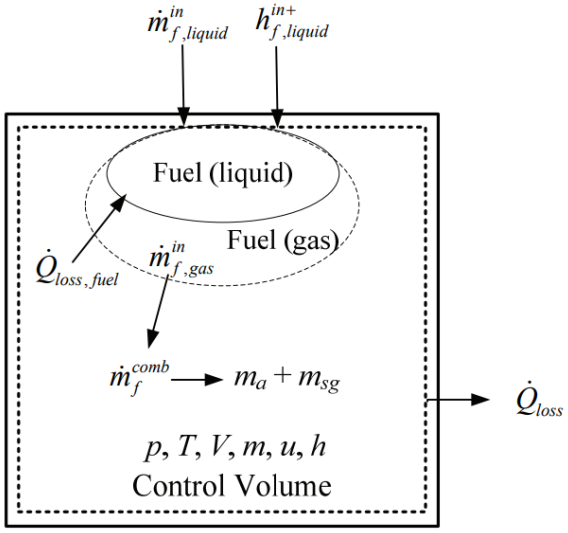

Figure 10.1: Single-zone combustion model (Ding, 2011)

$$\frac{d(m \cdot u)}{dt} = h^{in+} \cdot \dot{m}^{in} - h^{out+} \cdot \dot{m}^{out} + \dot{Q} - \dot{W} \tag{10.3}$$

$$\frac{dm}{dt} = \dot{m}^{in} - \dot{m}^{out} \tag{10.4}$$

Since no constituents are going out of the cylinder during the closed-cylinder process the mass flow out of the cylinder is equal to zero: $\dot{m}^{out} = 0$. The mass flow into the cylinder is equal to the fuel inflow: $\dot{m}^{in} = \dot{m}^{in}_{f,liquid}$. As for the energy balance, the enthalpy of liquid should be included: $\dot{m}^{in} \cdot h^{in+} = \dot{m}^{in}_{f,liquid} \cdot h^{in+}_{f,liquid}$. It is assumed that the mass within the cylinder at any point in time is determined by the mass of the fuel vapour m_f, the mass of air m_a, and the mass of the stoichiometric gas m_{sg}. Using these assumptions results in the following expression for the energy balance:

$$\frac{d(m_f \cdot u_f + m_a \cdot u_a + m_{sg} \cdot u_{sg})}{dt} = \dot{m}^{in}_{f,liquid} \cdot h^{in+}_{f,liquid} + \dot{Q} - \dot{W} \tag{10.5}$$

By determining the partial derivative on the left side of the equation the following expression is obtained:

$$m_f \cdot \frac{du_f}{dt} + m_a \cdot \frac{du_a}{dt} + m_{sg} \cdot \frac{du_{sg}}{dt} = \dot{m}^{in}_{f,liquid} \cdot h^{in+}_{f,liquid} - u_f \cdot \frac{dm_f}{dt} - u_a \cdot \frac{dm_a}{dt} - u_{sg} \cdot \frac{dm_{sg}}{dt} + \dot{Q} - \dot{W} \tag{10.6}$$

The following assumptions were made about the left side of the equation. The mass of fuel vapour is assumed to be zero and the internal energy for air and stoichiometric gas can be calculated by using the specific heat as a function of temperature:

$$m_f = 0 \tag{10.7}$$

$$du_a = c_{v,a} \cdot dT \tag{10.8}$$

$$du_{sg} = c_{v,sg} \cdot dT \tag{10.9}$$

This means the left side of the equation 10.6 can be reduced to:

$$m_a \cdot \frac{du_a}{dt} + m_{sg} \cdot \frac{du_{sg}}{dt} = (m_a \cdot c_{v,a} + m_{sg} \cdot c_{v,sg}) \cdot \frac{dT}{dt} = m \cdot c_v \cdot \frac{dT}{dt} \tag{10.10}$$

How the specific heat c_v is calculated will be explained later in this section. The right side of the equation 10.6 can be simplified by looking at the change in mass for fuel, air, and stoichiometric gas. The index *comb* indicates that this is a reactant product of combustion. Looking at the equations below. It is assumed that the mass of fuel is determined by the mass of fuel that is injected excluding the part that disappears because of combustion. For air, the change is the mass that is used alongside fuel for combustion. For stoichiometric gas, the change is equal to the part that is created by combustion.

$$\frac{dm_f}{dt} = \dot{m}_f^{in} - \dot{m}_f^{comb} \tag{10.11}$$

$$\frac{dm_a}{dt} = -\dot{m}_a^{comb} \tag{10.12}$$

$$\frac{dm_{sg}}{dt} = \dot{m}_{sg}^{comb} \tag{10.13}$$

It is assumed that air with fuel reacts according to equation 10.14 and that the ratio between fuel and air equals the stoichiometric ratio σ.

$$\dot{m}_f^{comb} + \dot{m}_a^{comb} = \dot{m}_{sg}^{comb} \tag{10.14}$$

The fuel that is used for combustion is defined as ξ. Using equations 10.11, 10.12, 10.13, and 10.14 along with σ and ξ the following relations can be obtained for the changes in mass:

$$\frac{dm_f}{dt} = \dot{m}_f^{in} - \xi \tag{10.15}$$

$$\frac{dm_a}{dt} = -\sigma \cdot \xi \tag{10.16}$$

$$\frac{dm_{sg}}{dt} = (1+\sigma) \cdot \xi \tag{10.17}$$

By using these equations and rearranging the terms the following expression can be obtained for the energy balance.

$$m \cdot c_v \cdot dT = \dot{m}_f^{in} \cdot (h_{f,liquid}^{in+} - u_f) + \xi \cdot [(u_f + \sigma \cdot u_a - (1+\sigma) \cdot u_{sg})] + \dot{Q} - \dot{W} \tag{10.18}$$

Two assumptions are made concerning the fuel. It is assumed that the injected fuel evaporates and combusts immediately after it is injected. The heat of combustion u_{comb} is defined by equation 10.19 while the energy of the fuel is defined by equation 10.20 (Ding, 2011). For the heat $\dot{Q}$ and work $\dot{W}$ during the closed-cylinder process it is assumed that they are equal to the heat losses Q_{loss} and indicated work by the piston W_i. Both have been explained in chapter 7. These assumptions mean that equation 10.3 can be rearranged to obtain equations 10.1 and 10.2.

$$u_{comb} = u_f + \sigma \cdot u_a - (1+\sigma) \cdot u_{sg} \tag{10.19}$$

$$e_f = h_{f,liquid}^{in+} - u_f \tag{10.20}$$

The next step is to look more closely at how the values for the thermodynamic properties are determined, starting with u_{comb}. u_f is determined by 10.21.

$$u_f = h_f^{ref} + \Delta h_f - R_f \cdot T \tag{10.21}$$

h_f^{ref} is the enthalpy at the reference temperature and is determined by reference enthalpy and the evaporation enthalpy (Ding, 2011). Δh_f considers the change in enthalpy because of a deviation from the reference temperature. This is done according to a power series shown in equation 10.22 (Stapersma, 2010a). The power series is based on the normalized temperature θ shown in equation 10.23. T_{shift} and T_{norm} are 273.15 [K] and 1000 [K] respectively. R_f is calculated by using the universal gas constant and the molecular mass of the fuel, and T is the in-cylinder temperature.

$$\Delta h_f = \sum_{k=1}^{m+1} b_k \cdot \theta^{k-1} \tag{10.22}$$

$$\theta = \frac{T - T_{shift}}{T_{norm}} \tag{10.23}$$

For the exact reference values and coefficients for the power series, please consult Appendix II of Ding (2011). As for the internal energy of air and stoichiometric gas u_a and u_{sg}, they are calculated using a similar method. Below the equations will be shown for air but please note that the equations for stoichiometric gas can be obtained by simply replacing a with sg. The internal energy is calculated by using equation 10.24.

$$u_a = h_a^{ref} + \Delta h_a - R_a \cdot T \tag{10.24}$$

For all three of the properties included in equation 10.24: h_a^{ref}, Δh_a, and R_a. It is assumed that their value can be determined based on the composition of individual species that make up the gas mixture (Stapersma, 2010a). These species are for example N_2, O_2, CO_2, etc. For each of the aforementioned thermodynamic properties, their value is determined by using the value of the individual species and multiplying it with their mass fraction x_j. This is shown in equations 10.25, 10.26, and 10.27 for h_a^{ref}, Δh_a, and R_a respectively.

$$h_a^{ref} = \sum_j x_j^a \cdot h_j^{ref} \tag{10.25}$$

$$\Delta h_a = \sum_{k=1}^{m+1} \sum_j x_j^{da} \cdot b_k^a \cdot \theta^{k-1} \tag{10.26}$$

$$R_a = \sum_j x_j^a \cdot R_j \tag{10.27}$$

Fundamental for this method is that air and stoichiometric gas have a specific composition of these individual species. This composition of the stoichiometric gas for both the anti-causal and causal model is based on the selected fuel. This is done for example for three typical marine fuels in table 10.1. These fuels are Light Diesel Oil (DMA), Blended Marine Diesel Oil (DMC), and Heavy Fuel Oil (RMH).

Table 10.1: Mass fractions for stoichiometric gas and dry air (Stapersma, 2010a)

Constituents	**Dry air**	**Stoichiometric gas DMA**	**Stoichiometric gas DMC**	**Stoichiometric gas RMH**
N_2	75.53 %	70.65 %	70.53 %	70.37%
O_2	23.15 %	0 %	0 %	0%
Ar	1.28 %	1.20 %	1.20 %	1.20%
CO_2	0.05 %	20.31 %	21.02 %	21.60%
H_2O	0 %	7.79 %	7.10 %	6.41%
SO_2	0 %	0.01 %	0.13 %	0.41%
Fuel NO	0 %	0.04 %	0.03 %	0.01%

To obtain the simplification which is used in equation 10.10, c_v has to be determined for both air and stoichiometric gas. This is done according to equation 10.28. For c_p, a power series is again used to determine its value for the individual species (equation 10.29). The total c_p value is again calculated by taking into account the mass fraction of the individual species that make up air and stoichiometric gas.

$$c_v = c_p - R \tag{10.28}$$

$$c_p = \sum_{k=1}^{m} a_k \cdot \theta^{k-1} \tag{10.29}$$

Now the ratio between air and stoichiometric gas is changing during the closed-cylinder process. So the total values for c_v and R are determined by the quality of the mixture x (equation 10.30). x is calculated by using CRR and the trapped conditions according to equation 10.30. x is used along with equations 10.31 and 10.32 to determine the values for R and c_v respectively.

$$x = \frac{m_1 \cdot x_1 - \sigma \cdot \int_{t_0}^{t_1} CRR}{m_1 + \int_{t_0}^{t_1} CRR} \tag{10.30}$$

$$R = x \cdot R_a + (1 - x) \cdot R_{sg} \tag{10.31}$$

$$c_v = x \cdot c_{v,a} + (1 - x) \cdot c_{v,sg} \tag{10.32}$$

to illustrate that c_v is a function of the temperature, c_v is shown in figure 10.2 for air, stoichiometric gas, and the total mixture. The quality of the mixture and the temperature are also shown here. Figure 10.2a shows that c_v follows the same trend as the temperature during the closed-cylinder process. In figure 10.2b it can be seen that the c_v is initially almost identical to $c_{v,a}$ but this changes after the start of combustion, indicated by the sudden change in the quality of the mixture. This is when the value of c_v shifts more towards $c_{v,sg}$.

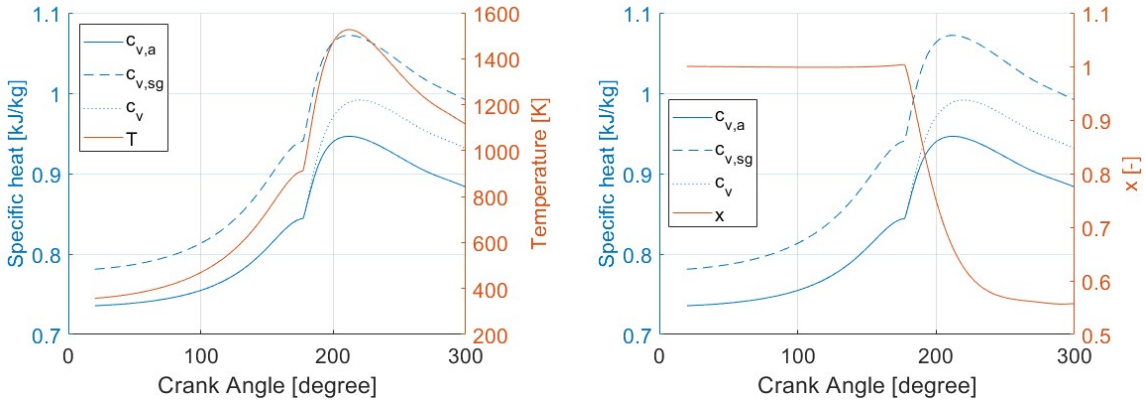

(a) Specific heat and temperature as a function of the crank angle

(b) Specific heat and quality of mixture as a function of the crank angle

Figure 10.2: Thermodynamic, temperature, and quality of the mixture as a function of the crank angle

The second term in equations 10.1 and 10.2 is the energy of the fuel e_f. e_f is determined by equation 10.20. u_f in equation 10.20 has already been discussed in this section. The first term in that equation is $h_{f,liquid}^{in+}$, which is shown in equation 10.33.

$$h_{f,liquid}^{in+} = h_{f,liquid}^{in} + h_{kin} \tag{10.33}$$

$$h_{kin} = \frac{p_{fuel} - p}{\rho_{lfuel}} \tag{10.34}$$

The first term in equation 10.33 is the enthalpy of the fuel inflow into the cylinder $h_{f,liquid}^{in}$. The second term h_{kin} is the kinetic energy caused by the difference in fuel injection pressure and in-cylinder pressure and is calculated by using equation 10.34. $h_{f,liquid}^{in}$ is calculated by using equation 10.35, with $u_{f,liquid}$ being calculated by equation 10.36 (Ding, 2011) and ρ_{lfuel} being calculated by equation 10.37 (Stapersma, 2010d). $u_{f,liquid}^{ref}$ is calculated by using equation 10.38, with $h_{f,liquid}^{ref}$ being determined by equation 10.39.

$$h_{f,liquid} = u_{f,liquid} + \frac{p}{\rho_{f,liquid}} \tag{10.35}$$

$$u_{f,liquid} = u^{ref}_{f,liquid} + \Delta u_{f,liquid} \tag{10.36}$$

$$\rho_{lfuel} = \rho_{lfuel,15} - \rho_{lfuel,corr} \cdot (T_{fuel,inj} - 15) \tag{10.37}$$

$$u^{ref}_{f,liquid} = h^{ref}_{f,liquid} - \frac{p_{ref}}{\rho_{f,liquid}} \tag{10.38}$$

$$h^{ref}_{f,liquid} = h_{comb} + (1+\sigma) \cdot h^{ref}_{sg} - \sigma \cdot h^{ref}_{a} \tag{10.39}$$

h^{ref}_a and h^{ref}_{sg} have already been discussed in this section. h_{comb} is calculated by using 10.40 (BS MA 100 - 82, 1982). $\Delta u_{f,liquid}$ is again estimated by using a power series as is shown in equation 10.41 (Stapersma, 2010a).

$$h_{comb} = 1000 \cdot \left(46423 - \frac{8792 \cdot (\rho^2_{f,15})}{1000000} + \frac{3170 \cdot \rho_{f,15}}{1000} - 9420\right) \cdot x_S \tag{10.40}$$

$$\Delta u_{f,liquid} = \sum_{k=1}^{m+1} c_k \cdot \theta^{k-1} \tag{10.41}$$

x_S in equation 10.40 is the sulphur content of the fuel. For ammonia-diesel combustion, several things will need to be changed about this combustion model. These changes will be discussed in section 10.3.

10.2. Heat release rate

Chapter 5 has already discussed injection strategies and the shape of the heat release rate of ammonia-diesel combustion. However, the CIMAC papers were not included in this chapter since it was written before this event took place. Therefore, this section will focus again on those two topics for ammonia-diesel operation. The previous section has explained how the thermodynamic properties are modelled. Based on this combustion model, it is important to consider how ammonia and its pilot fuel are injected into the cylinder. The pilot fuel will most likely be injected as a liquid. However, ammonia can be injected into the cylinder in several ways. It can be injected as a liquid (Oba et al., 2023) very similar to the pilot fuel. It can also be injected as gaseous fuel directly into the cylinder (J. Zhu et al., 2023). Furthermore, it can also be injected into the air intake, creating an air and ammonia mixture supplied to the cylinder (Niki et al., 2023). Additionally, the ratio between the two fuels during injection and their timing should be considered as well. Two example injection strategies are shown in figure 10.3.

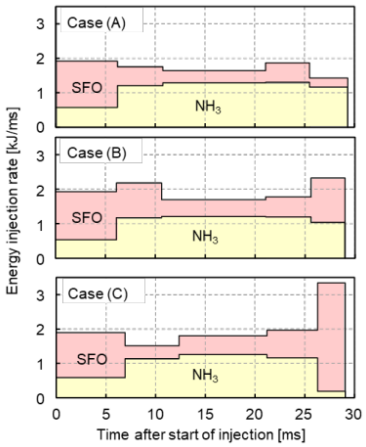

(a) Injection strategy (Oba et al., 2023)

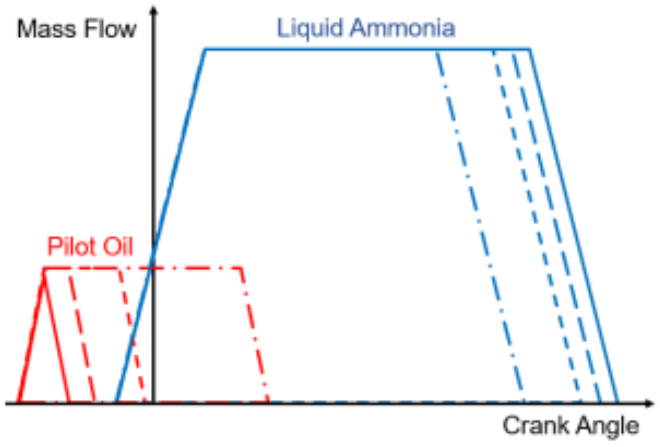

(b) Injection strategy (Zhou et al., 2023)

Figure 10.3: Different injection strategies for ammonia-diesel

Looking at the two injection strategies in figure 10.3, several situations occur during the closed-cylinder process. The fuels can still be present and therefore reacting in the cylinder separately, but they can also be reacting simultaneously. This is important to consider since the combustion model needs to take into account what constituents are present in the cylinder. The ratio between the two fuels will also be important to consider. The rest of this section will discuss the shape of the heat release rate of ammonia-diesel, this will be done for several different injection strategies of ammonia. As for the shape of the heat release rate, the first example is shown in figure 10.4. The injection strategies of Case (A) and Case (C) are shown in figure 10.3. Case (S) shows the heat release rate of diesel only.

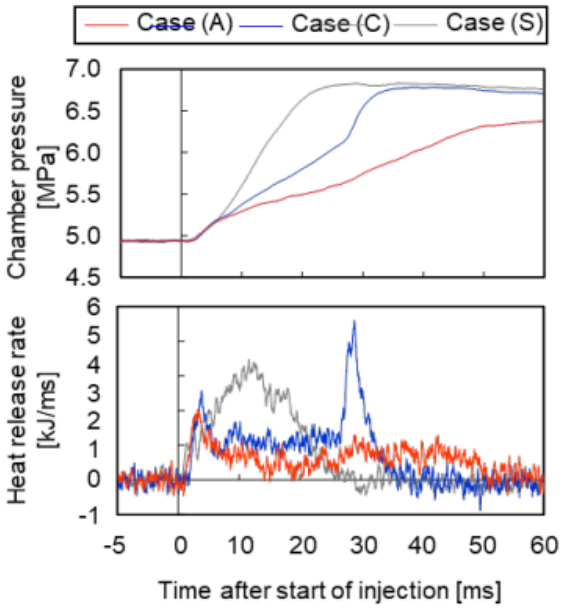

Figure 10.4: Heat release rate as a function of time (Oba et al., 2023)

One major difference between ammonia-diesel and diesel operation is that the combustion seems to be a more gradual process and that the peak value caused by premixed combustion can be lower than the peak value of diffusive combustion of diesel only. The later peak shown in the blue curve is caused by the sudden significant injection of pilot fuel as is shown in figure 10.3 (case C). Another example of the heat release rate is shown in figure 10.5. Figure 10.5 shows the heat release rate for ammonia being premixed in the air intake.

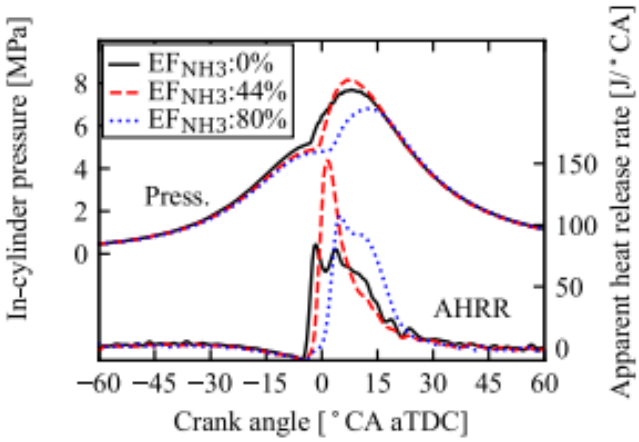

Figure 10.5: Heat release rate as a function of the crank angle (Niki et al., 2023)

Analysing the shape in figure 10.5, increasing the ammonia energy fraction of the fuel seems to increase

the peak in both premixed heat release and pressure at first. However, after the energy fraction exceeds a certain value this effect seems to reverse. What is consistent is that the start of combustion is delayed, most likely because of the higher combustion threshold of ammonia discussed in chapter 5. The same phenomena for the ammonia energy fraction are observed from the results in figure 10.6. These results are produced for direct injection of ammonia into the cylinder.

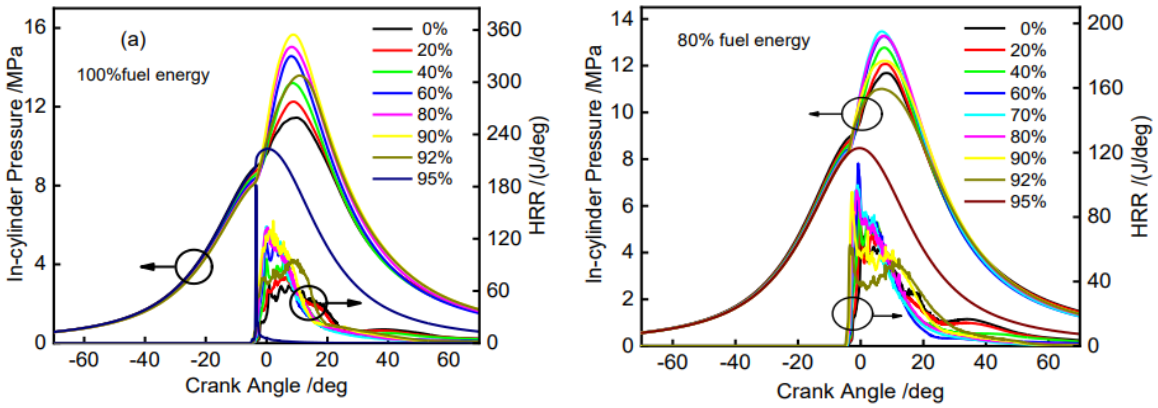

Figure 10.6: Heat release rate as a function of the crank angle (Z. Zhang, Chen, et al., 2023)

The observation that the peak value of diffusive combustion might be higher than the value of premixed combustion is also shown in figures 10.8 and 10.9. However, it should be noted that for the results produced by Zhou et al. (2023), the injection scheme that is used (figure 10.7) influences the heat release shape dramatically. For figure 10.8, both fuels are directly injected as a liquid. For figure 10.9, ammonia is directly injected although very early. Important to note is that the diesel is ignited in a pre-chamber here instead of directly injected. Looking at figures 10.8 and 10.9, it looks like the heat release of the pilot fuel can be distinguished from the overall heat release shape. For figure 10.8, this could be caused by the fact that the diesel is injected before ammonia. As for figure 10.9, this is most likely caused by the jet flame that enters the combustion chamber.

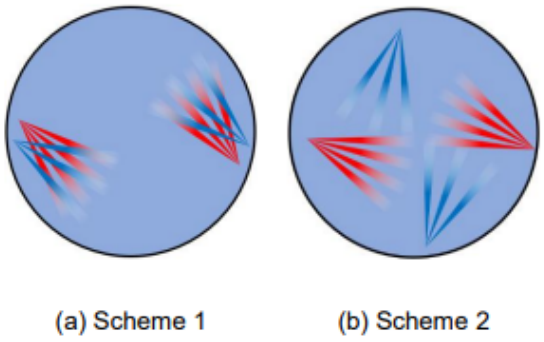

Figure 10.7: Two different injection schemes (Zhou et al., 2023)

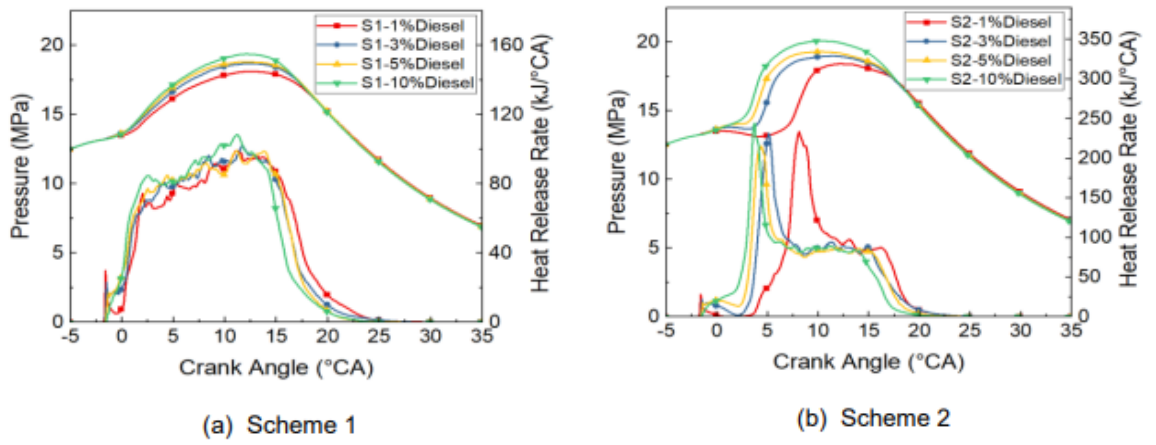

Figure 10.8: Heat release as a function of the crank angle for two different injection schemes (Zhou et al., 2023)

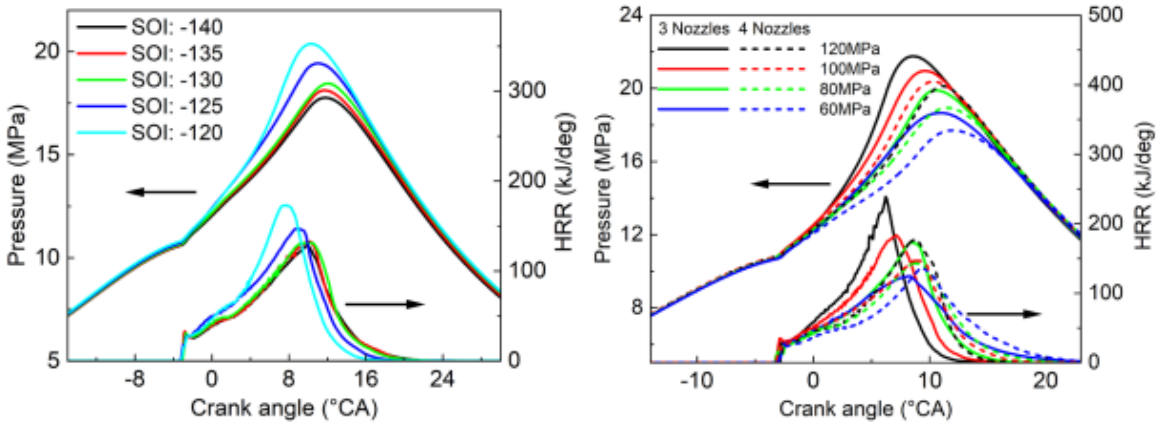

Figure 10.9: Heat release rate as a function of the crank angle (Wu et al., 2023)

Hermann et al. (2023) compared the RCO of methane combustion to ammonia combustion, while also discussing the difference between ammonia combustion using a pilot fuel and using a reactive jet. As can be seen in figure 10.10, Ammonia has a slower burn rate compared to methane. Looking at the heat release rate shown in figure 10.13, the shape, in this case, is very similar compared to diesel combustion, especially for pilot fuel operation. Ammonia is injected to form a premixture in the air intake. Because of the slower burn rate, the heat release rate just after the start of combustion is again slower compared to diesel combustion. For reactive jet operation, the shape is more inconsistent. Sometimes it shows a shape very similar to pilot operation. However, sometimes it also shows a more uniform shape.

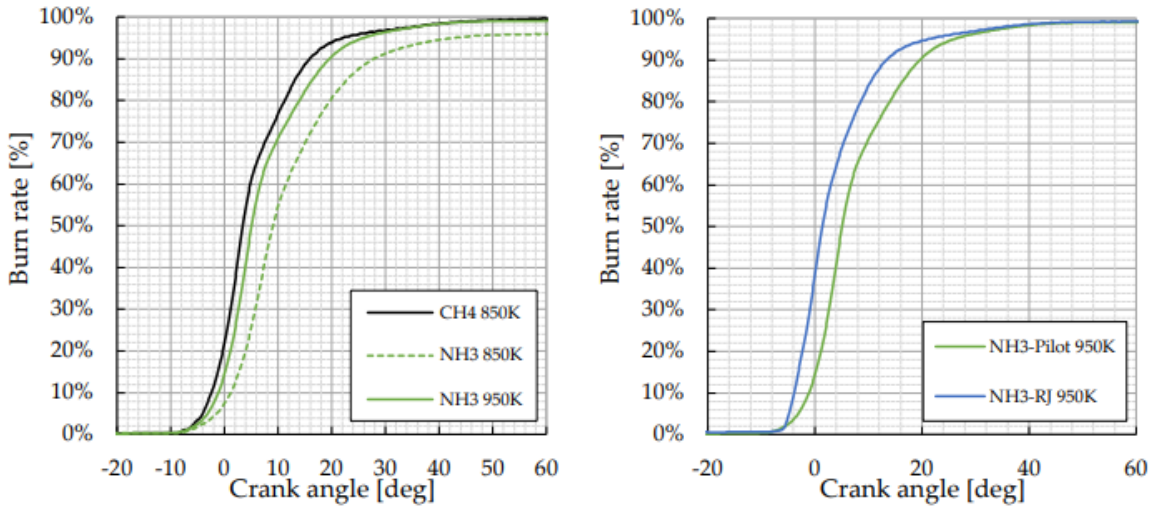

Figure 10.10: Reaction coordinate as a function of the crank angle (Hermann et al., 2023)

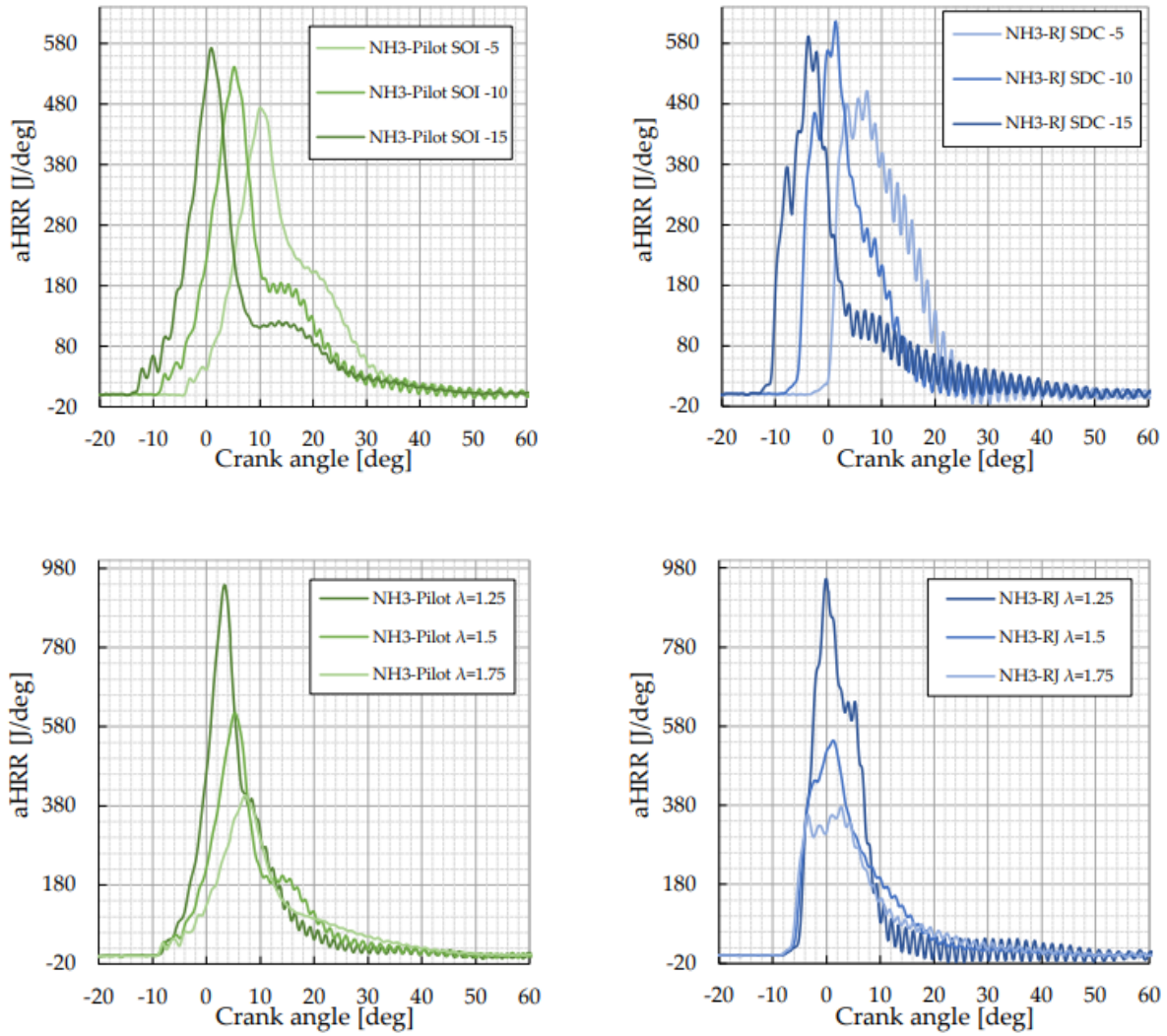

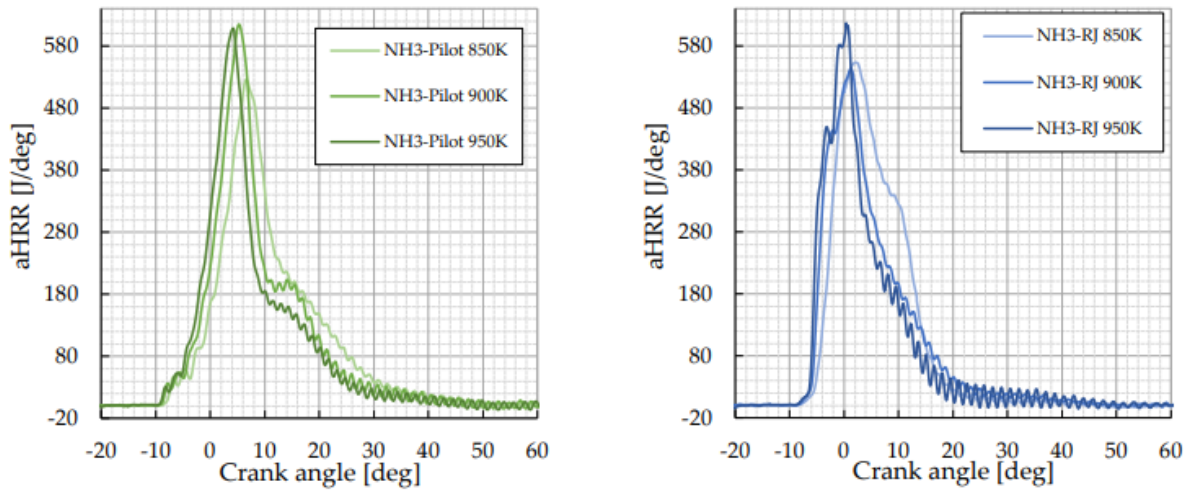

Figure 10.13: Heat release rate as a function of the crank angle (Hermann et al., 2023)

The final example for both the RCO as well as the heat release rate is shown in figure 10.14. In this example, ammonia is injected into the air intake to form a premixture of air and ammonia. The RCO shape overall is again similar to the diesel operation. As for the heat release rate, the results show both of the shapes mentioned above. Namely, the left figure shows a higher peak value for diffusive combustion compared to premixed combustion while the right figure shows the opposite. Interestingly, for the diesel operation, the diffusive combustion has a higher value, when this is not what is expected as was discussed in chapter 4.

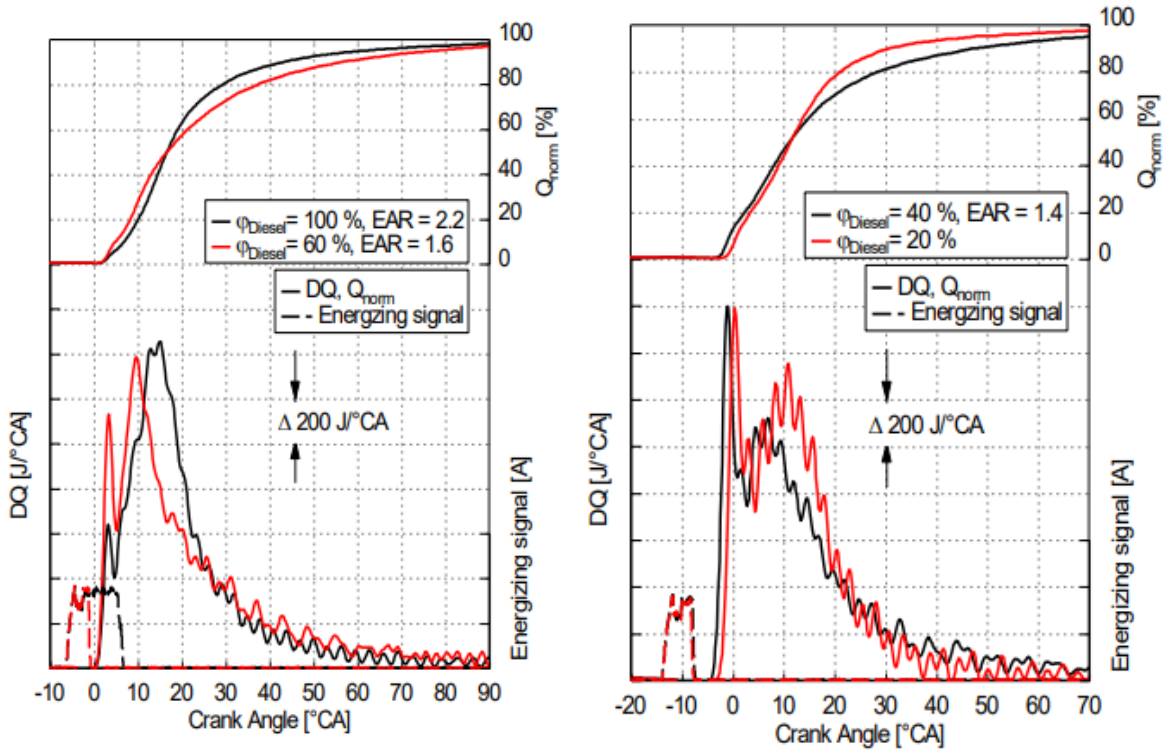

Figure 10.14: Heat release rate as a function of the crank angle (Wermuth et al., 2023)

So overall the shape of ammonia-diesel combustion can be similar to diesel but can also be different, depending on the injection strategy that is applied. The main differences will lie in the higher value for diffusive combustion compared to premixed combustion, the steepness of the initial peak due to premixed combustion, and whether or not the pilot fuels heat release curve can be distinguished from

ammonia's. To address in particular the third difference, it is advised to use separate Wiebe functions for each fuel. This has not been applied yet in chapter 9. Other than that, the shape parameters of the Wiebe function along with the application of multiple Wiebe functions should give ample freedom to simulate ammonia-diesel combustion. However, only repeating the pressure data analysis process for ammonia-diesel operation will give the definitive answer for one particular engine with a specific injection strategy.

10.3. Proposed changes

Section 10.1 has explained the single-zone combustion model that has been used for the anti-causal as well as causal model. Section 10.2 has discussed observations about the injection strategies and shape of the heat release rate obtained from studying literature. It is clear, that for modelling the thermodynamic properties, different assumptions have to be made for different intervals of the closed-cylinder process. Unlike the current design of the anti-causal and causal simulation model. This section will not give the equations for every single scenario that is possible since this would take too much time. Instead, it will focus on the situation where ammonia and the pilot fuel combustion are happening simultaneously. The three scenarios that are considered are liquid injection of ammonia into the cylinder, gaseous injection of ammonia into the cylinder, and gaseous injection of ammonia into the air intake resulting in a gas mixture of fresh air and ammonia. Reactive jet ignition which has also been discussed in the previous section will not be considered. For all three scenarios, the pilot fuel is injected as a liquid. They will be referred to in this section as scenarios 1, 2, and 3 respectively.

The combustion model starts with the mass and energy balance. The assumption that there is no mass flow out ($\dot{m}^{out} = 0$) of the system is still considered valid for all three scenarios. For the mass and enthalpy that flow into the system, scenarios 1 and 2 will have an additional component namely the ammonia either as liquid or gas. This is shown in equations 10.42 and 10.43 respectively. For scenario 3, the ammonia does not flow into the system during the closed-cylinder process so, therefore, this equation is the same as for diesel (equation 10.44).

$$\dot{m}^{in} \cdot h^{in+} = \dot{m}^{in}_{pilot} \cdot h^{in+}_{pilot} + \dot{m}^{in}_{ammonia,liquid} \cdot h^{in+}_{ammonia,liquid} \tag{10.42}$$

$$\dot{m}^{in} \cdot h^{in+} = \dot{m}^{in}_{pilot} \cdot h^{in+}_{pilot} + \dot{m}^{in}_{ammonia,gas} \cdot h^{in+}_{ammonia,gas} \tag{10.43}$$

$$\dot{m}^{in} \cdot h^{in+} = \dot{m}^{in}_{pilot} \cdot h^{in+}_{pilot} \tag{10.44}$$

The mass balance will be the same for all three scenarios. Namely, there will be an additional component for the ammonia fuel:

$$m = m_{pilot} + m_{ammonia} + m_a + m_{sg} \tag{10.45}$$

However, the stoichiometric gas is important to consider. Section 10.1 explained that stoichiometric gas is modelled as a mixture of individual species. The mass fraction for each species is constant and is determined by the selected fuel. This means the same method has to be applied to the stoichiometric gas produced by ammonia combustion. Namely to find the individual species and their mass fraction as a reactant product of ammonia combustion, similar to what has been shown in table 10.1.

The left side of equation 10.3 requires partial differentiation for each of the masses in the mass balance.

$$\begin{aligned}\frac{d(m \cdot u)}{dt} = {} & m_{pilot} \cdot \frac{du_{pilot}}{dt} + m_{ammonia} \cdot \frac{du_{ammonia}}{dt} + m_a \cdot \frac{du_a}{dt} + m_{sg} \cdot \frac{du_{sg}}{dt} \\ & + u_{pilot} \cdot \frac{dm_{pilot}}{dt} + u_{ammonia} \cdot \frac{dm_{ammonia}}{dt} + u_a \cdot \frac{dm_a}{dt} + u_{sg} \cdot \frac{dm_{sg}}{dt}\end{aligned} \tag{10.46}$$

For diesel combustion, the assumption was made that the injected fuel instantly evaporates and combusts, so no fuel vapour is present within the cylinder. For ammonia in particular, this is a highly questionable assumption because of the higher combustion threshold discussed in chapter 5. This

means that this fact has to be taken into account, meaning that the fuel might evaporate only after it's injected (in the case of scenario 1) and will only combust somewhat later than the pilot fuel. However, since this section will only look at the situation where both fuels are reacting simultaneously, this is not further explored here. At some point, the threshold will be reached where both fuels will be reacting. This means that the same simplification can be made for the first part of this partial derivative as for diesel combustion which is shown in equation 10.47.

$$m_a \cdot \frac{du_a}{dt} + m_{sg} \cdot \frac{du_{sg}}{dt} = (m_a \cdot c_{v,a} + m_{sg} \cdot c_{v,sg}) \cdot \frac{dT}{dt} = m \cdot c_v \cdot \frac{dT}{dt} \tag{10.47}$$

As for scenario 3, this simplification cannot be made anyway, since the gaseous ammonia is present at the start of the closed-cylinder process. There will still be a change in mass for ammonia since it is used for combustion. The resulting equation for scenario 3 is shown in equation 10.48.

$$m_{ammonia} \cdot \frac{du_{ammonia}}{dt} + m_a \cdot \frac{du_a}{dt} + m_{sg} \cdot \frac{du_{sg}}{dt} + u_{pilot} \cdot \frac{dm_{pilot}}{dt} + u_{ammonia} \cdot \frac{dm_{ammonia}}{dt} + u_a \cdot \frac{dm_a}{dt} + u_{sg} \cdot \frac{dm_{sg}}{dt} \tag{10.48}$$

For all three scenarios, it is assumed that the following equations hold within the cylinder:

$$\dot{m}_{pilot}^{comb} + \dot{m}_a^{comb} = \dot{m}_{sg,pilot}^{comb} \tag{10.49}$$

$$\dot{m}_{ammonia}^{comb} + \dot{m}_a^{comb} = \dot{m}_{sg,ammonia}^{comb} \tag{10.50}$$

Both equations will produce stoichiometric gas that is made up of different individual species. Nevertheless, if it is assumed that there is a distinct ratio between these two gas mixtures determined by the ratio between ammonia and pilot fuel, the two gas mixtures can be added together to obtain the total stoichiometric gas in the cylinder:

$$\dot{m}_{sg} = \dot{m}_{sg,ammonia} + \dot{m}_{sg,pilot} \tag{10.51}$$

For all three scenarios, the following equations can be constructed for the change in mass for fuel, air, and stoichiometric gas.

$$\dot{m}_{pilot} = \dot{m}_{pilot,gas}^{in} - \xi_{pilot} \tag{10.52}$$

$$\dot{m}_{ammonia} = \dot{m}_{pilot,gas}^{in} - \xi_{ammonia} \tag{10.53}$$

$$\dot{m}_a = -\sigma_{pilot} \cdot \xi_{pilot} - \sigma_{ammonia} \cdot \xi_{ammonia} \tag{10.54}$$

$$\dot{m}_{sg} = (1 + \sigma_{pilot}) \cdot \xi_{pilot} + (1 + \sigma_{ammonia}) \cdot \xi_{ammonia} \tag{10.55}$$

This is an issue since the anti-causal model is designed to find the total combustion reaction rate ξ. Therefore, the following assumptions have to be made concerning ξ. The mass fraction of the injected ammonia compared to the total fuel mass that is injected is called f:

$$f = \frac{\dot{m}_{ammonia}}{\dot{m}_{ammonia} + \dot{m}_{pilot}} \tag{10.56}$$

f can be constant during the injection or can vary as was shown in figure 10.3. Then the relation between the mass fractions of ammonia and diesel is as follows:

$$\dot{m}_{ammonia} = \frac{f}{1 - f} \cdot \dot{m}_{pilot} \tag{10.57}$$

Since it is also assumed that injected fuel evaporates and combusts instantly, the same relation is true between the reaction rate of the two fuels, and the relationship between them and the total reaction rate:

$$\xi_{ammonia} = \frac{f}{1-f} \cdot \xi_{pilot} \tag{10.58}$$

$$\xi_{ammonia} = f \cdot \xi \tag{10.59}$$

$$\xi_{pilot} = (1-f) \cdot \xi \tag{10.60}$$

This means that an expression can be found as a function of the total reaction rate ξ which is necessary for the anti-causal model. By using f, σ_{pilot}, and $\sigma_{ammonia}$ the following expressions can be derived for the heat of combustion and energy of fuel for scenarios 1 and 2.

$$u_{comb,1-2} = (1-f) \cdot u_{pilot} + f \cdot u_{ammonia} + ((1-f) \cdot \sigma_{pilot} + f \cdot \sigma_{ammonia}) \cdot u_a - ((1-f)(1+\sigma_{pilot}) + f \cdot (1+\sigma_{ammonia})) \cdot u_{sg} \tag{10.61}$$

$$e_{f,1-2} = h_{pilot}^{in+} \cdot (1-f) + u_{pilot} \cdot (1-f) + f \cdot h_{ammonia}^{in+} + u_{ammonia} \cdot f \tag{10.62}$$

These expressions can be substituted into equation 10.1 to obtain the expression for the anti-causal model. As for equation 10.2, the causal model offers more freedom to simulate the combustion reaction rate for ammonia and the pilot fuel separately. So for the causal model, the individual properties of each fuel can be used.

As for the stoichiometric gas, another question needs to be answered first. If the same method is applied for ammonia combustion as was described in section 10.1. Then the ratio between the stoichiometric gas of pilot fuel and ammonia needs to be incorporated. Since there is an expression for the mass change of total stoichiometric gas and for the individual components as well this ratio is fairly straightforward:

$$\frac{\dot{m}_{sg,pilot}}{\dot{m}_{sg}} = \frac{(1+\sigma_{pilot})(1-f)}{(1+\sigma_{pilot})(1-f) + (1+\sigma_{ammonia})f} \tag{10.63}$$

$$\frac{\dot{m}_{sg,ammonia}}{\dot{m}_{sg}} = \frac{(1+\sigma_{ammonia})f}{(1+\sigma_{pilot})(1-f) + (1+\sigma_{ammonia})f} \tag{10.64}$$

As for scenario 3, the situation becomes somewhat more complicated. The assumption that is critical for finding ξ is that the fuel that is injected into the cylinder evaporates and combusts. However, since the fuel is already present within the cylinder this assumption cannot be made. If the assumption can be made that the pilot fuel and ammonia react according to the previously mentioned ratio f then the following equations will result. As for the gas composition, this does not consist anymore of just air and stoichiometric gas. Therefore, the following relations will be used:

$$x_a = \frac{m_a}{m_a + m_{sg} + m_{ammonia}} \tag{10.65}$$

$$x_{sg} = \frac{m_{sg}}{m_a + m_{sg} + m_{ammonia}} \tag{10.66}$$

$$x_{ammonia} = \frac{m_{ammonia}}{m_a + m_{sg} + m_{ammonia}} \tag{10.67}$$

$$x_{sg} = (1 - x_a - x_{ammonia}) \tag{10.68}$$

This means that for x_a and $x_{ammonia}$ the following expressions can be used:

$$x_a = \frac{m_1 \cdot x_{a,1} - (\sigma_{pilot} \cdot (1-f) + \sigma_{ammonia} \cdot f) \int_{t_0}^{t_1} \xi dt}{m_1 + \int_{t_0}^{t_1} \xi dt} \tag{10.69}$$

$$x_{ammonia} = \frac{m_1 \cdot x_{ammonia,1} - f \int_{t_0}^{t_1} \xi dt}{m_1 + \int_{t_0}^{t_1} \xi dt} \tag{10.70}$$

$x_{a,1}$ and $x_{ammonia,1}$ are the initial mass fraction of air and ammonia respectively. If these relations are used then the following expression can be derived for the change in internal energy shown in equation 10.48:

$$\begin{aligned} m_{ammonia} \cdot \frac{du_{ammonia}}{dt} + m_a \cdot \frac{du_a}{dt} + m_{sg} \cdot \frac{du_{sg}}{dt} = (1 - x_{sg} - x_{ammonia}) \cdot m \cdot c_{v,a} \cdot \frac{dT}{dt} \\ + (1 - x_a - x_{ammonia}) \cdot m \cdot c_{v,sg} \cdot \frac{dT}{dt} + (1 - x_{sg} - x_a) \cdot m \cdot c_{v,ammonia} \cdot \frac{dT}{dt} = m \cdot c_v \cdot \frac{dT}{dt} \end{aligned} \tag{10.71}$$

Now as for the final steps, there will be no difference between scenarios 1 and 2 and scenario 3. This means that $u_{comb,3}$ will be the same as $u_{comb,1-2}$. As for $e_{f,3}$, the enthalpy of ammonia should not be included here since no ammonia is injected during the closed-cylinder process.

The equations that have been derived in this section do not address the fundamental difference in the process between diesel and ammonia-diesel combustion. Namely for these proposed changes to work, the start of combustion, end of combustion, and ratio between the injected fuels have to be identified before the anti-causal model is constructed. This means that different thermodynamic properties will be used for different crank angle intervals of the closed-cylinder process. This will require a more complicated model for the thermodynamic properties than is currently used. Interestingly, this strategy might already be useful to analyse diesel combustion. In the current model, the injection strategy is not included in the thermodynamic properties. For both, however, implementation and validation only can confirm that these proposed changes will ultimately achieve their desired effect.

The next step would be the implementation of the conceptual changes described in this section. This would require finding all of the coefficients and values that ultimately determine the thermodynamic properties, that were discussed in section 10.1. This chapter has discussed the design of the single-zone combustion model, that is used for the anti-causal as well as the causal simulation model. Additionally, this chapter has discussed important observations from studying literature about injection strategies and the shape of the heat release rate. Based on these observations, this chapter has proposed conceptual changes to the single-zone combustion model that would make it suitable for ammonia-diesel operation. The next chapter will discuss the conclusions and recommendations of this thesis.

11

Conclusions and recommendations

This chapter will discuss the conclusions and recommendations of this thesis. Chapter 2 constructed an overall research question for this thesis, while chapter 6 discussed the sub-research questions that have been constructed for the main research part of this thesis. These sub-research questions along with the main research question will be answered in section 11.1. This thesis also has several recommendations for future research which will be presented in section 11.2.

11.1. Conclusions

- **How can the necessary parameters be found for both the Seiliger approach and Wiebe function to characterize the closed-cylinder process in an internal combustion engine and how will this process be different on a conceptual level when it attempts to characterize ammonia-diesel instead of diesel combustion?**
  The parameters can be found through the pressure data analysis process as it's been called in this thesis. This consists of using an anti-causal model that requires the pressure as a function of the crank angle as input, along with the engine parameters. The model produces a lot of results but the most important are the maximum pressure, maximum temperature, heat input, and indicated work which are referred to as the equivalence criteria. Another important result would be the Reaction Coordinate (RCO). The equivalence criteria are necessary input for the Newton-Rhapson solver to find the Seiliger parameters. The RCO can be represented by a Wiebe function, with its parameters found using the Matlab curve fitting tool. This tool uses the Least Square Theory. The Wiebe parameters are used to model the heat release rate for the causal model. The causal model produces the same results as the anti-causal model but by using a Wiebe function, the results are much smoother.

  The Newton-Rhapson solver is something which does not have to be changed when applied for ammonia-diesel combustion. As for the anti-causal and causal simulation models, they both have to model the thermodynamic properties within the cylinder. This is done according to a single-zone combustion model. This part of both simulation models has to change drastically if it is to be used for ammonia-diesel combustion. The combustion model assumes that there are three constituents present in the cylinder during the closed-cylinder process. Namely air, stoichiometric gas, and the fuel that is injected. The model assumes that the injected fuel evaporates and combusts almost instantly after injection. Therefore, the injected fuel equals the Combustion Reaction Rate (CRR). This is crucial since the structure of the anti-causal model requires the thermodynamic properties to be a function of CRR. As for the properties of air and stoichiometric gas. They are assumed to be determined by the individual properties that air and stoichiometric gas consist of. This composition is considered to be constant. For stoichiometric gas, the composition depends on the fuel that is selected. The initial quality of the mixture determines the ratio between air and stoichiometric gas. This is determined by the effectiveness of the scavenging process. The ratio between the stoichiometric gas and air changes during the closed-cylinder process. It is assumed that this can be determined by the amount of air that is used for combustion along

with CRR to form stoichiometric gas.

Now the fundamental difference between ammonia-diesel and diesel operation is that the injection strategy, Start Of Combustion (SOC), End Of Combustion (EOC), and ratio between ammonia and diesel need to be incorporated in modelling the thermodynamic properties. Analysing the heat release rate of ammonia combustion with a pilot fuel, it is clear that many different situations take place within the cylinder. The pilot fuel can react individually while ammonia is present or not present in the cylinder. Both can react simultaneously. Ammonia can also react individually, although it's unlikely that the pilot fuel is not reacting in this instance because of Ammonia's higher combustion threshold. The thermodynamic properties for the situation where either one of the fuels is reacting on its own are fairly straightforward. The same method can be applied while using the correct properties for the fuel. If the two fuels are reacting simultaneously then the ratio between them has to be defined to make sure the anti-causal model is still able to determine the total CRR.

The assumption that the injected fuel evaporates and combusts almost instantaneously is considered highly questionable for ammonia. This assumption simplifies the combustion model since no fuel vapour is present in this scenario. However, two things about ammonia make this simplification questionable. First of all, the ammonia can be injected into the air intake to form a premixture. This means ammonia is already present within the cylinder at the start of the closed-cylinder process. Second, because of the higher combustion threshold, it's unlikely that the injected ammonia will evaporate and combust straight away. Therefore, ammonia fuel vapour will almost certainly be present before it starts to react. This has to be incorporated into the mass and energy balance for the closed-cylinder process.

As for the Wiebe function, two things are important to consider. The shape of the heat release rate and RCO of ammonia-pilot combustion seems to be very similar to diesel operation. However, sometimes the peak value of diffusive combustion is much higher than that of premixed combustion. This could be because the pilot fuel only is responsible for the initial peak while the ammonia fuel is responsible for the diffusive combustion. Since the ammonia fuel represents a larger energy fraction this would make sense. Based on this and the method described for modelling the thermodynamic properties. The advice would be to use a separate Wiebe function for the two fuels. Each will have its values for SOC and EOC, something which was not done for the constructed Wiebe function in this thesis. The same can be said for the combustion efficiency, which should be lower for ammonia than for diesel if it is used as pilot fuel. Finally, in terms of the shape, the Wiebe shape parameters should give ample freedom in representing the heat release shape. Although this can not be definitively concluded by this thesis.

- **How representative is the Seiliger process at characterizing the diesel combustion process at different load points?**
  The Seiliger approach has been used to compute the temperature and pressure as a function of the crank angle. Because of its shape, it does a reasonable job of characterizing the pressure during combustion and the expansion stroke for the four load points that this thesis used. For the compression stroke, the Seiliger approach can produce a good representation at full power but becomes less representative as the power decreases. As for the temperature, the same can be said. The Seiliger approach is representative during the combustion and expansion phase of the closed-cylinder process. However, it is only accurate for the compression stroke at full power. The accuracy again decreases as the power decreases and the deviation is more significant than for the pressure. The Seiliger parameters have been found by using the indicated work W_i, heat input Q_{in}, maximum pressure p_{max}, and maximum temperature T_{max} as equivalence criteria. This means the parameters are iteratively determined to make sure they produce results as accurately as possible for these criteria. So it may seem unfair to say something about the accuracy here. However, even with limits in place for the parameters to make sure they are representative of the pressure and temperature curve, they still produce very accurate results for the equivalence criteria.

- **How representative is the Wiebe function at characterizing the diesel combustion process at different load points?**
  The Wiebe function has been used to compute all of the results that are also produced by the anti-causal model. The difference is that by using the Wiebe function, the causal model can produce much smoother results. For the pressure and temperature, the Wiebe function can adequately predict both the maximum pressure and temperature. These results are, however, less accurate compared to the results produced by the Seiliger approach. Nevertheless, it should be noted that the maximum pressure and temperature serve as equivalence criteria to find the Seiliger parameters. This means that it is expected that they produce accurate results for these parameters. The Wiebe parameters are not found with this intention. Instead, their purpose is to accurately represent the RCO produced by the anti-causal model. However, the Wiebe function can produce a better representation of the temperature if the entire closed-cylinder process is considered compared to the Seiliger approach. This is mainly due to its design. Overall, the Wiebe function used by the causal model results in a good representation of the pressure, temperature, and reaction coordinate, especially at higher loads. Similar to the Seiliger approach, the results become less accurate as the power decreases, in particular during the compression phase of the closed-cylinder process. As for the heat release rate, the Wiebe function provides a much smoother representation compared to the anti-causal model. The Wiebe function also produces results for the equivalence criteria. The maximum pressure and temperature have already been addressed. As for the work and heat, the Wiebe function is less accurate for both compared to the Seiliger approach. Again, this is somewhat expected because of how the Seiliger parameters are found. However, the results for the heat input in particular are not even close for the two lowest load points (75 [kW] and 150 [kW]). For the other two load points considered in this thesis, the results are closed, but still not accurate enough.

11.2. Recommendations

- One major uncertainty for both the anti-causal and causal simulation model is the way the heat losses are modelled. The literature study already concluded that modelling the heat losses in an internal combustion engine is difficult. It requires high-fidelity methods to do so but these methods are not suitable to apply because of their computational load. Therefore, empirical methods have to be used which are generally unable to model the heat losses. Especially during the compression stroke, this may cause the deviation between the measured pressure and pressure determined by the causal model. A recommendation would be to model the heat losses differently during the compression stroke by using an isentropic efficiency or taking into account the variation in wall temperature during combustion.

- The trapped conditions were considered as another factor that could cause the problem with the RCO. However, to make sure whether or not this is the case, the measured pressure should be checked to see if it was simply a problem with the sensor. Another alternative would be to adjust the starting values in such a way that the trapped conditions increase proportionally with the engine power, something which is normally the case. If the trapped pressure in particular has a lower starting value. The pressure might increase more rapidly, causing a bigger increase in the temperature and derivative of the temperature which could solve the RCO problem.

- The anti-causal model includes the thermodynamic properties of all of the constituents that are present in the cylinder during the closed-cylinder process. This means that the fuel is also included. This is even though during the first phase, no fuel is present within the cylinder. This is not a major issue since the combustion reaction rate that is calculated will be roughly equal to zero during this phase. However, this thesis ran into the issue that this was not the case at lower loads. To try and solve this problem, the anti-causal model should analyse the pressure curve after the cylinder is injected instead of at the start of the closed-cylinder process. This means that only the combustion phase is analysed by the model. For the first phase, another model will have to be constructed which is inconvenient but this might improve the accuracy since it better represents what is happening.

IV

Appendices

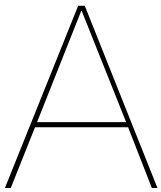

Scientific paper

This appendix contains a concept version of a scientific paper based on this Master's thesis.

Analysing the accuracy of a single-zone 0D combustion model for a CI two-stroke engine and identifying conceptual changes for ammonia-diesel operation

Frank Schenkel[a]

[a]*Faculty of Mechanical, Maritime and Materials Engineering Delft University of Technology, , , , ,*

Abstract

Low or zero-carbon fuels will have to be used to achieve the emissions goals set out by the International Maritime Organization in 2018. Ammonia is considered to be a possible candidate since it doesn't contain carbon. This study analyses two methods that characterize the closed-cylinder process of an internal combustion engine; the Seiliger approach and Wiebe function. Two things are the main focus of this thesis. Namely, the application of these methods and how this process will be conceptually different for ammonia-diesel combustion compared to diesel combustion. The application of this method means building an anti-causal and causal simulation model using Matlab Simulink. The anti-causal model processes the pressure as a function of the crank angle to determine the combustion reaction rate. The causal model simulates the combustion reaction rate using a Wiebe function to determine the pressure. The Wiebe function is determined based on the reaction coordinate produced by the anti-causal model. By using the Wiebe function, the causal model produces smoother results than the anti-causal model. The Seiliger parameters are determined by using a Newton-Rhapson solver. The results produced by this study generally show that the constructed method can produce accurate results. However, this accuracy is correlated to the operating conditions of the engine. As for the changes necessary for ammonia-diesel combustion. The fundamental difference for the constructed method according to this study is the fact that the combustion parameters; start and end of combustion for the two fuels have to be incorporated in the combustion model used for the anti-causal and causal model. This change has to be made, along with the assumption that the injected fuel evaporates and combusts almost instantaneously. This assumption is considered to be highly questionable for ammonia.

Keywords: ammonia, internal combustion engine, Wiebe, Seiliger

1. Introduction

The historical use of fossil fuels has led to an increase in Greenhouse Gases (GHG), with the most dominant greenhouse gas CO_2 increasing the global temperature (Nadeau et al., 2022). The rising temperature has increased the frequency of forest fires, flooding, heat waves, droughts, hurricanes, and dust storms (Lindsey and Blunden, 2023). The International Maritime Organization (IMO) has set out to reduce annual GHG by at least half in 2050 compared to 2008. Ammonia is studied as a potential zero-carbon fuel for the Maritime Industry, with companies like MAN Energy Solutions (MAN Energy Solutions, 2023) and Wärtsilä (Wärtsilä Corporation, 2022) developing an Internal Combustion Engine (ICE) capable of running on ammonia.

The downside of using ammonia in an ICE is that it has bad combustion characteristics (Mallouppas et al., 2022). To solve this issue, ammonia can either be injected alongside a more reactive fuel or by using a spark plug (Ayvalı et al., 2021). However, the large ignition energy that is required for large-bore marine engines limits the usage of a spark plug (Liu et al., 2022). For Compression Ignition (CI) marine engines this means a highly reactive fuel, which is referred to as the pilot fuel, is injected to assist combustion. If the goal is to eliminate CO_2 emissions then a zero-carbon fuel such as hydrogen should be used. However, as a first step, a combination of diesel alongside ammonia can at least reduce the CO_2 emissions. The diesel injection can overlap or be injected separately from the ammonia (Zhou et al., 2023). The ratio between the two fuels can also vary if the injection overlaps (Oba et al., 2023). Further examining the injection strategy of ammonia, it can be injected as a liquid in the cylinder (Oba et al., 2023), as a gas in the cylinder (Zhu et al., 2023), or as a gas in the air intake (Niki et al., 2023).

In 2023 the AmmoniaDrive research project started. This research project will study key performance indicators of a power concept for the Maritime Industry. This power plant concept uses ammonia for three purposes. Firstly, as fuel for the ICE. Secondly, as fuel for the Solid Oxide Fuel Cell (SOFC). The SOFC produces hydrogen which serves as the pilot fuel for the ICE. Finally, the ammonia will be used for Selective Catalytic Reduction (SCR) to reduce the emissions. The power plant concept is shown in figure 2.

The AmmoniaDrive project will study several aspects of the power plant. To do this, a suitable computer model will have to be constructed. Since the consortium will attempt to research the transient load characteristics of the power plant, the type of engine model that fits these criteria is the Mean Value Engine

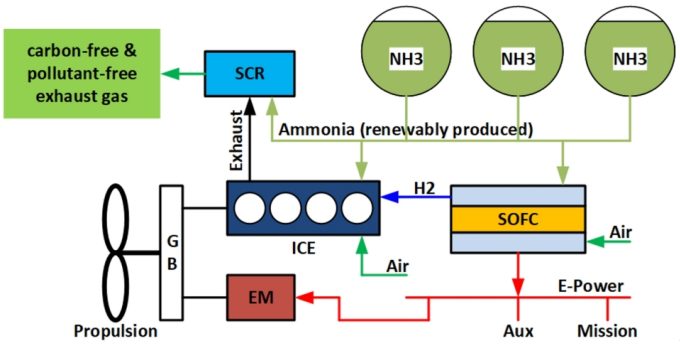

Figure 1: AmmoniaDrive power plant concept (de Vos et al., 2022)

Model (MVEM). This model is suitable for applications where the engine cycle has to be simulated faster than in real life (Lee and Jung, 2016). This means it can be used to study transient engine behaviour (Theotokatos, 2010) as well as be used as a building block for a model to simulate the entire power plant (Sui et al., 2017).

This study will look at a method constructed by Ding (2011). This method can find the necessary parameters for the Seiliger approach, a technique used to model the closed-cylinder process in an MVEM (Sui Congbiao, 2021). Additionally, the method uses a Wiebe function to model the combustion reaction rate during the closed-cylinder process. For this method, the measured pressure as a function of the crank angle along with information about the engine is required as input. By using the Wiebe function, a smoother pressure curve can be obtained, which is considered to be preferable compared to mathematical means of smoothing since it is based on first principles thermodynamics. This method requires the construction of both an anti-causal as well as a causal simulation model for the closed-cylinder process. Both models use a single-zone combustion model. This study will discuss on a conceptual level the necessary changes that have to be applied to this combustion model if it is to be used to analyse ammonia-diesel combustion. Conceptual changes mean that they are proposed for assumptions, algorithms, relationships, and data used to describe the reality of interest (Thacker et al., 2004). This study will perform the pressure data analysis process for a two-stroke CI engine that uses diesel as its fuel. The process will be performed at four operating points: 75 [kW], 150 [kW], 225 [kW], and 375 [kW] at a constant engine speed. These points correspond to 20%, 40%, 60%, and 100% power respectively.

2. Pressure data analysis process

The method constructed by Ding (2011) is called the pressure data analysis process. The first step is to build the anti-causal simulation model. This model will process the pressure curve as a function of the crank angle. The model produces several results, of which the equivalence criteria and the Reaction Coordinate (RCO) are most relevant for this study. The equivalence criteria are used alongside a Newton-Rhapson solver to find the Seiliger parameters. The RCO is used to find the Wiebe function for the causal simulation model. All three methods: the anti-causal model, the Seiliger approach, and the causal model produce results for the equivalence criteria and produce the pressure and temperature in the cylinder as a function of the crank angle.

2.1. Anti-causal simulation model

The anti-causal simulation model is derived from the single-zone combustion model designed by Stapersma (2010b). The model determines the Combustion Reaction Rate (CRR) as is shown in equation 1. As was mentioned the pressure is measured, while the volume and its derivative w.r.t. time are determined by the geometry of the cylinder (Stapersma, 2010b). The temperature is calculated by using the ideal gas law. The heat losses are modelled according to equation 2. The heat transfer coefficient α is calculated according to the method constructed by Woschni (1967). The heat losses are assumed to exist for three surfaces in the cylinder, the cylinder wall, the cylinder head, and the piston head. The wall temperatures are kept constant for the model. As for the thermodynamic properties c_v, m, u_{comb}, e_f, and R, they are determined according to the method constructed by Stapersma (2010d). These parameters are also dependent on each other so therefore the model is constructed in Matlab Simulink according to the schematic representation shown in figure 2.

$$CRR = \frac{p \cdot \frac{dV}{dt} + m \cdot c_v \cdot \frac{dT}{dt} + \dot{Q}_{loss}}{u_{comb} + e_f} \tag{1}$$

$$\dot{Q}_{loss} = \alpha \cdot A \cdot (T - T_{wall}) \tag{2}$$

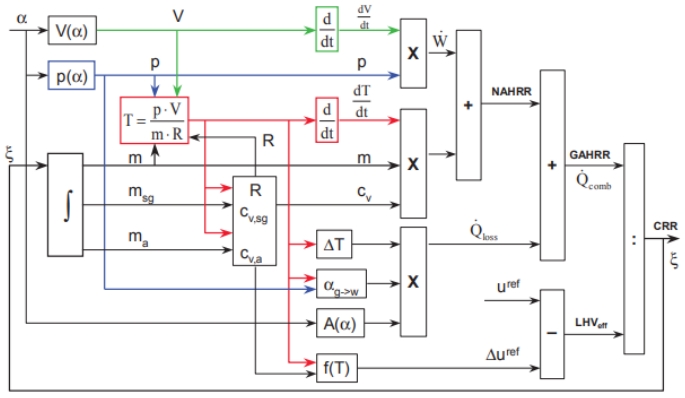

Figure 2: Anti-causal simulation model Stapersma (2010b)

2.2. Finding the Seiliger parameters

Before explaining how the Newton-Rhapson solver is used, the Seiliger approach should be discussed first. The Seiliger

approach divides the closed-cylinder process into five phases with six distinct points as listed below:

- 1-2: polytropic compression, indicating the net heat loss
- 2-3: iso-volumetric combustion
- 3-4: isobaric combustion and expansion
- 4-5: isothermal combustion and expansion
- 5-6: polytropic expansion indicating the net heat input caused by the combustion process

The volume, pressure, and temperature can be related between the different points by using the Seiliger parameters: r_c, n_c, r_{exp}, n_{exp}, a, b, and c as is shown in table 1.

Table 1: Seiliger parameters (Sui Congbiao, 2021)

Stage	Volume ratio	Pressure ratio	Temperature ratio
1-2	$\frac{V_1}{V_2} = r_c$	$\frac{p_2}{p_1} = r_c^{n_c}$	$\frac{T_2}{T_1} = r_c^{n_c-1}$
2-3	$\frac{V_3}{V_2} = 1$	$\frac{p_3}{p_2} = a$	$\frac{T_3}{T_2} = a$
3-4	$\frac{V_4}{V_3} = b$	$\frac{p_4}{p_3} = 1$	$\frac{T_4}{T_3} = b$
4-5	$\frac{V_5}{V_4} = c$	$\frac{p_4}{p_5} = c$	$\frac{T_5}{T_4} = 1$
5-6	$\frac{V_6}{V_5} = r_e$	$\frac{p_5}{p_6} = r_e^{n_{exp}}$	$\frac{T_6}{T_5} = r_e^{1-n_{exp}}$

The Newton-Rhapson solver is an iterative process that estimates the value of a variable by using the function and the function's derivative. The method requires an initial value for the variable and updates the value according to equation 3.

$$x_{n+1} = x_n - \frac{f(x_n)}{f'(x_n)} \tag{3}$$

Now to apply the Seiliger approach, not one but multiple variables have to be found so the equation has to be rewritten according to equations 4 and 5.

$$\mathbf{x}[n+1] = \mathbf{x}[n] - \mathbf{A}^{-1}\mathbf{f}[n] \tag{4}$$

$$\mathbf{f} = \begin{bmatrix} f_1(x_1, \cdots, x_n) \\ \vdots \\ f_n(x_1, \cdots, x_n) \end{bmatrix}, \mathbf{A} = \begin{bmatrix} \frac{\partial f_1}{\partial x_1} & \cdots & \frac{\partial f_1}{\partial x_n} \\ \vdots & \ddots & \vdots \\ \frac{\partial f_n}{\partial x_1} & \cdots & \frac{\partial f_n}{\partial x_n} \end{bmatrix} \tag{5}$$

Of the Seiliger parameters, r_c and n_c are not determined by the Newton-Rhapson solver but can be calculated directly by using equations 6 and 7.

$$r_c = \frac{V_1}{V_2} = \frac{V(EC)}{V(SOC)} \tag{6}$$

$$n_c = log\left(\frac{p_2}{p_1} - r_c\right) \tag{7}$$

The subscripts 1 and 2 indicate stages 1 and 2 of the Seiliger approach, which are the start of the closed-cylinder process and the Start Of Combustion (SOC) respectively. The start of the closed-cylinder process is the crank angle where the exhaust valve closes for a two-stroke engine, while SOC is determined from the RCO produced by the anti-causal model.

As for the other parameters, r_{exp} is determined by the other Seiliger parameters b and c along with r_{26}. r_{26} is the ratio between the volume of stages 2 and 6 respectively. Stage 6 of the Seiliger approach is defined as the point where the exhaust valve opens.

$$r_{exp} = \frac{V_6}{V_5} = \frac{V_6}{b \cdot c \cdot V_2} = \frac{1}{r_{26} \cdot b \cdot c} \tag{8}$$

The volume at stage 6 is equal to the volume in the cylinder when the exhaust valve opens:

$$V_6 = V_{EO} \tag{9}$$

As for the final four Seiliger parameters, four equations are required. These equations are constructed to calculate the equivalence criteria: p_{max}, T_{max}, w_{in}, and q_{in}. The equivalence criteria are calculated by the anti-causal model. The initial values for the Seiliger parameters are used to compute p_3, T_4, $q_{in,seil}$, and $w_{in,seil}$. These parameters are the same as the equivalence criteria.

$$p_3 = p_1 \cdot r_c^{n_c} \cdot a \tag{10}$$

$$T_4 = T_1 \cdot r_c^{n_c} \cdot a \cdot b \tag{11}$$

$$q_{in,seil} = q_{23} + q_{34} + q_{45} + q_{56} \tag{12}$$

$$w_{in,seil} = w_{12} + w_{34} + w_{45} + w_{56} \tag{13}$$

Table 2: specific work Seiliger approach (Stapersma, 2010a)

Stage	specific work w [J/kg]
1-2	$-c_{v,12} \cdot T_1 \cdot \frac{\gamma_{12}-1}{n_c-1} \cdot (r_c^{n_c-1}-1)$
3-4	$c_{v,34} \cdot T_1 \cdot (\gamma_{34}-1) \cdot r_c^{n_c-1} \cdot a \cdot (b-1)$
4-5	$c_{v,45} \cdot T_1 \cdot (\gamma_{45}-1) \cdot r_c^{n_c-1} \cdot a \cdot b \cdot ln(c)$
5-6	$c_{v,56} \cdot T_1 \cdot \frac{\gamma_{56}-1}{n_e-1} \cdot r_c^{n_c-1} \cdot a \cdot b \cdot \left(1-\frac{1}{r_e^{n_e-1}}\right)$

Table 3: specific heat Seiliger approach (Stapersma, 2010a)

Stage	specific heat q [J/kg]
2-3	$c_{v,23} \cdot T_1 \cdot r_c^{n_c-1} \cdot (a-1)$
3-4	$c_{v,34} \cdot T_1 \cdot \gamma_{34} \cdot r_c^{n_c-1} \cdot a \cdot (b-1)$
4-5	$c_{v,45} \cdot T_1 \cdot (\gamma_{45}-1) \cdot \cdot r_c^{n_c-1} \cdot a \cdot b \cdot ln(c)$
5-6	$-c_{v,56} \cdot T_1 \cdot \left(1-\frac{\gamma_{56}-1}{n_e-1}\right) \cdot r_c^{n_c-1} \cdot a \cdot b \cdot \left(1-\frac{1}{r_e^{n_e-1}}\right)$

The Newton-Rhapson solver updates the values for each cycle and the parameters are calculated again. This process is stopped when the values produced for the equivalence criteria by the Seiliger parameters fall within the desired tolerances.

2.3. Causal simulation model

The causal simulation model is essentially the anti-causal simulation model with its building blocks rearranged. There is one major difference, the CRR is simulated with a Wiebe function instead of calculated. This also means that instead of using the measured pressure, the pressure is calculated. The main equation for the causal model (equation 14) can be derived from equation 1, a schematic representation of the causal model is shown in figure 3.

$$\frac{dT}{dt} = \frac{(u_{comb}+e_f)\cdot\xi - \dot{Q}_{loss} - p\cdot\frac{dV}{dt}}{m\cdot c_v} \tag{14}$$

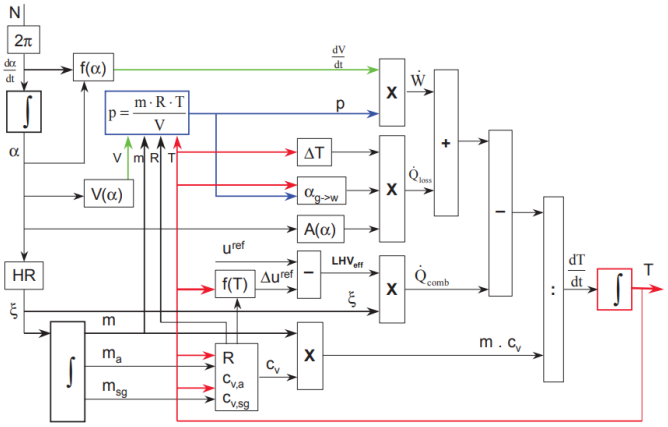

Figure 3: Causal simulation model Stapersma (2010b)

CRR is modelled by using a double-Wiebe function. The equation for CRR is shown in equation 15, while the double-Wiebe function is shown in equation 16.

$$CRR = Z \cdot \frac{m_{f,0}}{\Delta t_{comb}} \tag{15}$$

$$Z = b_1 \cdot a \cdot (m_1+1) \cdot \tau^{m_1} \cdot e^{-a\cdot\tau^{m_1+1}} + b_2 \cdot a \cdot (m_2+1) \cdot \tau^{m_2} \cdot e^{-a\cdot\tau^{m_2+1}} \tag{16}$$

$m_{f,0}$ is the mass of the fuel that combusts. a in the Wiebe function is determined by the combustion efficiency as is shown in equation 17 while τ is the non-dimensional time coefficient as is shown in equation 18.

$$a = -ln(1-\eta_{comb}) \tag{17}$$

$$\tau = \frac{t - t_{SOC}}{t_{EOC} - t_{SOC}} \tag{18}$$

b_1 and b_2 are the weighting factors for each of the two Wiebe functions that are used, while m_1 and m_2 are the shape factors. Since Z is the normalized combustion reaction rate, the sum of b_1 and b_2 has to equal 1. The weighting factors and shape factors along with a are found using the Matlab curve fitting tool which applies the least square method.

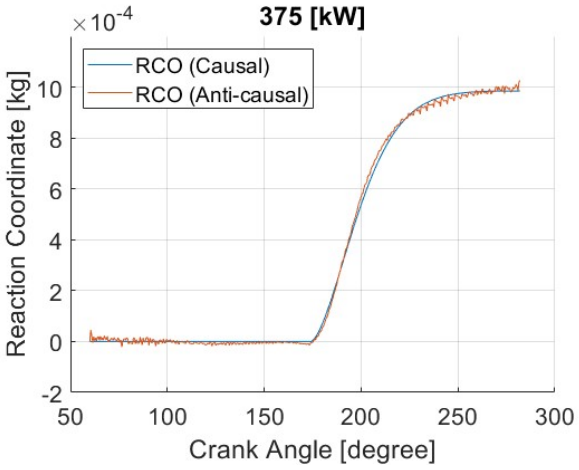

Figure 4: Reaction coordinate as a function of the crank angle

As for the Start Of Combustion (SOC) and the End Of Combustion (EOC), the reaction coordinate is used. An example of RCO is shown in figure 4. The SOC is evident from the RCO when looking at it, namely, this is where the RCO start to increase sharply. As for EOC, this is somewhat more difficult. It is defined as the point where the RCO intersects with the measured amount of fuel. Please note that this automatically assumes a combustion efficiency of 100% which isn't necessarily the case. This method has still been used, however, since it's difficult to determine EOC (Ding, 2011).

2.4. Results

One thing this study found is the fact that the pressure measurements have to be accurate for the anti-causal model to produce realistic results. The pressure sensor can struggle to measure the lower pressures at the start and end of the closed-cylinder process. This can result in a negative decreasing value for RCO, which makes little sense since this would indicate a negative mass of fuel that is injected. This can only be adjusted through careful calibration. and has been done for this study.

The pressure data analysis process has first been verified to see if it is operating as intended. This is done by using the pressure curve produced by the causal simulation model constructed by Ding (2011). This pressure curve is used as input for this study and the results show that the final pressure curve is essentially reproduced as expected. The pressure curve produced by the Seiliger parameters is also representative. Therefore the process is working as intended. The results produced for the equivalence criteria are shown in table 4.

Table 4: Results produced by anti-causal, Seiliger, and causal model

Results	**75 [kW]**	**150 [kW]**	**225 [kW]**	**375 [kW]**
p_{max} (anti-causal)	75.63 [bar]	88.87 [bar]	102.9 [bar]	130.03 [bar]
p_{max} (Seiliger)	75.63 [bar]	88.87 [bar]	102.9 [bar]	130.03 [bar]
p_{max} (causal)	75.28 [bar]	89.21 [bar]	103.38 [bar]	129.86 [bar]
T_{max} (anti-causal)	1046.6 [K]	1074.9 [K]	1121 [K]	1532.9 [K]
T_{max} (Seiliger)	1046.6 [K]	1074.9 [K]	1121 [K]	1532.9 [K]
T_{max} (causal)	1061.5 [K]	1064.2 [K]	1093.8 [K]	1553.9 [K]
W_{in} (anti-causal)	6.51 [kJ]	7.43 [kJ]	9.78 [kJ]	14.94 [kJ]
W_{in} (Seiliger)	6.51 [kJ]	7.43 [kJ]	9.78 [kJ]	14.94 [kJ]
W_{in} (causal)	6.18 [kJ]	7.18 [kJ]	9.54 [kJ]	14.73 [kJ]
Q_{in} (anti-causal)	16.61 [kJ]	18.91 [kJ]	21.99 [kJ]	34.25 [kJ]
Q_{in} (Seiliger)	16.61 [kJ]	18.91 [kJ]	21.99 [kJ]	34.25 [kJ]
Q_{in} (causal)	10.32 [kJ]	12.64 [kJ]	18.79 [kJ]	32.38 [kJ]

The results produced by the Seiliger approach are very accurate. This is to be expected since the Newton-Rhapson solver is trying to find values for the Seiliger parameters, whose purpose is to produce as accurate results as possible for these equivalence criteria. As for the causal simulation model, the results are still adequate but somewhat less accurate, especially for the heat input Q_{in}. For 75 [kW] and 150 [kW], this is partially because the RCO produced by the anti-causal model is still increasing after the measured fuel consumption value is reached. Since the causal simulation model only simulates heat input up to this value the total heat input will be less. This can only partially be blamed, however, because for 225 [kW] and 375 [kW], this is not the case and yet there is still a deviation The results for the other three equivalence criteria are satisfactory. The inaccuracy produced by the Wiebe function for the heat input was also concluded by Sapra et al. (2020). The pressure curves produced for all four operating are shown in figures 5, 6, 7, and 8.

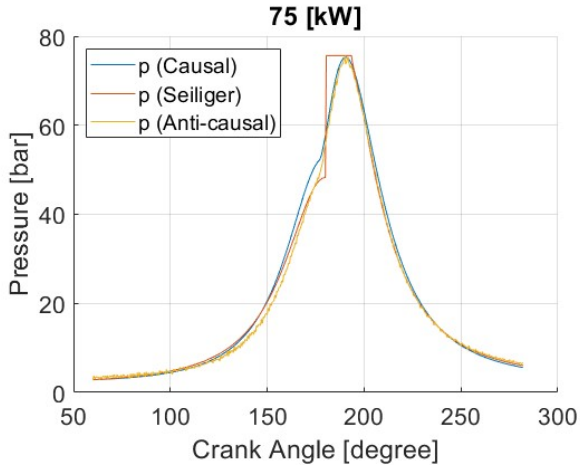

Figure 5: Pressure as a function of the crank angle

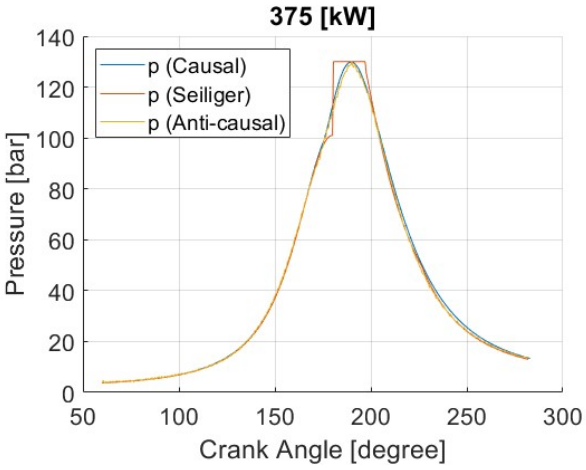

Figure 8: Pressure as a function of the crank angle

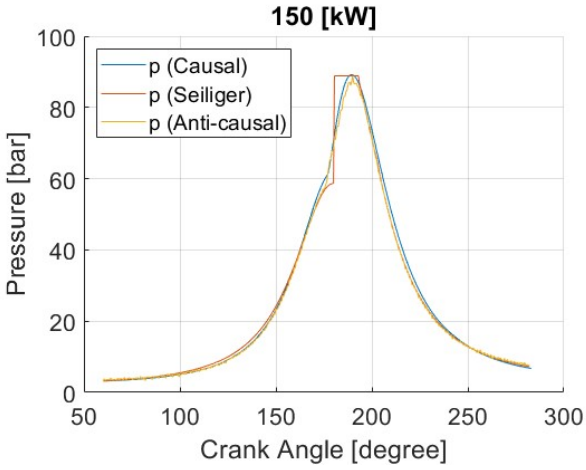

Figure 6: Pressure as a function of the crank angle

The pressure curves produced by the causal simulation model and Seiliger approach are generally a good approximation for the measured pressure. However, during the compression stroke in particular there seems to be a slight deviation which gets worse as the power decreases. As for the combustion phase and expansion stroke, it seems to be the case that both the causal simulation model and the Seiliger approach can produce an accurate result. For all four operating points, the Seiliger approach produced more accurate results for the maximum pressure. However, if the entire pressure curve during the closed-cylinder process is considered, the causal model produces a more representative pressure curve. The temperature curves produced for all four operating are shown in figures 5, 6, 7, and 8.

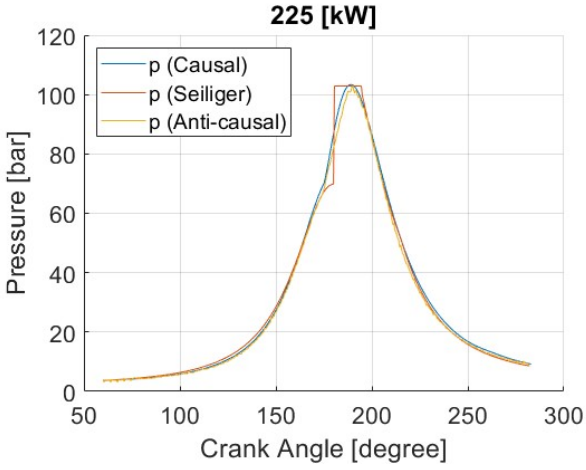

Figure 7: Pressure as a function of the crank angle

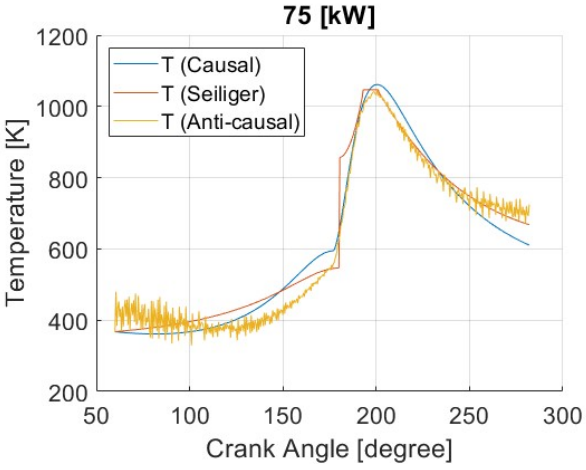

Figure 9: Temperature as a function of the crank angle

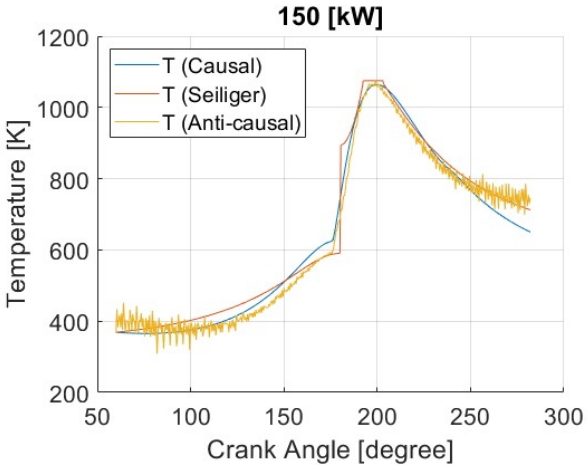

Figure 10: Temperature as a function of the crank angle

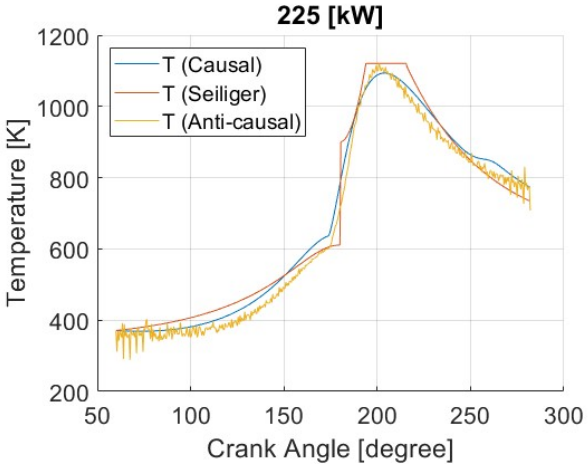

Figure 11: Temperature as a function of the crank angle

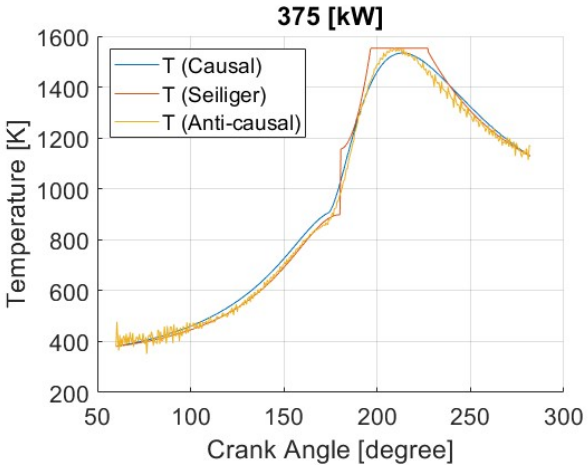

Figure 12: Temperature as a function of the crank angle

Analysing the temperature curves, the deviation during the compression stroke becomes more significant for the temperature compared to the pressure curve. For the temperature at the two lowest operating points, the temperature decreases during the compression stroke which is unrealistic. The deviation is less significant during the combustion and expansion phases. Similar to the pressure curve the Seiliger approach is better at predicting the maximum temperature while the causal model is more representative if the entire process is considered. It should be noted that the pressure curve should be prioritized over the temperature curve since it is directly measured instead of calculated. Furthermore, the temperature in the cylinder not only shows temporal variation but a large spatial variation as well (Stapersma, 2010c).

3. Conceptual changes for ammonia-diesel combustion

To identify the conceptual changes necessary for ammonia-diesel combustion, the combustion model used for both the anti-causal and causal simulation models should be analysed in more detail. The combustion model is used to derive both equations 1 and 14.

3.1. Combustion model

The single-zone combustion model is derived by modelling the closed-cylinder process as a control volume and applying the mass and energy balance. An illustration of the single-zone combustion model is shown in figure 13. The energy and mass balances are shown in equations 19 and 20 respectively.

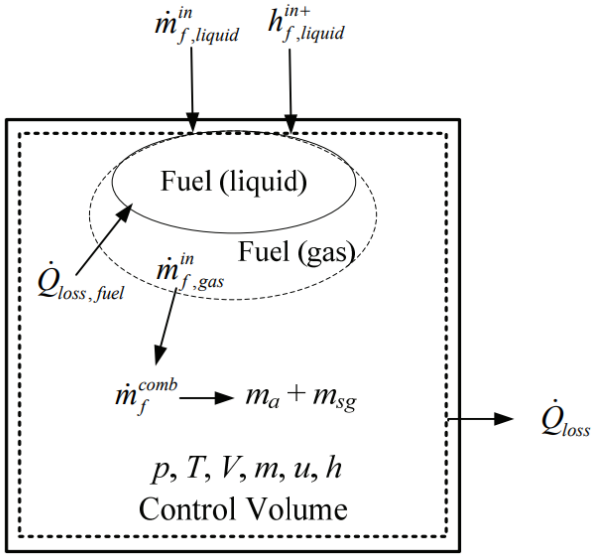

Figure 13: Single-zone combustion model (Ding, 2011)

$$\frac{d(m \cdot u)}{dt} = h^{in+} \cdot \dot{m}^{in} - h^{out+} \cdot \dot{m}^{out} + \dot{Q} - \dot{W} \tag{19}$$

$$\frac{dm}{dt} = \dot{m}^{in} - \dot{m}^{out} \tag{20}$$

The energy balance can be simplified, starting with the right side of the equation. It is assumed that nothing flows out of the cylinder during the closed-cylinder process (equation 21).

As for the mass flow into the cylinder, this is equal to the fuel that is injected (equation 22). The heat transfer to surroundings ($\dot{Q}$) is modelled as the heat losses and has been discussed when explaining the anti-causal model. As for the work ($\dot{W}$), this is calculated by using equation 23.

$$\dot{m}^{out} \cdot h^{out+} = 0 \tag{21}$$

$$\dot{m}^{in} \cdot h^{in+} = \dot{m}^{in}_{f,liquid} \cdot h^{in+}_{f,liquid} \tag{22}$$

$$\dot{W} = p \cdot \frac{dV}{dt} \tag{23}$$

As for the left side of the energy balance and the mass balance, it is assumed that at all times the mass consists of three substances. Namely, fuel, air, and stoichiometric gas. This means that the partial derivative on the left side of the energy balance can be re-written according to equations 24 and 25.

$$\frac{d(m \cdot u)}{dt} = \frac{d(m_f \cdot u_f + m_a \cdot u_a + m_{sg} \cdot u_{sg})}{dt} \tag{24}$$

$$\begin{aligned} m_f \cdot \frac{du_f}{dt} + m_a \cdot \frac{du_a}{dt} + m_{sg} \cdot \frac{du_{sg}}{dt} \\ + u_f \cdot \frac{dm_f}{dt} + u_a \cdot \frac{dm_a}{dt} + u_{sg} \cdot \frac{dm_{sg}}{dt} \end{aligned} \tag{25}$$

It is assumed that at no point during the closed-cylinder process, fuel vapour is present within the cylinder. Additionally air and stoichiometric gas behave like an ideal gas and therefore the following assumptions can be made for the change in internal energy:

$$m_f = 0 \tag{26}$$

$$du_a = c_{v,a} \cdot dT \tag{27}$$

$$du_{sg} = c_{v,sg} \cdot dT \tag{28}$$

This means that a simplification can be made for the first three terms of equation 24 as is shown in equation 29. As for the ratio between air and stoichiometric gas, this is calculated according to equation 30.

$$m_a \cdot \frac{du_a}{dt} + m_{sg} \cdot \frac{du_{sg}}{dt} = (m_a \cdot c_{v,a} + m_{sg} \cdot c_{v,sg}) \cdot \frac{dT}{dt} = m \cdot c_v \cdot \frac{dT}{dt} \tag{29}$$

$$x = \frac{m_1 \cdot x_1 - \sigma \cdot \int_{t_0}^{t_1} CRR}{m_1 + \int_{t_0}^{t_1} CRR} \tag{30}$$

c_v is assumed to be a function of temperature and the ratio between air and stoichiometric gas. As for the change in mass for the three substances, the change is mass of the fuel is equal to the amount that is injected ($\dot{m}^{in}_{f,gas}$) subtracting the amount of fuel that is used for combustion ($\dot{\xi}$). Additionally, it is assumed that the injected fuel reacts with air to form stoichiometric gas and that the ratio between air and fuel is the stoichiometric ratio σ. This means that the following three expressions are obtained for the change in mass:

$$\frac{dm_f}{dt} = \dot{m}^{in}_{f,gas} - \dot{\xi} \tag{31}$$

$$\frac{dm_a}{dt} = -\sigma \cdot \dot{\xi} \tag{32}$$

$$\frac{dm_{sg}}{dt} = (1 + \sigma) \cdot \dot{\xi} \tag{33}$$

Using these relations the following expression can be obtained for the energy balance:

$$\begin{aligned} m \cdot c_v \cdot \frac{dT}{dt} = \dot{m}^{in}_f \cdot (h^{in+}_{f,liquid} - u_f) \\ + \dot{\xi} \cdot [(u_f + \sigma \cdot u_a - (1 + \sigma) \cdot u_{sg})] \\ + \dot{Q_{loss}} - p \cdot \frac{dV}{dt} \end{aligned} \tag{34}$$

This expression is simplified by introducing the heat of combustion u_{comb} and the energy of the fuel e_f.

$$u_{comb} = u_f + \sigma \cdot u_a - (1 + \sigma) \cdot u_{sg} \tag{35}$$

$$e_f = h^{in+}_{f,liquid} - u_f \tag{36}$$

Finally, it is assumed that the injected evaporates and combusts almost instantaneously, ($m^{in}_{f,gas} = \dot{\xi}$). Using this and u_{comb} and e_f means that equations 1 and 14 can be derived. As for the thermodynamic properties c_v, R, u_{comb} and e_f they are determined according to the method constructed by Stapersma (2010d).

3.2. Proposed changes

Having explained the combustion model that is used in both the anti-causal simulation model as well as the causal simulation model. The proposed changes will now have to be identified. For the Newton-Rhapson solver, no changes will have to be applied. For the entire pressure data analysis process, the fundamental difference will be that the combustion characteristics have to be known before the anti-causal is used. This study has shown how the anti-causal model can be used to obtain the start and end of combustion. For ammonia-diesel operation, this has to be known before the pressure data analysis process can be started. This is the case because if an accurate value for CRR is to be obtained, the correct thermodynamic properties have to be used. This means that for the two fuels, it should be known when they are reacting, and what the ratio is between the two based on mass, volume, or energy. As for the equations specifically, this study will consider three scenarios: liquid injection of ammonia into the cylinder, gaseous injection of ammonia into the cylinder, and gaseous injection of ammonia into the air intake resulting in a

gas mixture of fresh air and ammonia. For all three scenarios, the pilot fuel is injected as a liquid. They will be referred to in this section as scenarios 1, 2, and 3 respectively. The only situation that is considered here is that both fuels are reacting since single-fuel operation is fairly straightforward for the single-zone combustion model.

The combustion model starts with the mass and energy balance. The assumption that there is no mass flow out ($\dot{m}^{out} = 0$) of the system is still valid for all three scenarios. For the mass and enthalpy that flow into the system. Scenarios 1 and 2 will have an additional component namely the ammonia either as liquid or gas. This is shown in equations 37 and 38 respectively. For scenario 3, the ammonia does not flow into the system during the closed-cylinder process so, therefore, this equation is the same as for diesel (equation 39).

$$\dot{m}^{in} \cdot h^{in+} = \dot{m}^{in}_{pilot} \cdot h^{in+}_{pilot} + \dot{m}^{in}_{ammonia,liquid} \cdot h^{in+}_{ammonia,liquid} \tag{37}$$

$$\dot{m}^{in} \cdot h^{in+} = \dot{m}^{in}_{pilot} \cdot h^{in+}_{pilot} + \dot{m}^{in}_{ammonia,gas} \cdot h^{in+}_{ammonia,gas} \tag{38}$$

$$\dot{m}^{in} \cdot h^{in+} = \dot{m}^{in}_{pilot} \cdot h^{in+}_{pilot} \tag{39}$$

The mass balance will be the same for all three scenarios. Namely, there will be an additional component for the ammonia fuel:

$$m = m_{pilot} + m_{ammonia} + m_a + m_{sg} \tag{40}$$

However, the stoichiometric gas is important to consider. (Stapersma, 2010d) explained that stoichiometric gas is modelled as a mixture of individual species. The mass fraction for each species is constant and is determined by the selected fuel. This means the same method has to be applied to the stoichiometric gas produced by ammonia combustion. Re-writing the partial derivative will now require the addition of ammonia as is shown in equation 41.

$$\begin{aligned}\frac{d(m \cdot u)}{dt} &= m_{pilot} \cdot \frac{du_{pilot}}{dt} + m_{ammonia} \cdot \frac{du_{ammonia}}{dt} \\ &+ m_a \cdot \frac{du_a}{dt} + m_{sg} \cdot \frac{du_{sg}}{dt} + u_{pilot} \cdot \frac{dm_{pilot}}{dt} \\ &+ u_{ammonia} \cdot \frac{dm_{ammonia}}{dt} + u_a \cdot \frac{dm_a}{dt} + u_{sg} \cdot \frac{dm_{sg}}{dt}\end{aligned} \tag{41}$$

For diesel combustion, the assumption was made that the injected fuel instantly evaporates and combusts, so no fuel vapour is present within the cylinder. For ammonia in particular, this is a highly questionable assumption because of the higher combustion threshold (Mallouppas et al., 2022). This means that this fact has to be taken into account, meaning that the fuel might evaporate only after it's injected (in the case of scenario 1) and will only combust somewhat later than the pilot fuel. However, since this section will only look at the situation where both fuels react simultaneously, this is not further explored here. At some point, the threshold will be reached where both fuels will react. This means that the same simplification can be made for the first part of this partial derivative as for diesel combustion which is shown in equation 42.

$$m_a \cdot \frac{du_a}{dt} + m_{sg} \cdot \frac{du_{sg}}{dt} = (m_a \cdot c_{v,a} + m_{sg} \cdot c_{v,sg}) \cdot \frac{dT}{dt} = m \cdot c_v \cdot dT \tag{42}$$

As for scenario 3, this simplification cannot be made anyway, since the gaseous ammonia is present at the start of the closed-cylinder process. It is still valid to assume that no fuel vapour of the pilot fuel will be present. This means that the following expression is obtained when rewriting the partial derivative for scenario 3.

$$\begin{aligned}m_{ammonia} \cdot \frac{du_{ammonia}}{dt} &+ m_a \cdot \frac{du_a}{dt} \\ &+ m_{sg} \cdot \frac{du_{sg}}{dt} + u_{pilot} \cdot \frac{dm_{pilot}}{dt} \\ &+ u_{ammonia} \cdot \frac{dm_{ammonia}}{dt} + u_a \cdot \frac{dm_a}{dt} + u_{sg} \cdot \frac{dm_{sg}}{dt}\end{aligned} \tag{43}$$

For all three scenarios, it is assumed that the following reactions are taking place within the cylinder:

$$\dot{m}^{comb}_{pilot} + \dot{m}^{comb}_{a} = \dot{m}^{comb}_{sg,pilot} \tag{44}$$

$$\dot{m}^{comb}_{ammonia} + \dot{m}^{comb}_{a} = \dot{m}^{comb}_{sg,ammonia} \tag{45}$$

Both reactions will produce stoichiometric gas that is made up of different individual species. Nevertheless, if it is assumed that there is a distinct ratio between these two gas mixtures determined by the ratio between ammonia and pilot fuel, the two gas mixtures can be added together to obtain the total stoichiometric gas in the cylinder:

$$\dot{m}_{sg} = \dot{m}_{sg,ammonia} + \dot{m}_{sg,pilot} \tag{46}$$

For all three scenarios, the following equations can be constructed for the change in mass for fuel, air, and stoichiometric gas.

$$\dot{m}_{pilot} = \dot{m}^{in}_{f,pilot} - \xi_{pilot} \tag{47}$$

$$\dot{m}_{ammonia} = \dot{m}^{in}_{f,ammonia} - \xi_{ammonia} \tag{48}$$

$$\dot{m}_a = -\sigma_{pilot} \cdot \xi_{pilot} - \sigma_{ammonia} \cdot \xi_{ammonia} \tag{49}$$

$$\dot{m}_{sg} = (1 + \sigma_{pilot}) \cdot \xi_{pilot} + (1 + \sigma_{ammonia}) \cdot \xi_{ammonia} \tag{50}$$

This is of course an issue since the anti-causal model is designed to find the total combustion reaction rate ξ. Therefore, the following assumptions have to be made concerning ξ. The

mass fraction of the injected ammonia compared to the total fuel mass that is injected is called f:

$$f = \frac{\dot{m}_{ammonia}}{\dot{m}_{ammonia} + \dot{m}_{pilot}} \tag{51}$$

Then the relation between the mass fractions of ammonia and diesel is as follows:

$$\dot{m}_{ammonia} = \frac{f}{1-f} \cdot \dot{m}_{pilot} \tag{52}$$

Since the only scenario that is considered here is that the injected fuel evaporates and combusts almost instantly, the same relation is true between the reaction rate of the two fuels, and the relationship between them and the total reaction rate:

$$\xi_{ammonia} = \frac{f}{1-f} \cdot \xi_{pilot} \tag{53}$$

$$\xi_{ammonia} = f \cdot \xi \tag{54}$$

$$\xi_{pilot} = (1-f) \cdot \xi \tag{55}$$

This means that an expression can be found as a function of the total reaction rate ξ which is necessary for the anti-causal model. By using f, σ_{pilot}, and $\sigma_{ammonia}$ the following expressions can be derived for the heat of combustion and energy of fuel for scenarios 1 and 2.

$$\begin{aligned} u_{comb,1-2} = (1-f) \cdot u_{pilot} + f \cdot u_{ammonia} + ((1-f) \cdot \sigma_{pilot} \\ + f \cdot \sigma_{ammonia}) \cdot u_a - ((1-f)(1+\sigma_{pilot}) \\ + f \cdot (1+\sigma_{ammonia})) \cdot u_{sg} \end{aligned} \tag{56}$$

$$e_{f,1-2} = h^{in+}_{pilot} \cdot (1-f) + u_{pilot} \cdot (1-f) + f \cdot h^{in+}_{ammonia} + u_{ammonia} \cdot f \tag{57}$$

These expressions can be substituted into equation 1 to obtain the expression for the anti-causal model. As for equation 14, the causal model offers more freedom to simulate the combustion reaction rate for ammonia and the pilot fuel separately. So for the causal model, the individual properties of each fuel can be used.

As for the stoichiometric gas, another question needs to be answered first. If the same method is applied for ammonia combustion. Then the ratio between the stoichiometric gas of pilot fuel and ammonia needs to be incorporated. Since there is an expression for the mass change of total stoichiometric gas and for the individual components as well this ratio is fairly straightforward:

$$\frac{\dot{m}_{sg,pilot}}{\dot{m}_{sg}} = \frac{(1+\sigma_{pilot})(1-f)}{(1+\sigma_{pilot})(1-f) + (1+\sigma_{ammonia})f} \tag{58}$$

$$\frac{\dot{m}_{sg,ammonia}}{\dot{m}_{sg}} = \frac{(1+\sigma_{ammonia})f}{(1+\sigma_{pilot})(1-f) + (1+\sigma_{ammona})f} \tag{59}$$

As for scenario 3, the situation becomes somewhat more complicated. The assumption that is critical for finding ξ is that the fuel that is injected into the cylinder evaporates and combusts. However, since the fuel is already present within the cylinder this assumption cannot be made. If the assumption can be made that the pilot fuel and ammonia react according to the previously mentioned ratio f then the following equations will result. As for the gas composition, this does not consist anymore of just air and stoichiometric gas. Therefore, the following relations will be used:

$$x_a = \frac{m_a}{m_a + m_{sg} + m_{ammonia}} \tag{60}$$

$$x_{sg} = \frac{m_{sg}}{m_a + m_{sg} + m_{ammonia}} \tag{61}$$

$$x_{ammonia} = \frac{m_{ammonia}}{m_a + m_{sg} + m_{ammonia}} \tag{62}$$

$$x_{sg} = (1 - x_a - x_{ammonia}) \tag{63}$$

This means that for x_a and $x_{ammonia}$ the following expressions can be used:

$$x_a = \frac{m_1 \cdot x_{a,1} - (\sigma_{pilot} \cdot (1-f) + \sigma_{ammonia} \cdot f) \int_{t_0}^{t_1} \xi \cdot dt}{m_1 + \int_{t_0}^{t_1} \xi \cdot dt} \tag{64}$$

$$x_{ammonia} = \frac{m_{ammonia,in} - f \int_{t_0}^{t_1} \xi \cdot dt}{m_1 + \int_{t_0}^{t_1} \xi \cdot dt} \tag{65}$$

$m_{ammonia,in}$ is the mass of ammonia present at the beginning of the closed-cylinder process. If these relations are used then the following expression can be derived for the change in internal energy shown in equation 43:

$$\begin{aligned} m_{ammonia} \cdot \frac{du_{ammonia}}{dt} + m_a \cdot \frac{du_a}{dt} + m_{sg} \cdot \frac{du_{sg}}{dt} = \\ (1 - x_{sg} - x_{ammonia}) \cdot m \cdot c_{v,a} \cdot \frac{dT}{dt} \\ + (1 - x_a - x_{ammonia}) \cdot m \cdot c_{v,sg} \cdot \frac{dT}{dt} \\ + (1 - x_{sg} - x_a) \cdot m \cdot c_{v,ammonia} \cdot \frac{dT}{dt} = m \cdot c_v \cdot \frac{dT}{dt} \end{aligned} \tag{66}$$

Now as for the final steps, there will be no difference between scenarios 1 and 2 and scenario 3. This means that $u_{comb,3}$ will be the same as $u_{comb,1-2}$. As for $e_{f,3}$, the enthalpy of ammonia should not be included here since no ammonia is injected during the closed-cylinder process. This means that the resulting equation is the same as equation 36.

The derived equations in this study are designed for the situation when both fuels are reacting. This is done since the current combustion model can simulate one fuel. For the entire closed-cylinder process, different thermodynamic properties will have to be used for different crank angle intervals. To implement

these changes, the combustion characteristics have to be known before the anti-causal model is applied, which is the main difference compared to the current design. Interestingly, this strategy might already be useful to analyse diesel combustion. In the current model, the injection strategy is not included in the thermodynamic properties. For both, however, implementation and validation only can confirm that these proposed changes will ultimately achieve their desired effect.

4. Conclusions & recommendations

- Analysing the pressure data analysis process originally constructed by Ding (2011), no changes have to be made to the Newton-Rhapson solver. However, the single-zone combustion model that is used in both the anti-causal as well as causal simulation model does require changes. The fundamental change that has to be applied to the combustion model is that the combustion characteristics for each of the fuels have to be known prior to using the anti-causal model. This has to be done because the correct thermodynamic properties for the substances present in the cylinder have to be used if an accurate value for the combustion reaction rate is to be obtained. This is not the case for the current model since the properties of diesel can be used at all times.
- The anti-causal model is sensitive when it comes to the measured pressure as a function of the crank angle. This pressure curve is the main input for the anti-causal model. The pressure curve can show inaccuracies in particular at lower pressures if they're not optimized to measure these. These inaccuracies can result in an unrealistic result for the reaction coordinate. this effect can be mitigated to an extent through calibration.
- The Wiebe function which is used for the causal simulation model and the Seiliger approach produced results for the equivalence criteria; p_{max}, T_{max}, w_{in}, and q_{in}, and the pressure and temperature as a function of the crank angle. The Seiliger approach produces very accurate results for the equivalence criteria while the Wiebe function produces sufficiently accurate results except for the heat input Q_{in}. As for the pressure curves, the results from both models are accurate during the combustion and expansion phases. For the compression phase, however, there is a deviation that increases when the power decreases. The same can be said for the temperature curves, but the deviation is far more substantial.

References

Ayvalı, T., Edman Tsang, S. C., and Van Vrijaldenhoven, T. (2021). The Position of Ammonia in Decarbonising Maritime Industry: An Overview and Perspectives: Part I : Technological advantages and the momentum towards ammonia-propelled shipping. *Johnson Matthey Technology Review*, 65(2):275–290.

de Vos, P., Somers, L. M. T., Tinga, T., Foekema, E. M., van der Zwaan, B., and Negenvorn, R. R. (2022). The AmmoniaDrive Consortium. *SWZ Maritime 143*, pages 24–27.

Ding, Y. (2011). *Characterising Combustion in Diesel Engines using parameterised finite stage cylinder process models*. PhD thesis, VSSD, Delft.

Lee, B. and Jung, D. (2016). Thermodynamics-based mean-value engine model with main and pilot injection sensitivity. *Proceedings of the Institution of Mechanical Engineers, Part D: Journal of Automobile Engineering*, 230(13):1822–1834.

Lindsey, R. and Blunden, J. (2023). Climate Change: Global Temperature.

Liu, L., Wu, Y., and Wang, Y. (2022). Numerical investigation on the combustion and emission characteristics of ammonia in a low-speed two-stroke marine engine. *Fuel*, 314:122727.

Mallouppas, G., Ioannou, C., and Yfantis, E. A. (2022). A Review of the Latest Trends in the Use of Green Ammonia as an Energy Carrier in Maritime Industry.

MAN Energy Solutions (2023). Groundbreaking First Ammonia Engine Test Completed.

Nadeau, K. C., Agache, I., Jutel, M., Annesi Maesano, I., Akdis, M., Sampath, V., D'Amato, G., Cecchi, L., Traidl-Hoffmann, C., and Akdis, C. A. (2022). Climate change: A call to action for the United Nations. *Allergy*, 77(4):1087–1090.

Niki, Y., Hirata, K., Kobayashi, K., and Shimizu, Y. (2023). Development of premixed ammonia combustion strategy with minimum emissions for marine diesel engines. In *CIMAC Congress*, Busan.

Oba, H., Ito, K., Matsuda, C., Ichikawa, Y., Niki, Y., and Takasaki, K. (2023). Fundamental study of the effect of stratified NH3 injection system for nitrogen compounds reduction. In *CIMAC Congress*, Busan.

Sapra, H., Godjevac, M., De Vos, P., Van Sluijs, W., Linden, Y., and Visser, K. (2020). Hydrogen-natural gas combustion in a marine lean-burn SI engine: A comparitive analysis of Seiliger and double Wiebe function-based zero–dimensional modelling. *Energy Conversion and Management*, 207:112494.

Stapersma, D. (2010a). *Diesel Engines Volume 1 Performance Analysis*. NLDA & Delft UT, 8 edition.

Stapersma, D. (2010b). *Diesel Engines Volume 3 Combustion*. NLDA & Delft UT, Delft, 6 edition.

Stapersma, D. (2010c). *Diesel Engines Volume 4 Emissions and Heat Transfer*. NLDA & Delft UT, Delft, 6 edition.

Stapersma, D. (2010d). *Diesel Engines Volume 6: Thermodynamic principles II*.

Sui, C., Song, E., Stapersma, D., and Ding, Y. (2017). Mean value modelling of diesel engine combustion based on parameterized finite stage cylinder process. *Ocean Engineering*, 136:218–232.

Sui Congbiao (2021). Energy Effectiveness and Operational Safety of Low-Powered Ocean-going Cargo Ship in Various (Heavy) Operating Conditions Congbiao SUI . Technical report.

Thacker, B. H., Doebling, S. W., Hemez, F. M., Anderson, M. C., Pepin, J. E., and Rodriguez, E. A. (2004). Concepts of Model Verification and Validation. Technical report, Los Alamos National Laboratory, Los Alamos.

Theotokatos, G. (2010). On the cycle mean value modelling of a large two-stroke marine diesel engine. *Proceedings of the Institution of Mechanical Engineers Part M: Journal of Engineering for the Maritime Environment*, 224(3):193–205.

Wärtsilä Corporation (2022). Wärtsilä coordinates EU funded project to accelerate ammonia engine development.

Woschni, G. (1967). A Universally Applicable Equation for the Instantaneous Heat Transfer Coefficient in the Internal Combustion Engine.

Zhou, S., Zhou, H., Xi, H., Zhou, W., Zhu, Y., and Feng, Y. (2023). Research on combustion and emission characteristics of marine ammonia engine. In *CIMAC Congress*, Busan.

Zhu, J., Zhou, D., Yang, W., Qian, Y., Mao, Y., and Lu, X. (2023). Investigation on the potential of using carbon-free ammonia in large two-stroke marine engines by dual-fuel combustion strategy. *Energy*, 263:125748.

B

Mean value engine modelling techniques

This appendix will discuss general methods that are used in a Mean Value Engine Model (MVEM). This appendix contains information about the open-cylinder process and the non-cylinder components. The closed-cylinder process already has been discussed in chapter 3. This appendix will consider general methods but also specifically what is used by the reference MVEM developed by Sui Congbiao (2021). The non-cylinder components are discussed in general and for the reference MVEM in sections B.1 and B.2 respectively. The open-cylinder process is discussed in general and for the reference MVEM in sections B.3 and B.4 respectively. The contents of this chapter were originally included in the literature study for this thesis. However, they did not prove to be relevant for the main research part and were, therefore, excluded. These topics were studied to answer the following questions:

How are the components of an internal combustion engine generally modelled in a mean value engine model?

How do the methods used in the reference model compare to those generally used in a mean value engine model?

This question is answered at the end of this appendix. The definition of the symbols, abbreviations, and subscripts used in this section can be found in the nomenclature of this report.

B.1. Non-cylinder components

An Internal Combustion Engine (ICE) can use turbocharging to increase its performance, a turbocharger uses a compressor to compress the air that goes into the cylinder. This will increase the amount of fuel that can be used and therefore the developed power (Stapersma & Klein Woud, 2002). There are different possible turbocharging concepts, such as two-stage or sequential turbocharging (Stapersma, 2010c). A basic design of a turbocharger is shown in figure B.1. There are several components which the air goes through before it reaches the cylinder of the engine, such as an air filter, compressor, intercooler, and air intake manifold. The compressor of a turbocharger is in turn powered by a turbine. The turbine uses hot exhaust gasses to power itself. So the exhaust gasses that leave the cylinder will first enter the exhaust manifold before entering the turbine. The conditions of the air, such as temperature, pressure, and mass are important for the overall engine model. The conditions of the air at the inlet filter are usually assumed to be equal to ambient air conditions (Stapersma, 2010c). Calculating how the conditions of the air change through the compressor, intercooler, and inlet receiver determines the composition of the air when it enters the cylinder. Subsequently, knowing the conditions of the air after it leaves the cylinder through the exhaust gas receiver will determine the conditions of the air that passes through the turbine. This in turn will determine the performance of the turbine.

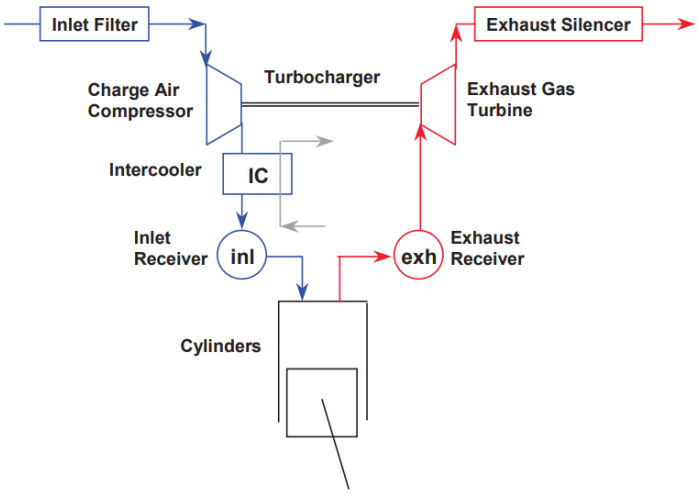

Figure B.1: Overview of a turbocharger concept (Stapersma, 2010c)

This section will give a general overview of how all of the components of the ICE are modelled except for the cylinders, which will be done in section B.3. This section will not give a detailed step-by-step description of every MVEM from the studied literature. Instead, it will give a general overview of methods that are consistently used throughout MVEMs.

Studying the selected literature for this chapter, there are two aspects of which there seems to be a consensus in MVEMs. Theotokatos (2010), Feng et al. (2019), Guan et al. (2015), R. Li et al. (2013), Llamas and Eriksson (2019), Shen et al. (2020), Tang et al. (2017), Hendricks (1989), Alegret et al. (2015), and S. Zhu et al. (2020) assume that the air behaves like an ideal gas. This means that equation B.1 (Moran et al., 2017) can be used to relate the pressure p, mass m, temperature T, Volume V, and gas constant R.

$$p \cdot V = m \cdot R \cdot T \tag{B.1}$$

All of the authors mentioned above, except for Feng et al. (2019), Tang et al. (2017), and S. Zhu et al. (2020) use the following relation to compute the engine speed n_e and/or turbocharger speed n_{TC}:

$$n_e = \frac{60 \cdot M}{2\pi \cdot J} \tag{B.2}$$

With M being the developed torque and J being the polar moment of inertia to calculate n. Looking at figure B.1, the first component that the air will enter is the air filter. The air filter does not affect the air conditions all that much, with Theotokatos (2010), Guan et al. (2015), and Shen et al. (2020) only taking into account the pressure drop over the air filter. After this, the air will enter the compressor. Theotokatos (2010), Guan et al. (2015), R. Li et al. (2013), Llamas and Eriksson (2019), Shen et al. (2020), and Alegret et al. (2015) all use the compressor performance maps for the efficiency and some for the mass flow as well. These performance maps are used in combination with some form of interpolation/extrapolation methods to estimate efficiency. The efficiency is used along with the pressure ratio to calculate the exiting temperature of the compressor. After the compressor, the air will enter the intercooler. It is important to calculate the temperature of the air that leaves the intercooler and the pressure drop. The temperature can be calculated using a polynomial for the intercooler effectiveness as is done by Theotokatos (2010), Guan et al. (2015), and Llamas and Eriksson (2019) or through performance maps obtained from experimental data as is done by R. Li et al. (2013), and S. Zhu et al. (2020). All of the authors mentioned above take into account the pressure drop as well. The polynomial that is used to calculate the effectiveness is a function of the air mass flow, while the efficiency is considered to be a function of both the air mass flow as well as the engine speed. After the intercooler, the air will enter the inlet receiver. To calculate the mass flow through the cylinder, an approach used by Theotokatos (2010), Guan et al. (2015), Shen et al. (2020), and S. Zhu et al. (2020) is to model the engine intake and exhaust manifold as two orifices connected in series. To do this, the equivalent

flow area A_{eq} is calculated using equation B.3. The corresponding mass flow during scavenging m_{sc} is calculated using equation B.4.

$$A_{eq} = \frac{n_{cyl}}{360^\circ} \int_{180^\circ}^{180^\circ} \frac{A_s(\phi) \cdot A_e(\phi)}{\sqrt{A_s(\phi)^2 A_s(\phi)^2}} d\phi \tag{B.3}$$

$$\dot{m}_{sc} = c_d A_{eq} \frac{p_s}{\sqrt{R_g T_s}} \sqrt{\frac{2\gamma_s}{\gamma_s - 1} \left[\left(\frac{p_e}{p_s} \right)^{\frac{2}{\gamma_s}} - \left(\frac{p_e}{p_s} \right)^{\frac{\gamma_s + 1}{\gamma_s}} \right]} \tag{B.4}$$

With p_s and p_e being the pressures in the scavenging receiver and exhaust gas receiver respectively, T_s being the temperature in the scavenging receiver, c_d being the orifice flow coefficient, and γ_s being the ratio of specific heats for the scavenging receiver. For modelling the inlet and exhaust manifold in general, Theotokatos (2010), Guan et al. (2015), Llamas and Eriksson (2019), and Shen et al. (2020) use a control volume. This means that for the control volume the conservation of both mass and energy is used. The equation for mass and energy conversion for transient conditions is shown in equation B.5 and B.6 respectively (Moran et al., 2017).

$$\frac{dm_{CV}}{dt} = \sum_i \dot{m}_i - \sum_o \dot{m}_o \tag{B.5}$$

$$\frac{dE_{CV}}{dt} = \dot{Q}_{CV} - \dot{W}_{CV} + \sum_i \dot{m}_i \left(h_i + \frac{v_i^2}{2} + g z_i \right) - \sum_o \dot{m}_o \left(h_o + \frac{v_o^2}{2} + g z_o \right) \tag{B.6}$$

Looking at equation B.6, the kinetic energy and potential energy terms are neglected since this would require a physical representation of the control volume, something which is not included in an MVEM. As was mentioned in the introduction of this chapter, the in-cylinder process will be discussed in section B.3. After the exhaust gas receiver, the air will enter the turbine. Similar to the compressor, Theotokatos (2010), Guan et al. (2015), R. Li et al. (2013), Llamas and Eriksson (2019), Shen et al. (2020), and Alegret et al. (2015) all use the turbine performance maps to calculate the efficiency.

B.2. Non-cylinder components reference model

The reference model contains all of the mentioned components from the previous section with the addition of an auxiliary blower. The auxiliary blower is used to increase the pressure of the scavenging air at low loads because the turbocharger is unable to generate a sufficient pressure (Andersen, 2015). The method that is used in the reference model to model the non-cylinder components is based on the work of Schulten and Stapersma (2003). The method uses a resistance and volume element for each component, such as the air filter, compressor, etc. The resistance element calculates the mass flow over the components as a function of the pressure difference using equation B.4. The volume elements use the mass in and outflow along with the conservation of both mass and energy to calculate the state of the volume, using the same equations (B.5 and B.6) as discussed in the previous section. A schematic example of a resistance and volume element is shown in figure B.2.

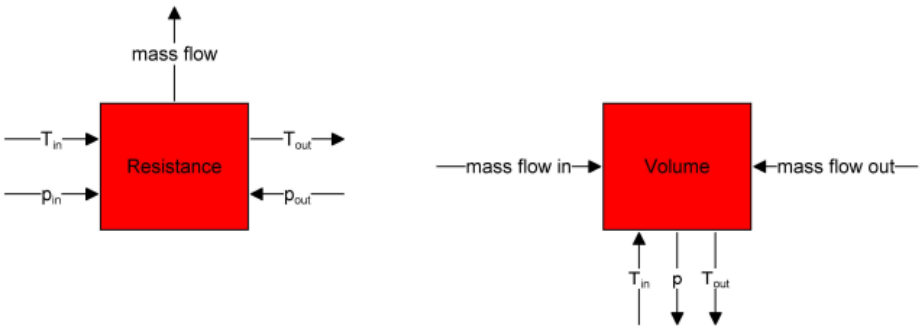

Figure B.2: Volume and resistance elements

By doing this for each of the components, an overall network will be constructed as is shown in figure B.3. This network is implemented into the program Matlab Simulink. Because of the method which is implemented, Matlab is required to solve this network, since it can only be solved numerically.

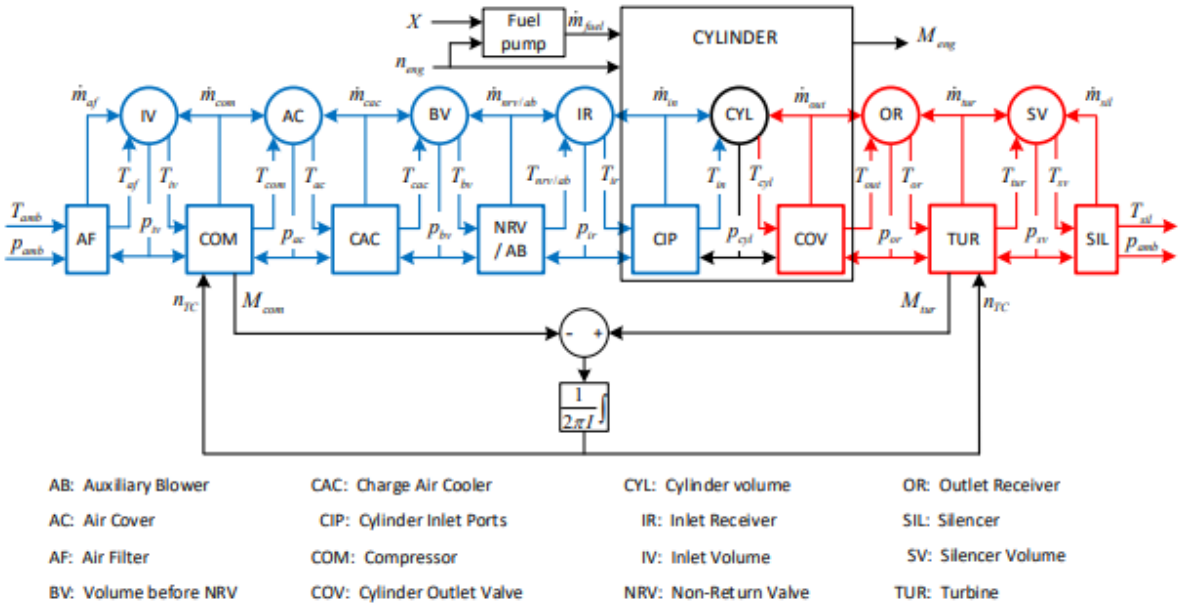

Figure B.3: Contructed network of resistance and volume elements (Sui Congbiao, 2021)

As was mentioned in the previous section the model implements the conservation of energy equation (equation B.6) in the volume element. In addition to this, each volume element can also take into account potential heat losses according to equation B.7. α is a heat transfer coefficient which depends on the medium within the volume element. T_{wall} is the temperature of the wall and A is the area.

$$\dot{Q}_{loss} = -\alpha \cdot A \cdot (T - T_{wall}) \tag{B.7}$$

Similar to the literature studied in the previous section, the reference model also uses intercooler effectiveness, which is a function of the normalised air mass flow through the intercooler. The model uses the compressor efficiency map provided by the manufacturer. The turbine efficiency is calculated based on a separately developed generic method. To calculate the compressor pressure ratio the model uses the Buchi balance (equation B.8 (Stapersma, 2010c)).

$$\pi_{comp} = \left[1 + \delta \cdot \chi \cdot \eta_{TC} \cdot \tau_{TC} \left(1 - \frac{1}{\pi_{tur}^{\frac{\gamma_{gas}-1}{\gamma_{gas}}}} \right) \right]^{\frac{\gamma_{air}}{\gamma_{air}-1}} \tag{B.8}$$

$$\delta = \frac{1}{(1+\lambda)} \tag{B.9}$$

π_{turb} is the turbine pressure ratio, δ is dependent on the air excess ratio λ, τ_{TC} is the turbocharger temperature ratio which is the turbine inlet temperature divided by the compressor inlet temperature, χ is the ratio between the specific heat c_p of the exhaust gas and the air, η_{TC} is the turbocharger efficiency, γ_{gas} and γ_{air} are the specific heat ratios of the gas and air respectively. This equation requires a good prediction for the compressor, turbine, and mechanical efficiency (Sui Congbiao, 2021). The turbocharger's mechanical efficiency is taken into account as a function of the rotational speed and the pressure at the compressor outlet. Additionally, the model also uses a parametric model developed for the compressor and turbine off-design conditions. The compressor surge index is also taken into account to make sure compressor surge is avoided. Compressor surge is the effect of an unstable rotary compressor, a sudden decrease in mass flow and pressure ratio, caused by a low mass flow and high backpressure (Stapersma & Klein Woud, 2002).

B.3. In-cylinder process

This section will look at how the cylinder itself can be modelled in an MVEM. The process that occurs within the cylinder will ultimately determine the performance of the engine (Feng et al., 2019). Modelling the process within the cylinder will also determine the conditions of the air that passes through the exhaust manifold. Similarly to section B.1, this section will not discuss in detail how every MVEM models the in-cylinder process. Instead, it will discuss the general approach used throughout the studied literature.

Similar to the non-cylinder components, the cylinder is also modelled in an MVEM as a control volume with mass and energy conservation applied. This is done by Theotokatos (2010), Shen et al. (2020), and Feng et al. (2019). Two types of models that can be used for the gas exchange process which are often mentioned in the studied literature, are the perfect displacement and perfect mixing models. A perfect displacement model assumes that no mixing takes place between the exhaust gasses and the scavenged air. The two substances have the same density and it is assumed that the scavenged air simply "pushes" the exhaust gasses out of the cylinder. It does so at both a constant pressure and volume without any heat transfer. The perfect mixing model assumes the opposite, the scavenged air instantly mixes with the exhaust gasses creating a homogeneous substance. This process also assumes it occurs at constant pressure and volume without any heat transfer (Andersen, 2015). In reality, the truth lies somewhere in the middle. A portion of the exhaust gasses will be displaced by the fresh air while a part will also mix with the exhaust gasses (Feng et al., 2019). Both models are used in the literature and the authors usually try to expand them to address this issue. Feng et al. (2019) introduce a scavenging quality parameter which could be adjusted manually to account for this. Llamas and Eriksson (2019) use an expansion of the perfect displacement model developed by Andersen (2015). This model does take into account the difference in density between the exhaust gasses and scavenged air. The model also takes into account the gas which is displaced during the expelling phase. A similar technique is used by Alegret et al. (2015), with a combination of the perfect mixing and displacement model being used through tuning parameters. R. Li et al. (2013) use a steady state volumetric efficiency (η_{vol}) map to compute the mass flow in the cylinder. With η_{vol} being a function of the air intake pressure and engine speed.

So far the scavenging models that were described were single-zone models. However, multi-zone models are also used to model the gas exchange process. Guan et al. (2015) uses a two-zone model during scavenging and a single-zone model during the blowdown. The two-zone model consists of

a zone containing the exhaust gasses and a zone containing the fresh air. Both zones are modelled as a control volume. To calculate the mass flow rate of the fresh air entering the cylinder, a so-called mixing factor is used which should be calibrated at each load point. Tang et al. (2017) use a three-zone two-phase model. The three zones are a mixing zone, a displacement zone, and a shortcut zone. All three zones coexist during the first phase while only the mixing zone and shortcut zone exist during the second phase. Figure B.4 shows a schematic depiction of this.

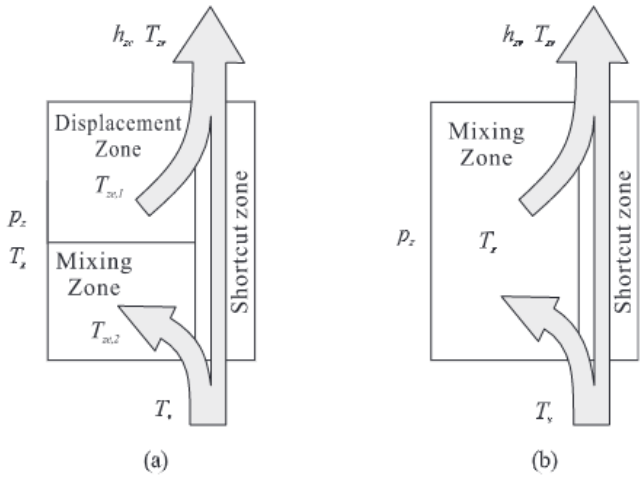

Figure B.4: Three-zone two-phase gas exchange model developed by Tang et al. (2017)

S. Zhu et al. (2020) model the gas exchange process using a bottoming Brayton cycle. A Brayton cycle is normally used for the thermodynamic modelling of gas turbines (Moran et al., 2017).

B.4. In-cylinder process reference model

The engine cycle can be divided into an open and a closed-cylinder process. The open-cylinder process often being referred to as the gas exchange process. The gas exchange process of a two-stroke ICE can be divided into a blowdown, a scavenging, and an expelling process. The reference model models the blowdown as a polytropic process, while it is assumed that temperature does not change during the expelling process. This means that only the volume and the mass within the cylinder will change. Sui Congbiao (2021) concluded two things about the scavenging process, that the process is very important for the performance of a two-stroke ICE, and that a single-zone model using either a perfect displacement or mixing model is not realistic for the prediction of the scavenging process of a two-stroke ICE. Therefore, a two-zone model was developed. Zone A contains exclusively the exhaust gasses, while zone B contains a perfect mixture of exhaust gasses and fresh air. A schematic representation of this two-zone model is shown in figure B.5.

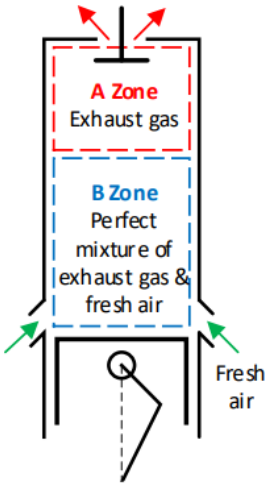

Figure B.5: Scavenging model (Sui Congbiao, 2021)

In addition to this, the scavenging process is divided into two stages. During stage I both zone A and B coexist in the cylinder. Zone A will gradually decrease to zero during stage I, given both the scavenging time and mass flow are sufficient. This means that only zone B exists during stage II. The cylinder is modelled as a control volume with the conservation of both mass and energy applied. The initial size of zone A ($S_A(0)$) is a parameter that is adjusted manually. The size of $S_A(0)$ has a significant effect on the results produced by the model. Increasing the value for $S_A(0)$ means a sharper reduction in the temperature in the cylinder and a lower final temperature. Increasing the value for $S_A(0)$ also results in a higher scavenging efficiency, given sufficient time for scavenging.

Based on the findings that have been discussed the answers to the questions posed at the beginning of this appendix can now be answered.

How are the components of an internal combustion engine generally modelled in a mean value engine model?

MVEMs model the components as a control volume applying the conservation of both mass and energy for all of the engine components (Theotokatos, 2010) (Guan et al., 2015) (Llamas & Eriksson, 2019) (Shen et al., 2020). For components such as the air filter, air intake inlet, and exhaust gas receiver this is sufficient. For the compressor, turbine, and intercooler, no single approach is used. Some of the studied MVEMs use experimental data such as efficiency maps to model these components (Theotokatos, 2010) (Guan et al., 2015) (R. Li et al., 2013) (Llamas & Eriksson, 2019) (Shen et al., 2020) (Alegret et al., 2015). Experimental data can also be used to model the intercooler (Theotokatos, 2010) (Guan et al., 2015) (R. Li et al., 2013) (Llamas & Eriksson, 2019) (S. Zhu et al., 2020), as well as for the turbine (Theotokatos, 2010) (Guan et al., 2015) (R. Li et al., 2013) (Llamas & Eriksson, 2019) (Shen et al., 2020) (Alegret et al., 2015).

For the in-cylinder process, a distinction can generally be made between the open-cylinder process and the closed-cylinder process. The open-cylinder process can be divided into blowdown, scavenging, and expelling. The scavenging process is very important for the overall performance of a two-stroke ICE (Sui Congbiao, 2021). MVEMs apply two general methods for modelling the scavenging process: the perfect mixing and the perfect displacement model. Using either one of these approaches on their own is not an accurate representation of the scavenging process (Sui Congbiao, 2021). This is why most of the studied MVEMs try to combine the two methods along with a single-zone model (Feng et al., 2019) (Llamas & Eriksson, 2019) (Alegret et al., 2015), (R. Li et al., 2013). Other MVEMs apply a two-zone (Guan et al., 2015) or even a three-zone (Tang et al., 2017) model for scavenging. Including multiple zones can make the model more accurate but increases the model's computational load.

How do the methods used in the reference model compare to those generally used in a mean value engine model?

The reference model applies many of the same methods that are used in the MVEMs found in the studied literature. The model uses a network of volume and resistance elements for the components for which the conservation of mass and energy is applied. For the compressor and turbine efficiency maps are used and for the intercooler the effectiveness. The model applies a two-zone model for the scavenging process of the engine, while the closed-cylinder process is modelled using an air standard analysis. Overall the reference model can be placed more on the complex side if it is placed into the spectrum of MVEMs. The two-zone scavenging model is an expansion compared to some of the studied MVEMs from the literature.

C

Emissions

This appendix contains information about emissions. This topic was originally included in the studied literature of this thesis. However, it did not prove to be relevant for the main research part. The emissions were studied for both diesel combustion as well as ammonia dual-fuel combustion. The topics are discussed in sections C.1 and C.2 respectively. The main focus will be on NO_x emissions, since both the combustion of diesel and ammonia produce these emissions. The definition of the symbols, abbreviations, and subscripts used in this section can be found in the nomenclature of this report.

C.1. Emissions diesel combustion

As was mentioned in chapter 1, emissions have become a relevant topic of scientific discussion, especially greenhouse gas (GHG) emissions such as CO_2 in recent years. However, CO_2 emissions are far from the only pollutant emissions of an Internal Combustion Engine (ICE), other examples examples are NO_x, SO_x, HC, C, CO, and PM (Stapersma, 2010e). In addition to the goals set out by the International Maritime Organization (IMO) to reduce GHG emissions, the IMO has also implemented regulations which limit the NO_x emissions allowed and the Sulphur content allowed in Marine fuels (Chu Van et al., 2019). Chapter 4 has discussed how ignition and injection strategies respectively can influence the emissions produced by the ICE. Other methods to reduce emissions consist of Exhaust Gas Recirculation (EGR) and Selective Catalytic Reduction (SCR) to reduce NO_x emissions (Chu Van et al., 2019), oxidising catalysts to reduce both CO as well as HC emissions (Stapersma, 2010e), and implementing scrubber technology to remove SO_x and PM (Abadie et al., 2017). Chapter 3 stated that an MVEM is not capable of predicting the emissions of an ICE because it generally neglects in-cylinder variations. However, several attempts have been made throughout the studied literature. S. Zhu et al. (2020) stated that if the goal is to predict the engine performance and emissions then a 0D model with more complexity and a higher computational load is required. Theotokatos et al. (2018) stated that for the accurate prediction of emissions multi-zone combustion models are required in combination with emission kinetic models. Both will increase the model complexity and computational load. Asprion et al. (2013) state that an empirical model or a combination of a physical and empirical model can also be used to estimate the emissions produced.

Guardiola et al. (2015) propose a model that calculates the NO_x emissions for a system which includes EGR. The model is a combination between an empirical and a physics-based model. The model takes into account the variations for steady-state operations with empirically calibrated factors. These factors take into account the variations in ambient conditions, engine temperature, air intake temperature, and air intake mass flow. These factors are calibrated based on available engine maps. For dynamic operations, another empirically calibrated factor is taken into account. This factor corrects the predicted emissions based on the in-cylinder temperature. The model ignores any variation in the fuel injection settings. The model has a mean relative error of around 7% for steady-state operations, with an error of around 30% for low NO_x emissions and around 10% for high NO_x emissions. The mean relative error for dynamic operations is less than 10%. The authors conclude that based on the low calibration effort and accuracy of the results the model is a feasible method for EGR control and onboard diagnosis of

NO_x emissions. Molina et al. (2014) constructed a model that applies Response Surface Methodology. The NO_x emissions are calculated based on the mass of the fuel injected, intake oxygen mass fraction and the different burn angles. Burn angles (B%) are angles that indicate at what angular position the different mass fractions are burned. These angles are based on the mass of the fuel injected, intake oxygen mass fraction, the start of the main injection, the start of the pilot injection, air intake pressure, and the fuel injection pressure. If the model is calibrated with experimental data for the in-cylinder pressure the mean error of the predicted NO_x emissions is 6%. Maroteaux and Saad (2015) constructed a two-zone combustion model. The model includes an unburned and a burned zone. This design was chosen as a compromise between multi-zone spray models which require a high computational load and a single-zone model which requires look-up tables. The NO_x emissions are calculated based on the extended Zeldovich mechanism. Results for the NO_x emissions have a mean relative error of around 6.5% compared to measurements. The authors conclude that the model can produce accurate estimations for NO_x emissions for a wide range of engine operations. Asprion et al. (2013) created a separate model to calculate the NO_x emissions of a diesel engine. The model is a combination of an empirical and a physics-based representation. The model that is constructed requires less computational time than an MVEM. The only inputs that are required for the model are the engine speed, injected fuel mass, pressure and composition of the charge air, and the start of combustion with its corresponding pressure and temperature. In terms of accuracy, even during transient operations, the models' relative errors are kept below 10% for the largest possible variation of input parameters. However, the model does not take into account the influence of multiple injections and any fundamental changes to the combustion characteristics. Scappin et al. (2012) created a zero-dimensional model for the prediction of NO_x emissions and the performance of a two-stroke diesel engine. The model uses a two-zone combustion model with one zone containing the remaining cylinder gasses and a zone with combustion. The combustion process is divided into intervals. For each interval, the flame temperature and production composition are calculated. The NO_x emissions are calculated according to the Zeldovich mechanism. The model is validated using two different cases. The first case concludes that the model can predict both the specific fuel consumption and NO_x emissions within a 95% confidence interval. The second case predicts that based on measured engine input data, the model can predict the maximum pressure, the compression pressure, specific fuel consumption, power output per cylinder, and NO_x emissions within an accuracy of 5%. Based on these results, the authors conclude that the model has the desired computational time with sufficient accuracy to predict essential engine parameters.

C.2. Emissions ammonia combustion

Chapter 5 has already discussed to some extent what factors determine the emissions of either ammonia-diesel or ammonia-hydrogen combustion. This section will expand on that. The important exhaust emissions of ammonia-diesel operation are NO_x, N_2O, CO_2 (J. Zhu et al., 2023), unburned ammonia, HC, CO, and soot (Kane et al., 2019). The concerns about the above-mentioned emissions were already discussed in chapter 1. Furthermore, unburned ammonia is an emission that is also present for ammonia-powered CI engines because of the slow flame speed and long quenching distance of ammonia (Dimitriou & Javaid, 2020). J. Zhu et al. (2023) studied the emissions of a large two-stroke marine engine based on the Ammonia Substitution Ratio (ASR) previously mentioned in chap 5. The results are shown in figure C.1.

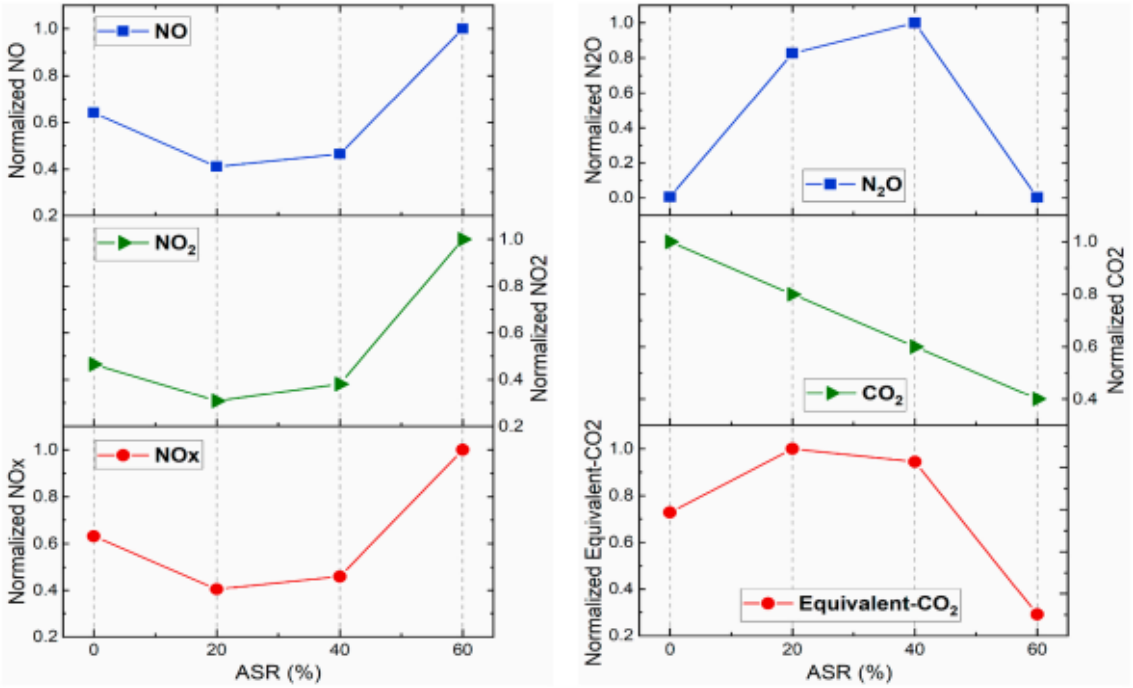

Figure C.1: Emissions of a large two-stroke marine engine using diesel-NH_3 fuel as a function of ASR (J. Zhu et al., 2023)

What can be seen by looking at figure C.1, is that the NO_x emissions first decrease. However, after the ASR exceeds 40%, they start to increase significantly. Reiter and Kong (2011) stated that this would happen when the ammonia fuel energy ratio would exceed 60% This can be explained because first the combustion temperature is lowered by the addition of ammonia reducing the thermal-bound NO_x produced emissions. However, using ammonia means that the NO_x is not exclusively thermal-bound but instead mostly fuel-bound which is why they are also not affected by the compression ratio of the engine (Mounaïm-Rousselle et al., 2022). N_2O shows the opposite kind of behaviour, first increasing because of the addition of ammonia but ultimately decreasing because of the higher combustion temperatures. Kane et al. (2019) stated the same kind of behaviour. The authors designed an engine concept that uses an intake-fumigated ammonia-hydrogen mixture as fuel for a four-stroke engine to allow for high-fuel replacements. The authors conclude that NO_x emissions first decrease as the Ammonia Fuel Fraction (AFF) is increased because the intake air-fuel mixture reduces local hotspots. This reduces the thermal-bound NO_x emissions which offset the fuel-bound NO_x emissions. However, this benefit will diminish itself as AFF increases beyond a certain value (looking at the results roughly beyond 50%) thus increasing the NO_x emissions. Kane et al. (2019) also found that N_2O emissions first increase but later decrease when AFF is increased. The authors finally also looked into the production of CO, HC, and soot emissions and found that CO and HC emissions are increased but soot emissions remain mostly constant as AFF is increased. The trade-off between NO_x and N_2O is very similar to the one between NO_x compared to HC and soot for conventional diesel engines. Important to note, however, is that when the energy is injected into the cylinder, NO_x emissions from dual-fuel mode are significantly higher than for diesel only (Z. Zhang, Long, et al., 2023). According to (Lhuillier et al., 2019), increasing the equivalence ratio will decrease NO emissions while unburned ammonia emissions are increased. It should be noted that this study was conducted for an SI engine. Mounaïm-Rousselle et al. (2022) investigated the emissions for a spark-assisted compression ignition (SACI) engine and found that unburned ammonia emissions increased linearly with the compression ratio of the engine mainly because of fuel trapped in the combustion chamber crevices. Kane et al. (2019) stated that unburned ammonia emissions were the highest for low engine loads because the main driving force for unburned ammonia emissions is the combustion temperature.

The emissions that could be cause for concern from ammonia-hydrogen emissions are N_2O, unburned ammonia, and NO_x, (Zheng, 2020). However, even though ammonia and hydrogen do not contain

carbon, HC and CH_2O can still be formed at high pressures and temperatures due to the reaction of CO_2 and H_2 forming CH_4. The same reaction also contributes to soot production and CO emissions. Soot can also be generated because of incomplete combustion of the engine's lubricant (B. Wang, Yang, Wang, Hu, Duan, et al., 2023). B. Wang, Yang, Wang, Hu, Duan, et al. (2023) looked at the different factors that affected the production of CO and soot and concluded that increasing the compression ratio slightly increases the production of CO and soot while advancing the injection timing increases both significantly. Looking at the NO_x, NO_2 and N_2O emissions, all three either increase slightly or do not change at all if the compression ratio is increased. If the injection timing is advanced, NO_x and NO_2 emissions decrease while N_2O emissions increase. This is probably due to the lower combustion temperature that is achieved when the fuel injection timing is advanced. This behaviour is thus similar to the behaviour of ammonia-diesel combustion. Y. Wang et al. (2021) Studied the NO_x emissions as a function of the temperature, equivalence ratio, and hydrogen ratio. The results are shown in figure C.2.

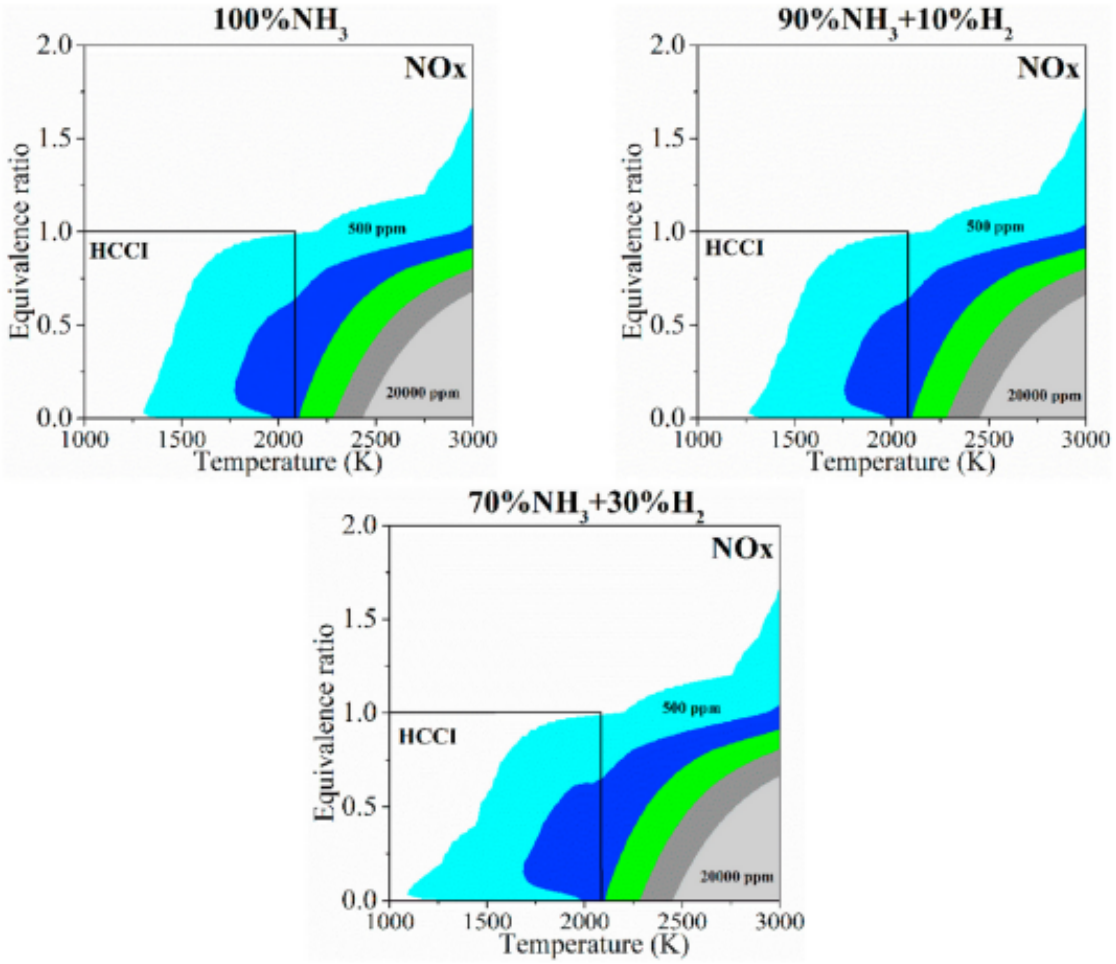

Figure C.2: NO_x emissions as a function of temperature, equivalence ratio, and hydrogen ratio (Y. Wang et al., 2021)

Looking at figure C.2, it seems that the hydrogen ratio does not have a large effect on the NO_x emissions based on the results. The equivalence ratio does have a significant effect on the NO_x emissions. Reducing the temperature still has a slight effect, but not the same as it has for conventional diesel engines. The reason for this was already explained in this section. Some methods that were discussed in chapter 4 try to reduce the NO_x emissions by lowering the combustion temperature. This can be done for example with Exhaust Gas Recirculation (EGR) or Homogeneous Compression Charge Ignition (HCCI). These methods can still be applied to ammonia-fuelled engines. However, because the NO_x emissions for ammonia-fuelled engines are dominated by fuel-bound NO_x instead of thermal-

bound NO_x (J. Li et al., 2014) these methods will not have the same effect. However, Y. Wang et al. (2021) stated that EGR reduces the oxygen concentration in the combustion which will reduce the NO_x emissions. The authors conclude by saying that combining EGR with another after-treatment method would make it possible to eliminate most of the NO_x emissions. Pochet et al. (2017) concludes that full EGR could theoretically be used to cancel fuel-related NO_x emissions but this would require methods to compensate for the loss in combustion efficiency and the use of Selective Catalytic Reduction (SCR) to reduce the N_2O production.

Chapter 6 has answered the following research question:

What are the main similarities and differences between the diesel combustion process and the ammonia combustion process?

With the emission characteristics that were studied in this appendix, the answer given in chapter 6 can be expanded:

During diesel combustion, the main emissions that will be formed are CO_2, NO_x, SO_x, HC, C, CO, and PM (Stapersma, 2010e). For ammonia-diesel combustion the important emissions will be NO_x, N_2O, CO_2 (J. Zhu et al., 2023), unburned ammonia, CO, HC, and soot (Kane et al., 2019). For ammonia-hydrogen, it will be N_2O, unburned ammonia, and NO_x, (Zheng, 2020). NO_x emissions primarily depend on the in-cylinder temperature for diesel combustion. These thermally-bound NO_x emissions remain during ammonia-diesel and ammonia-hydrogen combustion. However, these NO_x will be dominated by the fuel bound NO_x for ammonia-diesel (J. Zhu et al., 2023) and ammonia-hydrogen (Koekkoek, 2021) combustion. This means that some proposed methods for the reduction of NO_x emissions such as Exhaust Gas Recirculation (EGR) and Homogeneous Compression Charge Ignition (HCCI) will not have the same desired effect on the NO_x emissions. N_2O emissions are very important since they have 280 times the Global Warming Potential of CO_2 (United Nations Climate Change, n.d.) over a time span of 20 years. The ammonia-hydrogen ratio does not seem to affect the emissions much, but the equivalence ratio and temperature still influence the emissions (Y. Wang et al., 2021). The ammonia-diesel ratio has a strong influence on the emissions produced. Increasing the ammonia-diesel ratio will increase the NO_x emissions and decrease the N_2O and CO_2 emissions (J. Zhu et al., 2023). For an SI engine, the equivalence ratio influences the NO and unburned ammonia emissions, with an increase in the equivalence ratio reducing the former while the latter is increased. Unburned ammonia emissions also increase for higher compression ratios because of fuel trapped in the combustion chamber crevices (Mounaïm-Rousselle et al., 2022), and at low engine loads since the main driving force for unburned ammonia emissions is the combustion temperature (Kane et al., 2019).

Bibliography

Abadie, L. M., Goicoechea, N., & Galarraga, I. (2017). Adapting the shipping sector to stricter emissions regulations: Fuel switching or installing a scrubber? *Transportation Research Part D: Transport and Environment*, *57*, 237–250. https://doi.org/10.1016/j.trd.2017.09.017

Agarwal, A. K., Srivastava, D. K., Dhar, A., Maurya, R. K., Shukla, P. C., & Singh, A. P. (2013). Effect of fuel injection timing and pressure on combustion, emissions and performance characteristics of a single cylinder diesel engine. *Fuel*, *111*, 374–383. https://doi.org/10.1016/j.fuel.2013.03.016

Alberer, D., Hjalmarsson, H., & del Re, L. (Eds.). (2012). *Identification for Automotive Systems* (Vol. 418). Springer London. https://doi.org/10.1007/978-1-4471-2221-0

Alegret, G., Llamas, X., Vejlgaard-Laursen, M., & Eriksson, L. (2015). Modeling of a large marine two-stroke diesel engine with cylinder bypass valve and EGR system. *IFAC-PapersOnLine*, *28*(16), 273–278. https://doi.org/10.1016/j.ifacol.2015.10.292

Andersen, F. H. (2015). *Integrated Analysis of the Scavenging Process in Marine Two-stroke Diesel Engines* (Doctoral dissertation). Technical University of Denmark. Lyngby.

Annand, W. J. D. (1963). Heat Transfer in the Cylinders of Reciprocating Internal Combustion Engines. *Proceedings of the Institution of Mechanical Engineers*, *177*(1), 973–996. https://doi.org/10.1243/PIME{_}PROC{_}1963{_}177{_}069{_}02

Asprion, J., Chinellato, O., & Guzzella, L. (2013). A fast and accurate physics-based model for the NOx emissions of Diesel engines. *Applied Energy*, *103*, 221–233. https://doi.org/10.1016/j.apenergy.2012.09.038

Atchison, J. (2022). Ammonia-powered vessels & maritime engines: development updates. https://www.ammoniaenergy.org/articles/ammonia-powered-vessels-maritime-engines-development-updates/

Ayvalı, T., Edman Tsang, S. C., & Van Vrijaldenhoven, T. (2021). The Position of Ammonia in Decarbonising Maritime Industry: An Overview and Perspectives: Part I : Technological advantages and the momentum towards ammonia-propelled shipping. *Johnson Matthey Technology Review*, *65*(2), 275–290. https://doi.org/10.1595/205651321X16043240667033

Broatch, A., Olmeda, P., Margot, X., & Escalona, J. (2019). New approach to study the heat transfer in internal combustion engines by 3D modelling. *International Journal of Thermal Sciences*, *138*, 405–415. https://doi.org/10.1016/j.ijthermalsci.2019.01.006

BS MA 100 - 82. (1982). *British Standards Institution Specification for Petroleum Fuels for Marine Oil Engines and Boilers* (tech. rep.). BSI.

Chiong, M.-C., Chong, C. T., Ng, J.-H., Mashruk, S., Chong, W. W. F., Samiran, N. A., Mong, G. R., & Valera-Medina, A. (2021). Advancements of combustion technologies in the ammonia-fuelled engines. *Energy Conversion and Management*, *244*, 114460. https://doi.org/10.1016/j.enconman.2021.114460

Chu Van, T., Ramirez, J., Rainey, T., Ristovski, Z., & Brown, R. J. (2019). Global impacts of recent IMO regulations on marine fuel oil refining processes and ship emissions. *Transportation Research Part D: Transport and Environment*, *70*, 123–134. https://doi.org/10.1016/j.trd.2019.04.001

Clear, J. (n.d.). All Models Are Wrong, Some Are Useful. https://jamesclear.com/all-models-are-wrong#:~:text=In%201976%2C%20a%20British%20statistician,is%20correct%20in%20all%20cases.

Dahlström, J. (2016). *Experimental Investigations of Combustion Chamber Heat Transfer in a Light-Duty Diesel Engine* (Doctoral dissertation). Lund University.

De Cuyper, T., Broekaert, S., Chana, K., De Paepe, M., & Verhelst, S. (2017). Evaluation of empirical heat transfer models using TFG heat flux sensors. *Applied Thermal Engineering*, *118*, 561–569. https://doi.org/10.1016/j.applthermaleng.2017.02.049

Department of Health. (2005). The Facts About Ammonia.

de Vos, P., Somers, L. M. T., Tinga, T., Foekema, E. M., van der Zwaan, B., & Negenvorn, R. R. (2022). The AmmoniaDrive Consortium. *SWZ Maritime 143*, 24–27. http://resolver.tudelft.nl/uuid:dd34837a-65d4-497c-b989-8330887d7d89

de Vries, N. (2019). *REPORT (THESIS) Safe and effective application of ammonia as a marine fuel* (tech. rep.). https://repository.tudelft.nl/

Di Blasio, G., Agarwal, A. K., Belgiorno, G., & Shukla, P. C. (Eds.). (2022). *Clean Fuels for Mobility*. Springer Singapore. https://doi.org/10.1007/978-981-16-8747-1

Dimitriou, P., & Javaid, R. (2020). A review of ammonia as a compression ignition engine fuel. *International Journal of Hydrogen Energy*, *45*(11), 7098–7118. https://doi.org/10.1016/j.ijhydene.2019.12.209

Ding, Y. (2011). *Characterising Combustion in Diesel Engines using parameterised finite stage cylinder process models* (Doctoral dissertation). VSSD. Delft.

Eichelberg, G. (1939). Some new investigations on old combustion engine problems. *Engineering*, *148*, 547–550.

Eichelberg, G. (1922). *Temperaturverlauf und Wärmespannungen in Verbrennungsmotoren* (Doctoral dissertation). ETH Zurich.

Elser, K. (1954). *Der instationäre Wärmeübergang in Dieselmotoren: theoretische und experimentelle Untersuchungen.* Leemann.

Faber, J., Hanayama, S., Shuang, Z., Pereda, P., Comer, B., Hauerhof, E., Schim van der Loeff, W., Smith, T., Zhang, Y., Kosaka, H., Adachi, M., Bonello, J.-M., Galbraith, C., Gong, Z., Koichi, H., Hummels, D., Kleijn, A., Lee, D. S., Liu, Y., … Xing, H. (2021). *Fourth IMO GHG Study 2020 Full Report* (tech. rep.). International Maritime Organization. London.

Feng, Y., Wang, H., Gao, R., & Zhu, Y. (2019). A Zero-Dimensional Mixing Controlled Combustion Model for Real Time Performance Simulation of Marine Two-Stroke Diesel Engines. *Energies*, *12*(10), 2000. https://doi.org/10.3390/en12102000

Finol, C. A., & Robinson, K. (2006). Thermal modelling of modern engines: A review of empirical correlations to estimate the in-cylinder heat transfer coefficient. *Proceedings of the Institution of Mechanical Engineers, Part D: Journal of Automobile Engineering*, *220*(12), 1765–1781. https://doi.org/10.1243/09544070JAUTO202

GAMMA Technologies. (2023). GT-POWER. https://www.gtisoft.com/gt-power/

Gholami, A., Jazayeri, S. A., & Esmaili, Q. (2022). A detail performance and CO2 emission analysis of a very large crude carrier propulsion system with the main engine running on dual fuel mode using hydrogen/diesel versus natural gas/diesel and conventional diesel engines. *Process Safety and Environmental Protection*, *163*, 621–635. https://doi.org/10.1016/j.psep.2022.05.069

Guan, C., Theotokatos, G., & Chen, H. (2015). Analysis of Two Stroke Marine Diesel Engine Operation Including Turbocharger Cut-Out by Using a Zero-Dimensional Model. *Energies*, *8*(6), 5738–5764. https://doi.org/10.3390/en8065738

Guardiola, C., Pla, B., Blanco-Rodriguez, D., & Calendini, P. O. (2015). ECU-oriented models for NOx prediction. Part 1: a mean value engine model for NOx prediction. *Proceedings of the Institution of Mechanical Engineers, Part D: Journal of Automobile Engineering*, *229*(8), 992–1015. https://doi.org/10.1177/0954407014550191

Hendricks, E. (1989). Mean Value Modelling of Large Turbocharged Two-Stroke Diesel Engines. *Journal of Engines*, *98*, 986–998.

Hermann, K., Wüthrich, S., Süess, P., Cartier, P., de Moura, R., & Weisser, G. (2023). Initial investigations into ammonia combustion at conditions relevant for marine engines. *CIMAC Congress*.

Ichikawa, Y., Niki, Y., Takasaki, K., Kobayashi, H., & Miyanagi, A. (2022). NH3 combustion using three-layer stratified fuel injection for a large two-stroke marine engine: Experimental verification of the concept. *Applications in Energy and Combustion Science*, *10*, 100071. https://doi.org/10.1016/j.jaecs.2022.100071

Imhoff, T. B., Gkantonas, S., & Mastorakos, E. (2021). Analysing the performance of ammonia powertrains in the marine environment. *Energies*, *14*(21). https://doi.org/10.3390/en14217447

International Maritime Organization, ((2019). IMO's work to cut GHG emissions from ships.

Jayashankara, B., & Ganesan, V. (2010). Effect of fuel injection timing and intake pressure on the performance of a DI diesel engine – A parametric study using CFD. *Energy Conversion and Management*, *51*(10), 1835–1848. https://doi.org/10.1016/j.enconman.2009.11.006

Ji, W., Li, A., Lu, X., Huang, Z., & Zhu, L. (2019). Numerical study on NOx and ISFC co-optimization for a low-speed two-stroke engine via Miller cycle, EGR, intake air humidification, and injection strategy implementation. *Applied Thermal Engineering*, *153*, 398–408. https://doi.org/10.1016/j.applthermaleng.2019.03.035

Jurić, Z., Kutija, R., Vidović, T., & Radica, G. (2022). Parameter Variation Study of Two-Stroke Low-Speed Diesel Engine Using Multi-Zone Combustion Model. *Energies*, *15*(16), 5865. https://doi.org/10.3390/en15165865

Kane, S. P., Zarling, D., & Northrop, W. F. (2019). Thermochemical and Sensible Energy Recuperation Using Thermally-Integrated Reactor and Diesel-Ammonia Dual Fueling Strategy. *ASME 2019 Internal Combustion Engine Division Fall Technical Conference*. https://doi.org/10.1115/ICEF2019-7241

Karim, G. A. (2003). Combustion in Gas Fueled Compression: Ignition Engines of the Dual Fuel Type. *Journal of Engineering for Gas Turbines and Power*, *125*(3), 827–836. https://doi.org/10.1115/1.1581894

Kim, K., Roh, G., Kim, W., & Chun, K. (2020). A preliminary study on an alternative ship propulsion system fueled by ammonia: Environmental and economic assessments. *Journal of Marine Science and Engineering*, *8*(3). https://doi.org/10.3390/jmse8030183

Koekkoek, A. A. (2021). *An Ammonia-Fuelled Solid Oxide Fuel Cell-Internal Combustion Engine Hybrid System for Ships* (tech. rep.). http://repository.tudelft.nl/.

Kontoulis, P., Chryssakis, C., & Kaiktsis, L. (2008). Analysis of Combustion and Emissions in a Large Two-Stroke Marine Diesel Engine, Using CFD and T-ϕ Mapping.

Lee, B., & Jung, D. (2016). Thermodynamics-based mean-value engine model with main and pilot injection sensitivity. *Proceedings of the Institution of Mechanical Engineers, Part D: Journal of Automobile Engineering*, *230*(13), 1822–1834. https://doi.org/10.1177/0954407015624525

Lhuillier, C., Brequigny, P., Contino, F., & Mounaïm-Rousselle, C. (2020). Experimental study on ammonia/hydrogen/air combustion in spark ignition engine conditions. *Fuel*, *269*, 117448. https://doi.org/10.1016/j.fuel.2020.117448

Lhuillier, C., BREQUIGNY, P., Contino, F., & Rousselle, C. (2019). Combustion Characteristics of Ammonia in a Modern Spark-Ignition Engine. https://doi.org/10.4271/2019-24-0237

Li, J., Huang, H., Kobayashi, N., He, Z., & Nagai, Y. (2014). Study on using hydrogen and ammonia as fuels: Combustion characteristics and NO _x formation. *International Journal of Energy Research*, *38*(9), 1214–1223. https://doi.org/10.1002/er.3141

Li, R., Huang, Y., Li, G., Han, K., & Song, H. (2013). Calibration and Validation of a Mean Value Model for Turbocharged Diesel Engine. *Advances in Mechanical Engineering*, *5*, 579503. https://doi.org/10.1155/2013/579503

Li, T., Zhou, X., Wang, N., Wang, X., Chen, R., Li, S., & Yi, P. (2022). A comparison between low- and high-pressure injection dual-fuel modes of diesel-pilot-ignition ammonia combustion engines. *Journal of the Energy Institute*, *102*, 362–373. https://doi.org/10.1016/j.joei.2022.04.009

Li, Y., & Kong, S.-C. (2011). Coupling conjugate heat transfer with in-cylinder combustion modeling for engine simulation. *International Journal of Heat and Mass Transfer*, *54*(11-12), 2467–2478. https://doi.org/10.1016/j.ijheatmasstransfer.2011.02.015

Lindsey, R., & Blunden, J. (2023). Climate Change: Global Temperature. https://www.climate.gov/news-features/understanding-climate/climate-change-global-temperature

Lindstrand, N. (n.d.). Unlocking ammonia's potential for shipping. https://www.man-es.com/discover/two-stroke-ammonia-engine

Liu, L., Tan, F., Wu, Z., Wang, Y., & Liu, H. (2022). Comparison of the combustion and emission characteristics of NH3/NH4NO2 and NH3/H2 in a two-stroke low speed marine engine. *International Journal of Hydrogen Energy*, *47*(40), 17778–17787. https://doi.org/10.1016/j.ijhydene.2022.03.239

Liu, L., Wu, Y., & Wang, Y. (2022). Numerical investigation on the combustion and emission characteristics of ammonia in a low-speed two-stroke marine engine. *Fuel*, *314*, 122727. https://doi.org/10.1016/j.fuel.2021.122727

Llamas, X., & Eriksson, L. (2019). Control-oriented modeling of two-stroke diesel engines with exhaust gas recirculation for marine applications. *Proceedings of the Institution of Mechanical Engineers Part M: Journal of Engineering for the Maritime Environment*, *233*(2), 551–574. https://doi.org/10.1177/1475090218768992

Ma, F., Zhao, C., Zhang, F., Zhao, Z., Zhang, Z., Xie, Z., & Wang, H. (2015). An Experimental Investigation on the Combustion and Heat Release Characteristics of an Opposed-Piston Folded-Cranktrain Diesel Engine. *Energies*, *8*(7), 6365–6381. https://doi.org/10.3390/en8076365

Mallouppas, G., Ioannou, C., & Yfantis, E. A. (2022). A Review of the Latest Trends in the Use of Green Ammonia as an Energy Carrier in Maritime Industry. https://doi.org/10.3390/en15041453

MAN Energy Solutions. (2023). Groundbreaking First Ammonia Engine Test Completed. https://www.man-es.com/company/press-releases/press-details/2023/07/13/groundbreaking-first-ammonia-engine-test-completed

Maroteaux, F., & Saad, C. (2015). Combined mean value engine model and crank angle resolved in-cylinder modeling with NOx emissions model for real-time Diesel engine simulations at high engine speed. *Energy*, *88*, 515–527. https://doi.org/10.1016/j.energy.2015.05.072

Mavrelos, C., & Theotokatos, G. (2018). Numerical investigation of a premixed combustion large marine two-stroke dual fuel engine for optimising engine settings via parametric runs. *Energy Conversion and Management*, *160*, 48–59. https://doi.org/10.1016/j.enconman.2017.12.097

Molina, S., Guardiola, C., Martín, J., & García-Sarmiento, D. (2014). Development of a control-oriented model to optimise fuel consumption and NOX emissions in a DI Diesel engine. *Applied Energy*, *119*, 405–416. https://doi.org/10.1016/j.apenergy.2014.01.021

Moran, M. J., Shapiro, H. N., Boettner, D. D., & Bailey, M. B. (2017). *Moran's principles of engineering thermodynamics* (9th ed.). John Wiley & Sons, Inc.

Mounaïm-Rousselle, C., Mercier, A., Brequigny, P., Dumand, C., Bouriot, J., & Houillé, S. (2022). Performance of ammonia fuel in a spark assisted compression Ignition engine. *International Journal of Engine Research*, *23*(5), 781–792. https://doi.org/10.1177/14680874211038726

Muše, A., Jurić, Z., Račić, N., & Radica, G. (2020). Modelling, performance improvement and emission reduction of large two-stroke diesel engine using multi-zone combustion model. *Journal of Thermal Analysis and Calorimetry*, *141*(1), 337–350. https://doi.org/10.1007/s10973-020-09321-7

Nadeau, K. C., Agache, I., Jutel, M., Annesi Maesano, I., Akdis, M., Sampath, V., D'Amato, G., Cecchi, L., Traidl□Hoffmann, C., & Akdis, C. A. (2022). Climate change: A call to action for the United Nations. *Allergy*, *77*(4), 1087–1090. https://doi.org/10.1111/all.15079

Nemati, A., Ong, J. C., & Walther, J. H. (2022). CFD analysis of combustion and emission formation using URANS and LES under large two-stroke marine engine-like conditions. *Applied Thermal Engineering*, *216*, 119037. https://doi.org/10.1016/j.applthermaleng.2022.119037

Niki, Y., Hirata, K., Kobayashi, K., & Shimizu, Y. (2023). Development of premixed ammonia combustion strategy with minimum emissions for marine diesel engines. *CIMAC Congress*.

Oba, H., Ito, K., Matsuda, C., Ichikawa, Y., Niki, Y., & Takasaki, K. (2023). Fundamental study of the effect of stratified NH3 injection system for nitrogen compounds reduction. *CIMAC Congress*.

Paykani, A., Kakaee, A.-H., Rahnama, P., & Reitz, R. D. (2016). Progress and recent trends in reactivity-controlled compression ignition engines. *International Journal of Engine Research*, *17*(5), 481–524. https://doi.org/10.1177/1468087415593013

Pochet, M., Truedsson, I., Foucher, F., Jeanmart, H., & Contino, F. (2017). Ammonia-Hydrogen Blends in Homogeneous-Charge Compression-Ignition Engine. https://doi.org/10.4271/2017-24-0087

Prevljak, N. H. (2022). World's first all-electric fast ferry named in Norway. https://www.offshore-energy.biz/worlds-first-all-electric-fast-ferry-named-in-norway/

Rakopoulos, C. D., & Giakoumis, E. G. (2006). *Review of Thermodynamic Diesel Engine Simulations under Transient Operating Conditions* (tech. rep.).

Rakopoulos, C., Kosmadakis, G., & Pariotis, E. (2010). Critical evaluation of current heat transfer models used in CFD in-cylinder engine simulations and establishment of a comprehensive wall-function formulation. *Applied Energy*, *87*(5), 1612–1630. https://doi.org/10.1016/j.apenergy.2009.09.029

Raptotasios, S. I., Sakellaridis, N. F., Papagiannakis, R. G., & Hountalas, D. T. (2015). Application of a multi-zone combustion model to investigate the NOx reduction potential of two-stroke marine diesel engines using EGR. *Applied Energy*, *157*, 814–823. https://doi.org/10.1016/j.apenergy.2014.12.041

Reiter, A. J., & Kong, S.-C. (2008). Demonstration of Compression-Ignition Engine Combustion Using Ammonia in Reducing Greenhouse Gas Emissions. *Energy & Fuels*, *22*(5), 2963–2971. https://doi.org/10.1021/ef800140f

Reiter, A. J., & Kong, S.-C. (2011). Combustion and emissions characteristics of compression-ignition engine using dual ammonia-diesel fuel. *Fuel*, *90*(1), 87–97. https://doi.org/10.1016/j.fuel.2010.07.055

Sapra, H., Godjevac, M., De Vos, P., Van Sluijs, W., Linden, Y., & Visser, K. (2020). Hydrogen-natural gas combustion in a marine lean-burn SI engine: A comparitive analysis of Seiliger and double Wiebe function-based zero–dimensional modelling. *Energy Conversion and Management*, *207*, 112494. https://doi.org/10.1016/j.enconman.2020.112494

Scappin, F., Stefansson, S. H., Haglind, F., Andreasen, A., & Larsen, U. (2012). Validation of a zero-dimensional model for prediction of NOx and engine performance for electronically controlled marine two-stroke diesel engines. *Applied Thermal Engineering*, *37*, 344–352. https://doi.org/10.1016/j.applthermaleng.2011.11.047

Scharl, V., & Sattelmayer, T. (2022). Ignition and combustion characteristics of diesel piloted ammonia injections. *Fuel Communications*, *11*, 100068. https://doi.org/10.1016/j.jfueco.2022.100068

Schulten, P. J. M., & Stapersma, D. (2003). Mean Value Modelling of the Gas Exchange of a 4-stroke Diesel Engine for Use in Powertrain Applications. https://doi.org/10.4271/2003-01-0219

Seol, J.-H., Pham, V. C., & Lee, W.-J. (2021). Effects of the Multiple Injection Strategy on Combustion and Emission Characteristics of a Two-Stroke Marine Engine. *Energies*, *14*(20), 6821. https://doi.org/10.3390/en14206821

Shen, H., Zhang, J., Yang, B., & Jia, B. (2020). Development of a Marine Two-Stroke Diesel Engine MVEM with In-Cylinder Pressure Trace Predictive Capability and a Novel Compressor Model. *Journal of Marine Science and Engineering*, *8*(3), 204. https://doi.org/10.3390/jmse8030204

Sigurdsson, E., Ingvorsen, K., Jensen, M., Mayer, S., Matlok, S., & Walther, J. (2014). Numerical analysis of the scavenge flow and convective heat transfer in large two-stroke marine diesel engines. *Applied Energy*, *123*, 37–46. https://doi.org/10.1016/j.apenergy.2014.02.036

Sitkei, G. (1962). Beitrag zur Theorie des Wärmeüberganges im Motor Konstruktion. *Konstruktion*, *14*(2), -67.

Stapersma, D. (2010a). *Diesel Engines Volume 6: Thermodynamic principles II*.

Stapersma, D. (2010b). *Diesel Engines Volume 1 Performance Analysis* (8th ed.). NLDA & Delft UT.

Stapersma, D. (2010c). *Diesel Engines Volume 2 Turbocharging* (8th ed.). NLDA & Delft UT.

Stapersma, D. (2010d). *Diesel Engines Volume 3 Combustion* (6th ed.). NLDA & Delft UT.

Stapersma, D. (2010e). *Diesel Engines Volume 4 Emissions and Heat Transfer* (6th ed.). NLDA & Delft UT.

Stapersma, D., & Klein Woud, H. (2002). *Design of Propulsion and Electric Power Generation Systems*. IMarEST.

Stone, R. (1999). *Introduction to Internal Combustion Engines*. Macmillan Education UK. https://doi.org/10.1007/978-1-349-14916-2

Sui, C., Song, E., Stapersma, D., & Ding, Y. (2017). Mean value modelling of diesel engine combustion based on parameterized finite stage cylinder process. *Ocean Engineering*, *136*, 218–232. https://doi.org/10.1016/j.oceaneng.2017.03.029

Sui Congbiao. (2021). *Energy Effectiveness and Operational Safety of Low-Powered Ocean-going Cargo Ship in Various (Heavy) Operating Conditions Congbiao SUI □□□* (tech. rep.).

Sun, X., Liang, X., Shu, G., Wang, Y., Wang, Y., & Yu, H. (2017). Effect of different combustion models and alternative fuels on two-stroke marine diesel engine performance. *Applied Thermal Engineering*, *115*, 597–606. https://doi.org/10.1016/j.applthermaleng.2016.12.093

Tang, Y., Zhang, J., Gan, H., Jia, B., & Xia, Y. (2017). Development of a real-time two-stroke marine diesel engine model with in-cylinder pressure prediction capability. *Applied Energy*, *194*, 55–70. https://doi.org/10.1016/j.apenergy.2017.03.015

Tech HK. (2023). Medstraum | The World's First 100% Electric High-Speed Ferry. https://www.youtube.com/watch?v=3TaCke228oc

Thacker, B. H., Doebling, S. W., Hemez, F. M., Anderson, M. C., Pepin, J. E., & Rodriguez, E. A. (2004). *Concepts of Model Verification and Validation* (tech. rep.). Los Alamos National Laboratory. Los Alamos.

Theotokatos, G. (2010). On the cycle mean value modelling of a large two-stroke marine diesel engine. *Proceedings of the Institution of Mechanical Engineers Part M: Journal of Engineering for the Maritime Environment*, *224*(3), 193–205. https://doi.org/10.1243/14750902JEME188

Theotokatos, G., Guan, C., Chen, H., & Lazakis, I. (2018). Development of an extended mean value engine model for predicting the marine two-stroke engine operation at varying settings. *Energy*, *143*, 533–545. https://doi.org/10.1016/j.energy.2017.10.138

United Nations Climate Change. (n.d.). Global Warming Potentials (IPCC Second Assessment Report). https://unfccc.int/process/transparency-and-reporting/greenhouse-gas-data/greenhouse-gas-data-unfccc/global-warming-potentials

van Duijn, J. (2021). *Modelling diesel-ammonia two-stroke engines* (Doctoral dissertation). Delft University of Technology. Delft.

Wang, B., Yang, C., Wang, H., Hu, D., Duan, B., & Wang, Y. (2023). Study on injection strategy of ammonia/hydrogen dual fuel engine under different compression ratios. *Fuel*, *334*, 126666. https://doi.org/10.1016/j.fuel.2022.126666

Wang, B., Yang, C., Wang, H., Hu, D., & Wang, Y. (2023). Effect of Diesel-Ignited Ammonia/Hydrogen mixture fuel combustion on engine combustion and emission performance. *Fuel*, *331*, 125865. https://doi.org/10.1016/j.fuel.2022.125865

Wang, Y., Zhou, X., & Liu, L. (2021). Theoretical investigation of the combustion performance of ammonia/hydrogen mixtures on a marine diesel engine. *International Journal of Hydrogen Energy*, *46*(27), 14805–14812. https://doi.org/10.1016/j.ijhydene.2021.01.233

Wang, Y., Zhou, X., & Liu, L. (2023). Feasibility study of hydrogen jet flame ignition of ammonia fuel in marine low speed engine. *International Journal of Hydrogen Energy*, *48*(1), 327–336. https://doi.org/10.1016/j.ijhydene.2022.09.198

Wärtsilä Corporation. (2022). Wärtsilä coordinates EU funded project to accelerate ammonia engine development. https://www.wartsila.com/media/news/05-04-2022-wartsila-coordinates-eu-funded-project-to-accelerate-ammonia-engine-development-3079950

Wermuth, N., Malin, M., Schubert-Zallinger, C., Engelmayer, M., Wimmer, A., Schlick, H., & Kammerdiener, T. (2023). Decarbonization of high-power systems: ammonia-hydrogen and ammonia-diesel combustion in HS engines. *CIMAC Congress*.

Woschni, G. (1967). A Universally Applicable Equation for the Instantaneous Heat Transfer Coefficient in the Internal Combustion Engine. https://doi.org/10.4271/670931

Wu, Y., Liu, L., Wang, Y., & Wu, J. (2023). The effect of injection strategy on combustion and emissions of ammonia Marine engine. *CIMAC Congress*.

Xin, Q. (, & Zheng, J. (2009). Theoretical Analysis of Internal Combustion Engine Miscellaneous Heat Losses. https://doi.org/10.4271/2009-01-2881

Yao, M., Zheng, Z., & Liu, H. (2009). Progress and recent trends in homogeneous charge compression ignition (HCCI) engines. *Progress in Energy and Combustion Science*, *35*(5), 398–437. https://doi.org/10.1016/j.pecs.2009.05.001

Yousefi, A., Guo, H., Dev, S., Lafrance, S., & Liko, B. (2022). A study on split diesel injection on thermal efficiency and emissions of an ammonia/diesel dual-fuel engine. *Fuel*, *316*, 123412. https://doi.org/10.1016/j.fuel.2022.123412

Yousefi, A., Guo, H., Dev, S., Liko, B., & Lafrance, S. (2022). Effects of ammonia energy fraction and diesel injection timing on combustion and emissions of an ammonia/diesel dual-fuel engine. *Fuel*, *314*, 122723. https://doi.org/10.1016/j.fuel.2021.122723

Žák, Z., Emrich, M., Takáts, M., & Macek, J. (2016). In-Cylinder Heat Transfer Modelling. *Journal of Middle European Construction and Design of Cars*, *14*(3), 2–10. https://doi.org/10.1515/mecdc-2016-0009

Zhang, E., Liang, X., Zhang, F., Yang, P., Cao, X., Wang, X., & Yu, H. (2019). Evaluation of Exhaust Gas Recirculation and Fuel Injection Strategies for Emission Performance in Marine Two-Stroke Engine. *Energy Procedia*, *158*, 4523–4528. https://doi.org/10.1016/j.egypro.2019.01.872

Zhang, Y., Xu, L., Zhu, Y., Xu, S., & Bai, X.-S. (2023). Numerical study on liquid ammonia direct injection spray characteristics under engine-relevant conditions. *Applied Energy*, *334*, 120680. https://doi.org/10.1016/j.apenergy.2023.120680

Zhang, Y., Yan, Y., Yang, R., Wang, Q., Zhang, B., Gan, Q., Liu, Z., & Fu, J. (2022). Study of In-Cylinder Heat Transfer Boundary Conditions for Diesel Engines Under Variable Altitudes Based on the CHT Model. *Frontiers in Energy Research*, *10*. https://doi.org/10.3389/fenrg.2022.828215

Zhang, Z., Long, W., Dong, P., Tian, H., Tian, J., Li, B., & Wang, Y. (2023). Performance characteristics of a two-stroke low speed engine applying ammonia/diesel dual direct injection strategy. *Fuel*, *332*, 126086. https://doi.org/10.1016/j.fuel.2022.126086

Zhang, Z., Chen, W., Wei, W., Zhang, H., & Li, G. (2023). Effects of Fuel Ratio and Injection Strategy on Ammonia -Diesel Engine. *CIMAC Congress*.

Zhao, F., Assanis, D. N., Asmus, T. N., Dec, J. E., Eng, J. A., & Najt, P. M. (2003). *Homogeneous Charge Compression Ignition Engines*. SAE International.

Zheng, X. S. (2020). *An investigation of hydrogen-ammonia combustion inside internal combustion engines* (tech. rep.). http://repository.tudelft.nl/.

Zhou, S., Zhou, H., Xi, H., Zhou, W., Zhu, Y., & Feng, Y. (2023). Research on combustion and emission characteristics of marine ammonia engine. *CIMAC Congress*.

Zhu, J., Zhou, D., Yang, W., Qian, Y., Mao, Y., & Lu, X. (2023). Investigation on the potential of using carbon-free ammonia in large two-stroke marine engines by dual-fuel combustion strategy. *Energy*, *263*, 125748. https://doi.org/10.1016/j.energy.2022.125748

Zhu, S., Gu, Y., Yuan, H., Ma, Z., & Deng, K. (2020). Thermodynamic analysis of the turbocharged marine two-stroke engine cycle with different scavenging air control technologies. *Energy*, *191*, 116533. https://doi.org/10.1016/j.energy.2019.116533